Modeling the Relation between Suction, Effective Stress and Shear Strength in Partially Saturated Granular Media

by
Nabi Kartal Toker

B.S., Civil Engineering (1999)
Middle East Technical University, Ankara, TURKEY

M.S., Civil and Environmental Engineering (2002)
Massachusetts Institute of Technology, Cambridge, MA, USA

Submitted to the Department of Civil and Environmental Engineering
in Partial Fulfillment of the Requirements for the Degree of

Doctor of Philosophy in Civil and Environmental Engineering
at the
Massachusetts Institute of Technology

June 2007

Signature of Author.....
Department of Civil and Environmental Engineering
May, 4, 2007

Certified by.....
John T. Germaine
Senior Research Associate of Civil and Environmental Engineering
Thesis Supervisor

Certified by.....
Patricia J. Culligan
Professor of Civil and Environmental Engineering
Thesis Supervisor

Accepted by.....
Professor Daniele Veneziano
Chairman, Departmental Committee for Graduate Students

Modeling the Relation between Suction, Effective Stress, and Shear Strength in Partially Saturated Granular Media

by
Nabi Kartal Toker

Submitted to the Department of Civil and Environmental Engineering
on May 4, 2007
in Partial Fulfillment of the Requirements for the Degree of
Doctor of Philosophy in Civil and Environmental Engineering

ABSTRACT

Decades of geotechnical research firmly established that the mechanical properties (shear strength and deformation characteristics) of soils are related to soil's "effective stress", i.e. the stress carried by the solid matrix. The remaining stress is carried by the pore fluid in the form of pore pressure. In unsaturated soils, the coexistence of water and air results in negative pore pressure, which are termed "soil suction". A clear link between soil suction and effective stress has not yet been established.

This research develops a model for linking effective stress to total stress and soil suction for uniform, spherical particles, at low water contents. The model includes the analytical formulation of water geometry and forces at the micro-scale. The change in effective stress due to soil suction is estimated from this particle contact scale, taking account of the particle packing. A method for inferring the effective stress in an unsaturated soil from strength test results is also proposed.

In order to examine the partially saturated mechanical behavior of granular materials, a triaxial test setup was modified to accommodate an MIT Tensiometer as its pedestal. Materials consisting of uniform spherical glass beads were tested, under both saturated and unsaturated conditions, at conditions that matched those of the model. In order to accommodate the unique difficulties of constituting a specimen made of glass beads, new test preparation procedures were developed. New data correction methods, which are applicable to a broad range of triaxial test measurements, were also proposed.

With the experimental program, new behavioral features unique to the glass beads were observed. Coupling saturated and unsaturated shear strength via the proposed method also enabled the effects of suction on effective stress to be inferred. Experimentally obtained increases in effective stress due to suction were significantly larger than those estimated by the model. However, many observed aspects of unsaturated behavior were in parallel to those predicted by the model. Therefore, discrepancies between observations and the theory developed here might originate from the method used to link effective stress to shear strength, leaving merit to the main model for effective stress in partially saturated granular media.

Thesis Supervisor: John T. Germaine
Title: Senior Research Associate
MIT

Thesis Supervisor: Patricia J. Culligan
Title: Professor of Civil and Environmental Engineering
Columbia University

ACKNOWLEDGEMENTS

The following people contributed to this work in various ways. My infinite thanks to

Dr. John T. Germaine, for never losing the friendly attitude, even throughout my delays,

Prof. Patricia J. Culligan, for continuing the supervision despite the hurdles of being in another city, and clearest and most to-the-point feedback,

Committee members (Professors Herbert H. Einstein, Andrew J. Whittle and John R. Williams), for all the useful feedback,

US Army Research Office, for funding part of the research,

Steven Rudolph, for manufacturing necessary equipment,

Naeem O. Abdulhadi, for performing part of the triaxial tests,

Cody L. Edwards, for performing the SMC tests,

Antonios Vytiniotis, for acting as liason and printing the thesis,

Cagla Meral, for keeping me sane with her love,

My parents, for their unending patience and support,

All my friends, including the ones mentioned above, for making it bearable with their companionship,

And my sister, for being the light at the end of the tunnel.

CONTENTS

LIST of FIGURES

LIST of TABLES

LIST of SYMBOLS

Chapter 2

h_s	osmotic suction
n/V	total ion concentration (molar)
R	universal gas constant
T	absolute temperature in Kelvins
u_w	pressure in the liquid phase (water)
u_a	pressure in the gas phase (air)
$(u_a - u_w)$	matric suction
ρ, r	orthogonal radii of curvature
β, η	angles on orthogonal planes
κ	mean curvature
σ_{ST}	air-water interfacial tension
σ_{ST}^{o}	uncorrected air-water interfacial tension at current temperature
P_v^{o}	uncorrected absolute vapor pressure at current temperature
V_n	molar volume
σ	normal total stress
σ'	effective stress
χ	parameter between 0 and 1
c_1, c_2, c_3	coefficients of an ellipsoid
y, x	variables
τ	shear strength
c'	cohesion
ϕ'	angle of internal friction
S	degree of saturation
ΔS	change in degree of saturation
S_r	residual saturation
u_{AE}	air entry pressure
$(\sigma_n - u_a)$	net normal stress
ϕ_b'	angle of shearing resistance
a_w	normalized area of water
A_w	area of pore water at a particular degree of saturation
A_{tw}	area of pore water at complete saturation
f',k	fitting parameters
ω	average coordination number
n	porosity
e	void ratio
$(\sigma'-\sigma)$	effective stress increment due to suction
y_x	partial derivative of y with respect to x
y_{xx}	partial second derivative of y with respect to x

Chapter 3

α	half of the inclusive angle of a pendular ring

θ	angle of intersection
x, y	coordinates
$y_{ring}(x)$	pendular ring coordinates
$y_{grain}(x)$	grain surface coordinates
(x_b,y_b)	coordinates where air-water interface touches grain surface
R	particle radius
a	neck radius of exact pendular ring
b	neck radius of torus approximation to pendular ring
r	second radius of torus approximation to pendular ring
κ	mean curvature
κ_1	principal curvature
κ_{xy}	curvature in the x-y plane
y_x	partial derivative of y with respect to x
y_{xx}	partial second derivative of y with respect to x
κ_{yz}	curvature in y-z plane
κ_2	second principal curvature
$(u_a - u_w)$	matric suction
A	cross-sectional area at the neck
V	volume of a rotational (around x-axis) body
F	magnitude of resultant water force
σ_{ST}	air-water interfacial tension
$(\sigma'-\sigma)$	effective stress increment due to water
$\vec{F}_{resultant}$	resultant water force
$A_{element}$	area of a repeatable planar element bisecting one particle.
D	particle diameter
τ	shear strength
c'	cohesion
χ	Bishop's coefficient
ϕ'	angle of internal friction
$(\sigma_n - u_a)$	net normal stress
ϕ_b'	angle of unsaturated shearing resistance
a_w	normalized area of water
π	osmotic suction
ω	average coordination number
e	void ratio

Chapter 4

V_{ref}	reference voltage
V_{in}	input voltage
R_1,R_2	resistance
K_m	axial stiffness of membrane
E_m	elastic modulus of membrane

A_m	cross sectional area of membrane
P_m	unstretched perimeter of membrane
CF	calibration factor
V_{out}	output voltage

Chapter 5

H_o	initial specimen height
w_p	preparation water content
[1]	mass of the scoop + glass beaker
[2]	mass of scoop + beaker + dry sample
[3]	mass of scoop + beaker + moist sample
m_{dry}	dry mass of the specimen
A_o	initial area
σ_c	confinement stress
σ_c'	effective confinement stress
ΔH	axial displacement
ΔV	volume change, in saturated tests only
F_{read}	axial load reading
σ_{cell}	cell pressure
u	pore pressure, in saturated tests only
$u_a - u_w$	matric suction, in unsaturated tests with tensiometer
D_o	initial specimen diameter
V_o	initial specimen volume
A_f	final area of the specimen
$(V_f)_a$	apparent final volume of the specimen
e_{ini}	initial void ratio
G_s	specific gravity of specimen
ε_x	Axial strain
ε_v	Volumetric strain
A_c	specimen area with cylindirical correction
A	specimen area
A_p	specimen area with parabolic correction
A_{pf}	final specimen area with parabolic correction
K_m	stiffness of the membrane
F_m	axial force carried by the membrane
σ_m	radial pressure applied by the membrane
ε_{mx}	initial axial strain of the membrane during setup
H_{mo}	initial membrane height
P_m	unstretched perimeter of the membrane
ε_{mv}	initial volume strain of the membrane
F	corrected axial force
σ_x	corrected axial total stress
σ_r	corrected radial total stress
σ_x'	corrected axial effective stress
σ_r'	corrected radial effective stress

σ_{oct}	octahedral or mean stress
2q	deviatoric stress
x, y	coordinate system for curvature calculations for yield stress determination
y_x	partial derivative of y with respect to x
y_{xx}	partial second derivative of y with respect to x
κ_{xy}	curvature in the x-y plane
κ_s	smoothened curvature
W_x	work done by axial stress
W_r	work done by radial stress

Chapter 6

G_s	specific gravity
2q	deviatoric stress
σ_c	confinement stress
ϵ_{vfinal}	final volumetric strain
e_{final}	final void ratio
ϵ_{axial}	axial strain
wc_{ini}	preparation water content

Chapter 7

2q	deviatoric stress
σ_c	confinement stress
ϵ_{axial}	axial strain
$(\sigma'-\sigma)$	stress increment due to water
ϕ,ϕ'	angle of internal friction
σ_{oct}	octahedral or mean stress
σ_{oct}'	effective octahedral or mean stress
M	slope of strength envelope
e	void ratio

1 INTRODUCTION

1. INTRODUCTION

Since the early twentieth century, geotechnical engineering has been based on the characterization of soil as a two-phase medium (solid+water or solid+air). However, a significant portion of geotechnical engineering problems involve partially saturated soils, which are three-phase media (solid+water+air) with significant behavioral differences from purely two-phase systems. Due to the existence of air and water together in the pore space, phenomena that are impossible to observe in two-phase media, such as capillarity due to the surface tension of water at a water-air interface, affect both the soil parameters and soil behavior. As a result, partially saturated soils present a variety of engineering challenges that require tools that go beyond those available for saturated soil mechanics. Example challenges include problems associated with rainfall induced failures (especially in slopes), expansive soils, and trafficability in semi-arid regions. The interest in such partially saturated problems started in the late 1950's, and has increased in the last decades (Fredlund & Rahardjo, 1993).

1.1. Problem Statement

The most significant difference between saturated and unsaturated soil mechanics is the negative water pressures, called *soil suction* (the exact definition of soil suction is given in detail in *Section 2.1.2*). This variable replaces the pore pressure, and blurs the concept of effective stress (i.e. stress carried by the solid matrix – *Section 2.3*). The principle of effective stress forms the basis of much of modern soil mechanics (Graham et al., 1992), as this principle governs the strength and deformation properties of dry and saturated soils. Due to its practicality, the principle of effective stress is a cornerstone of current geotechnical engineering practice. Although there is no method of measuring the magnitudes of effective stresses directly, it is possible to calculate effective stress in the case of saturated and dry soils. It the saturated case, water is assumed to act hydrostatically around each particle. In dry soils the pore fluid, air, is assumed to be at atmospheric pressure.

The applicability of the effective stress principle to partially saturated soils (Bishop, 1959) is often contested (Burland, 1964; Matyas & Radakrishna, 1968; Fredlund & Morgenstern, 1977; Alonso et al, 1990; Fredlund, 2006) despite the fact that there has been very little research on the fundamental concept of effective stress or determination of its magnitude in unsaturated media. The majority of partially saturated soil research introduces soil suction as a separate stress variable to provide a practical solution for engineering application. This approach is not as fundamentally sound as use of the effective stress principle of saturated soil mechanics. Furthermore, two additional incentives to adopt the use of the effective stress concept in saturated soil mechanics are discussed in the following paragraphs.

First, effective stress is defineable for partially saturated soils, because the solid matrix of such soils carry stress. There is no proof that the mechanical behavior of a partially saturated soil differs from that of the saturated version of the exact same soil with the exact same effective stress. On the other hand, there is currently no proven method to compute the effective stress. Thus, the prevalent denouncement of the effective stress principle for unsaturated soils seems due more to an inability to quantify the effective stress itself, than to a fundemental flaw with the principle.

Second, while many ways of analyzing the mechanical behavior of partially saturated soils have been suggested, none of them unifies the practice the way effective stress does for the mechanics of two-phase soils. A framework that is not fundamentally well-defined has to change itself for every different kind of soil, or even for different states of the same soil. If any framework for partially saturated soils is to gain widespread usage, it has to somehow be linked to the well-established foundations of soil mechanics, which primarily mean that it has to be based upon effective stress.

Building an effective stress principle for partially saturated soils would provide a more unified framework and a more consistent approach throughout soil mechanics. The few researchers (Houlsby, 1997; Li, 2003; Berney, 2004; each discussed in *chapter 2*), who express effective stress explicitly or implicitly, rely on mathematics and/or physics far too advanced for any purpose other than research. Thus, need for practicality is an additional aspect that needs to be addressed in the development of the unified framework.

1.2. Research Goals

The primary aim of this research is to increase our understanding of the mechanics of unsaturated particulate materials by defining and formulating a methodology to utilize the effective stress concept to describe partially saturated soil behavior. The following sections present an overview of this research with the superscripts in the text referring to specific boxes in *Figure 1*.

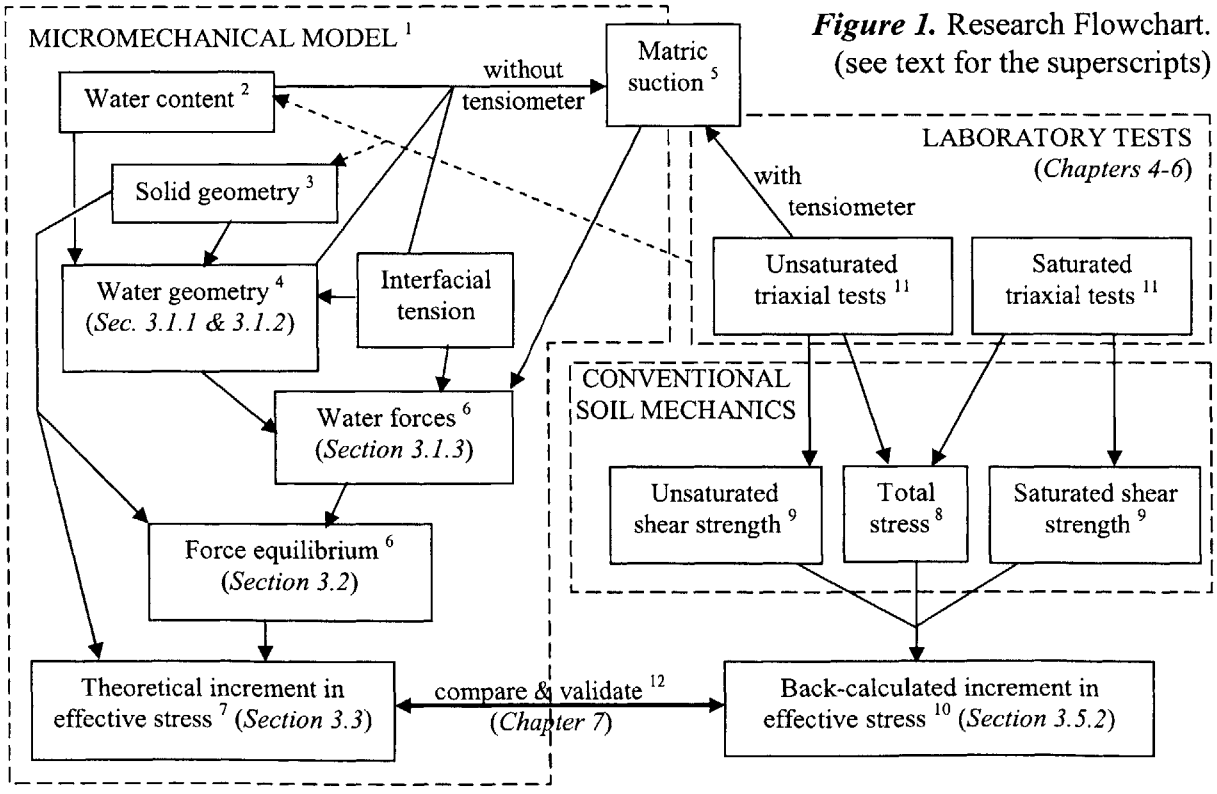

Figure 1. Research Flowchart. (see text for the superscripts)

1.2.1. Calculation of Effective Stress in Unsaturated Soils

A micromechanical model [1] to compute the increment of effective stress from the saturated to the unsaturated state will be proposed for particulate systems of uniform (mono-disperse) spheres. For a given water content [2] and void ratio [3], the pore water geometry [4] and stress (suction) [5] will be calculated. Theoretical values of upper and lower limits of effective stress increment due to suction will be computed (as well as an intermediate geometry) for uniform packings of uniform granular materials, from the analytical solutions for contact forces [6] on individual particles. Depending on where the packing of the sample in question lies with respect to the uniform packings, the increment in effective stress [7] caused by water forces can be estimated.

1.2.2. Experimental Verification

Although there is no direct method of effective stress determination, it is possible to deduce effective stresses in unsaturated soils by comparing the measured applied (total) stresses [8] on unsaturated soils with the calculated effective stresses on saturated soils, following similar stress paths (Towner, 1983) (this is discussed in greater detail in *section 3.5.2*). Following this logic, the main focus of the experimental program is to observe the increment in strength [9], associated with suction, and then infer the increment in effective stress [10]. As Towner suggested, experiments (triaxial strength tests) on both [11] saturated and unsaturated specimen, with similar stress paths, will be performed. These experimental results will then be compared [12] to the increment in effective stress range predicted in the hypothetical part of the research [7]. Note that the lack of success in the experimental program would not automatically disprove the main model linking suction to effective stress, as the link between effective stress and shear strength for unsaturated materials may also be source of discrepancies. Sample materials that are as close to the assumed ideal case as possible (i.e. uniformly sized, rigid, smooth, inert spheres) will be selected for the experiments. As will become apparent in the following chapters, the expected difference between saturated and unsaturated materials is of a similar order of magnitude as some of the measurement corrections, indicating the difficulty of this comparison.

1.2.3. Equipment and Procedure Development

Incorporation of a suction measurement device into the triaxial test setup will aid accurate understanding of mechanisms and phenomena occuring in unsaturated soils. The measurement device is a modified version of the MIT tensiometer (*sections 2.2.1* and *4.1*). Standard triaxial test procedures have to be modified to accommodate both the tensiometer and the extremely low strength of the sample materials. Non-standard corrections to measurements will be applied to test measurements, with the aim of achieveing better precision.

1.3. Outline of the Thesis

The next chapter (*2*) of this thesis provides detailed background information and a literature review pertinent to the research. To improve the reader's understanding, it also includes a description of the conventions and terminology used throughout the thesis. New ideas and hypotheses that were developed along the course of research are explained in *Chapter 3*. Details of the equipment and corresponding modifications throughout this research are presented in *Chapter 4*. Details of the methodology for the experimental work are presented in *Chapter 5* in the form of step-by-step procedures. In *Chapter 6*, the experiments performed to verify the hypothesis described in the third chapter are presented. This is followed by *Chapter 7*, which consists of a corresponding discussion and interpretations of the test results. *Chapter 8* concludes the thesis with explanations of how far this research progressed towards achieving its goals, as well as recommendations for future research.

All related tables and figures are integrated into the text. They, and the equations, are numbered separately in every chapter. Appendices at the end of some of the chapters provide information that are not necessary to understand the text, but may be helpful for the continuation of this research in the future.

The figures are in color in the formal copies of this thesis. However, for the sake of black and white copies, the descriptions in the text are without color, with the associated color given in parentheses. For example, a red curve in the same coordinate space as a light blue curve may be referred to as "the darker (red) curve".

2 LITERATURE REVIEW

2. LITERATURE REVIEW

2.1. Pore Water under Tension

2.1.1. Tensile Strength of Water

The scientific discovery of water's ability to withstand tension dates back to 1730 by the Bernoulli brothers. In 1754, Euler first described this phenomenon mathematically, showing that if the velocity of a fluid could be sufficiently increased, its pressure could become negative. In 1850, Berthelot performed the first experiment in which water sustained a magnitude of tension (5MPa) greater than the vapor pressure of water (99kPa). He filled a sealed glass tube with warm distilled water, applied tension thermally by cooling the system down, and inferred the tension from the sudden increase in the volume of the tube at the rupture of water. He also postulated that the value he was measuring was the adhesion of water to the surface of the tube and not the true tensile strength of pure water (Trevana, 1987). In the past decades, scientists (Lewis, 1961; Henderson & Speedy, 1980; Ohde et al., 1989) used similar techniques to Berthelot's to measure tension in water. The highest tension measurement using Berthelot setup was 27.7 MPa by Trevana (1987).

Calculating from homogenous nucleation theory (thermodynamical theory on initiating phase change within pure, uniform substances), Fisher (1948) estimated the tensile strength of pure water to be 140 MPa. Zheng et al. (1991) extrapolated the same magnitude from their experiments on supercooled water. General scientific opinion is that the true tensile strength

Figure 2.1. Tensile strength of water around a bubble (Toker, 2002).

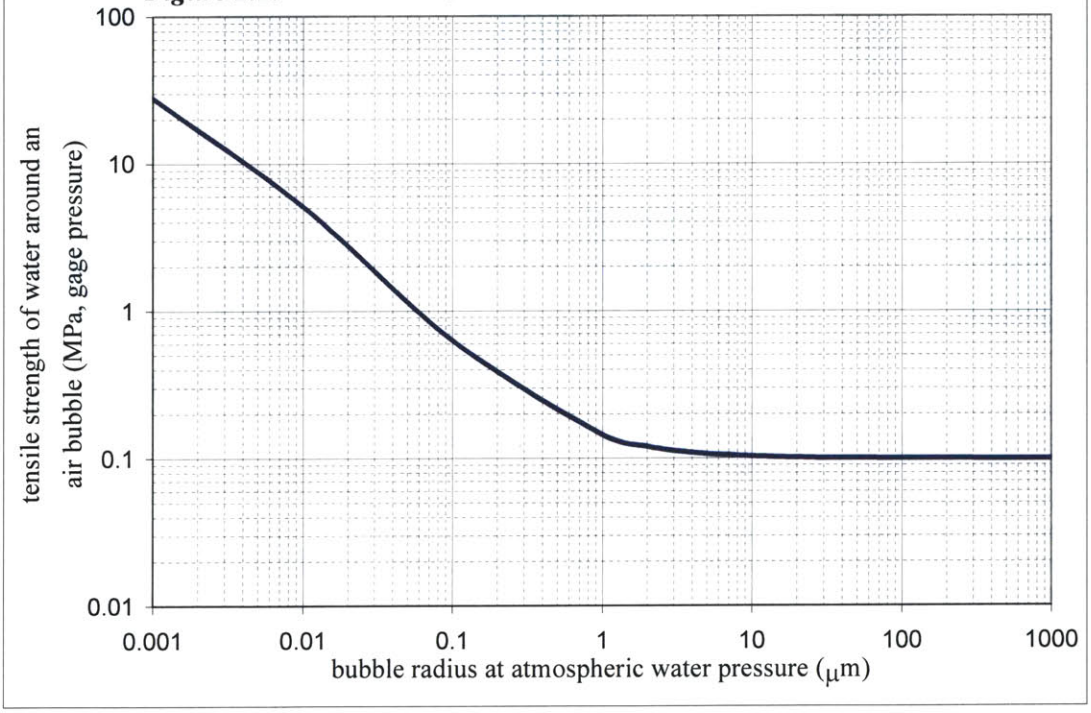

of pure water is not easily observeable because water fails in tension at its interfaces with other materials. Most commonly this phenomenon (termed as cavitation) occurs at air-water interfaces. The tensile strength of water with air bubbles can be calculated thermodynamically in terms of energy (Fisher, 1948), or mechanically in terms of pressure (Toker, 2002) as shown in *Fig.2.1.* For engineering purposes, almost all observeable water bodies have impurities (air bubbles) large enough to reduce the tensile strength down to the vapor pressure of water. The vapor pressure of water is approximately -99kPa in gage pressure (17.5 mmHg or 2.33 kPa in absolute pressures) at 20C° and changes geometrically with temperature (Dalton, 1802).

2.1.2. Total Potential of Soil Water

The term "potential" means the amount of work required to move from a reference state to the state under consideration. Therefore, *total potential of soil water* is the amount of useful work that must be done per unit quantity of pure water to transfer reversibly and isothermally an infinitesimal quantity of water from a pool of pure water at the reference elevation and external gas pressure to the soil water at the elevation of the soil under consideration (Aitchison 1965).

The general definition of potential above includes various different aspects of changing the state of the water. To understand and account for each of these, the total potential can be separated into components as shown in *Figure 2.2.* With the directions of transfer shown in this figure, gravitational and pressure potentials are positive (i.e. work must be done on the

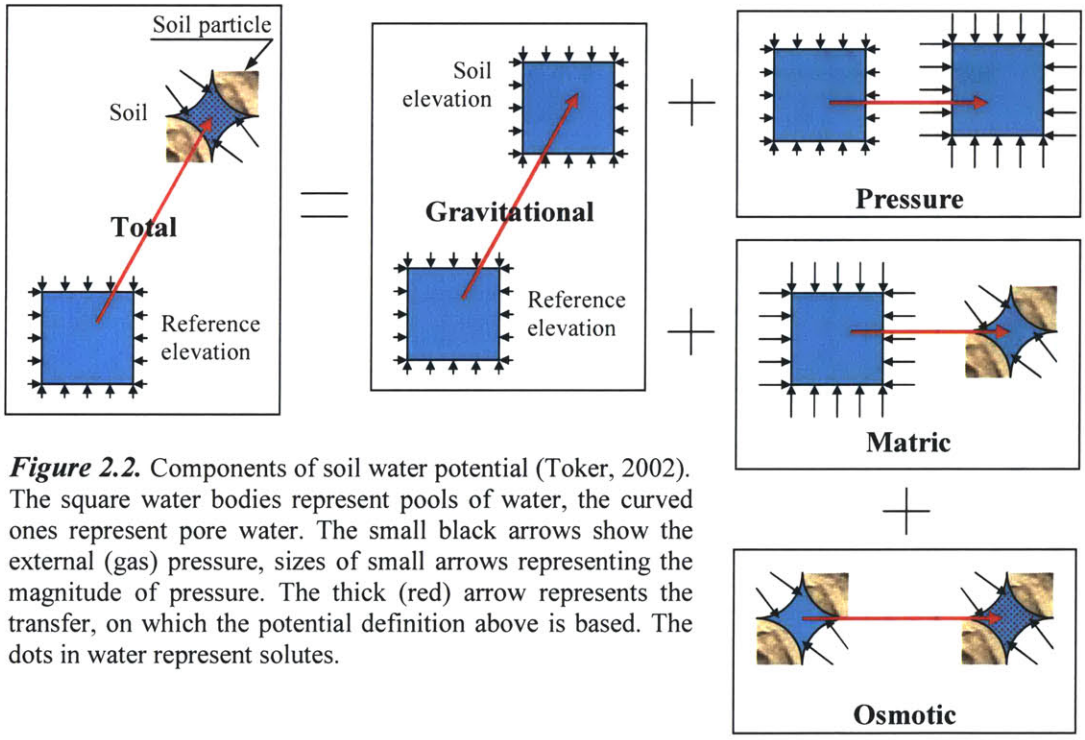

Figure 2.2. Components of soil water potential (Toker, 2002). The square water bodies represent pools of water, the curved ones represent pore water. The small black arrows show the external (gas) pressure, sizes of small arrows representing the magnitude of pressure. The thick (red) arrow represents the transfer, on which the potential definition above is based. The dots in water represent solutes.

water to transfer it in the direction shown in the figure with the thick arrow), although they may be negative depending on the elevation and pressure values. Matric and osmotic potential are always less than zero (i.e. when the two water bodies are connected, water naturally flows as shown in the figure in the figure with the thick arrow).

2.1.2.1. Soil Suction

Among the potential components described above, the first two (gravitational and pressure) lose their existence in the case of soil science, because soil water doesn't change elevation at a certain point under consideration, and the external gas pressure (i.e. barometric pressure) varies negligibly. This leaves only the last two potential components (matric and osmotic) in effect, as far as soil science is concerned. The total of these two potential components is termed *soil suction.* It is also called total suction, moisture tension or negative pore pressure.

The exact definition of soil suction, parallel to the potential definitions above, is as follows: Soil suction, i.e. – (matric + osmotic potential) is the amount of useful work that must be done per unit quantity of pure water to transfer reversibly and isothermally an infinitesimal quantity of water from the soil water to a pool of pure water at the same elevation and atmospheric pressure (Aitchison, 1965). Although thermodynamical aspects of the problem of soil suction (a.k.a. water tension, water potential, or capillarity) have been addressed in a theorethical manner by several scientists over the centuries (Van der Waals, 1893; Einstein, 1901; Fisher, 1923; Aitchison, 1965; Coussy & Fleureau, 2002), its mechanical aspects have mostly been studied from a practical point of view.

2.1.2.2. Osmotic Suction

This is the component of suction due to solute concentration differences, and is equal to the positive of the osmotic potential value. It can be observed in soils with soluble materials. Osmotic suction (h_s) can be expressed as

$$h_s = n/V \cdot R \cdot T \qquad \textit{Eq.2.1}$$

where n/V is the total ion concentration (molar), R is the universal gas constant, T is the absolute temperature in Kelvins (Petrucci, 1989). In most practical problems encountered in geotechnical engineering, significant changes in osmotic suction do not occur (Nelson & Miller, 1992). For this research, osmotic suction is not a factor because, as the following sections will describe, this research focuses on physical forces in water.

2.1.2.3. Matric Suction

This is the component of suction due to physics of the water-air interfaces, and is equal to positive of the matric potential value. Any soil may have pores small enough where the surface forces are large enough to prevent the body forces from draining the pores, i.e. the soil has a capacity to store water. Some energy (in the form of negative pressure) has to be applied to withdraw the water, which is held in place by the potential energy of the tensile

forces created due to curved air-water interfaces. These forces in the pore water are termed matric suction. Matric suction is also called capillary potential.

Matric suction ($u_a - u_w$) is defined as the negative pressure, or tension, in the pore water. It is the pressure difference across a curved surface, as illustrated in *Fig.2.3*, and can be formulated as the following chain of force equilibrium equations:

$$(u_a-u_w).\rho.d\eta.r.d\beta = 2.\sigma_{ST}.(\rho.\, d\eta.d\beta/2 - r.\, d\beta.d\eta/2)$$

$$(u_a - u_w).\rho.\, r = \sigma_{ST}.(\rho - r) \qquad \textit{Eqs.2.2.}$$

$$u_a - u_w = (1/r - 1/\rho).\sigma_{ST} = 2\kappa\, .\, \sigma_{ST} \qquad \textit{Eq.2.3.}$$

where κ is the mean curvature, and σ_{ST} is the air-water interfacial tension. Under equilibrium conditions, potential differences are constant, therefore soil suction, and hence the mean curvature of the interface, is constant. *Eq.2.3* is known as the Young-Laplace Equation (Laplace, 1806).

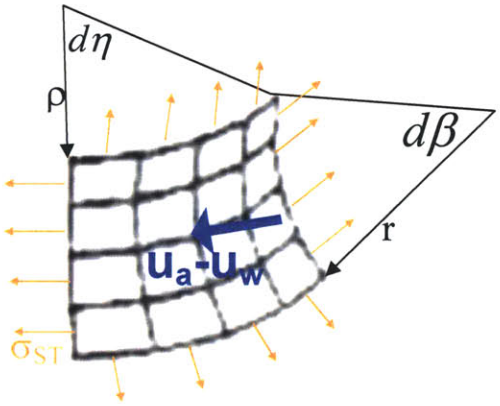

Fig.2.3. An infinitesimal element of an air-water interface. η and β are in orthogonal planes.

As noted by *Equations 2.4* and *2.5*, extremely small radii, high values of interface curvature and matric suction affect even the magnitudes of surface tension and vapor pressure (Adamson, 1960). But their effect is significant only in the case of radii of curvature below 10nm and matric suctions above 5 MPa. The suction magnitudes studied in this thesis never exceed 1 MPa, and in almost all cases are smaller than the vapor pressure. Therefore surface tension and vapor pressure can be considered constant as long as temperature is constant. These effects have been taken into account for the small radius / high tension range of *Fig 2.1* using the following formulae from Adamson (1960):

$$\sigma_{ST} = \sigma_{ST}^{\,o} \cdot \frac{1}{1+\kappa \cdot 2\times 10^{-8}(cm)} \qquad \textit{Eq. 2.4.}$$

$$P_V = P_V^{\,o} \cdot e^{2\cdot\kappa\cdot\sigma_{ST}\cdot\frac{V_n}{R\cdot T}} \qquad \textit{Eq. 2.5.}$$

where V_n is the molar volume, R is the universal gas constant, T is the temperature in Kelvins, $\sigma_{ST}^{\,o}$ and $P_v^{\,o}$ are respectively the air-water interfacial tension and the absolute vapor pressure for a flat surface at the temperature T. *Equation 2.5* is known as Kelvin Equation II.

Soil suction is important to geotechnical engineers due to the fact that strength, deformation and hydraulic conductivity vary with it. According to Rumpf (1961), suction and interfacial tension combined are one of the five mechanisms that keep particle agglomerations together (the other four are: solid bridges, bonding materials, molecular attraction and interlocking). Similarly, soil suction has an impact on shear strength, which will be discussed in *Section 2.4*.

2.1.2.4. Suction Measurement

In practice, soil suction is measured by many indirect methods, using correlations through various measurable parameters. Different tension measurement devices are catalogued frequently in the literature (Fredlund & Rahardjo, 1993; Lee & Wray, 1995; Ridley & Wray, 1996; Toker, 2002; Toker et al., 2004). Among the variety of techniques, only *tensiometers* measure suction directly. All other techniques measure other parameters, which indirectly correspond to a suction value through predetermined calibrations.

Table 2.1. Techniques of measuring or inducing soil suction.

Technique (ASTM Code or Reference*)	**Suction Type**	**Parameter Measured**	**Range (bar)**
Porous Plate (D2325-68)	matric (i)	u_w = 1atm, u_a controlled	0.1 – 1
Pressure Membrane (D3152-72)	matric (i)	u_w = 1atm, u_a controlled	0 – 15
Pressure Axis Translation (Southworth,1980)	matric	positive u_w , u_a controlled	0 – 15
Filter Paper (D5298-94)	matric (w)	contacting paper water content	0.3 – 1000
Filter Paper (D5298-94)	total (r)	nearby paper water content	4 – 1000
Time Domain Reflectometry (Conciani et al., 1996)	matric (w)	dielectric constant of device	0 – 5
Heat Dissipation Sensor	matric (w)	thermal conductivity of device	0 – 7
Gypsum Porous Block	matric (w)	electrical conductivity of device	0.1 – 30
Tensiometer	matric	water tension	0 – 0.9
Tensiometer (IC, ***MIT***, Sasktch.)	matric	water tension	0 – 15
Squeezing (D4542-95)	osmotic	ion concentration	0 – 350
Humidity Chamber	total (i)	relative humidity of air	1 – 10000
Psychrometers	total (r)	temperature at evaporation	0.5 – 700
Centrifuge (D425-88)	matric (i)	capillarity	0 – 30

The letters beside the suction type designate the following: (r) indicates that the measured parameter correlates to suction through ***r***elative humidity of air; (w) indicates that the measured parameter correlates to suction through the ***w***ater content of the sensor, which has a unique suction - water content relationship; and (i) means the technique does not measure the suction of the soil – instead, it ***i***nduces the chosen suction value in the soil specimen.

Table 2.1, presents known techniques of inducing or measuring soil suction. A suction inducing technique can be incorporated into an interpolation scheme to make suction measurements using multiple sets of equipment and specimen simultaneously (Coleman & Marsh, 1961). However, these are not useable for real-time measurements during a test on a single specimen.

The techniques that are based on translation of the pressure axis rely on the assumption of air and water continuity at all times. If either phase is discontinuous, unifying the pressure throughout that pore phase will not be possible. In addition, the methods that rely on the axis translation principle will not simulate the behaviour of a discrete air bubble in the pore space. Under tension, instead of air entry through the surface, cavitation in pores may be initiated from such air bubbles. Under compression, however, a bubble can not cavitate.

Techniques that calculate suction measurements indirectly through relative humidity, such as filter paper method, do not provide a fine resolution (the suction difference between 99% and 100% relative humidity is more than 1 MPa or 10 kgf/cm^2).

2.1.3. Tensiometers

Tensiometers used to be simple field instruments, which establish hydraulic connection between the pore water and a pressure measurement device through a porous stone (*Figure 2.4*). These field tensiometers can measure suction only upto values less than the vapor pressure of water (usually 80-90 kPa). In the past decade, a new design and procedure yielded the first high capacity tensiometer, the Imperial College tensiometer (Ridley & Burland, 1993). In order to maximize the capacity of their device, the designers minimized the pore size of its porous stone. Different than the field tensiometers, their procedurial novelty was high-pressure saturation before every usage. The designers also gave weight to keeping the volume of water connecting the stone to the pressure sensor as small as possible.

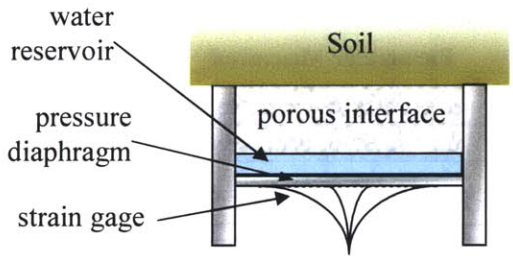

Figure 2.4. Conceptual sketch of tensiometer.

Soon after, Saskatchewan (Guan & Fredlund, 1997) and MIT (see *Section 2.2.1*) tensiometers, which followed the IC tensiometer principles, were designed. In the recent years, high-capacity tensiometers have been the subject of a broad spectrum of research areas, such as miniaturization (Muraleetharan & Granger, 1999), incorporation into triaxial testing (Wong et al., 2001), saturation efficiency (Tarantino et al., 2000), design improvements and utilization in continuous soil moisture characteristic curve measurement (see *Section 2.2.2*).

2.1.4. Soil Moisture Characteristic Curve

As early as the 19th century, soil scientists proposed the separation of pore water into three distinct phases, according to its potential (Briggs, 1897): gravimetric or bulk water, capillary or pendular water, and hygroscopic or adsorbed water. Adsorbed water is a few-molecule thick cover on all solid surfaces, capillary water is trapped in liquid bridges around particle-to-particle contacts (*Fig.2.5.b*; detailed analysis in *section 3.1*), and the rest of the pore volume is filled with bulk water (*Fig.2.5.a*).

All three portions of water are fully present in saturated porous media. Removing the water causes an increase in matric suction. When the suction exceeds a treshhold termed the ***Air Entry Pressure***, it starts to lose the bulk water. Once all of the bulk water is drained (transition from *Fig.2.5.a* to *2.5.b*), the pendular water can be drained gradually if enough suction is applied. Conditions short of vacuum or very high temperatures, which include atmospheric conditions of a temperate climate, cannot separate the adsorbed water from the solids.

Fig.2.5.a. Bulk water at air entry

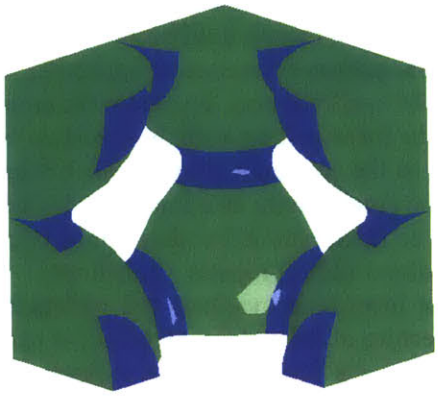

Fig.2.5.b. Pendular water

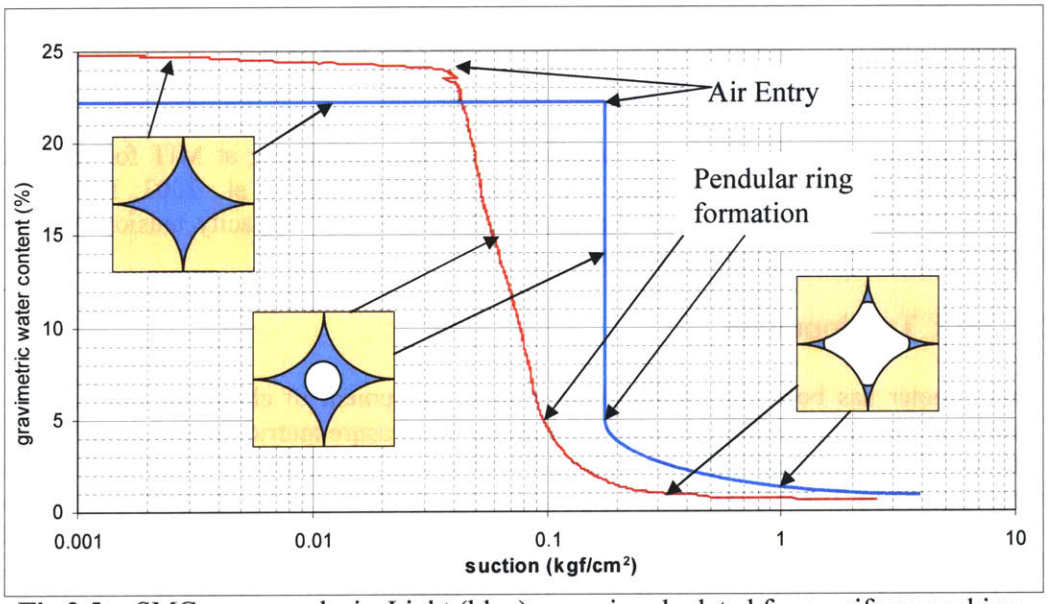

Fig.2.5.c. SMC curve analysis. Light (blue) curve is calculated for a uniform packing, whereas the dark (red) curve is from a test by MIT technique (*section 2.2.2*).

The relationship between the amount of water in a soil, and the associated matric suction in the pore water is described by the Soil Moisture Characteristic (SMC) curve (*Fig.2.5.c*). This amount of soil water is expressed as degree of saturation (ratio of water volume to void

volume), volumetric water content (ratio of water volume to solid volume) or gravimetric water content (ratio of water mass to solid mass). SMC curves are widely used in geotechnical engineering for predicting various aspects of mechanical behavior (Fredlund, 2006). There is hysterisis in SMC curves between drying and wetting (for a given water content, a wetting curve is lower in both suction and water content).

In practice, the SMC curve is obtained in many different ways:
- An equation from known soil properties, primarily the grain size distribution, from which pore size distribution is correlated, can be devised for the SMC curve (Arya & Paris, 1981).
- The SMC can be measured at a rate of about one data point per day, each data point being obtained from a test on a different specimen, by techniques involving use of the porous-plate apparatus, pressure membrane apparatus, or filter paper (ASTM D2325-68, D3152-72 and D5298-94 respectively). To obtain the entire SMC curve takes about 10 – 15 days.
- It can be measured on a single specimen by a method proposed by Lu et al. (2006), which is as slow as the conventional methods outlined above, but has the advantage of also obtaining hydraulic conductivity as a function of water content.
- It can be fitted onto a few data points using one of the several – Zapata et al. (2000) reports 10, Fredlund (2006) reports 12 different – curve-fitting equations. These regressions may or may not incorporate various soil parameters into their correlations, as they cannot capture every feature of the SMC with their 2-4 parameters.
- A continuous SMC curve on a single specimen can be measured rapidly (in less than 5 days), by the syringe pump method (Znidarcic et al., 1991), by a mercury intrusion porosimeter (Kong & Tan, 2000), or by the MIT technique (Toker et al., 2004; *Section 2.2.2* of this thesis).

2.2. Previous Research at MIT

Research relative to unsaturated soil mechanics has been continuing at MIT for ten years (Sjoblom, 2000; Sjoblom & Germaine, 2001; Toker, 2002; Toker et al., 2003; Toker et al. 2004). Until 2003, the main foci of the research had been high capacity tensiometers and methodology for obtaining drying SMC curves.

2.2.1. MIT Tensiometers

The tensiometer has been the suction measurement instrument of choice of researchers at MIT over the last ten years for its unmatched ability to measure matric suction directly. Over the course of previous research, nine different tensiometer designs were realized. A full list of these is given by Toker (2002). All versions had the dimensions of a standard triaxial base, because the original intent was incorporation of the tensiometer into triaxial strength tests. Different types of porous stones, strain-gaged pressure diaphragms, and sealing materials that connect the two key components to the stainless metal body were tried in different versions. The final design among these, version 6.1, is still in use.

In addition to designing the devices, improvements to the performance and reliability of the tensiometers was a research focus. The resulting findings that will be relevant to this research were:
- Tensiometers are difficult to use on drying cohesive specimen, because cohesive materials shrink and crack while drying. This often exposes the tensiometer to the atmosphere, affecting the measurements.
- Being composed of several different materials (steel, ceramic, epoxy, copper), tensiometers are temperature sensitive. Therefore they should be allowed to come in to thermal equilibrium with the environment before measurements can be considered reliable. Due to the same reason, the environment should be kept at a constant temperature during the thermal equilibrium and measurement phases.
- The pressure-sensing component has strain gage circuitry inside. As with any other electrical circuit, the strain gage emits energy in the form of heat. This can cause the tensiometer to be significantly warmer than the surrounding environment unless there is sufficient metal-to-metal contact for efficient heat dissipation. Creating such a thermodynamic gradient causes water to migrate away from the tensiometer, causing suction measurements to be larger than the actual value.

2.2.2. SMC Measurement

The MIT technique (US patent no 6,234,008) is able to obtain SMC curves using one test specimen and is faster than almost all of the conventional methods. It is the only SMC measurement technique that takes direct suction measurements. Furthermore, it obtains continuous curves, which is beyond the capabilities of the traditional ASTM techniques of the porous plate, pressure membrane and filter paper. In addition, the technique simulates the way soil suction develops naturally, by evaporation. This eliminates most of the problems and assumptions required for the application of other techniques, such as those involving axis translation (i.e., by applying positive pore water pressure and a greater pore air pressure, this method assumes the matric suction can be simulated by the difference between the two pore fluid pressures, disregarding the fact that it fails to simulate the behavior of isolated air pockets).

For the MIT technique, the tensiometer is pressure-saturated with water in a chamber at pressure values higher than the air entry pressure of the porous ceramic. The specimen may be pressure saturated with the tensiometer, or may be saturated separately. After a day of saturation, the tensiometer and the specimen are placed on a lab balance, as illustrated in *Figure 2.6*. Both the tensiometer and the balance are connected to a data acquisition system. As the tensiometer reads continuous suction data, the balance measures the total mass of the system throughout the test. At the air entry pressure of the porous ceramic stone of the tensiometer, the stone starts drying, and cavitation occurs in the water beneath the stone. After this point, no more measurement is possible without another pressure-saturation of the tensiometer, because the hydraulic connection between the soil and the pressure measuring diaphragm is broken. The residual water content is determined at the end of each test. The mass decrements (i.e. mass of evaporated water) between the data points are then used to back-calculate the variation of water content throughout the experiment.

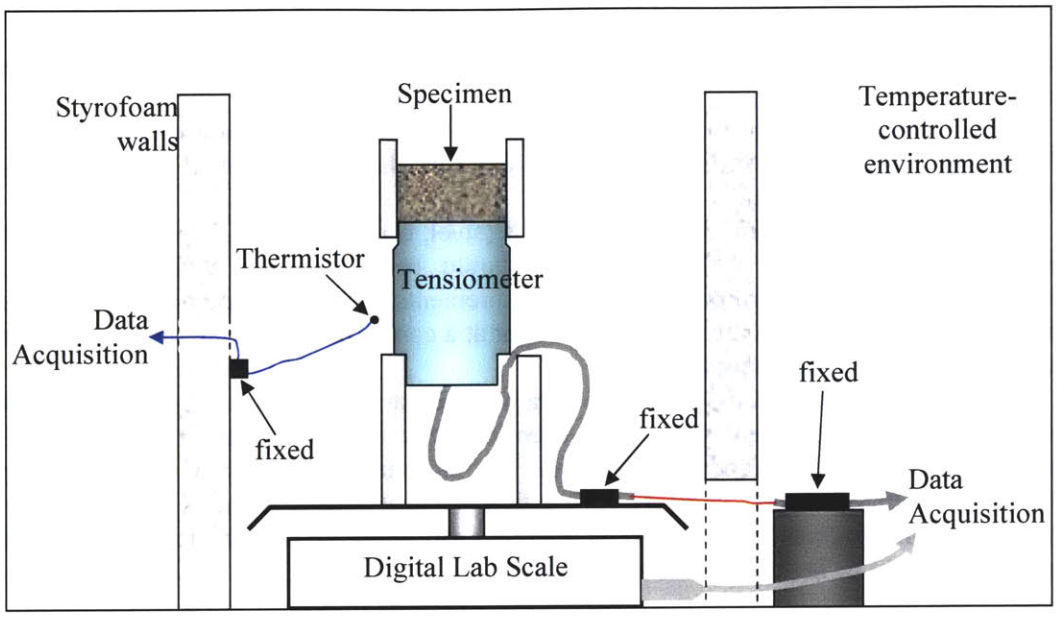

Figure 2.6. Schematic diagram of the test

This method was used (Toker, 2002) in investigating;

- the effects of grain size distribution on SMC curves,
- the correlation between average grain size and air entry pressure (see *Appendix 2.1*).

In its current form, the MIT technique is able to obtain drying SMC curves only. Modification possibilities are being investigated to extend its capabilities to cover wetting curves as well. Wetting SMC determination is not a part of this thesis, and thus, will not be discussed any further.

2.3. Effective Stress

The principles of traditional soil mechanics are based on the assumption of two-phase media (either totally dry or totally wet soil). For most soils, mechanical behavior (strength and stiffness) is unified by Terzaghi's effective stress principle (Terzaghi, 1925; Terzaghi, 1943), which divides normal total stress (σ) applied to the soil into effective stress (σ', the portion of boundary stress carried by the solid particles) and pore water pressure (u_w, the portion of the stress carried by the soil pore water), as described by *Eq.2.6*.

$$\sigma = \sigma' + u_w \qquad \textit{Eq.2.6.}$$

While examining Terzaghi's concept of effective stress more closely, Bishop (1959) analytically calculated for saturated soils that, for the purposes of solid volume change calculations, the effective stress can be treated as independent of both the contact areas between soil particles, and the average number of contacts per particle. He also proposed a

way to extend the effective stress principle to partially saturated soils by the following equation:

$$\sigma' = (\sigma - u_a) - \chi.(u_w - u_a) \qquad Eq.2.7.$$

where σ' is the effective stress, σ is the total stress, u_a is the pressure in the gas phase (air), u_w is the pressure in the liquid phase (water), and χ is a parameter between 0 and 1. Therefore, effective stress is always larger in a partially saturated soil compared to the same soil at full saturation. This is valid for both cases of pendular regime at low saturation and bulk water regime at high, but less than one, saturation levels (*Fig 2.7*).

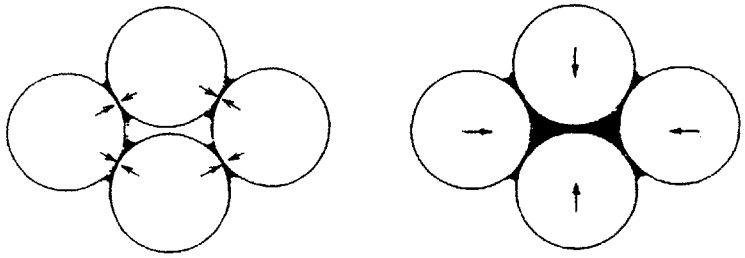

(a) Meniscus water (b) Bulk water

Fig.2.7 Increase in effective stress and contact forces due to matric suction in unsaturated soils (Yoshimura&Kato, 1998)

At lower degrees of saturation where there is a continuous gas phase at atmospheric pressure, when expressed in terms of gage pressure, *Eq.2.7* reduces into

$$\sigma' = \sigma - \chi.u_w \qquad Eq.2.8.$$

Bishop also asserted that the effective stress equations cannot be used for fine grained soils at low degrees of saturation. Jennings & Burland (1962) expanded this assertion into determination of the degree of saturation below which Bishop's hypothesis is invalid, for different types of soil. Later, Richards (1966) proposed adding an osmotic term to Bishop's equations. Matyas & Radakrishna (1968) suggested the addition of a surface tension term. They also found the usage of effective stress principle to be unsatisfactory for deformation calculations of unsaturated clays. Despite all the shortcomings in Bishop's equation, nobody attempted to calculate the effective stress in unsaturated soils, until recently (Likos & Lu, 2004, to be discussed in *Section 3.2*).

2.4. Shear Strength

In 1989, Escario & Juca proposed using 2.5^{th} degree ellipsoidal relationships (in the form of $c_1x^{2.5}+c_2y^{2.5}=c_3$) to relate shear strength to suction, based on experimental data from three different soils. Since then, there have been two fundamental approaches dominating the determination of shear strength of unsaturated soils. These are the effective stress approach and the independent state variables approach (both will be described in the following sections). Both of these approaches originated from the Coulomb strength equation:

$$\tau = c' + \sigma'.\tan\phi' \qquad \textit{Eq. 2.9.}$$

where τ is the shear strength, c' is a cohesion term to signify all attraction forces between particles, σ' is the effective stress normal to the shearing plane, and ϕ' is the angle of internal friction.

2.4.1. Effective Stress Approach

Following Bishop's idea, the shear strength of unsaturated soils can be calculated via a failure envelope (such as Coulomb strength equation) by substituting *Eq.2.7* or *2.8* into the strength equation of the envelope. Bishop's research group tested the shear strength of a variety of soils in order to examine the relation between the χ factor and degree of saturation (Donald, 1960; Bishop & Donald, 1961). Their results showed great variability from soil to soil (*Fig 2.8*).

As will be shown, to date, many engineers use χ values obtained by correlating from the degree of saturation (S). These correlations had been developed by comparing strength tests on unsaturated soils to the strength predicted by modifying the Coulomb strength equation with the substitution of *Eq.2.7* for the effective stress term. Some correlation examples are given below in increasing mathematical complexity:

- Aitchison (1960) derived the following equation, which was used by Donald (1960) in his results that are included in *Fig 2.8.*

$$\chi = u_w \cdot S + \sum_0^u 0.3 \cdot u_w \cdot \Delta S \qquad \textit{Eq. 2.10.}$$

- Öberg & Sällfors (1995) used *Fig 2.8* to conclude that χ can be considered equal to S for engineering purposes.

- Karube et al. (1996) proposed a linear relationship (*Eq 2.11.*) in which χ is zero at residual saturation (S_r) and 1 at full saturation:

$$\chi = \frac{S - S_r}{1 - S_r} \qquad \textit{Eq. 2.11.}$$

- Khalili & Khabbaz (1998) examined data from over a dozen different sources and soils. They proposed a general correlation that is not based on the degree of saturation, but on the air entry pressure (u_{AE}):

$$\chi = \left(\frac{u_w}{u_{AE}}\right)^{-0.55} \qquad \textit{Eq. 2.12.}$$

2.8.3. Miscellaneous

- The difference between effective and total stress (σ'-σ) in an unsaturated soil will be called ***effective stress increment due to suction***. It is the difference between the effective stress at the specific suction in the porous medium and the effective stress at zero or full saturation in the same medium.

- The narrowest cross-section of a pendular ring will be called the "neck" of the pendular ring (see *Fig.2.10*) for the rest of the thesis.

- The value of air-water interfacial tension will be used as 0.00728 N/m, which is the value for pure water at 20°C (Adamson, 1960).

- All comments about void ratio are also valid for relative density, as they are linearly dependant on each other.

- Partial derivatives are expressed in the subscript notation. This means:

$$y_x = \frac{\partial y}{\partial x} \qquad y_{xx} = \frac{\partial^2 y}{\partial x^2} \qquad \textit{Eqs.2.26}$$

Appendix

Appendix 2.1. Grain size – Air Entry Pressure correlation (Toker, 2002).

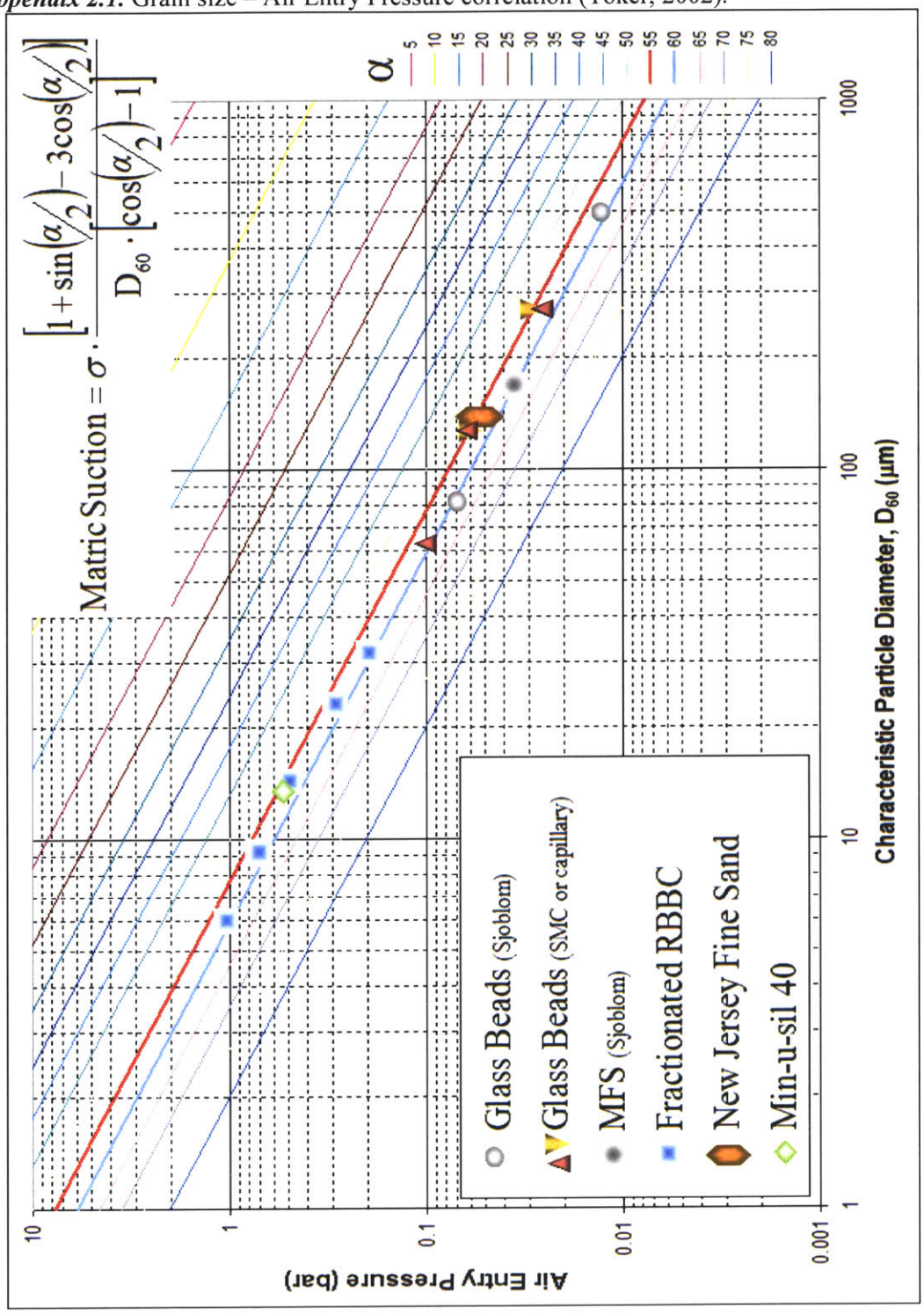

3

THEORETICAL APPROACH

3. THEORETICAL APPROACH

The theoretical portion of this research focuses on the micro-scale physics of the particle-fluid interaction. Afterwards, it seeks to upscale the analytical solutions of interparticle forces to engineering concepts of effective stress and shear strength. For ease in formulations, the soil will be assumed to consist of uniform, non-reactive, rigid, smooth spheres with small enough water content to have no bulk water. For the low saturation values (mass water contents below 5%) that are under consideration, all of the pressures acting on the solid matrix via the water are the result of forces in pendular ring formations (i.e. all water affecting the behavior is in pendular rings at particle contacts). Therefore, the effective stress is expected to be dependent on the mechanics of the pendular rings.

Section 3.1 analyzes a single pendular ring and calculates a single resultant of water forces. *Section 3.2* lays out a model framework of calculating the effective stress increment due to suction using the water force resultants. *Section 3.3* follows the framework to calculate the effective stress increment due to suction, for three idealized isotropic packings. *Section 3.4* proposes a way to experimentally infer the effective stress increment due to suction. *Section 3.5* gives the very few examples from the literature comparable to this study.

3.1. The Pendular Ring

3.1.1. Exact geometry

Although *Fig.2.8* depicts the pendular ring as a *torus* section (rotational body of a circle, rotated around an axis outside and coplanar with it) with two distinct radii, closer examination reveals that a torus section does not have constant curvature, which – as stated in *section 2.1.2* – is the case in partially saturated porous media under equilibrium. This section compares the actual pendular ring to the torus, in order to check the reliability of using the torus geometry in further calculations. In order to further simplify the equations, symmetry around the contact point is introduced by making the two particles identical.

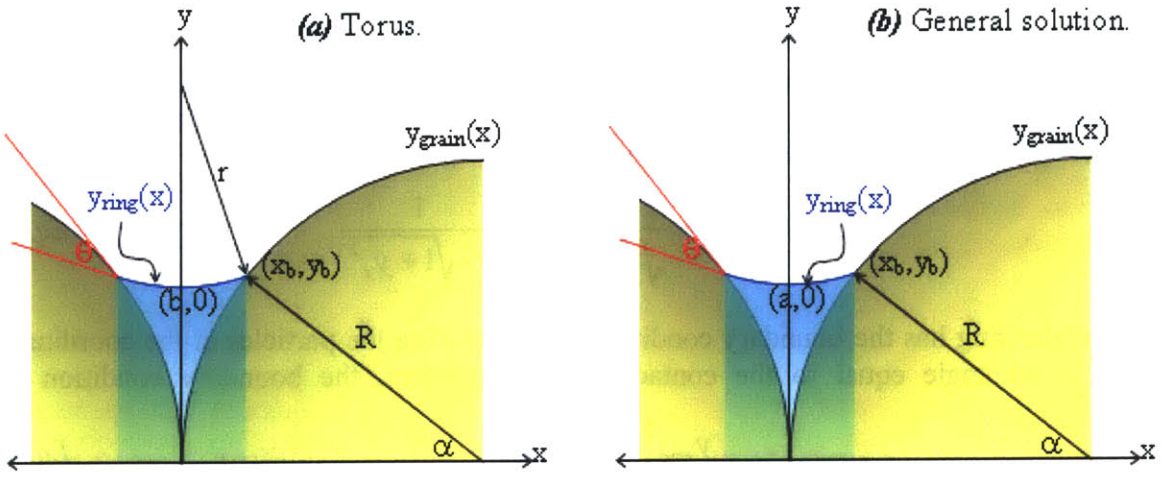

Fig.3.1. Variables to be used in the formulations.

Fig.3.1 illustrates some of the variables to be used in the next sections. Note, that this figure's rotation around the x-axis results in the complete three-dimensional geometry of a pendular ring. The z-axis is outward from the page. The "neck" of the pendular ring refers to the minimum diameter section, which occurs at x=0.

According to *Eq.2.3*, considering any particular suction value is equivalent to considering a unique mean curvature (κ) of the air-water interface (concave towards the air side). Therefore, for any given suction, the water will be bounded by a constant-curvature surface. The mean curvature can be written as the arithmetic average of any two curvatures in planes perpendicular to the surface as well as each other (*Eq.3.5*). In this case, one principal curvature (κ_1) is the curvature in the x-y plane which can be written in the form of general two-dimensional curvature equation:

$$\kappa_1 = \kappa_{xy} = \frac{y_{xx}}{\left(\sqrt{1+y_x^{\,2}}\right)^3} \qquad \textit{Eq.3.1}$$

A curvature in the y-z plane can be written as the reciprocal of radius of rotation, i.e. radius of curvature in this orientation (*Eq.3.2*). It is negative because the interface is concave towards the water phase in the y-z plane.

$$\kappa_{yz} = -\frac{1}{y} \qquad \textit{Eq.3.2}$$

However, the y-z plane is not perpendicular to the pendular surface at every point. It must be rotated around the z-axis to achieve orthogonality. This also means that κ_{yz} is a form of the second principal curvature (κ_2), modified according the slope of the pendular surface in the x-y plane:

$$\kappa_{yz} = \kappa_2 \cdot \sqrt{1+y_x^{\,2}} \qquad \textit{Eq.3.3}$$

Equations *3.2* and *3.3* can be merged to express κ_2:

$$\kappa_2 = -\frac{1}{y \cdot \sqrt{1+y_x^{\,2}}} \qquad \textit{Eq.3.4}$$

Combining the mean curvature definition, equations *3.1* and *3.4*, the two curvatures can be summed to give twice the mean curvature (in this case, the magnitude of κ_2 is negative, as the interface being concave on the water side requires water pressure to be larger than the air pressure – which is not the case for suction):

$$2\kappa = \kappa_1 + \kappa_2 = \frac{y_{xx}}{\sqrt{1+y_x^{\,2}}^{\,3}} - \frac{1}{y \cdot \sqrt{1+y_x^{\,2}}} \qquad \textit{Eq.3.5}$$

The pendular ring has the boundary condition of intersecting the particles at the coordinates (x_b,y_b), at an angle equal to the contact angle. Therefore, the boundary condition for intersection is

$$y_{ring}\Big|_{x_b} = y_{grain}\Big|_{x_b} \qquad \textit{Eq.3.6}$$

In terms of the normal vectors at (x_b,y_b), the boundary condition related to the angle of intersection can be written as the scalar product of the following vectors

$$\begin{bmatrix} (y_{ring})_x \\ -1 \end{bmatrix} \bullet \begin{bmatrix} (y_{grain})_x \\ -1 \end{bmatrix} = \left| \begin{matrix} (y_{ring})_x \\ -1 \end{matrix} \right| \cdot \left| \begin{matrix} (y_{grain})_x \\ -1 \end{matrix} \right| \cdot \cos\theta \qquad \textit{Eq.3.7}$$

$$(y_{ring})_x \cdot (y_{grain})_x + 1 = \sqrt{(y_{ring})_x^2 + 1} \cdot \sqrt{(y_{grain})_x^2 + 1} \cdot \cos\theta \qquad \textit{Eq.3.8}$$

For spherical grains, y_{grain} can be deduced as the equation of a circle from *Fig.3.1* as

$$y_{grain} = \sqrt{\pm 2xR - x^2} \qquad \textit{Eq.3.9}$$

where the 2xR term is positive for the grain on the right, and negative for the grain on the left. Because of symmetry, only one of the grains (in this case, the one on the right) needs to be considered in the formulations. The positive-termed form of *Eq.3.9*, if substituted into *Eq.3.8*, results in

$$(y_{ring})_x \cdot \frac{R - x_b}{\sqrt{2x_bR - x_b^2}} + 1 = \sqrt{(y_{ring})_x^2 + 1} \cdot \frac{R}{\sqrt{2x_bR - x_b^2}} \cdot \cos\theta \qquad \textit{Eq.3.10}$$

Regardless of the boundary conditions, the non-homogeneous differential equation of *3.5* is not solvable analytically (Glasstetter, 1991, attempted to solve this equation – albeit with a small mistake – but he deemed his final equations to be solvable only by numerical means, too). However, its homogeneous solution, i.e. the solution for the zero curvature and suction case, is known and can be compared with the torus. This solution is called a *catenoid*, which is the rotational surface created by a *catenary curve*. The catenary curve is the shape assumed by a uniform rope suspended from the ends. For the symmetrical case, which imposes y_x to be zero at the mid-point, the catenary curve is described by

$$y = a \cdot \cosh\left(\frac{x}{a}\right) = a \cdot \frac{e^{x/a} - e^{-x/a}}{2} \qquad \textit{Eq.3.11}$$

For the general case of non-zero curvatures, the shape becomes a distorted form of the catenoid. Only the zero-curvature case is studied here for the purpose of comparison to a torus.

Since the catenary and the circular arc will not match at every point, one variable at a specific location (such as the diameter or curvature at the particle face or pendular ring neck) must be fixed as the common parameter so that the rest of the curves can be compared. The diameter at the particle face is selected – meaning both catenoid and torus surfaces will touch the particle at the same loci.

Substituting *Eq.3.11* into *Eq.3.10*:

$$\frac{d}{dx}\left[a \cdot \cosh\left(\frac{x_b}{a}\right)\right] \cdot \frac{R - x_b}{\sqrt{2x_bR - x_b^2}} + 1 = \sqrt{\left\{\frac{d}{dx}\left[a \cdot \cosh\left(\frac{x_b}{a}\right)\right]\right\}^2 + 1} \cdot \frac{R}{\sqrt{2x_bR - x_b^2}} \cdot \cos\theta$$

$$a = \frac{x_b}{\ln \dfrac{R \cdot \sin\theta - \sqrt{2x_b - x_b^{\,2}}}{R \cdot (1 - \cos\theta) - x_b}} \qquad \textit{Eq.3.12}$$

Substituting *Eq.3.11* together with *Eq.3.9* into *Eq.3.6* results in

$$a \cdot \cosh\left(\frac{x_b}{a}\right) = \sqrt{2x_b R - x_b^{\,2}} \qquad \textit{Eqs.3.13}$$

Equations *3.12* and *3.13* is an equation pair with two unknowns. The values of a and x_b can be determined numerically. The resulting a value gives a unique catenary equation that fits the boundary condition in the form of *Eq.3.11*. In addition, now that (x_b,y_b) is known, the inclusive angle (α) can be determined as

$$\alpha = \arctan\frac{y_b}{R - x_b} = \arctan\frac{\sqrt{2x_b R - x_b^{\,2}}}{R - x_b} \qquad \textit{Eq.3.14}$$

For the torus solution, the equation is

$$x^2 + (y - r - b)^2 = r^2 \quad \Rightarrow \quad y = r + b - \sqrt{r^2 - x^2} \qquad \textit{Eqs.3.15}$$

Through trigonometry of the problem, the parameters of the torus can be expressed in terms of angles as the following dimensionless equations:

$$\frac{b}{R} = \sin\alpha + (1 - \cos\alpha) \cdot [\tan(\theta + \alpha) - \sec(\theta + \alpha)]$$
$$\frac{r}{R} = (1 - \cos\alpha) \cdot \sec(\theta + \alpha) \qquad \textit{Eqs.3.16}$$

When the preceding set of equations are solved numerically for various contact angles, the curves in *Appendix 3.1* are obtained. Contact angle can be affected by solid properties, surface roughness, and dissolved materials in water. For pure water on an absolutely clean glass surface, the contact angle is supposed to be less than 5° (Mattox, 1998). However, this level of cleanness is extremely difficult to achieve and sustain (Bohren, 1987). The calculations in this work will be continued for 30°, as an average value for water-air-glass boundaries, but the methodology is applicable to any other angle.

For a known pendular ring, its matric suction and volume can be calculated, as well as the cross-sectional area at its neck. For a contact angle of 30°, there is 0.17% difference between the radii of the two geometries of penduar rings at their narrowest sections, 0.34% between the corresponding areas, and 0.41% between the volumes (*Figure 3.2*). The difference between the two surfaces is larger in the case of smaller contact angles, but it is less than 5% for all quantities, even for $\theta = 0°$. For 30°, the differences are less than 0.5%. Therefore, the torus geometry can be used with only negligible errors.

3.1.2. Torus Solution

Although the torus is a very close approximation to the exact solution, it is not the exact solution. Hence, the mean curvature of a torus is not constant along the x-axis (*Figure 3.3*). A curvature must be selected as a representative mean curvature for the pendular ring. In the comparisons presented in *Appendix 3.1*, for all contact angles, the mean curvatures of the two surfaces (torus and distorted catenoid) are equal at approximately $x = 0.57x_b$, regardless of the contact angle. Using the curvature of the torus at this point will result in a suction value very close to the exact solution.

From the definition of matric suction, which leads to *Eq.2.3*, and the definitions of principal curvatures (*Eq.3.1 – Eq.3.5*), matric suction in a torus-shaped pendular ring would be

$$u_a - u_w = 2\kappa \cdot \sigma_{ST} = (\kappa_1 + \kappa_2) \cdot \sigma_{ST}$$

$$u_a - u_w = \sigma_{ST} \cdot \left(\frac{1}{r} - \frac{1}{y|_{0.57x_b} \cdot \sqrt{1 + (y_x|_{0.57x_b})^2}} \right) \qquad \textit{Eq.3.17}$$

If written in terms of angles, *Eq.3.17* becomes

$$u_a - u_w = \frac{\sigma_{ST}}{R} \cdot \left(\frac{\cos(\theta+\alpha)}{1-\cos\alpha} - \frac{\cos(\theta+\alpha) \cdot \sqrt{\sec^2(\theta+\alpha) - 0.57^2}}{\sin\alpha + (1-\cos\alpha) \cdot \left(\tan(\theta+\alpha) - \sqrt{\sec^2(\theta+\alpha) - 0.57^2} \right)} \right) \qquad \textit{Eq.3.18}$$

By simple geometry from *Figure 3.1*, the cross-sectional area at the neck is

$$A = \pi \cdot b^2 \qquad \textit{Eq.3.19}$$

The volume of a rotational (around x-axis) body can be calculated through integration as follows:

$$V = \pi \cdot \int y^2 dx \qquad \textit{Eq.3.20}$$

Here, the rotational body is the area between the ring surface and the grain surface. Using symmetry, *Eq.3.20* can be written for twice the half of the pendular ring, eliminating one of the grains from the equation:

$$V = 2\pi \cdot \int_0^{x_b} \left({y_{ring}}^2 - {y_{grain}}^2 \right) \cdot dx \qquad \textit{Eq.3.21}$$

After some integration, *Eq.3.21* can be dimensionlessly expressed in terms of angles as

$$\frac{V}{2\pi R^3} = \left[\left(\frac{r+b}{R} \right)^2 + \frac{r^2}{R^2} - 1 + \cos\alpha \right] (1-\cos\alpha) - \frac{r+b}{2R} \cdot \frac{r^2}{R^2} \cdot [\sin(2\theta + 2\alpha) + \pi - (2\theta + 2\alpha)] \qquad \textit{Eq.3.22}$$

where the fractions of dimensions are all composed of nothing but trigonometric functions of angles (see *Eqs.3.16*).

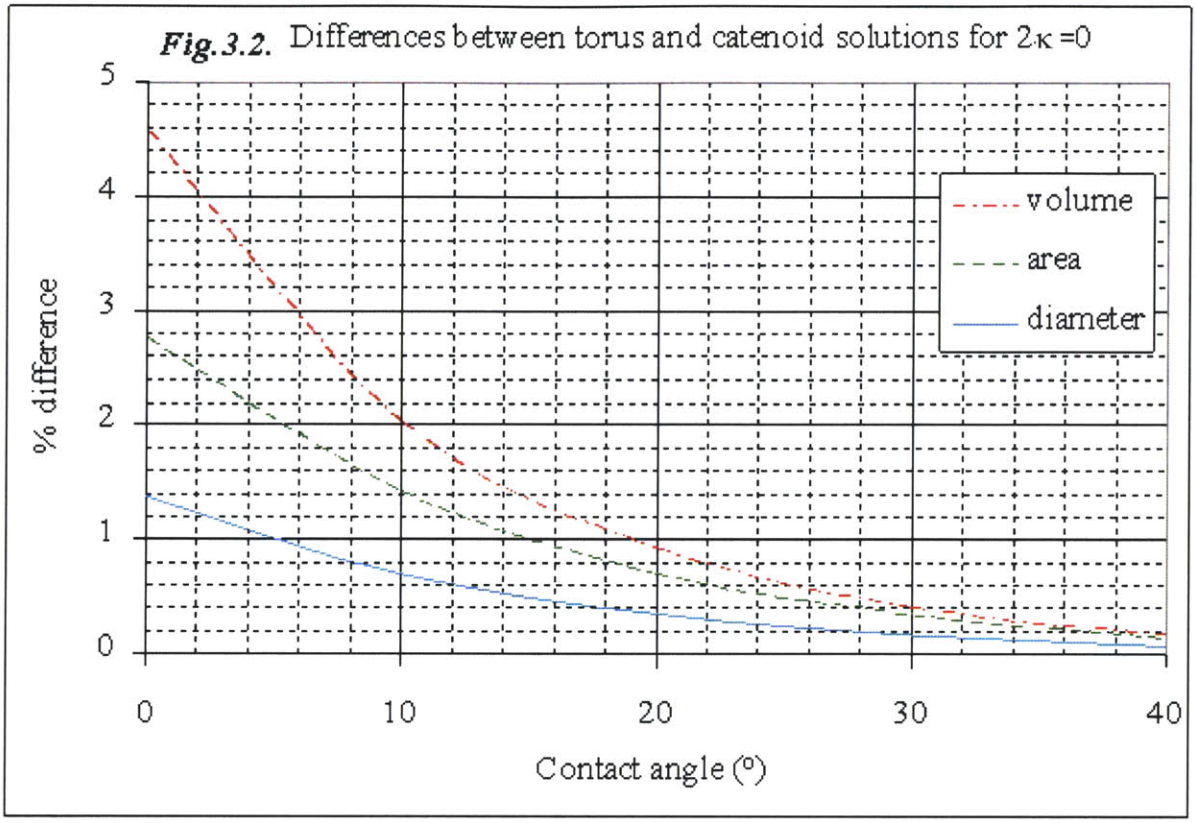

Fig.3.2. Differences between torus and catenoid solutions for $2\kappa = 0$

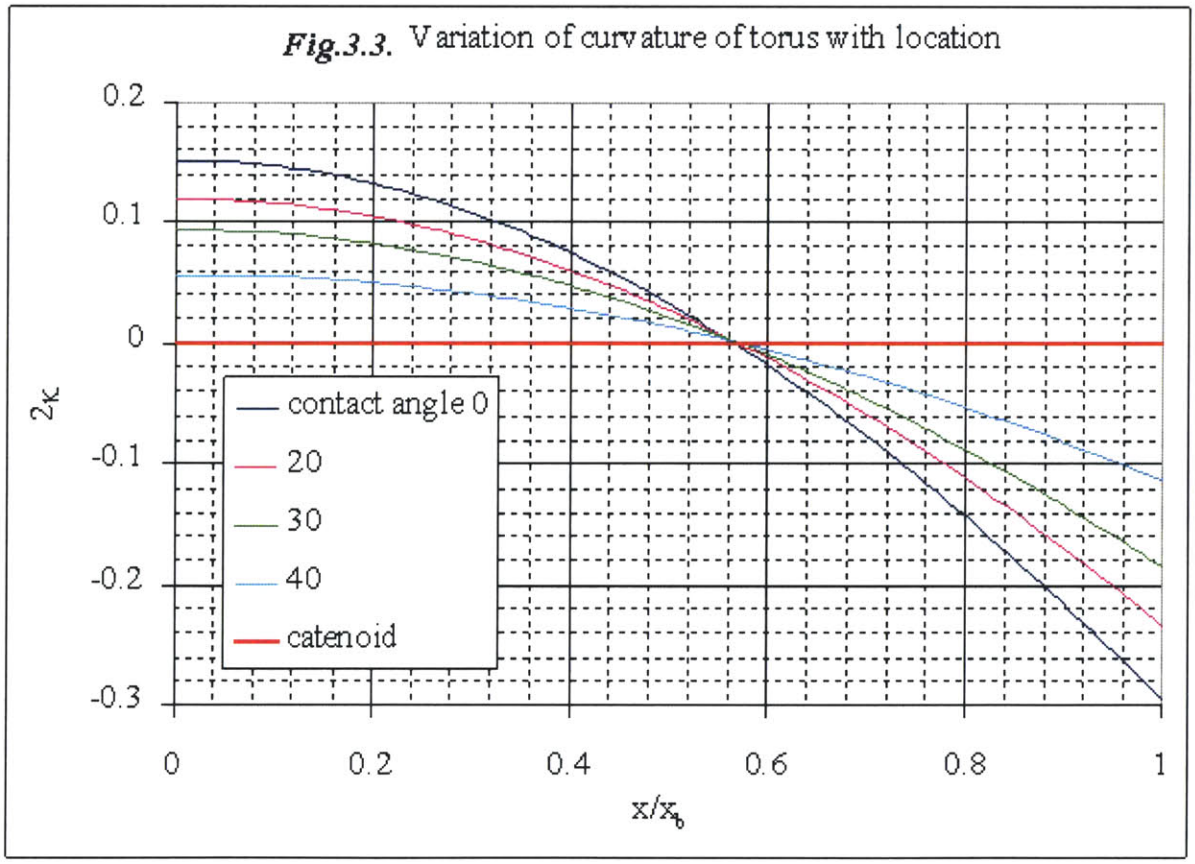

Fig.3.3. Variation of curvature of torus with location

3.1.3. Inner forces

A pendular ring pulls particles together by two types of tensions: matric suction inside the ring and surface tension around the perimeter. The total effect of a pendular ring on a particle can be examined by taking a cross-section at the neck of the ring (*Fig.3.4*). The resultant of these forces is:

$$F = \pi \cdot b^2 \cdot (u_a - u_w) + 2 \cdot \pi \cdot b \cdot \sigma_{ST}$$

$$\frac{F}{R} = \pi \cdot \left(\frac{b}{R}\right)^2 \cdot R(u_a - u_w) + 2 \cdot \pi \cdot \frac{b}{R} \cdot \sigma_{ST} \qquad \textit{Eqs.3.23}$$

Fig.3.4. Forces in a pendular ring (light forces). All forces in a pendular ring can be replaced by their resultant (dark force)

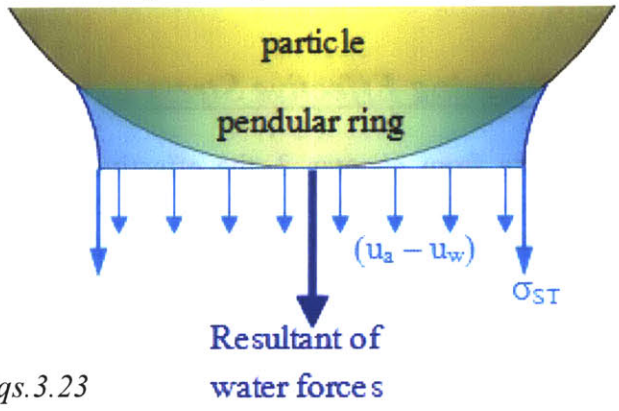

According to *Eqs.3.16*, *3.18* and *3.23*, the relation between F/R and $R(u_a-u_w)$ is independent of the grain size, R. This unique relationship is graphically represented as the analytical curve in *Fig.3.5*. The experimental and numerical points in the figure are for the sake of comparison. They are from Chateau et al. (2002), who developed a numerical model for pulling two moist spheres apart, and performed experiments to validate their model, as mentioned earlier in *section 2.6.2*. Their results don't match exactly because the spheres they used were 8 mm in diameter, at which scale gravity forces are no longer insignificant.

Figure 3.5. Normalized resultant water force vs suction

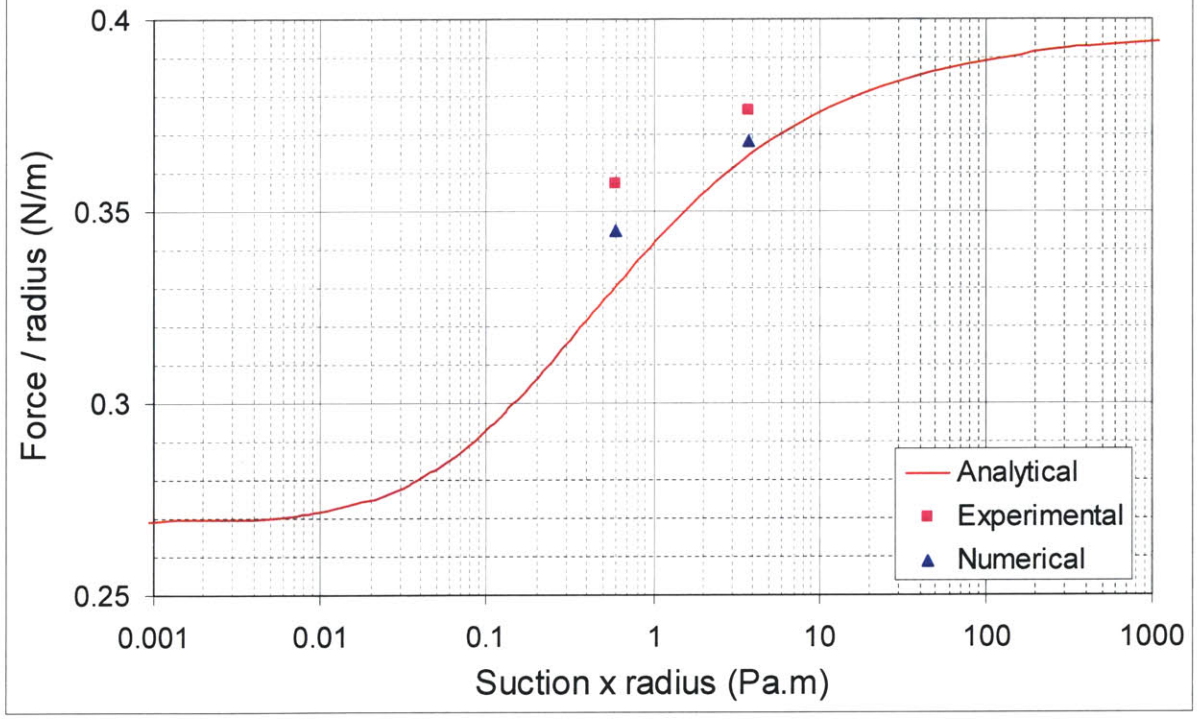

According to *Fig.3.5*, for a given grain size, the resultant force does not change much (less than 50%) over many orders of magnitude of matric suction. This is because as matric suction increases, the pendular ring shrinks, countering the effect from increased suction.

3.2. Defining Effective Stress

Repeating from *chapter 2*, the effective stress averaged over an area of a particulate material is the vector sum of all of the interparticle forces in a given direction divided by the total area under consideration (Mitchell, 1976).

If the area of consideration is selected

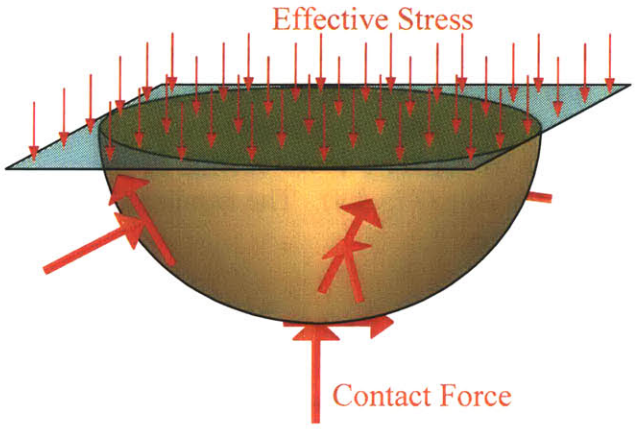

Fig.3.6. Decomposition of ***solid*** stresses and forces over half of a particle

such that it is repeatable over a cross-section of the granular material and it contains the full projection of exactly one particle by bisecting it, the effective stress can be depicted on the free-body diagram of half of a particle as in *Fig.3.6*. This is a depiction of the solid stresses and associated portions of contact forces, but it can also be considered as all of the stresses and contact forces in the totally dry case. At each particle contact, the contact forces have normal and shear components, whose vector sum divided by

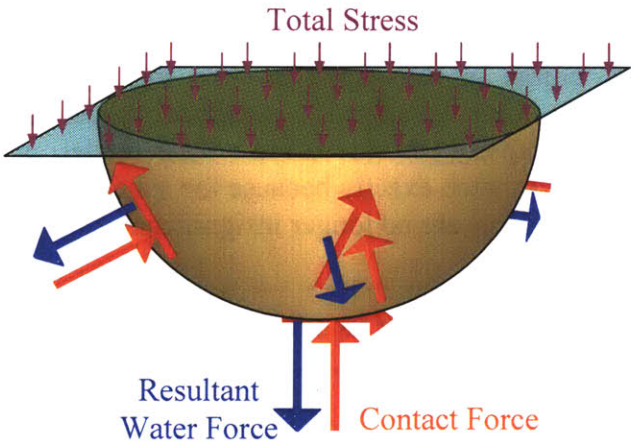

Fig.3.7. Decomposition of ***total*** stresses and forces over half of a particle

the area of the repeatable element, to obtain effective stress. These forces can not be measured as yet, so the effective stress can not be analytically formulated by such a direct approach (but they can be investigated via DEM simulations).

Following Terzaghi's and Bishop's logic, the effective stress can also be expressed as the total stress minus stress caused by water. Both total and water stresses and the contact forces associated to both cases can be assembled, as was done above for the solid stresses. Total stresses (*Fig.3.7*)

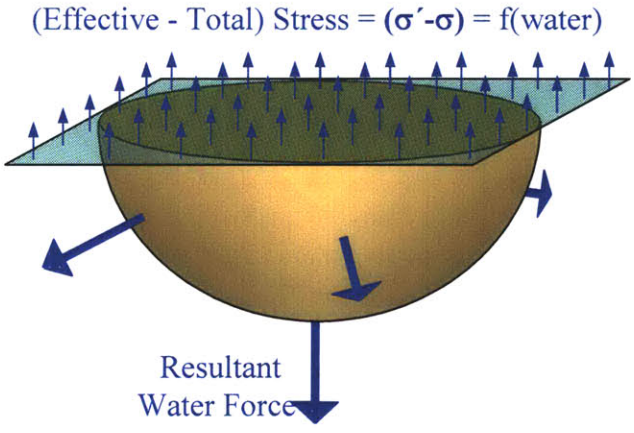

Fig.3.8. Decomposition of ***water*** stresses and forces over half of a particle

are externally applied, known magnitudes. For small water contents, the only water forces (*Fig.3.8*) are provided by the pendular rings, which can be reduced to a single calculable resultant normal force at each contact (*section 3.1.3*). Since water forces in the case of partially saturated soils are tensile, effective stress is larger than total stress. Their difference (stress increment due to water) is a function of these water forces – more specifically, the vector sum of all pendular ring water force resultants acting on one half of a particle, divided by the area of the repeatable element which contains this particle is :

$$\sigma'-\sigma = f(water) = \frac{\sum_{half-particle} \vec{F}_{resultant}(water)}{A_{element}} \qquad Eq.3.24$$

This is not a practically manageable problem for random assemblies of particles, in which case there will not be repeatable elements, and pendular rings between non-contacting particles will be a more frequent occurrence. A system with such complexity will not be analytically solvable, but it may be possible to simulate through DEM. In order to be analytically solvable, the particle geometry and coordination geometry are required for the entire particulate matrix. This is the reason for examining idealized packings in the next section, where all particles are identically connected and therefore representative of the entire matrix.

3.3. Solutions for Ideally Constituted Granular Materials

Any repetitive particle packing geometry is solvable, as examplified by Graton & Fraser (1935), who discussed cubic, orthorhombic, tetragonal and tetrahedral (rhombohedral) systematic assemblies of equal spheres (*Table 3.1*). Among these, only isotropic packings, namely cubic and tetrahedral, are considered. Anisotropic packing geometries (orthorhombic or tetragonal) may have anisotropy in the (σ'-σ) quantity as well, so they will not be examined in this research. With isotropic packings, (σ'-σ) will be calculated in different directions, to be compared to each other.

Table 3.1. Systematic packings of uniform spheres (the italic entries are from this work, the rest are from Graton & Fraser, 1935)

Packing	**Isotropy**	**Void ratio**	**Co-ordination number**
Cubic	*Yes*	0.910	6
Orthorhombic	*No*	0.654	8
Body-centered cubic	*Yes*	*0.470*	*8*
Tetragonal	*No*	0.433	10
Tetrahedral	*Yes*	0.350	12

The description and associated figures of the three packings below follow the same format. In the *Figures 3.9* to *3.11*, darker arrows indicate forces out of the plane of the page and lighter arrows denote forces into the page. Solid (red) arrows are the forces acting on one half

of the central particle, whereas dashed (blue) arrows show the remaining forces at contacts (symmetrical forces acting on the other half and forces in the plane of consideration). The magnitude of the resultant force of a pendular ring at each contact is F. In the figures, in order to avoid complicating the view, the particle is not shown. Instead, all F forces are drawn at a length equal to the particle radius. D is the particle diameter.

3.3.1. Cubic packing

Cubic packing, also called "isometric" packing, is the most basic idealization, constructed by placing a particle at every corner of an imaginary cube with side length equal to D. It is the loosest stable packing of confined uniform particles. All angles between the 6 contact points of each particle are 90°. The porous matrix consists of an octahedron-shaped pore for every particle, resulting in a porosity of $(1-\pi/6) = 0.476$.

Fig.3.9.b presents a plane bisecting four of the neighboring particles. This plane has symmerical copies in two other orientations. The repeatable area of the plane of consideration is a DxD square. There is only one F acting on half of the particle, and it is perpendicular to the plane of consideration. This results in

$$\sigma'-\sigma = F/D^2 \qquad \textit{Eq.3.25}$$

A second possible solution is illustrated in *Fig.3.9.c*, as a plane that bisects two neighboring particles and separates the remaining four symmetrically. This plane has symmerical copies in five other orientations. The repeatable area of the plane of consideration is a DxD$\sqrt{2}$ rectangle. The vector sum of the two F's acting on half of the particle is F$\sqrt{2}$. This agrees with *Eq.3.25* by resulting in

$$\sigma'-\sigma = \frac{F\sqrt{2}}{D^2\sqrt{2}} = F/D^2 \qquad \textit{Eq.3.26}$$

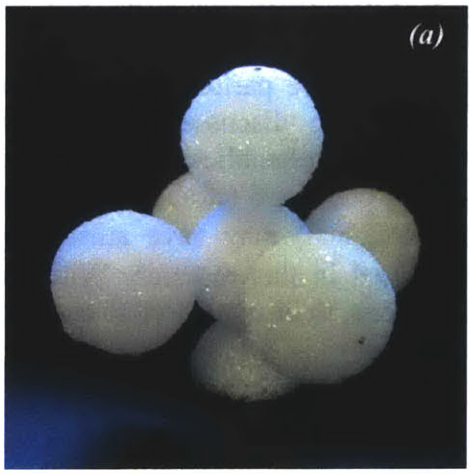

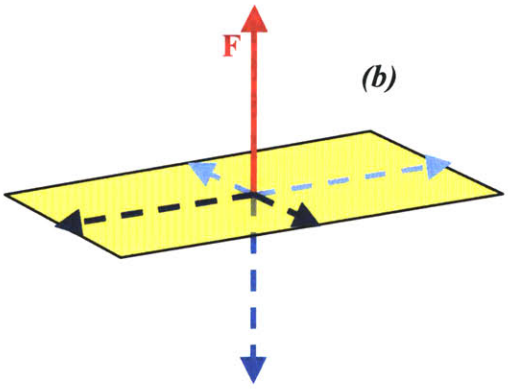

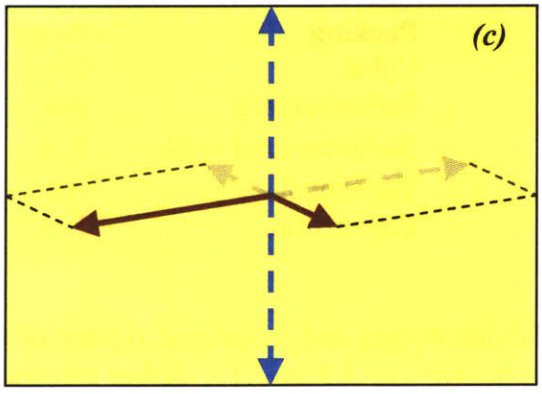

Fig. 3.9. Cubic packing

3.3.2. Body-centered cubic packing

This packing will be called "8-contact packing" for the sake of convenience through the rest of this work. Counterintuitively, this packing can not be constructed using an octahedron. If the particles are placed at the corners of an octahedron, the resulting arrangement is a rotated form of the tetrahedral packing. It is not orthorhombic packing either, it is significantly denser and isotropic.

The only way to evenly distribute 8 contacts over every particle in the matrix is by placing the particles at the centroid and all corners of a cube with the side length of $2D/\sqrt{3}$. In this packing, all angles between the 8 contact points are approximately 70°. The porous matrix consists of one and a half "short square prism" – shaped pores for every particle, resulting in a porosity of $(1-\pi\sqrt{3}/8) = 0.320$.

Fig.3.10.b demonstrates a plane that does not intersect any of the neighboring particles, dividing the contacts into symmetric groups of four on each side. This plane has symmerical copies in two other orientations. The repeatable area of the plane of consideration is a square with sides equal to $2D/\sqrt{3}$. The vector sum of the four F's acting on half of the particle is $4F\sqrt{3}$. This results in

$$\sigma'-\sigma = \frac{4F\sqrt{3}}{\left(2D/\sqrt{3}\right)^2} = \sqrt{3}\cdot F/D^2 \qquad Eq.3.27$$

A second possible solution is depicted in *Fig.3.10.c*, as a plane that that bisects four neighboring particles and separates the remaining two symmetrically. This plane has symmerical copies in five other orientations. The repeatable area of the plane of consideration is a rhombus with each side D and diagonals $2D/\sqrt{3}$ and $2D\sqrt{2}/\sqrt{3}$, respectively. The vector sum of the two F's acting on half of the particle is $2F\sqrt{2}/\sqrt{3}$. This agrees with *Eq.3.27* by resulting in

$$\sigma'-\sigma = \frac{\frac{2F\sqrt{2}}{\sqrt{3}}}{\frac{1}{2}\cdot\frac{2D}{\sqrt{3}}\cdot\frac{2D\sqrt{2}}{\sqrt{3}}} = \sqrt{3}\cdot F/D^2 \qquad Eq.3.28$$

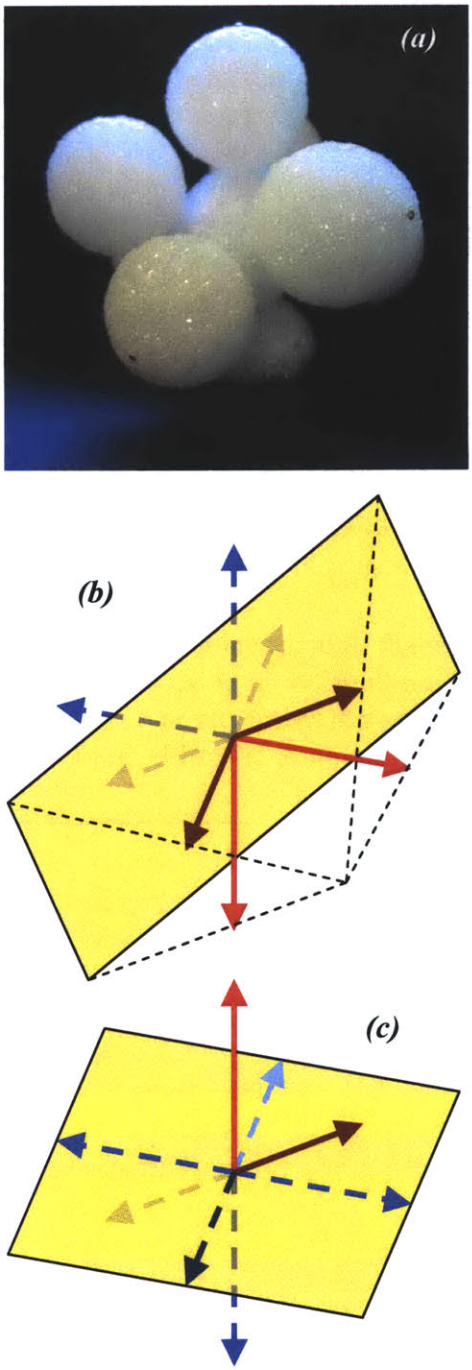

Fig. 3.10. 8-contact packing.

One noteworthy aspect of this packing is, that in addition to the eight contacting neighbors, each particle is very close to six other particles without touching them. The distance between these is $(2/\sqrt{3} - 1)$ D, which is approximately 0.155 D.

3.3.3. Tetrahedral packing

This packing is also called "rhombohedral" or "close" packing. It is constructed by placing a particle at every corner of an imaginary tetrahedron with side length equal to D. It is the densest possible packing of uniform spherical particles. All angles between the 12 contact points are 60°. The porous matrix consists of one octahedron-shaped pore and two tetrahedron-shaped pore for every particle, resulting in a porosity of $(1-\pi/3\sqrt{2}) = 0.260$.

Fig.3.11.b presents a plane bisecting six of the neighboring particles. This plane has symmerical copies in three other orientations. The repeatable area of the plane of consideration is a regular hexagon with side lengths of $D/\sqrt{3}$. The vector sum of the three F's acting on half of the particle is $F\sqrt{6}$. This results in

$$\sigma'-\sigma = \frac{F\sqrt{6}}{6\left(\frac{D}{\sqrt{3}}\right)^2 \sqrt{3}/4} = 2\sqrt{2}\cdot F/D^2 \qquad Eq.3.29$$

A second possible solution is illustrated in *Fig.3.11.c*, as a plane that that bisects four neighboring particles, none of which contact each other, and separates the remaining eight symmetrically. This plane has symmerical copies in two other orientations. The repeatable area of the plane of consideration is a DxD square. The vector sum of the four F's acting on half of the particle is $2F\sqrt{2}$. This agrees with *Eq.3.29* by resulting in

$$\sigma'-\sigma = \frac{2F\sqrt{2}}{D^2} = 2\sqrt{2}\cdot F/D^2 \qquad Eq.3.30$$

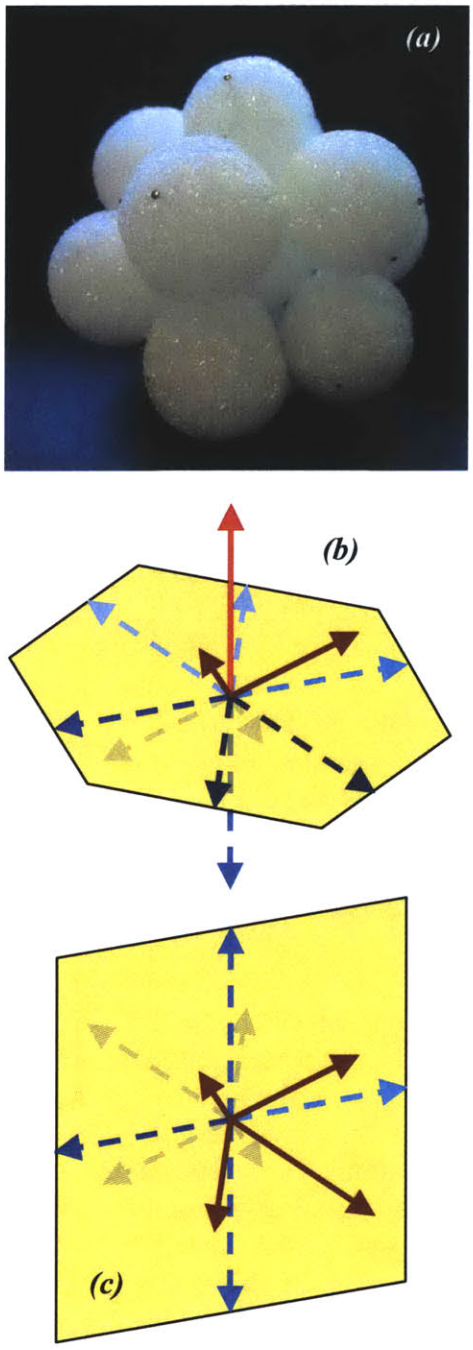

Fig. 3.11. Tetrahedral packing.

3.3.4. Results for Ideal Packings

As can be inferred from *equations 3.25* to *3.30*, the difference between effective and total stresses is always proportional to the magnitude of the resultant water force of a pendular

ring. This would dictate the nature of the relation between matric suction and $\sigma'-\sigma$ (*Fig.3.12*) to be of exactly the same shape as the matric suction versus resultant force curve (*Fig.3.5*).

In the case of each packing, per each repeatable element (i.e. particle), the number of pendular rings with calculable volumes is equal to the number of contacts. Therefore, the total volume of water per unit soil volume can be calculated for a given pendular ring size, which leads to engineering variables such as water content, suction – and through *Fig.3.12* and *3.13* – increment in effective stress. Note that these plots are for a contact angle of 30°. Equivalent plots for $\theta = 0°$, provided as *Appendices 3.2* and *3.3*, show a difference of about 15% in $(\sigma'-\sigma)$, with the smaller contact angles resulting in larger effective stress increments.

Figure 3.12. Normalized stress increment due to water vs. Matric suction, both normalized by particle radius.

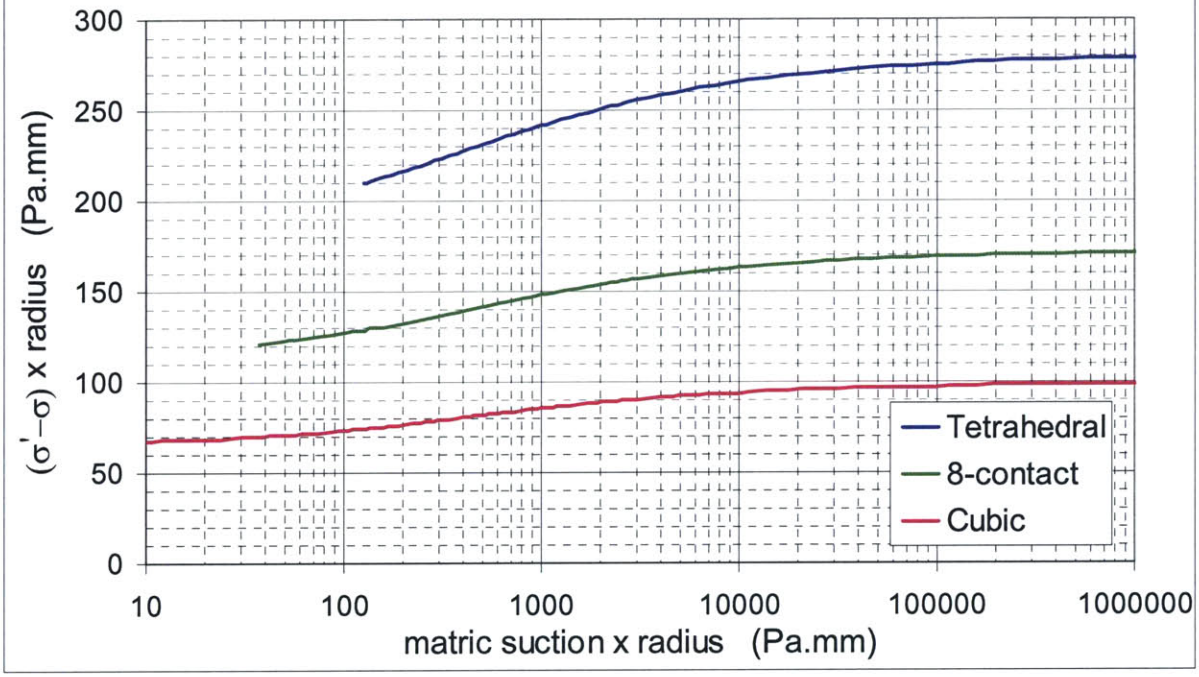

For gravimetric water content calculations, the particles are asumed to have a specific gravity of 2.2 (as given by the manufacturer in *section 6.1.1.2*). *Fig.3.13* shows the stress increment due to water not to be significantly affected by changes in water content. Note that the calculations are for the well-defined geometrical shape of a pendular ring. As the water content and the size of pendular rings approach zero, these calculations will no longer hold for the new form of the problem concerning only a few water molecules. *Figure 3.13* represents this as a singularity point for pendular water content of zero.

The residual portions of the SMC curves of the three uniform packings is plotted in *Fig.3.14*. It should be noted that these curves would be for both wetting and drying in the case of cubic and tetrahedral packings (that is, if the wetting and drying contact angles were the same). In case of the 8-contact packing, the curve represents only the wetting curve at lower suctions, as the drying curve would be higher in water content below a certain suction value. This is

because during drying there will be water pendular rings between non-contacting particles that are close to each other.

Fig.3.13. Gravimetric water content in pendular rings, for glass material vs. Normalized stress increment due to water

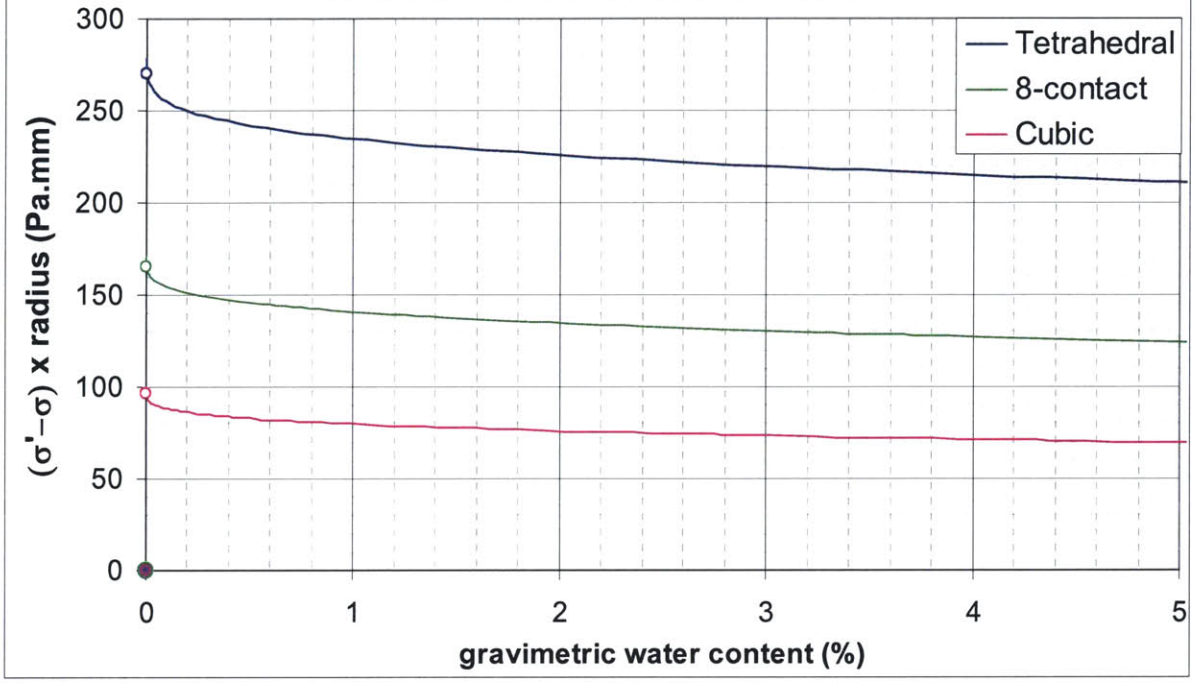

Fig.3.14. Residual parts of normalized SMC Curves for glass particles

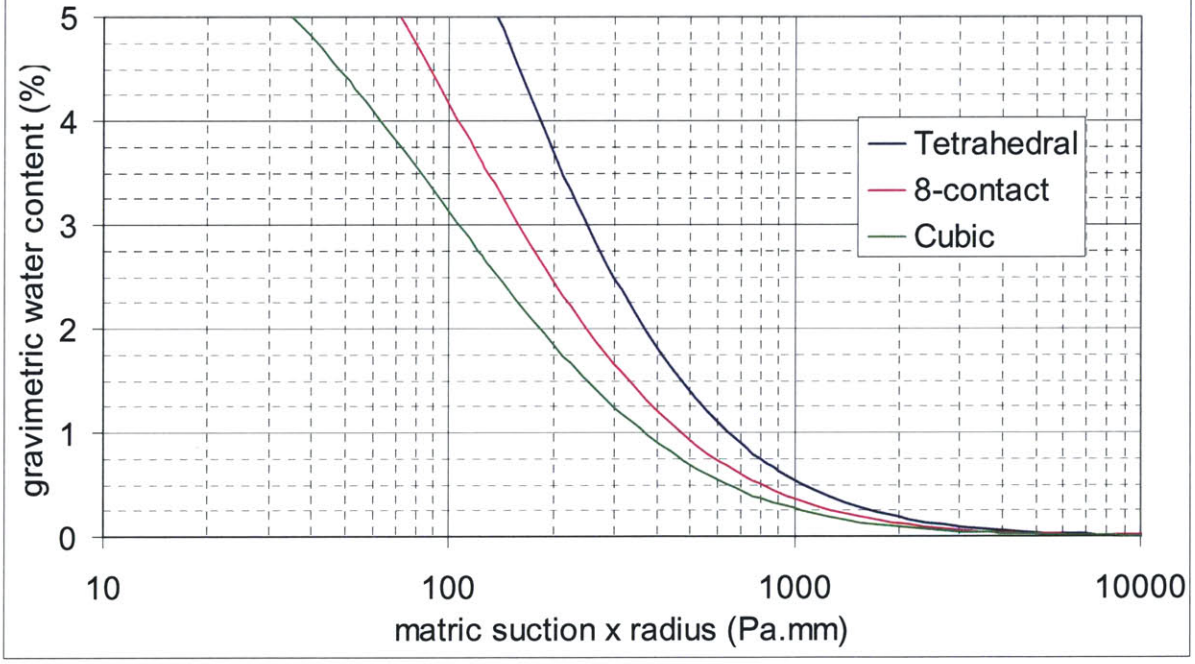

3.4. Shear Strength

3.4.1. Unification of Approaches

Before taking any step towards estimating the shear strength of partially saturated materials, it is necessary to examine and compare the two approaches that are described in *section 2.4.* Followers of the effective stress approach calculate strength by substituting Bishop's *Eq.2.8* into the Mohr-Coulomb strength equation (*Eq.2.9*) , which results in

$$\tau = c' + [(\sigma - u_a) - \chi.(u_w - u_a)].\tan\phi'$$

$$\tau = c' + (\sigma - u_a).\tan\phi' + (u_a - u_w).\chi.\tan\phi' \qquad \textit{Eqs.3.31}$$

The shear strength suggested by the independent state variables approach is

$$\tau = c' + (\sigma_n - u_a)\tan\phi' + (u_a - u_w)\tan\phi_b' \qquad \textit{Eq.3.32} \quad (\textit{Eq.2.13})$$

which seems to suggest that this would be a better approach if a unique ϕ_b' could be obtained for each soil, i.e. if the failure envelope was planar in $(\sigma_n\text{-}u_a) - (u_a\text{-}u_w) - \tau$ space. Non-linearity of the failure envelope in the $(u_a\text{-}u_w) - \tau$ plane was shown by Escario & Juca (1989) and also noted by the founders of the independent state variables approach, Fredlund et al. (1987). This agrees with the model framework proposed in this research, which results in a non-linear relation between suction and effective stress (*Fig.3.12*). In order to make *Eq.3.32* easier to use, Fredlund introduced a new parameter, a_w, such that

$$\tan\phi_b' = a_w \,.\, \tan\phi' \qquad \textit{Eq.3.33} \quad (\textit{Eq.2.14})$$

If *Eq.3.33* is substituted into *Eq.3.32*, *Eqs.3.31* are obtained with $\chi = a_w$. Since in essence they are both used as empirical fitting parameters, there is no proof of inequality of these parameters. Over the past decade numerous researchers suggested similar physical definitions for both a_w and χ, as well as identical correlations and methods to obtain them from tests (*Section 2.4*; compare *Eq.2.11* to *2.16*, or *2.12* to *2.17*, for example).

Therefore, it is the author's understanding that these two parameters are the same single parameter. Furthermore, the fact that both approaches use $(\sigma_n\text{-}u_a)$ and $(u_a\text{-}u_w)$ as independent state variables leads to the following result: Bishop's effective stress approach and Fredlund's independent state variables approach are two different ways of expressing a single unified approach.

However, this result does not shadow either one approach, as long as the approaches are studied in the context of the chronology of their development. Bishop's effective stress approach was originally suggested in an abstract fashion, whereas Fredlund's independent state variables approach arose from the need for an empirical and testing-based method that is able to represent soil behavior better than Bishop's approach. Eventual convergence of the empirical approach to its hypothetical counterpart shows that the effective stress approach

was as much on the right track as the independent variables approach, in addition to being the physically more sensible approach.

3.4.2. Hypothesis Linking Effective Stress to Shear Strength

When the strength gain due to suction is discussed in the literature, it is usually in terms of an additional cohesion for the same total stress state. Since the line of thought detailed in this thesis follows the effective stress approach's logic, the effective stress is defined as the state variable governing behavior. This means that gains in strength are expressed using terms of gain of effective stress (i.e. $\sigma'-\sigma$) instead of increasing the cohesion. These are interchangeable views (just like the two approaches discussed above) through the following equation

$$c' = (\sigma'-\sigma).\tan\phi' \qquad Eq.3.34$$

but one has the advantage of making more physical sense than the other. In both views, the same magnitude of suction is supposed to contribute to the same increase, regardless of the total stress, resulting in parallel failure envelopes and a unique angle of internal friction for each soil. This will be the basis for the experimental validation of the model.

Figure 3.15 illustrates the validation plan using σ_{oct} - q stress paths. The strength parameters of the Mohr-Coulomb failure envelope will be determined by running drained triaxial compression tests on saturated specimens (1). Results of the triaxial tests on unsaturated

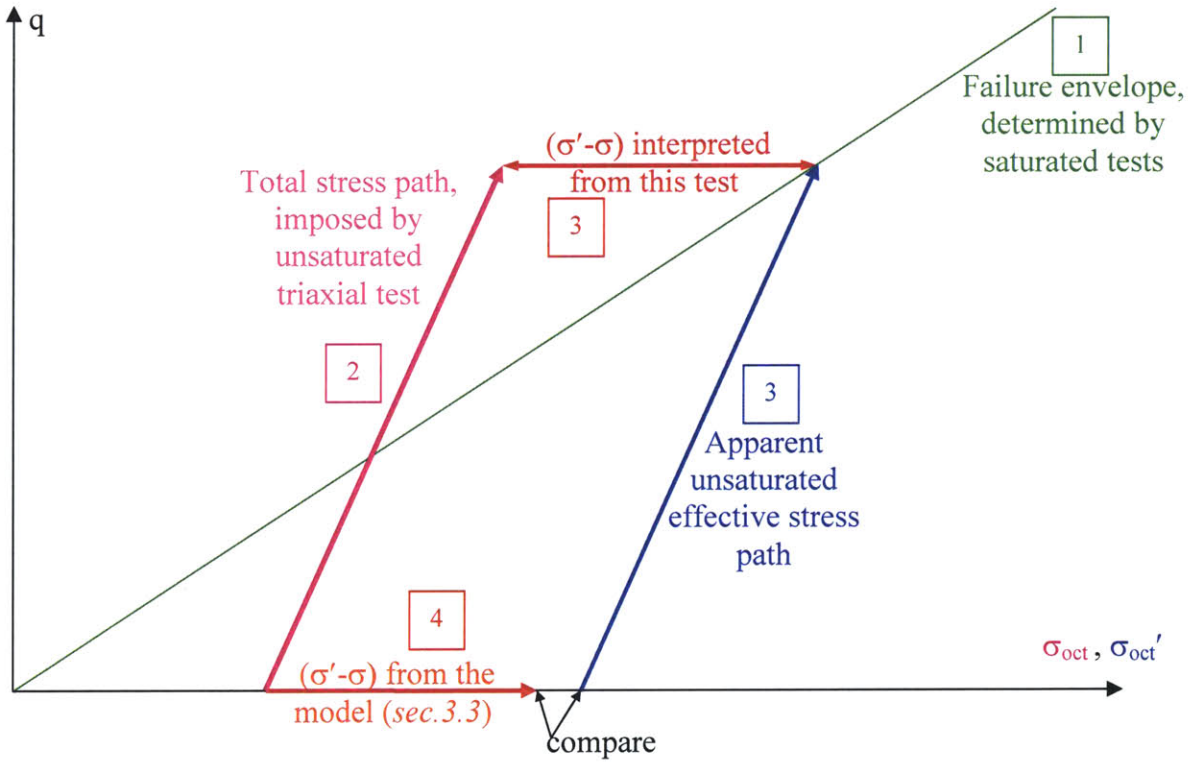

Figure 3.15. Graphical representation of the model validation through laboratory tests in σ_{oct} - q stress space. The numbered steps are discussed in the text.

specimens (2) will be used to back-calculate the actual effective stress at failure by equating the horizontal distance between the failure point on the total stress path and the failure envelope (3). The new hypothesis will provide the theoretical (effective-total) stress based on the water content, suction and density (4). Comparison between these two effective stress values will provide the basis for model evaluation.

From this point onwards, the word ***model*** will be used for the framework for analytically estimating the effective stress increment due to suction, proposed in *sections 3.2* and *3.3*. The word ***hypothesis*** will be used for inferring the effective stress increment due to suction, from the saturated and unsaturated shear strength envelopes, proposed in *section 3.4.2*.

3.5. Solutions by Other Sources

From their experiments and numerical calculations, Chateau et al. (2002) report that, the magnitude of the water force resultant varies very little for particles in contact, and is slightly larger for smaller water contents. For separating particles, the force diminishes much quicker for systems with less water, which means for a given separation distance, the water force is smaller in most cases with decreasing water content. Simulations by Yang et al. (2003) show larger forces for increasing water content, which agrees with Chateau's results for the case of non-contacting particles.

In 2004, Likos & Lu attempted to analyze the effective stress using a similar logic to the one presented in *section 3.2*. In order to avoid geometrical complexity and particle coordination issues, they simplified the problem by dividing only one resultant pendular force by the cross-sectional area of a single particle. Since both variables (ΣF and $A_{element}$) in *Eq.3.24* were calculated in a fundamentally incorrect way, their solution is not reliable. However, since they erred in similar proportions on the lower side of both the numerator and denominator of the ratio, their solution can be expected to give values close to those calculated in this research.

Sako et al. (2001) derived the following equation for the apparent cohesion due to suction:

$$c' = \frac{\pi}{\pi - 2} \cdot F \cdot \left(\omega \cdot \frac{1}{1+e} \cdot \frac{3}{\pi \cdot D^2} \right) \cdot \tan\phi' \qquad \textit{Eq.3.35}$$

where ω is the number of contact points per particle (i.e. coordination number). In order to compare with the results from *section 3.3*, *Eq.3.35* can be rewritten, by use of *Eq.3.34*, as:

$$\sigma' - \sigma = \frac{3}{\pi - 2} \cdot \frac{\omega}{1+e} \cdot F/D^2 \qquad \textit{Eq.3.36}$$

Respectively for cubic, body-centered cubic and tetrahedral packings; when coordination numbers of 6, 8 and 12 are plugged into this equation with corresponding void ratios, the results are 8.26 times larger than the results from *section 3.3*, for all three cases.

Appendices

3.1. Catenoid and torus solutions for various contact angles. Dimensions are in terms of grain radius.

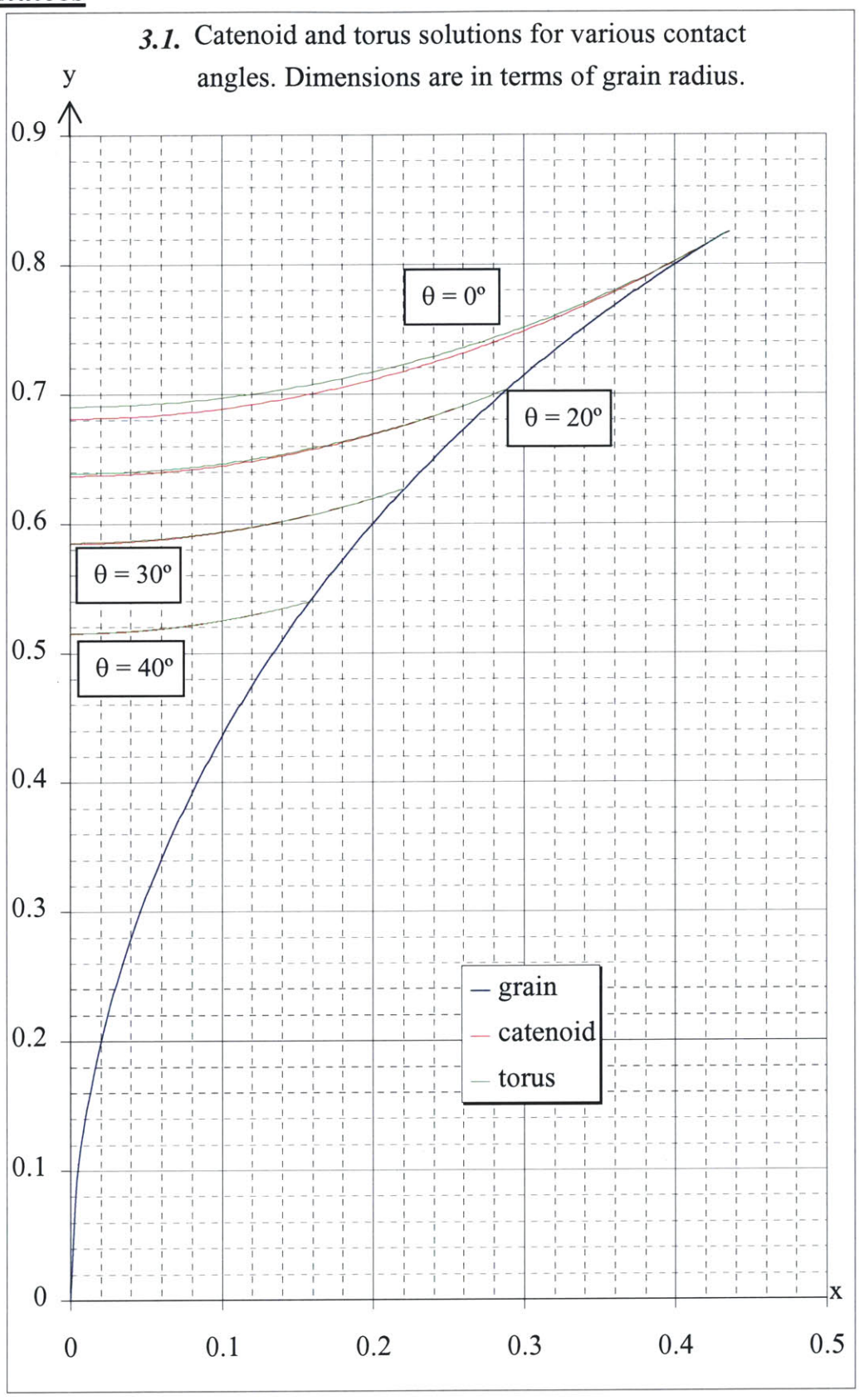

Appendix 3.2. Normalized stress increment due to water vs. Matric suction, both normalized by particle radius. ($\theta = 0^{\circ}$)

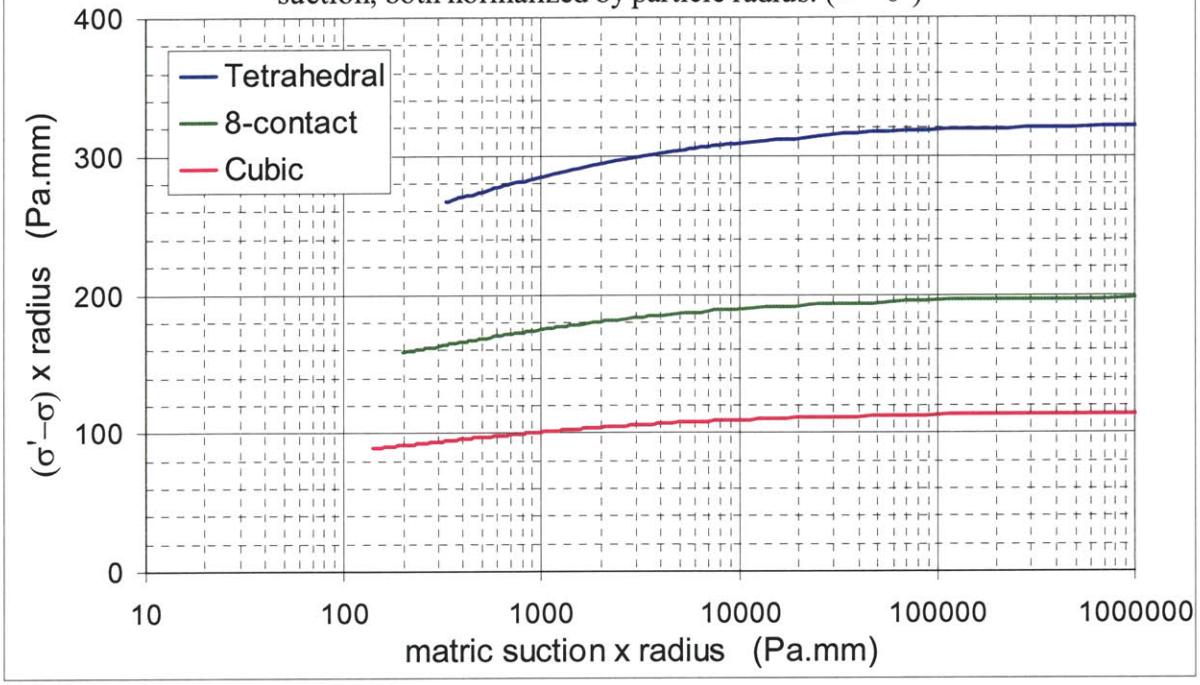

Appendix 3.3. Normalized stress increment due to water vs. Gravimetric water content in pendular rings, for glass material. ($\theta = 0^{\circ}$)

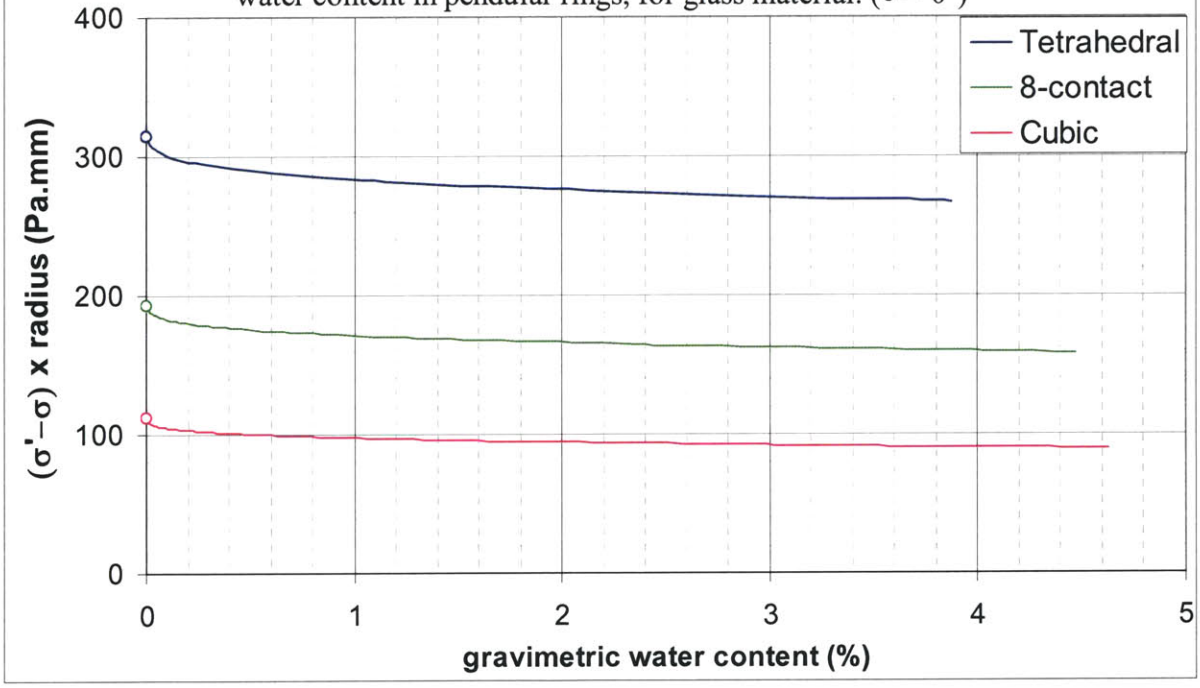

4 EQUIPMENT

4. EQUIPMENT

4.1. MIT Tensiometers

For the research on soil suction at MIT, nine versions of tensiometers were developed by Dr. Kurt Sjoblom (Sjoblom, 2000) and later the author (Toker, 2002). This was an evolutionary process, in which each new design attempted to improve on an aspect of the previous successful version. The last of the line prior to the research associated with this thesis was Version 6.1 (*section 4.1.4.1*).

Four new versions were developed during the course of this research. A summary of the various characteristics of these recent tensiometer designs are presented, together with the characteristics of Version 6.1, in *Table 4.1*. As far as the versions detailed here are concerned, the first digit of the version number designates the tensiometer's body geometry, and the second digit designates the type of porous interface (0 for Soil Moisture Corporation stone, 1 for Kochi University ceramic, 2 for Vycor porous glass). In the rest of the text, Tensiometer Version 6.1 will be abbreviated as T 6.1, Version 7.0 will be abbreviated as T 7.0, and so on.

Table 4.1. MIT Tensiometer history/statistics/performance/advantages and disadvantages over former models.

Device*	Year*	Inter face	Highest Measured Suction	Pressure Transducer	Disadvantages	Advantages over prior versions
T 6.1	2000	Kochi	13.2kgf/cm^2	200 psi	Not a triaxial pedestal	Replacable transducer
T 6.2	2003	Vycor plate	24 kgf/cm^2	200 psi	Saturation difficulty, fragile, slow response	Highest capacity in MIT
T 7.2 #	2005	Vycor rod	2 kgf/cm^2	1000 psi	as T62, low resolution, problematic interface	convenience in the saturation setup
T 7.0	2005	SMCo	0.8 kgf/cm^2	25 psi	Low capacity	as T7.1, high resolution
T 7.1	2006	Kochi	4.3 kgf/cm^2	200 psi	None	as T7.2, triaxial setup use

*: versions ordered chronologically, not by number.
#: the design was abandoned because it could not fulfill its design purposes.

In addition to the common design properties and materials below, another noteworthy detail of all of these versions is the rounding of the rim of the top face (see *Figure 4.1*). This is done to prevent this rim from cutting into o-rings (in case of SMC tests) and impermeable membranes (in case of triaxial tests).

A tensiometer can take measurements as long as the matric suction remains below a certain value (tensiometer capacity). The capacity of a tensiometer depends on the saturation procedure (applying greater vacuum and saturation pressure) and the porous interface (largest pore size).

4.1.1. Porous Interfaces

The working principle of a tensiometer is to establish a hydraulic connection between the pore water and a pressure measurement device through a porous interface that is attached to the tensiometer body with epoxy.

4.1.1.1. Soil Moisture Corporation Stone

This type of porous interface has widespread usage in suction measurement. Since long before the invention of a high capacity tensiometer, this type of material (known as a high air entry ceramic disc) has been used in pressure plate tests. Soil Moisture Corporation manufactures ceramics with a variety of air entry pressures and pore sizes. The porous stone of T7.0 was cored out of a 1-bar air entry disc, whose average pore diameter is 2.1 μm (Fredlund & Rahardjo, 1993).

4.1.1.2. Kochi University Ceramic

These porous materials (*Table 4.2*) were manufactured by Prof. Kazumichi Yanagisawa of Kochi University, Japan, as a part of his research on ceramics (Yanagisawa, 1994). The Kochi Ceramics are manufactured by hydrothermal sintering of silica gels, resulting in fused ceramics of very fine pore distributions (30-80nm average pore diameter, 3-22 kgf/cm^2 air entry pressure). Their advantages over the commercially available SMCo. stones can be summarized as providing the possibility of higher capacity, better inter-pore connectivity (easier saturation, without back-pressure) and compatibility with the pressure transducers for saturation purposes (For a detailed study, refer to Sjoblom, 2000).

Table 4.2. Preparation and usage of the Kochi silica compacts (from Toker, 2002).

Production at Kochi University							***Tensiometer use at MIT***	
Water (%)	T (°C)	Preload (MPa)	Time (min)	Sinter (MPa)	Time (min)	Year	Used in	AEP (kgf/cm^2)
4.45	300			20	60	1998	T7.1	4.3
10.2	300	60	10	2	60	1999	T6.1	3 - 15

Previous research (Toker, 2002) observed three drawbacks of Kochi ceramics. Since the research in Kochi University was not commercialized or standardized, their ceramic properties proved to be unpredictable. The second drawback of Kochi ceramics is a durability problem, which is specifically micro-cracking due to sudden changes of water tension upon air entry. Hence, the stones may start to disintegrate after any number of tests. Thirdly, the Kochi ceramics are available in very scarce quantities, for they were prototype products of research, that has not been pursued since 2000.

4.1.1.3. Vycor® Porous Glass

Vycor Porous glass (*Table 4.3*) was developed by Corning, Inc. (Corning, NY). For this research, pieces of the material were ordered with specified dimensions, from Advanced Glass & Ceramics (Holden, MA). This material was purchased as cylinders with diameters of 1 cm (20 pieces) and 2 cm (1 piece). The 2 cm cylinder was cored out of a glass manufactured as a plate, whereas the 1 cm cylinders were slices of a glass rod of the same diameter. An unidentified planar impurity from the manufacturing process is visible within the rod slices. The low suction capacity of the rod slice indicates that (at least part of) this visible impurity is a continuous planar pore, making the rod slices unusable in high capacity tensiometers.

Table 4.3. Specifications of Vycor Porous Glass 7930 (from *www.corning.com*)

Dry specific gravity:	1.5
Porosity:	0.28
Specific surface Area:	250 m^2/g
Avg. pore diameter:	4 nm
Avg. Modulus of Rupture at 25°C:	420 kgf/cm^2
Modulus of Elasticity at 25°C:	175000 kgf/cm^2

It should be noted that the permeability of both types of Vycor glass is observed to be extremely low from the beginning of saturation, as the water front takes more than one hour to pass through the glass with a pressure difference of several atmospheres when filling the tensiometer. Nevertheless, once saturated, the response time of tensiometers with Vycor glass to changes in pressure/suction was less than a minute. Therefore the glass might have some promise of future use in high capacity tensiometers.

4.1.2. Epoxy

The adhesive used for fixing the porous stones to the tensiometer body is Loctite® E-90FL Toughened, flexible, impervious and impact resistant Durabond® Epoxy Adhesive (see *Table 4.4* for properties). This is a different adhesive than the epoxy used in the tensiometers of the prior research (versions 6.1 and earlier used Stycast 2651MM, which is a more rigid epoxy). The Loctite E-90FL epoxy was primarily chosen for its flexibility, in order to reduce the bending moments within the porous interface during high tension.

Table 4.4. Specifications of Loctite E-90 Durabond (from *mymatweb.com*)

Viscosity:	71500cP
Hardness, Shore D:	60
Shear Strength:	70-211 kgf/cm^2
Peel Strength:	0.9-7 kgf/cm
Pot Life:	90 min

4.1.3. Metals

The tensiometer body is Stainless Steel 304 (see *Table 4.5* for properties). A copper gasket provides the seal between the pressure transducer and the stainless steel body.

Unlike rubber seals, a copper vacuum gasket seals by yielding under compression. Concentrating the stress on the sharp edges of the seal, which are pressed on the surfaces to be sealed, usually guarantees yielding. Copper Alloy 110 (*Table 4.5.*), which was the copper

alloy available at MIT Civil and Environmental Engineering Department machine workshop at that time, was used for this manufacture.

Table 4.5. Properties of Copper Alloy 110 and Stainless Steel 304

(from *www.efunda.com*)	***Cu110***	***S.S.304***
Specific Gravity	8.8-8.94	8
Poisson's Ratio	0.34	0.27-0.3
Young's Modulus (GPa)	117	193
Yield Strength (MPa)	69-365	205
Ultimate Strength (MPa)	221-455	515
Thermal Conductivity (W/m°K)	390	16.2
Thermal Expansion (10^{-6}/°C)	16.9	17.2

4.1.4. New Tensiometer Designs

4.1.4.1. Tensiometer Generation 6

The design purpose of Version 6 tensiometers was to have a device with a replaceable pressure transducer, and to minimize sensitivity to temperature changes (Toker, 2002; Toker et al., 2004), for usage in SMC curve measurements. It incorporated two essential components (a copper seal and tightening nut) to achieve these goals (*Figure 4.1*).

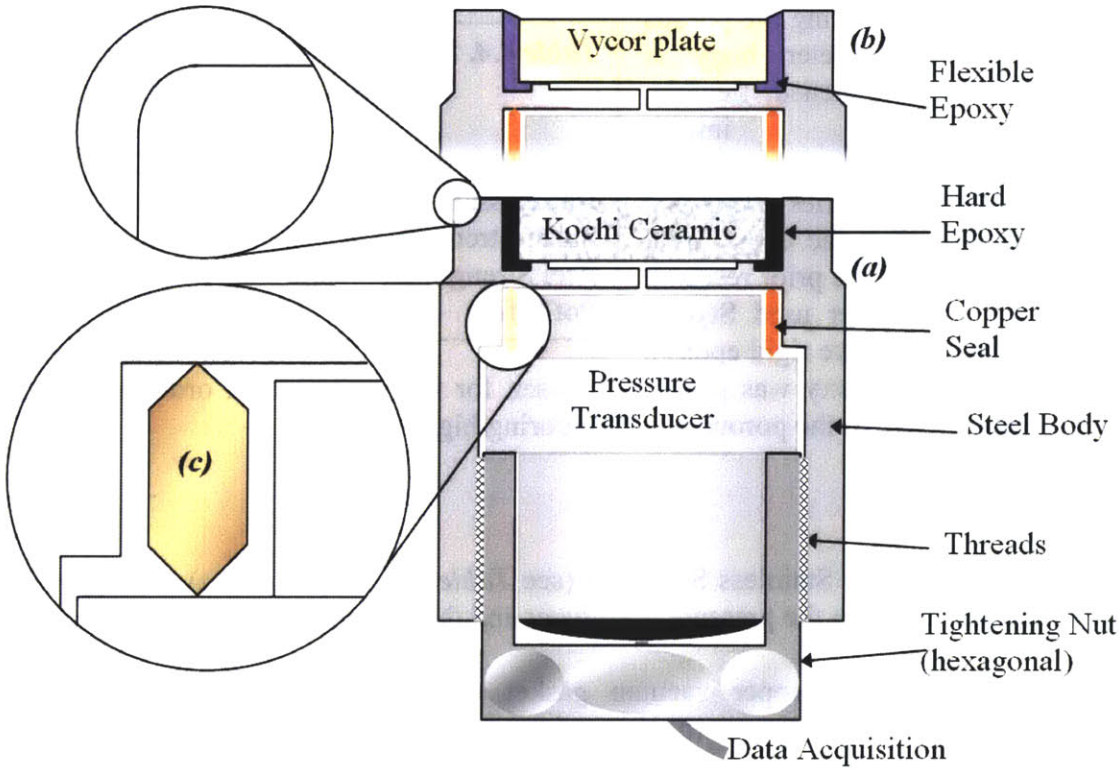

Figure 4.1.(a) MIT Tensiometer 6.1 (Toker, 2002) ***(b)*** MIT Tensiometer 6.2 ***(c)*** Copper seal.

Version 6.2 aimed to increase the capacity for suction measurement by replacing the porous interface (Kochi ceramic) with a material that has finer pores (Vycor glass). Two other modifications were incorporated with the purpose of countering the brittleness of the glass. First, the glass was installed with a slight recess from the top surface (*Figure 4.1.b*), because it is not machineable (The other porous materials are installed at an equal or higher level to the top surface, and then the entire top surface of stone, epoxy and steel is machined flat). The second difference is the use of a flexible (and also machineable) epoxy to reduce bending moments on the Vycor, as mentioned earlier in *section 4.1.2*.

4.1.4.2. Tensiometer Generation 7

Although the top face of the generation 6 tensiometers was of triaxial diameter, their geometry had some compatibility issues with incorporation into a triaxial setup. The geometry of generation 7, i.e. the tensiometer body that would act as triaxial pedestal, had to be changed to have constant diameter through its length. Its bottommost part is shaped as a hexagon for gripping purposes to hold it in place, while it is fixed to the triaxial base from the underside. The lower surface also has a groove for an o-ring, which establishes a seal between the base of the triaxial cell and the tensiometer. The tightening nut of generation 6 is replaced by a threaded pipe with a hexagonal mid-section, in order to fix the pressure transducer into the device. On the bottom end, a nut fits on the threads of this pipe in order to tighten the whole assembly together.

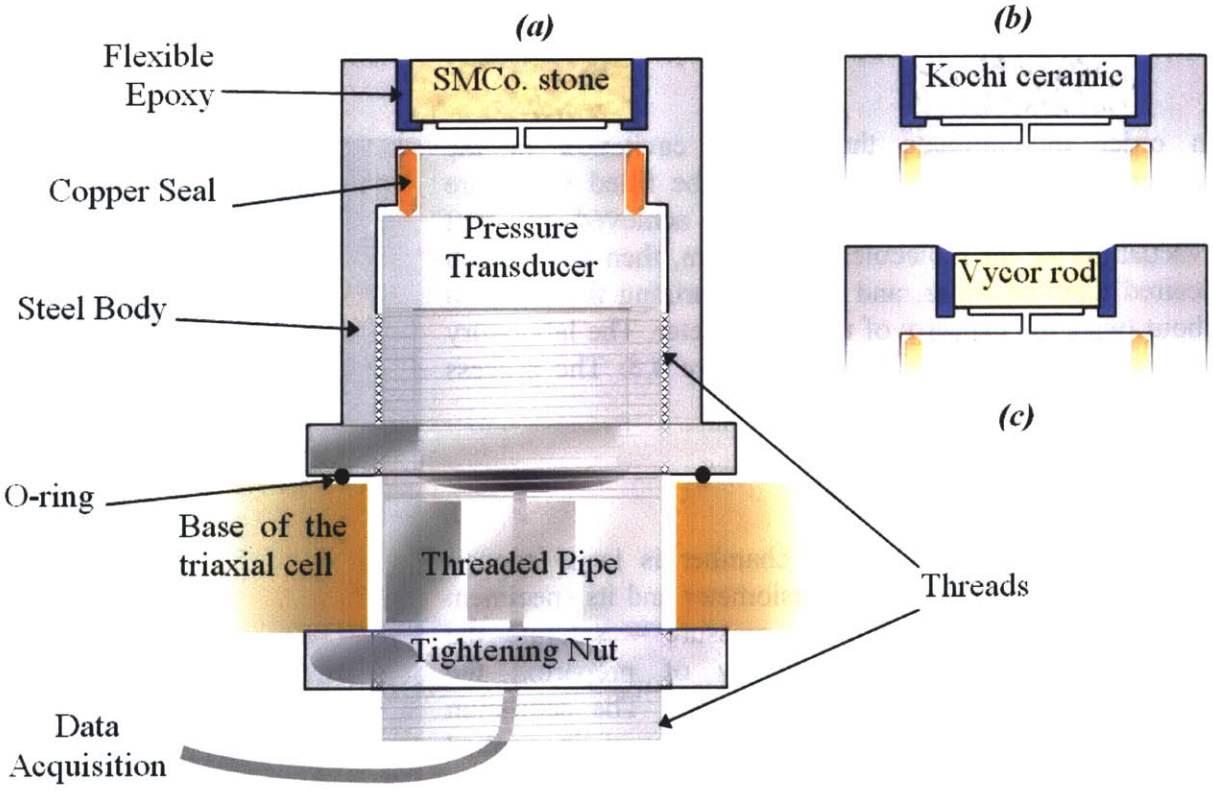

Figure 4.2.(a) MIT Tensiometer 7.0 ***(b)*** MIT Tensiometer 7.1 ***(c)*** MIT Tensiometer 7.2.

It is imperative to tighten the threaded pipe into the tensiometer with a much larger force (two large wrenches or a lathe) than that used on the nut to fix the tensiometer to the triaxial setup (tighten by hand). Otherwise, the copper seal within the tensiometer may break contact and thereby be rendered useless.

4.2. Saturation Setup

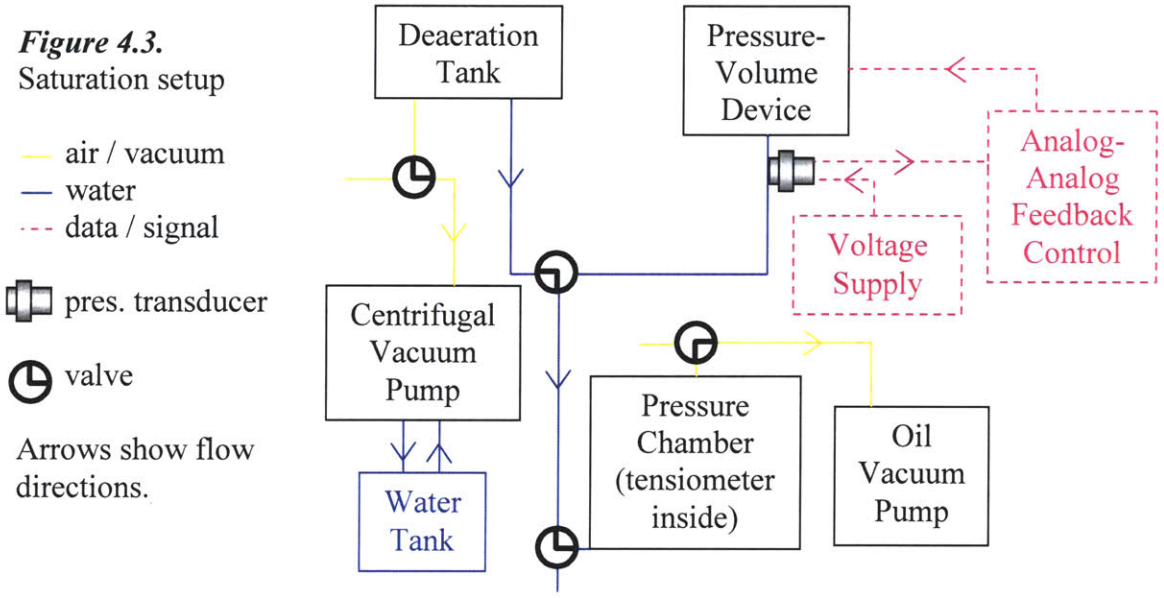

Figure 4.3. Saturation setup

In order to eliminate the risk of cavitation in the tensiometer, its pores and gaps must be filled with pure water without air bubbles. This is achieved by first evacuating the air molecules by vacuum, then filling with deaired distilled water, and then pressurizing the water to about twice the capacity of the tensiometer. The laboratory setup for saturation is illustrated *Figure 4.3.* The process will be detailed further in *Chapter 5.*

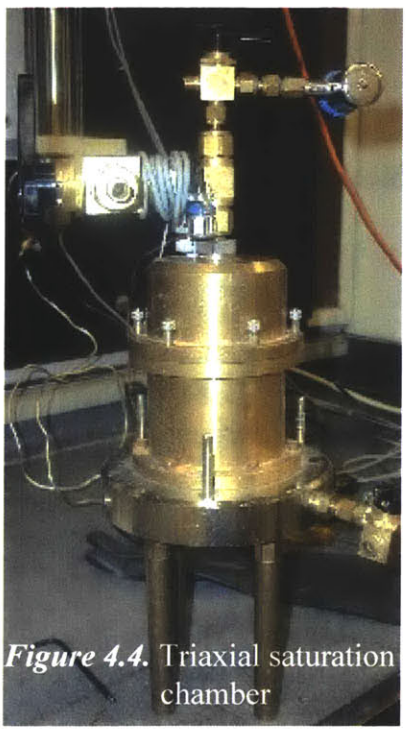

Figure 4.4. Triaxial saturation chamber

4.2.1. Pressure Chamber

The standard triaxial pressure chamber is large enough (~700cc) to enclose both the tensiometer and its specimen. This gives the opportunity to pressure – saturate the specimens, opening the possibility of preparing the specimen under a variety of conditions. The saturation chamber has multiple in/outlets. A vacuum is applied through top outlet, whereas the distilled deaired water supply and pressure control is connected to the base.

4.2.2. Vacuum Pumps

As shown in *Figure 4.3*, two vacuum pumps were used in the saturation setup. The one connected to the deaerator is a centrifugal pump driving a water-vacuum aspirator. It circulates water in a plexiglass holding tank, which is cooled by tap water. The pump that is used for evacuating all other equipment is an oil vacuum pump, which creates a vacuum with an eccentric cam. The centrifugal pump can draw the pressure down to the vapor pressure of water, whereas the oil pump is capable of reducing the pressure down to the vapor pressure of oil, which is about 1000 times smaller than that of water.

4.2.3. Deaerator

The Nold Deaerator is a plexiglass cylindrical tank of about 4 liters volume. It has a water pipe and an air pipe, connected to the bottom and top of the tank, respectively. It also contains a rotating disc on the bottom inside, for cavitating the water to free the air.

4.2.4. Pressure Volume Actuator

The ***P***ressure ***V***olume ***A***ctuator is standard equipment that had been designed (Andersen, 1991) and has been widely used in the MIT Geotechnical Laboratories. It consists of a 0.75-inch (19mm) diameter steel piston, a ball screw actuator (*section 4.2.4.1*) that moves the piston, and a DC servo-drive motor (*section 4.2.4.2*) that drives the worm of the ball screw actuator. The combined mechanical advantage of the servo-motor and the actuator gives the PVA the ability to pressurize upto 175 kgf/cm^2.

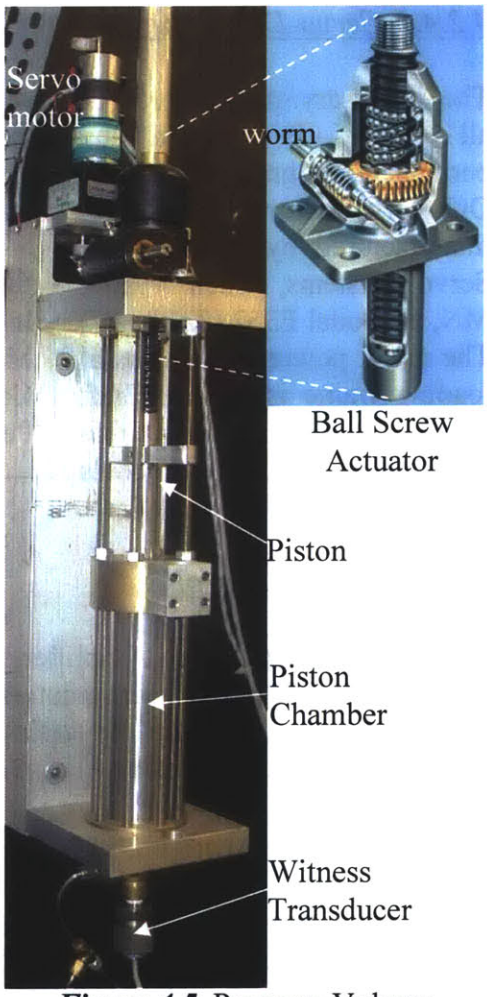

Figure 4.5. Pressure-Volume Actuator

Peripheral equipment can be attached to parts of this piece of equipment. In the case of the saturation setup, a 1000-psi (70kgf/cm^2) pressure transducer (a.k.a. witness transducer) is connected to the PVA's outlet to monitor the pressure (*Figure 4.5*). The two PVAs of the triaxial setup (*Figure 4.9*) each have a fluid reservoir at their outlets (the cell PVA has an oil reservoir, the pore PVA has a water reservoir). In addition, the pore PVA has a displacement transducer installed in parallel to its piston, for the purpose of volume measurement.

4.2.4.1. Ball Screw Actuator

The rotational movement supplied by the servo-motor is converted into a translational movement of the piston by a ball screw actuator. This mechanism is model 28630, manufactured by Duff-Norton, Charlotte, NC (*Table 4.6*).

Table 4.6. Specifications of Duff-Norton 28630 ball screw actuator (from manufacturer's website)

Capacity:	5 kN
Lifting Screw Diameter:	15.9 mm
Worm Gear Ratio:	5:1
Travel per Worm Turn:	1.02 mm

4.2.4.2. Servo-Drive Motor

The necessary piston force in all PVAs is exerted by permanent magnet, brushtype, DC servo-motors, which are manufactured by Electro-Craft Servo Systems, Eden Praire, MN, as model E352 (*Table 4.7*). The motor powering the triaxial loading frame is Electro-Craft E586. It is likely that production of these models have been discontinued.

Table 4.7. Specifications of Electro-Craft E-series servo-motors (from product instruction manual)

	E352	E586
Signal input voltage:	±10 V	
Input impedance:	22 kΩ	
Maximum speed:	7500 rpm	5000 rpm
Continuous torque:	263 gf.cm.	1500 gf.cm.
Peak torque:	525 gf.cm.	3000 gf.cm.

4.2.4.3. Motor Controller

The MAX-100 DC Servo Amplifier, manufactured by Electro-Craft, is a controllable power source for brushtype, DC servomotors. Its output regulates the speed of the servo-drive. This corresponds to controlling the strain rate in case of the triaxial loading frame, and, rate of pressurization/decompression in case of the PVAs of saturation and triaxial setups.

4.2.5. Voltage Supply

In this setup, two input voltages are needed. For this purpose, a Hewlett-Packard 6234A dual output power supply with two differently adjustable voltage outlets was used. Alternatively, two separate power supply adapters could have been employed. One of the voltages is connected to all pressure transducers (including the ones in tensiometers) at their input voltage (5.5 V). The other outlet connects to a voltage divider (*Figure 4.6*) for voltage reduction of 100 via *Equation 4.1* (4 V on the power supply equals 40 mV voltage output). This is used to set the target voltage (*section 5.1.1.1.4*) for the feedback control (*section 4.2.6*). All negative poles are grounded to earth.

Figure 4.6. The circuit bridge of the power supply:

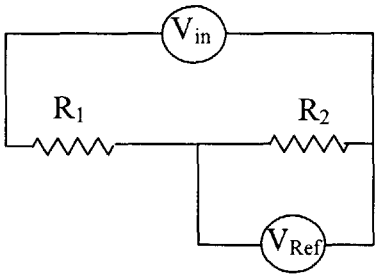

$$V_{Ref} = V_{in} \cdot \frac{R_2}{R_1 + R_2} \quad \text{...Eq.4.1}$$

4.2.6. Analog-Analog Feedback System

During the saturation process, a constant pressure is maintained on the tensiometer. This is accomplished by an analog-analog feedback system that was built by Dr. Kurt Sjoblom (2000). A basic block diagram of the feedback system is presented in *Figure 4.7.* The feedback circuit compares the preset reference voltage to the witness transducer reading, and a MAX-100 controller adjusts the servomotor proportional to the difference.

The feedback circuit is shown in *Appendix 4.2.* The circuit is made of three instrument amplifiers, which are model AD524 manufactured by Analog Devices, and are common in the laboratory. A gain of x10, which is wired into the output of the circuit, initiates a very fast response time in the motor.

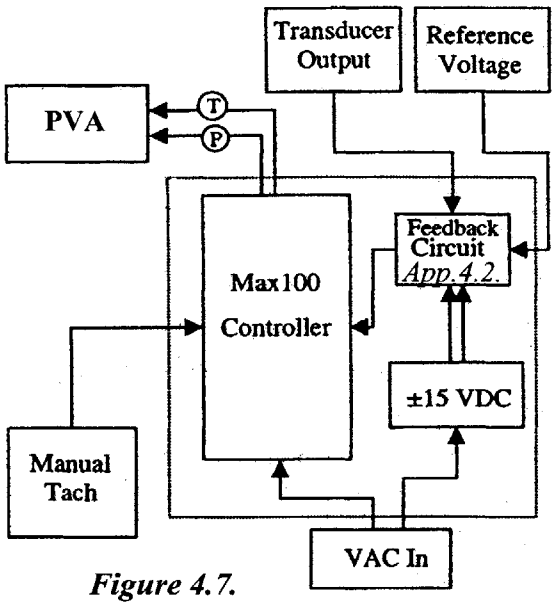

Figure 4.7.
Block diagram of the feedback system (Sjoblom, 2000).

4.2.7. Piping and Connections

Copper piping is used in the saturation setup for the lines that carry pressurized water. Non-pressurized lines are plastic. Connections are either brass or stainless steel swageloks, whereas the valves are all brass ball valves. Tubing and connections are of various diameters.

4.3. Triaxial Setup

The MIT Geotechnical Laboratory has been developing, using, and improving automated versions of conventional testing equipment for almost two decades. For triaxial equipment, this process started with the development of the MIT Automated Stress Path Triaxial Cell (Sheahan, 1991; Sheahan & Germaine, 1992), which was created by incorporating independent automation components into each controllable quantity (axial load, radial pressure, pore pressure) and connecting all automation mechanisms to a modified personal computer. This automated triaxial test setup has evolved over the years in terms of performance (improvement of the control algorithm and circuitry – Andersen, 1991) and application (purpose-specific variants). Variants include high-pressure capacity (Andersen, 1991), small strain measurement (Santagata, 1998), large diameter specimen, and now, a tensiometer. A schematic of the entire setup is presented as *Figure 4.8*, which also indexes sections of the thesis describing individual components.

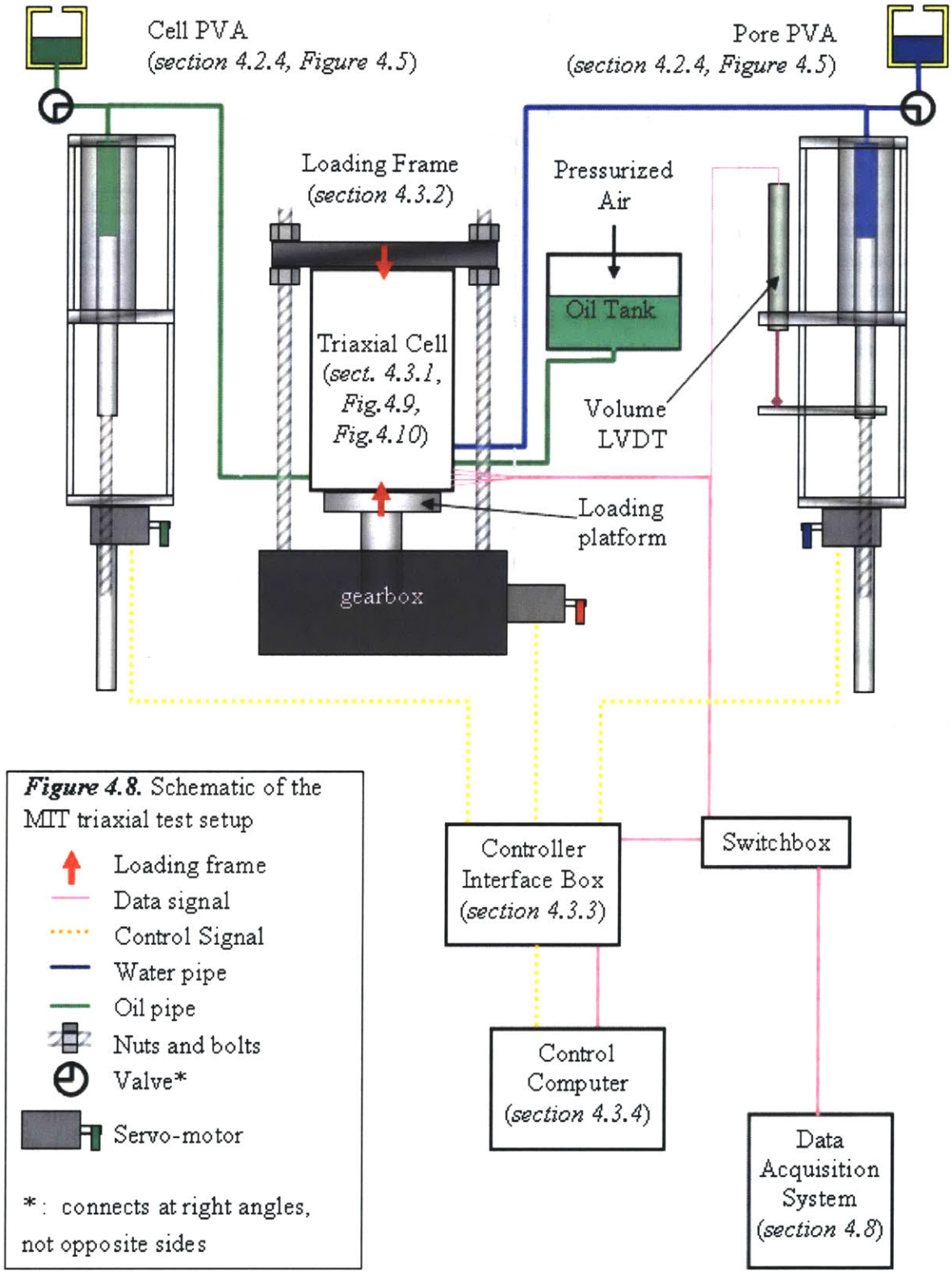

Figure 4.8. Schematic of the MIT triaxial test setup

4.3.1. Triaxial Cell

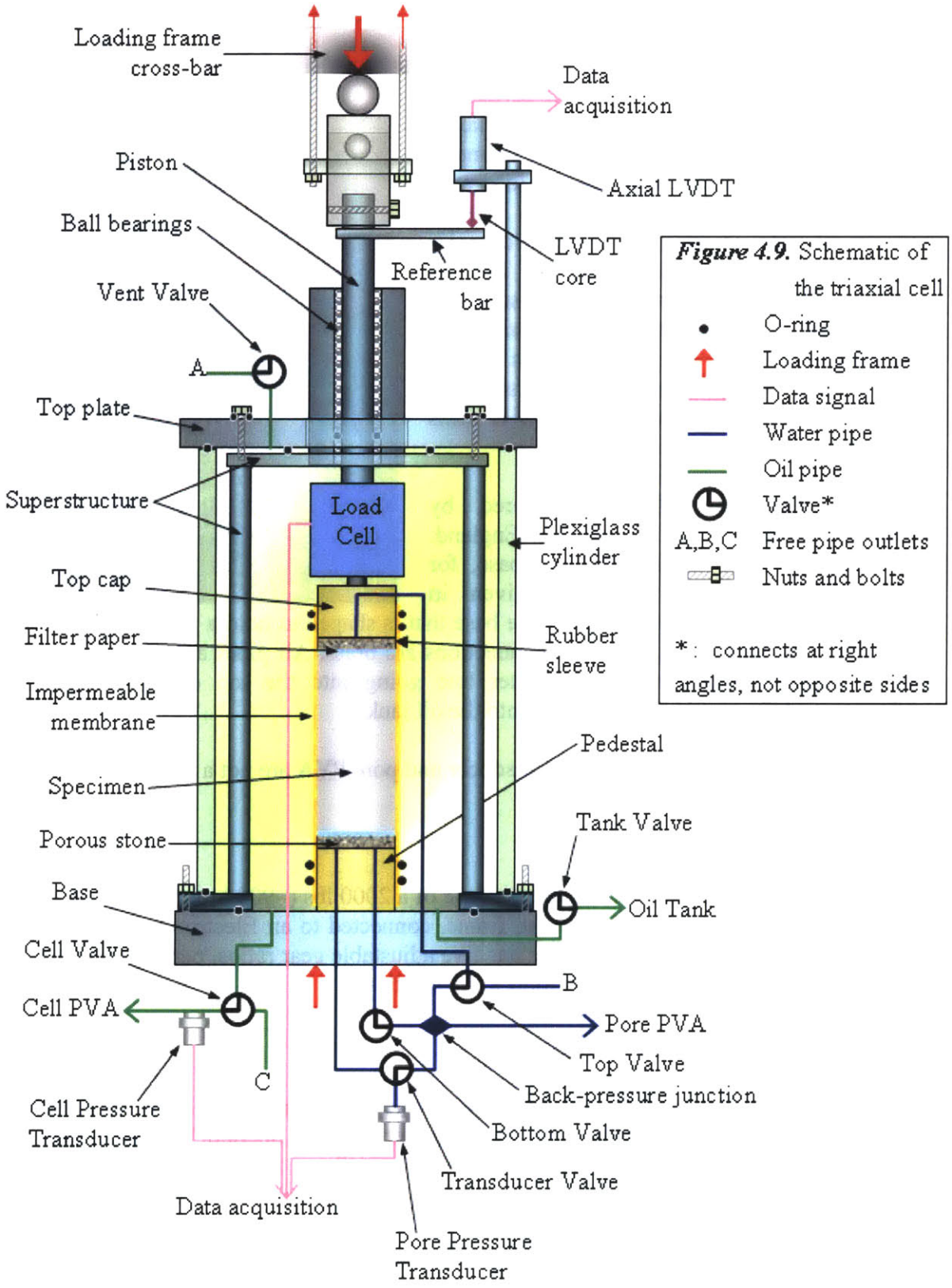

The triaxial cells used at MIT are custom-built at the Institute. Over the years, pieces of these cells have been modified and customized depending on the needs of researchers. The version used in this research is illustrated in *Figures 4.9* and *4.10*.


Figure 4.10. MIT triaxial cell

These cells accommodate a standard triaxial specimen of 8 cm height and 3.5 cm diameter (approximately), as well as an internal load cell. The plexiglass cylinder can sustain internal pressures of upto 15 kgf/cm^2, but this capacity deteriorates over time, down to as low as 6 kgf/cm^2. The top cap, load cell and piston seal assembly are all carried by a steel structure of three vertical columns. The top plate rests equally on the o-rings on top of both the superstructure and the plexiglass cylinder, such that it seals against both.

The base was originally manufactured by Wykeham Farrance Eng. Ltd., Slough, England. Its geometry is same as the modified base, for which the technical drawings are given in *Appendix 4.4*, except the center part of the base that is shaped to hold a pedestal instead of a tensiometer. All valves and swagelok connections are brass. All pipes are made of stainless steel or copper, except the plastic water line going into the top cap (for minimized resistance), and the plastic oil line going into the oil tank.

In unsaturated tests, the pore pressure transducer and pore PVA are not a part of the setup.

4.3.2. Loading Frame

The triaxial cell is axially loaded through the use of a 2000 lbs (~900 kg) capacity, bench-top Wykeham Farrance screw-driven loading frame, connected to an Electro-Craft E586 servo-drive motor (*section 4.2.4.2*). This frame has five adjustable gear ratios, permitting controlled strain rates when combined with the motor's capabilities.

4.3.3. Controller Interface Box

The servomotors of the triaxial setup can be controlled either manually or by the computer. The interface between the servomotors, the computer, and the operator's manual control is established by a control box (*Figure 4.11*). The box allows the user to switch between manual control through the use of a potentiometer (i.e. knob) and automated control by the computer. All three switches have the options of automated, manual, and off. MAX-100 cards, which power the servo-motors, are described in *section 4.2.4.3*.

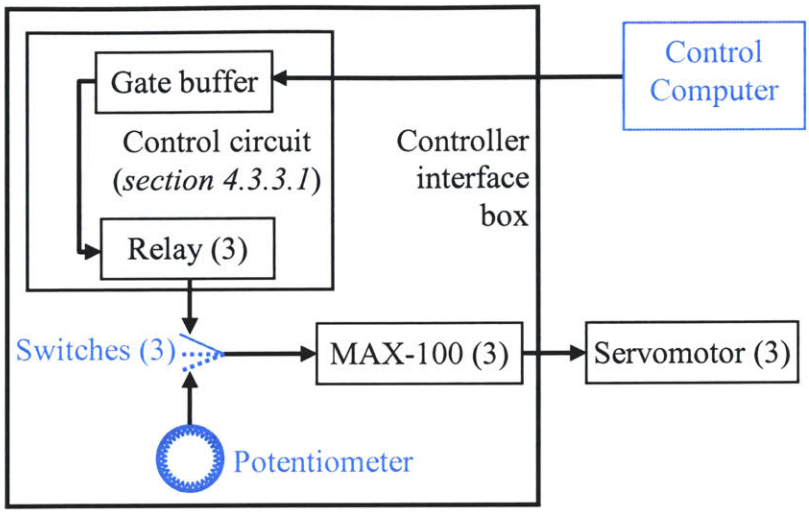

Figure 4.11. Simplified block diagram of the controller interface box.

(3) indicates that there are three of the noted components, separate for controlling each of axial displacement, pore and cell pressures.

Blue (light) components are the operator interface.

4.3.3.1. Control Circuit

The control circuit recieves computer outputs through a 25-pin connector, and distributes them to the individual MAX-100 cards. A detailed diagram of the circuit is in *Appendix 4.3*. The gate buffer is a DM7407N chip, which is manufactured by Fairchild Semiconductor, South Portland, ME. It contains six independent gates, each of which performs a buffer function. Relays are W171DIP-21 dual in-line package reed relay chips, manufactured by Magnecraft, Northfield, IL.

4.3.4. Control Computer

4.3.4.1. Hardware

The local data acquisition system is a Pentium-100 PC equipped with a high quality MIT-designed analog-to-digital conversion card and a commercial digital-to-analog output card.

The ***M***ulti-channel ***A***nalog-to-***D***igital ***C***onversion card is designed and built by Sheahan (1991) around Analog Devices Inc. model AD1170 high resolution, programmable integrating converter. The AD1170 offers independently programmable integration time (1-350 msec) and allows the user to specify the resolution (7-22 bits). For control purposes, the resolution is about 20 bits. For data acquisition, usable resolution is typically limited to 18 bits due to measurement and calibration noise error. The fastest usable data acquisition rate is about 1 second, whereas for control purposes, faster reading rates are used.

Each channel on the MADC is connected to a separate Analog Devices AD524 Precision Instrumentation Amplifier chip on the MADC, allowing the user to apply separate gain factors to individual channel output in order to improve precision. On the MADC used in this research, there is a gain of 10 on all pressure and load channels (all channels with outputs in the mV-range).

In triaxial setups of MIT, the MADC is used only for monitoring the ongoing experiments and guiding the control system, rather than the actual data acquisition (which is done by the CDAS described in *section 4.6.3*). Since great precision is not required for its task, the fine adjustments of zeros of the data channels on the MADC are not necessarily maintained.

The output card is manufactured by Strawberry Tree Inc. (now owned by IOtech), as the model ACAO-8. It is able to acquire and send voltage signals to external devices, as well as digital output to control relays, through upto 8 independent channels.

4.3.4.2. Software

The software is a QBASIC program written by Dr. John T. Germaine, for the specific purpose of interfacing the user with all the hardware of the MIT Automated Stress Path Triaxial Setup.

It requires inputs of specimen geometry, and transducer zeros and calibration factors to start. Once started, it displays the outputs of all transducers in both volts and engineering units (kgf/cm^2 for pressures, % for strains). An operator must be aware that these readings can be biased by the zero adjustments on the MADC cards, and are without the proper corrections. The program then allows the user to choose any one of the built-in control schemes, which are listed in *section 5.2.1.6*. The operator is able to define necessary specifics for the test, depending on the selected scheme. For example, a target strain rate can be input for consolidation and shear schemes. The program also shows the target values for each measured quantity, as well as the actual strain rate (which is not always equal to the target strain rate).

This program is also under continous modification, and has several more schemes added to those listed above at the time of this thesis.

4.3.5. Other Components

4.3.5.1. Cell Fluid

The ***silicone oil*** that is used as cell fluid is Dow-Corning "200 fluid", 20 centistokes silicone oil. This particular silicone oil's viscosity exhibits extremely low sensitivity to temperature (relative to other oils), is optically transparent and does not degrade, penetrate, or react with the o-ring seal or impermeable membrane materials within the duration of testing. Its electrically insulative nature is essential for the utilization of an internal load cell in the triaxial setup.

4.3.5.2. Membranes

The ***impermeable membrane*** is basic, unlubricated latex Trojan® brand condom manufactured by Church & Dwight Co., Inc., Princeton, NJ. The axial stiffness of the

Table 4.8. Properties of the impermeable membrane

Modulus of Elasticity :	14 kgf/cm^2
Perimeter (P_m) :	10.6 cm
Thickness:	88 μm

It requires inputs of specimen geometry, and transducer zeros and calibration factors to start. Once started, it displays the outputs of all transducers in both volts and engineering units (kgf/cm^2 for pressures, % for strains). An operator must be aware that these readings can be biased by the zero adjustments on the MADC cards, and are without the proper corrections. The program then allows the user to choose any one of the built-in control schemes, which are listed in *section 5.2.1.6.* The operator is able to define necessary specifics for the test, depending on the selected scheme. For example, a target strain rate can be input for consolidation and shear schemes. The program also shows the target values for each measured quantity, as well as the actual strain rate (which is not always equal to the target strain rate).

This program is also under continous modification, and has several more schemes added to those listed above at the time of this thesis.

4.3.5. Other Components

4.3.5.1. Cell Fluid

The ***silicone oil*** that is used as cell fluid is Dow-Corning "200 fluid", 20 centistokes silicone oil. This particular silicone oil's viscosity exhibits extremely low sensitivity to temperature (relative to other oils), is optically transparent and does not degrade, penetrate, or react with the o-ring seal or impermeable membrane materials within the duration of testing. Its electrically insulative nature is essential for the utilization of an internal load cell in the triaxial setup.

4.3.5.2. Membranes

The ***impermeable membrane*** is basic, unlubricated latex Trojan® brand condom manufactured by Church & Dwight Co., Inc., Princeton, NJ. The axial stiffness of the membrane ($K_m=E_m.A_m$) is equal to the product of all three properties given in *Table 4.8*, which is equal to 1.3 kgf.

Table 4.8. Properties of the impermeable membrane

Modulus of Elasticity :	14 kgf/cm^2
Perimeter (P_m) :	10.6 cm
Thickness:	88 μm

Rubber sleeves are cut from standard thickness (200 μm), triaxial (35 mm) diameter rubber membranes for soil testing. Their main purpose in the experiments of this research is helping the o-rings around the top cap, pedestal or tensiometer to seal. The sleeves also separate the impermeable membrane from the abrasive edges of the porous stones.

4.3.5.3. Filter Materials

Porous stones are 3.5 mm-thick pieces cut to triaxial diameter, from sintered carborandum grinding stones.

Nylon filters are cut to triaxial diameter, from 53 μm-thick sheets of Nitex® nylon monofilament fabrics, manufactured by Tetko Inc., Elmsford, NY. Compared to the widely used filter papers, these are extremely durable, reusable, softer, and offer less frictional resistance. A nylon filter can withstand dozens of tests, and be washed with abrasive lava soap after each test to remove oil from its surfaces.

4.4. Modified Triaxial Setup

In order to incorporate a 7th generation MIT tensiometer into the MIT triaxial setup, the following changes, which are also shown in *Figure 4.12*, are made to the setup in *Figure 4.9*:

- The center of a triaxial base was machined out to accommodate the geometry of the tensiometer. To-scale drawings of the modified triaxial base are given in *Appendix 4.4*.
- Instead of resting directly on the load frame, the triaxial base is supported by 4 columns on a platform, which is placed on the loading mechanism. This allows one to access to the tightening nut of the tensiometer, and adds room for the data cables.
- The top cap is connected to a distilled water reservoir through outlet B and the top valve.
- None of the remaining components among those related to pore water in the unmodified setup are needed in the modified setup. They are not physically removed, but the setup is isolated from them by closing the bottom and transducer valves. Hence they are not shown in *Figure 4.12*. These components are the pore pressure transducer, pore PVA, and pipes that lead to the pedestal in the unmodified setup.
- The data channel for the pore pressure transducer in the unmodified setup is connected to the tensiometer (which also measures pore pressure), instead.

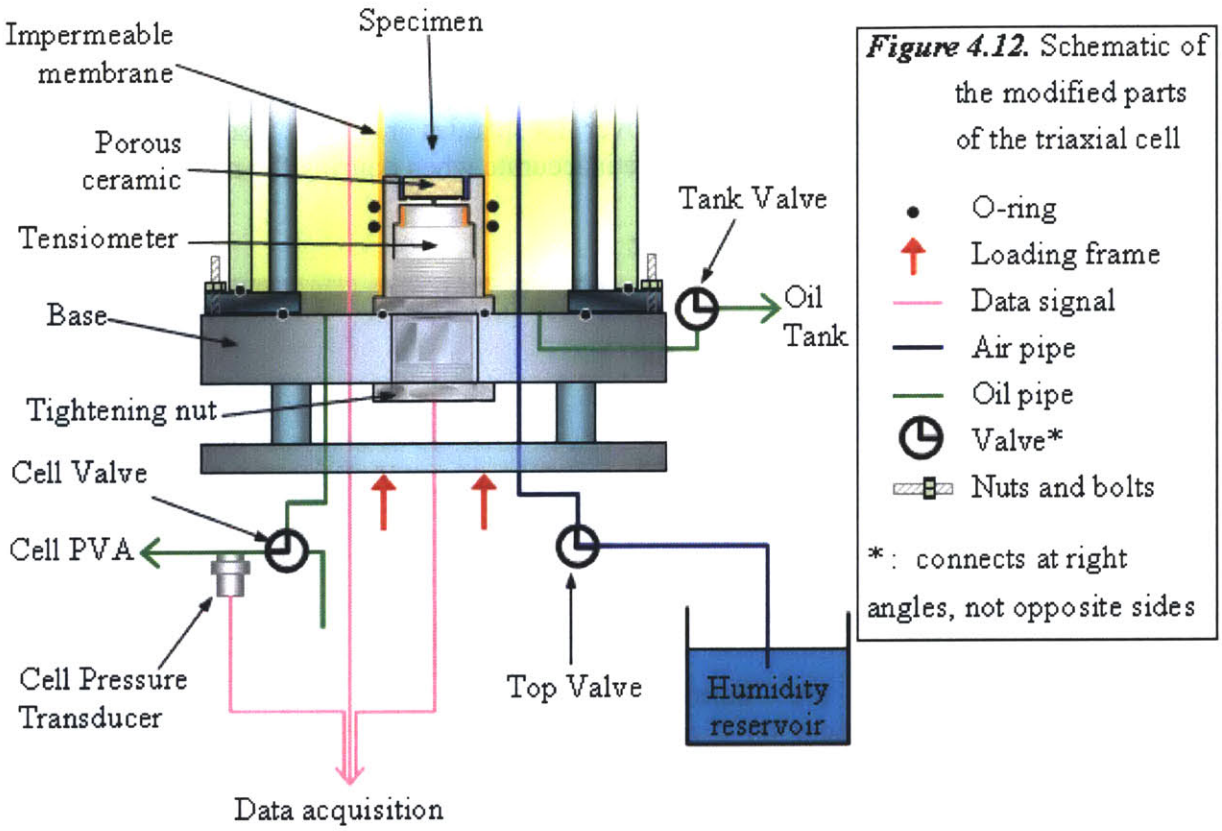

Figure 4.12. Schematic of the modified parts of the triaxial cell

4.5. Preparation Equipment

4.5.1. Specimen Mold

The aluminum mold consists of two half-cylinders held together by two clamps. The mold has an inner diameter equal to the diameter of a triaxial specimen (3.5 cm), except the bottom part which envelopes the pedestal or tensiometer, as well as the o-rings around them. The inner surface of the mold is covered with a paper towel to establish air flow from all around the specimen to two outlets (one at the middle of each half), to which a vacuum can be connected.

The normal procedure for triaxial testing of granular materials involves using a thick membrane. In order to minimize membrane corrections in this research, a single thin membrane (*section 4.3.5.2*) was used instead. To eliminate the risk of puncturing the membrane during setting up, the inner edges of the mold halves were rounded by the author. In order to ease usage, the center of the edges on one surface of one of the clamps are also rounded. The benefit of this modification will be discussed in *section 5.1.5*.

4.5.2. Scoop

For mixing and placing the samples, a stainless steel scoop with a U-shaped constant cross section (except a tapered end) was preferred over flat spatulas or spoons. The flat spatulas are unable to hold dry glass beads, and spoons are inaccurate when pouring the material.

4.5.3. Standard Pocket Penetrometer

A standard pocket penetrometer with its standard enlarged shoe is used for compacting specimens in the retaining ring on the tensiometer. The PPT that was used in this research is model CL-700 manufactured by Soiltest Inc. and has a capacity of 4.5 kg/cm^2.

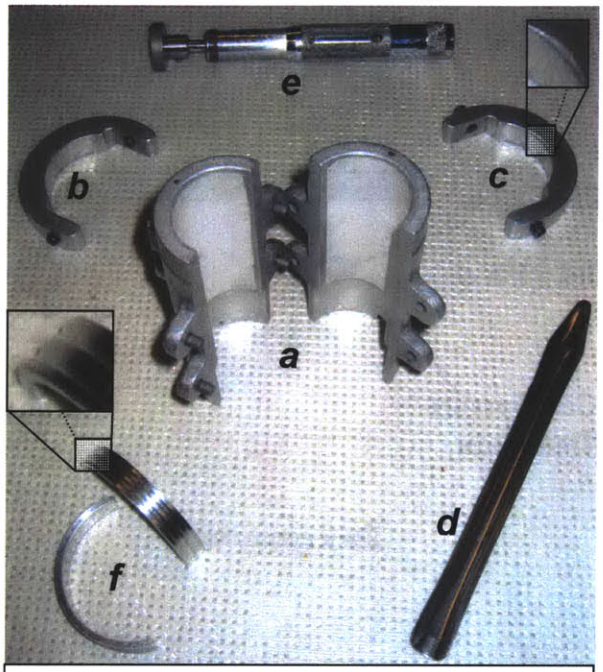

Figure 4.13. Preparation equipment.
a: specimen mold, **b**: upper mold clamp,
c: lower mold clamp, **d**: scoop,
e: standard pocket penetrometer,
f: new o-ring stretcher.

4.5.4. New O-Ring Stretcher

Triaxial-diameter o-rings are normally placed by first stretching them on a ring-shaped metal stretcher. Given the high stiffness of the o-rings, the common stretchers are as small as possible. The regular stretcher is 2.5 cm high and has a diameter of 5 cm, barely larger than the specimen diameter of 3.6 cm.

A particular stage of setting up for the experiments in this research (namely, step 13 in *section 5.1.5*) requires working on the inside of the stretcher. Working behind the regular metal stretcher is impossible because of its dimensions. A new 2-piece stainless steel stretcher was built to stretch thinner triaxial-diameter o-rings to larger diameters. The new stretcher is 6.5 cm in diameter, and 1cm high, allowing access between the stretcher and the top cap.

O-rings being excessively stretched are more likely to snap off the stretcher, especially if its height is less. To prevent this, two grooves of semi-circle cross-section circumvent the new stretcher (see left-inset in *Figure 4.13*). All edges of the stretcher and the grooves are rounded to prevent any damage to the o-rings.

4.5.5. Step-Cut Brush

During the setup procedure, excess particles are brushed off the upper rim of the specimen mold. Hairs of ordinary brushes may penetrate and disturb the specimen. In order to reduce this

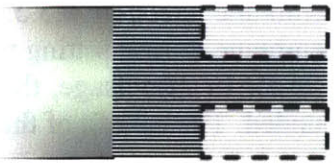

Figure 4.14. Schematic of the step-cut brush.

risk, and brush more efficiently, a flat brush was cut in the shape shown in *Figure 4.14* for this research.

4.5.6. Optical Vernier

This instrument is X-axis Z-axis Measuring A-I Microscope, manufactured by Titan Tool Supply Inc., Buffalo, NY. It has a focal distance adjustable between 9.5 and 10.5 cm. It can measure horizontal and vertical lengths with resolution of 0.001 inches (25.4 μm). The eyepiece is equipped with cross-hairs angled at multiples of 30° (see inset in *Figure 5.15*). See *section 5.3.1* for its usage.

4.6. Electronics

4.6.1. Transducers

4.6.1.1. Pressure Transducers

T62 and T71 employed a Data Instruments (Acton, MA) AB/HP 200 psi (14 kgf/cm^2) pressure transducer, which measures absolute pressures by the deflection of a steel diaphragm instrumented with strain gages. T72 utilized the 1000 psi (70 kgf/cm^2) version of the same model, and T70 used the 25 psi (1.8 kgf/cm^2) version. AB/HP (*Table 4.9*) is the standard transducer type widely used in a lot of applications at MIT Geotechnical Laboratories, so it is incorporated in the MIT tensiometers whenever applicable for the advantages of familiarity and reliability.

Table 4.9. Electrical characteristics of Data Instruments AB/HP pressure transducer

Linear Range	±1.8 kgf/cm^2 (25psi) ±14 kgf/cm^2 (200psi) ±70 kgf/cm^2 (1000psi)
Overload	2x w/o damage 5x w/o bursting
Excitation	5.5 V dc
Span (5Vdc at 25°C)	110±1mV
Accuracy	±0.25% of span

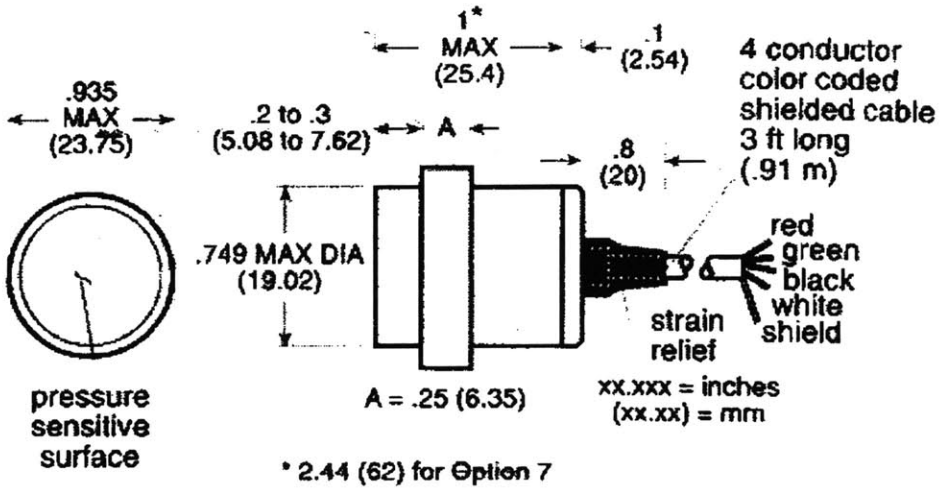

Figure 4.15. Dimensions of Data Instruments AB/HP pressure transducer.

4.6.1.2. Load Cells

The load cells used for axial load measurement are Data Instruments JP-100, and JP-500 (*Table 4.10*). This type of load cell is an S-shaped steel section instrumented with strain gages. JP-100 was used in the standard setup, whereas the modified setup used the JP-500.

Table 4.10. Electrical characteristics of the Data Instruments JP series load cell

Linear Range	0-45 kgf (JP-100) 0-227 kgf (JP-500)
Overload	1.5x w/o damage 3x w/o bursting
Excitation	5.5 Vdc or Vac
Span (5Vdc at 25°C)	165±1mV
Accuracy	±0.05% of span

During the tests, the load cell is submerged in silicon oil, which fills its gaps and cavities. After the test and dismantling of the setup, this oil continues to ooze out of the load cell for several hours, down to parts that are supposed to stay clean. Four holes are drilled at the lower edges of the casing of each load cell to quicken the flow of oil from inside the load cell out, once the triaxial cell is emptied. These holes were drilled with a 2-mm drill bit. Only the casing was drilled, without penetrating the steel core of the load cell.

4.6.1.3. Displacement Transducers

The axial displacement and pore volume change are measured by ***L***inear ***V***ariable ***D***ifferential ***T***ransformers (LVDT), manufactured by Trans-tek Inc, Ellington, CT (*Table 4.11*). These consist of a magnetic coil through which a core moves. The core, when displaced axially within the coil, produces an output voltage change directly proportional to the displacement. Both axial and volume LVDTs of the standard setup are model 0244, whereas the modified setup had a model 0243 for axial displacement measurement (the modified setup does not measure volume).

Table 4.11. Electrical characteristics of the Trans-Tek series 240 LVDT

Linear Range	± 0.9 cm (0243) ± 1.25 cm (0244)
Max. Usable Range	1.5x linear range
Excitation	5.5 Vdc or Vac
Span (5Vdc at 25°C)	±2 V
Accuracy	±0.5% of span

4.6.2. Calibration

Like most electronic sensors, those that were used in this research yield output voltages (V_{out}) which are measurements proportional to the input voltage (V_{in}). Therefore, for each device, the quantities measured are related to the normalized voltage output (ratio of output voltage to input voltage) by device-specific calibration factors (see *Eq.4.2*, where CF is the calibration factor). The calibration factors are determined by regression analysis against laboratory references, in which the MIT Geotech standard acceptance for linearity is $r^2 > 0.9999$. The laboratory maintains in-house standard references for force, pressure and displacement.

Appendices

Appendix 4.1. Metal parts of T 7.1 - 7.2. ***a)*** Upper body – Triaxial pedestal.

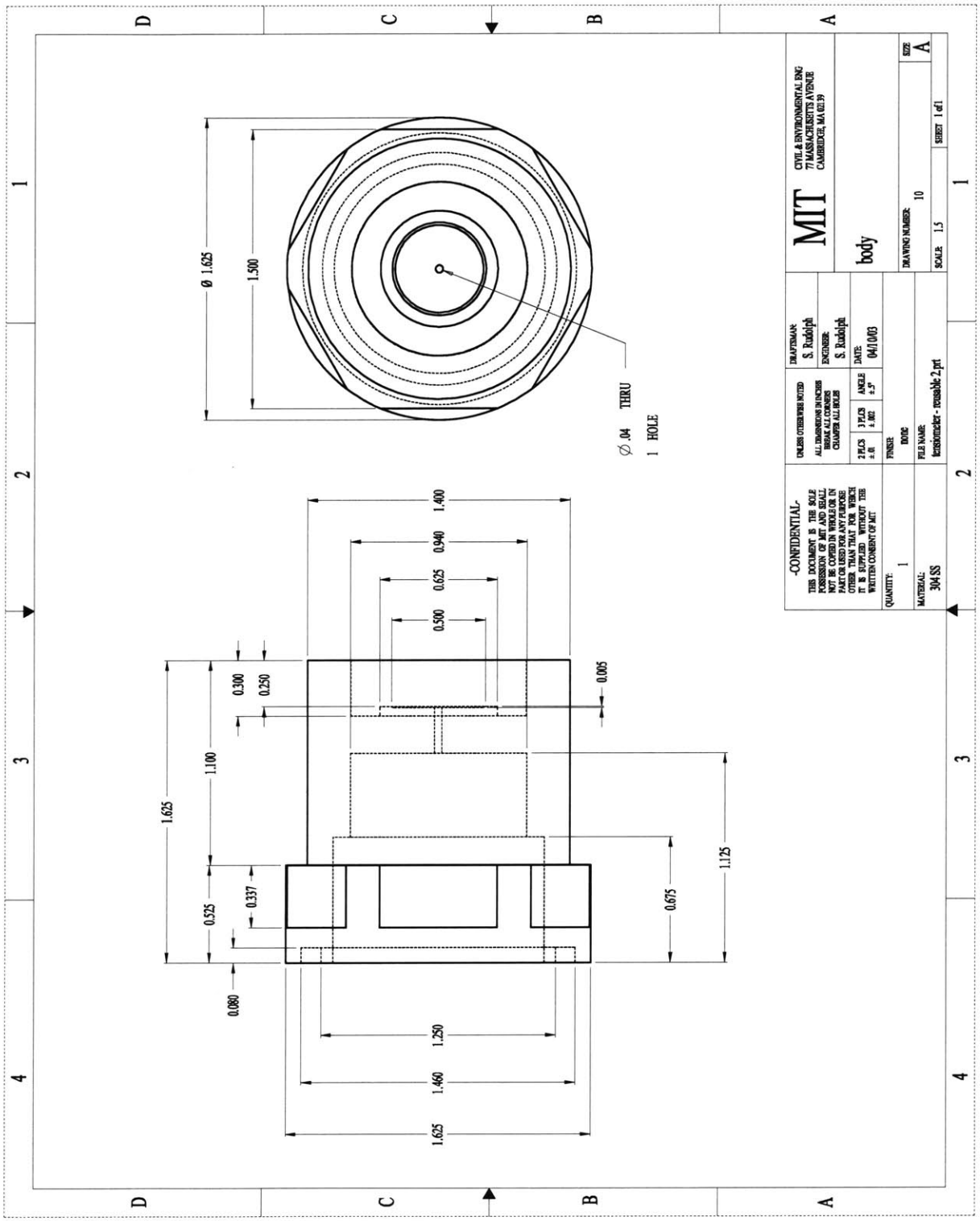

Appendix 4.1.b) Lower part: Tightening nut for pressure transducer – Piece to span through triaxial base.

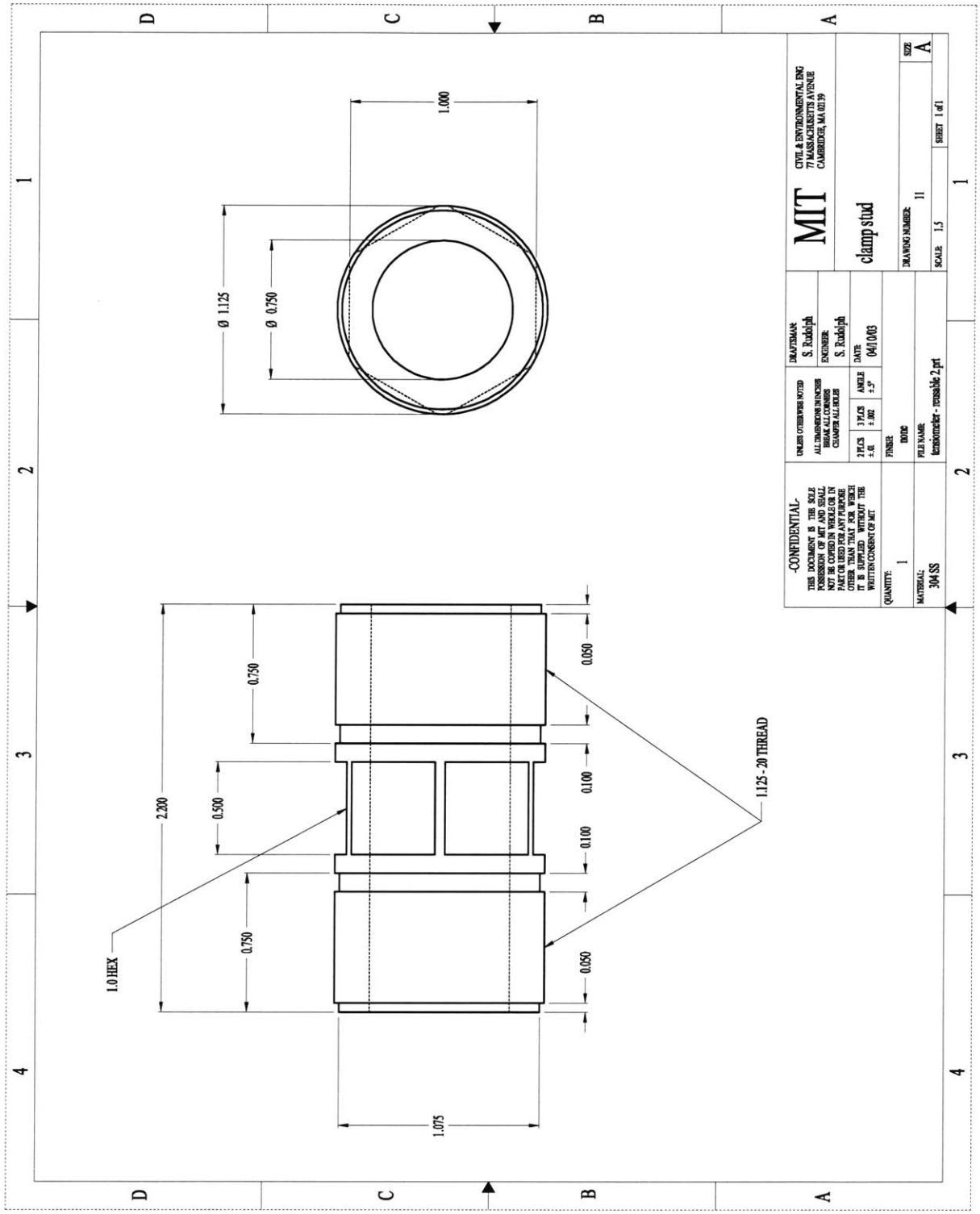

Appendix 4.1.c) Copper vacuum seal.

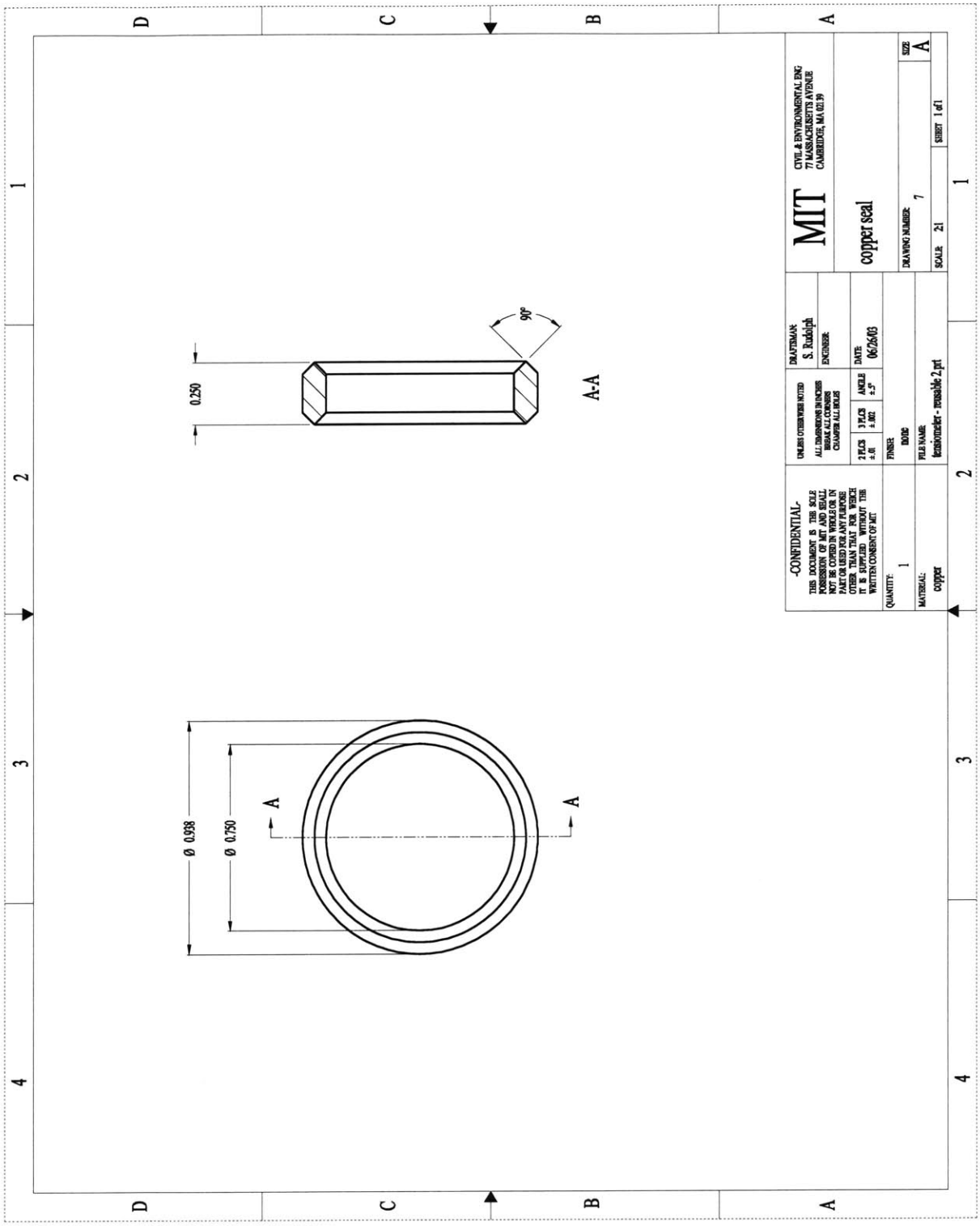

Appendix 4.1.d) Complete image.

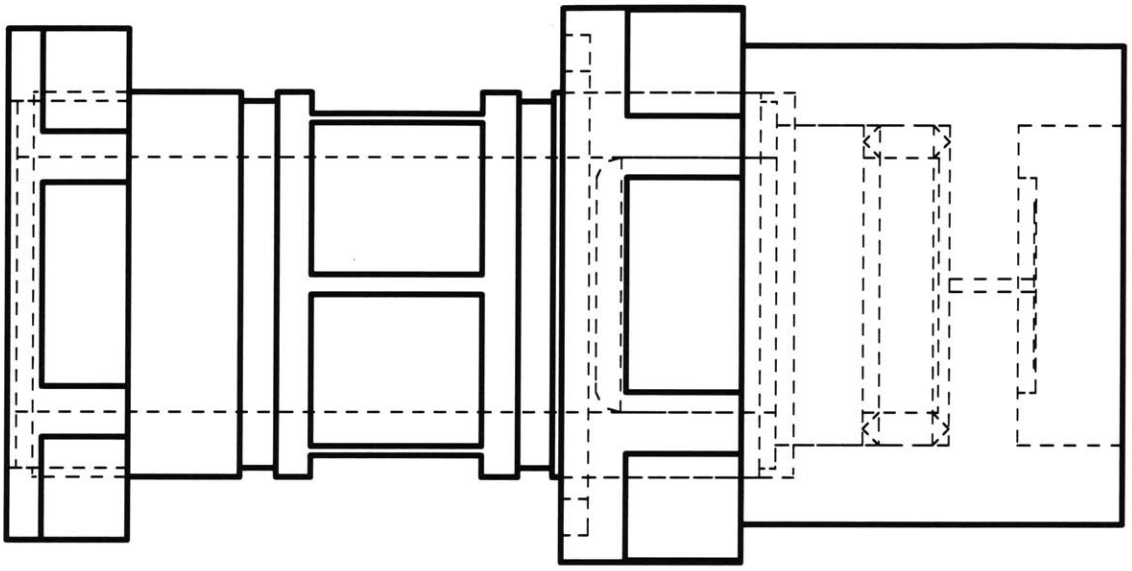

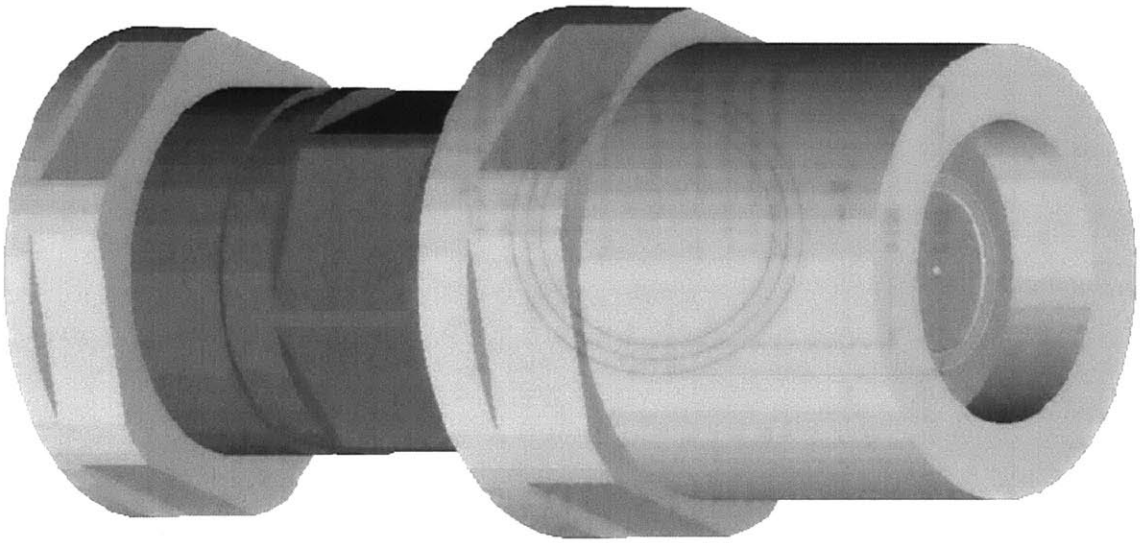

Appendix 4.2. Analog-analog feedback circuit of the saturation setup. (Sjoblom, 2000)

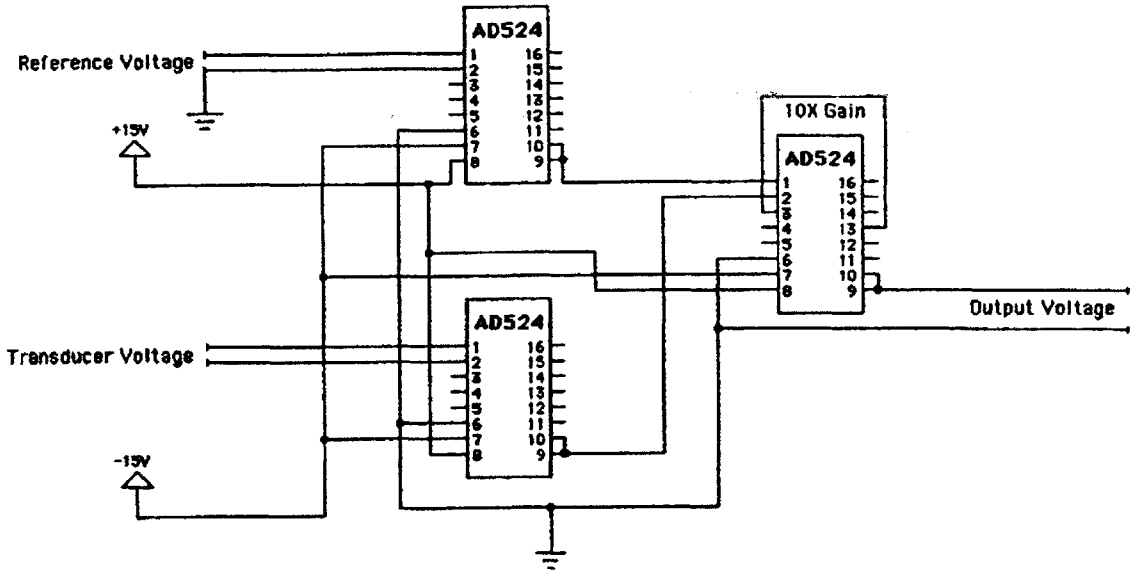

Appendix 4.3. Control circuit of the triaxial setup.

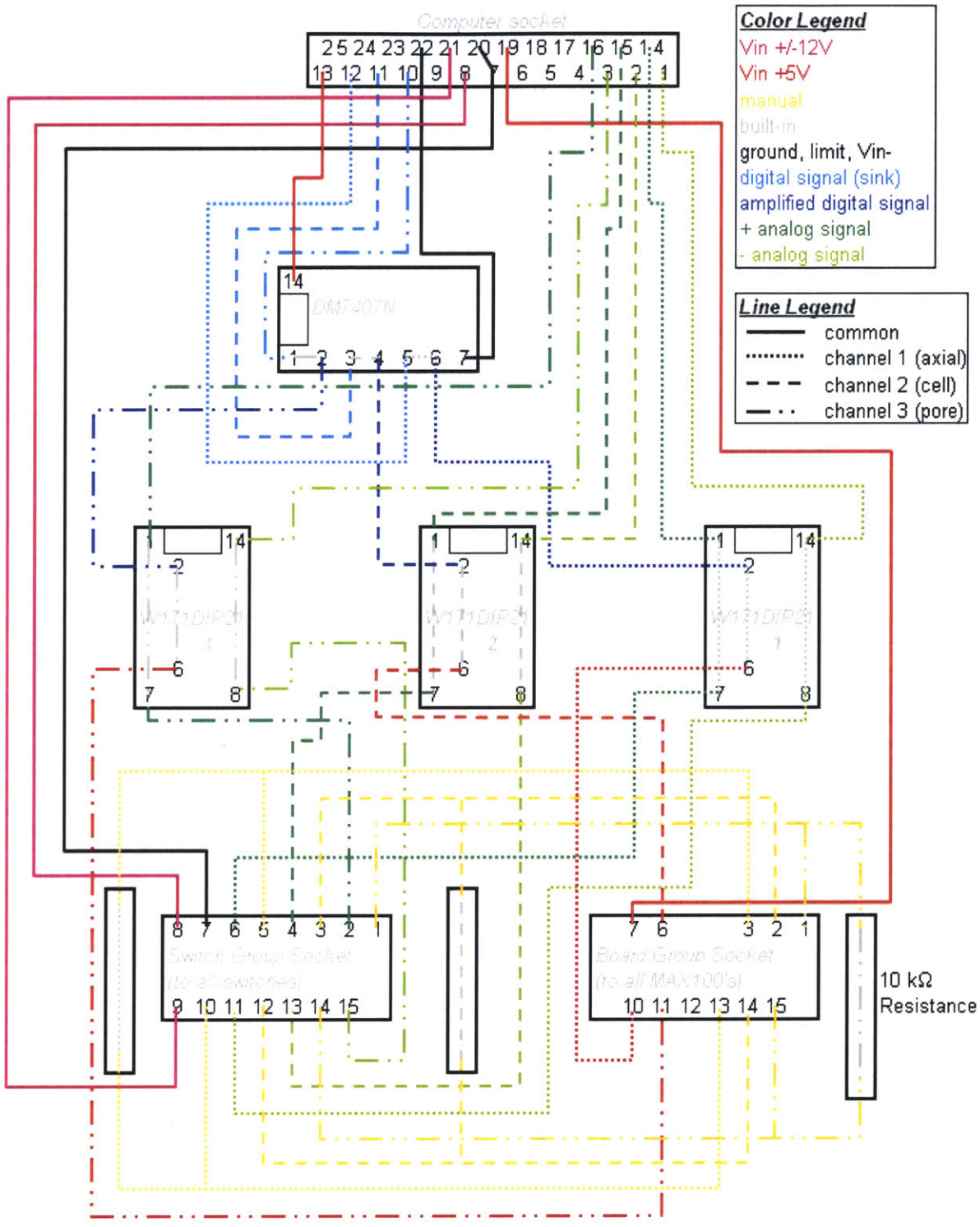

Appendix 4.4. Modified triaxial base.

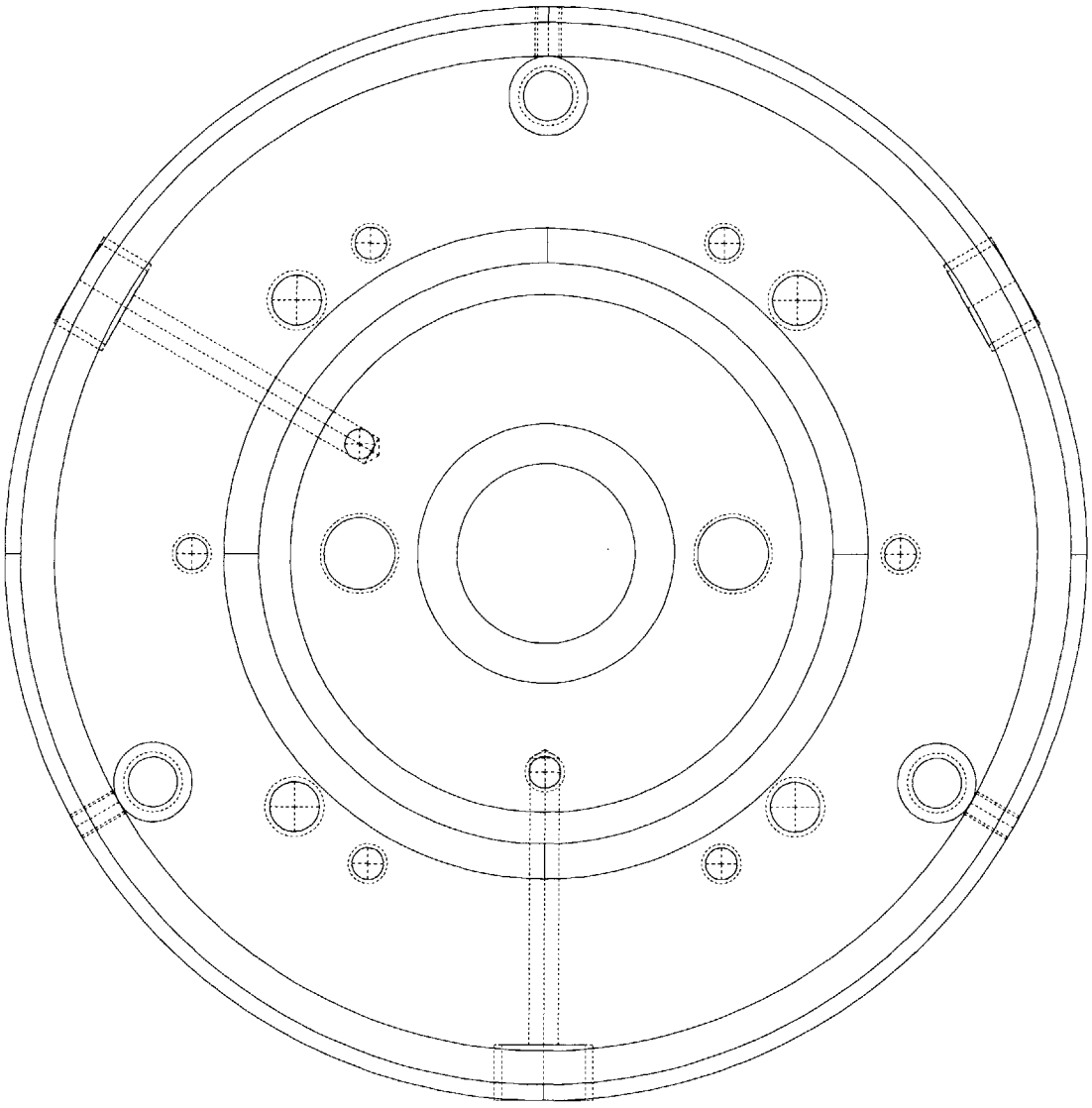

Appendix 4.4. continued.

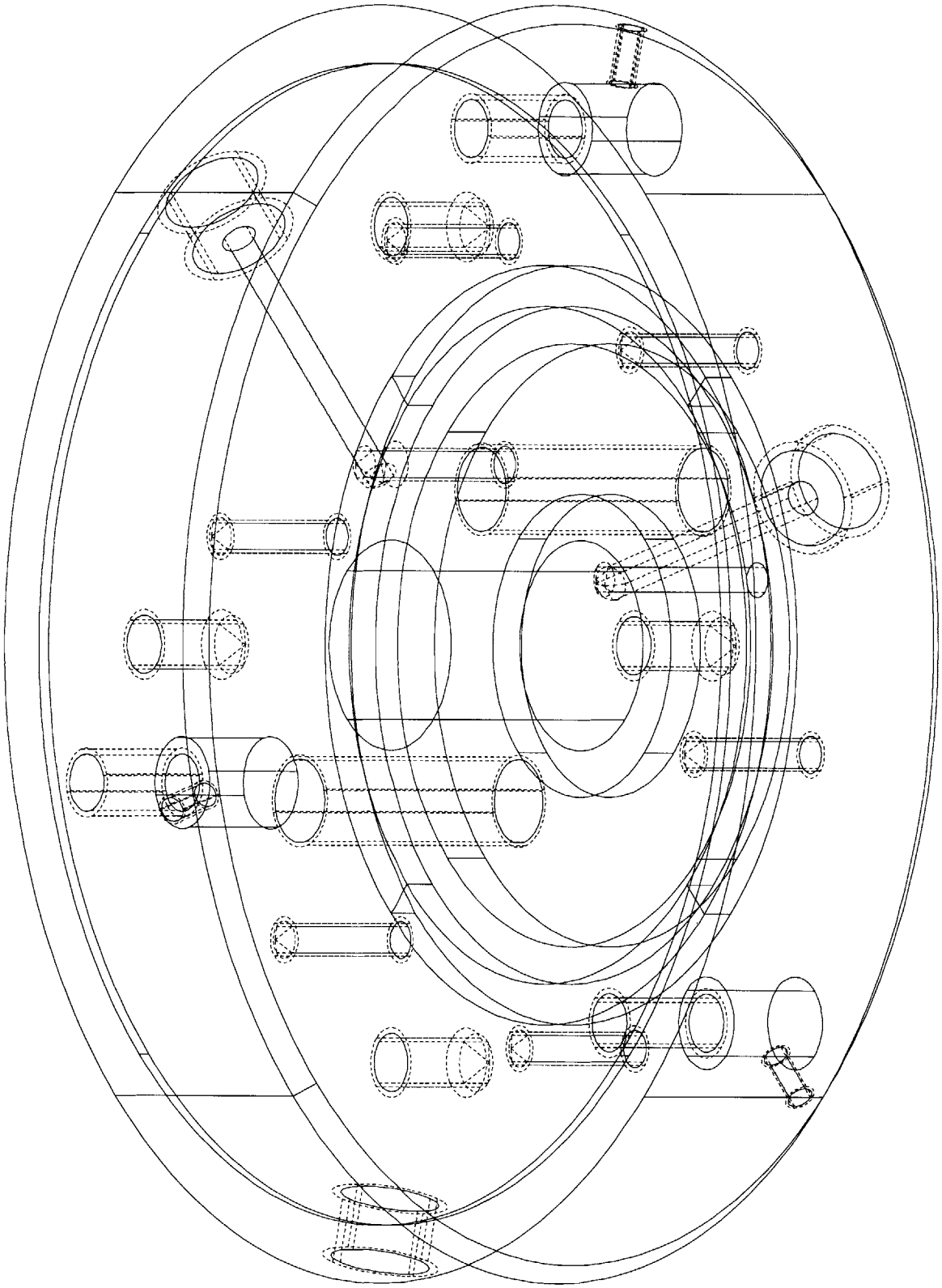

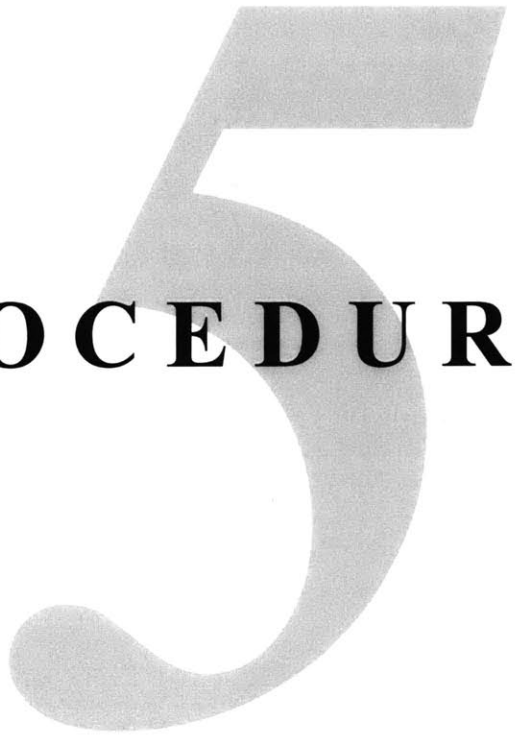

PROCEDURES

5. PROCEDURES

This chapter describes experimental procedures in an instructional manner, as opposed to simply reporting what has been done. These procedures were exactly followed for almost all of this research, so they indirectly report what has been done as well.

The triaxial tests are categorized into four types as: *saturated* tests; *sealed*, *unsealed* and *tensiometer* tests. The latter three are *unsaturated* tests. Only *tensiometer* tests are run in the *modified* setup, the remaining three use the *standard* setup. The important differences among the procedures of the test types are summarized in *section 5.2.5*. All of these labels are used within this, and oncoming, chapters.

Table 5.1. Classification of test types in this research.

Test type	***Saturation***	***Setup***
saturated		standard
sealed	unsaturated	
unsealed		
tensiometer		modified

5.1. Preparations

5.1.1. Tensiometer Saturation

This procedure is followed only for the triaxial tests on unsaturated materials using the modified base (*section 4.4*).

The saturation setup was previously illustrated in a simplified manner as *Figure 4.3*. However, the pipes and valves are not necessarily permanent connections. Therefore, the procedure will be detailed by explaining which component of the saturation setup is connected to which other component, rather than detailing which valve points which way (i.e. this section gives a functional description of the saturation process).

The necessary saturation procedure before a test is described in *sections 5.1.1.2* and *5.1.1.3*. *Section 5.1.1.1* below focuses on the operation and maintenance of the individual components of the saturation setup.

5.1.1.1. Operation of Individual Components

The components have specific operating tips and rules that should be followed precisely every time the particular piece of equipment is put in use. An overarching rule that is valid for all components of the saturation setup is to remember taking the water (or air) that is in the pipes into account. For example, if a container is to be deaired, the pipes that are going to be connected to it should be deaired, as well.

5.1.1.1.1. Centrifugal Vacuum Pump

- The pump's turbine is the disc-like portion on its side. The water intake pipe goes into the center of the turbine, and the outlet pipe is connected tangentially. The vacuum is applied to the saturation setup through a pipe on the side of the outlet pipe.
- Water in the circulation tank, from which the pump intakes and into which it gives out water, should always be recycling. That is, it should always have inflow and spillage of water, in order to keep the water cool (As noted in *section 4.2.2*, this pump reduces the pressure to the vapor pressure of water, which is lower for cooler temperatures).
- The outlet pipe of the pump into the water tank should have a small gap, through which air bubbles can join the flow. The air bubbles must be distinctly observable in the tank, as they float up to the water surface without being absorbed into the pump's intake. This is achieved by placing an insulated (to minimize rusting) electrical wire at a connection of this pipe. To prevent the pump from intaking bubbles, the ends of these two pipes should point at different directions in the tank.
- Before **operation**, all valves on the line to be vacuumed should be closed. After starting the pump, the valves may be opened starting from the one closest to the pump, and proceeding along the line.
- If the pump fails to start (making bubbles in the tank), the pump's water intake pipe might have too much air in it. Bring the pipe through which water fills the tank against the intake pipe to push water into it.
- Rarely, the pump starts but fails to apply the expected vacuum, when some water is trapped within the outlet. Pull the pipe through which vacuum is applied to the saturation setup out of the pump. For the saturation setup-side of this separation, point the pipe downward to empty any water within. For the pump-side, close it with a finger. Feel the vacuum build up and then suddenly pull your finger away to let a gush of air into the pipe. Repeat this cycle many (possibly 50-100) times in a few minutes, until you feel a significant increase in the pull of the vacuum on your finger. Reinsert the pipe to connect the pump to the rest of the setup.
- Before **turning** the pump **off** valves should be closed starting from the farthest and proceeding towards the pump. The pump may be turned off when the valve closest to the pump is closed.

5.1.1.1.2. Oil Vacuum Pump

- The oil should be at the operating level in the observation window. If it is low, oil can be added from a cap on the top. If it is too high, which can occur when water is mistakenly drawn into the pump, it can be drained from the tap at the bottom.
- Before **turning off**, its hose should be disconnected and the pump should be allowed to draw in air. Otherwise, oil vapor will backflow into the system.

5.1.1.1.3. Deaerator

- Take notice of the upper limit for water level, marked on the tank.
- If the deaerator is empty, it can be refilled by connecting its water pipe to a distilled water source, and vacuuming through the air pipe.

- To **deair** the water inside, apply a vacuum through the air pipe and turn the rotating disc on. This vacuum must be below 0.1 atm in absolute pressure for proper deairing. Water will be deaired in about 30-60 minutes.
- When the water in the deaerator is deaired, the continuous rattling noise of cavitation becomes clearly audible. Stop the rotating disc of the dearator.
- The air pipe should be opened to atmosphere before connecting the water pipe to atmosphere or any other water body. It should not be opened completely at once, so that a jet of air will not mix itself into the deaired water.

5.1.1.1.4. Analog-Analog Feedback Control

On the outside, the feedback control box has two switches, one knob, and three sockets (*Figure 5.1* – the socket that sends the control signal to the Pressure Volume Actuator is on the back, so it is not visible in the picture).

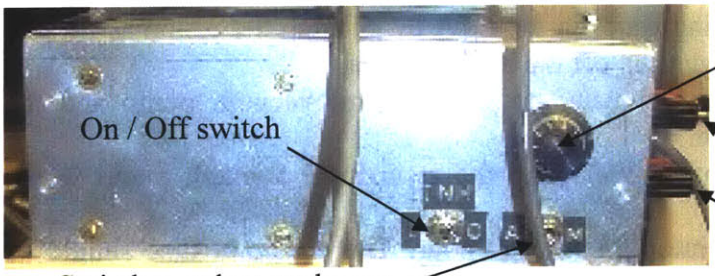

Figure 5.1. Analog-analog feedback controller

When the left switch points left, it turns the analog-analog controller on, allowing the usage of the rest of the box. When it is at the middle, it prevents the controller from moving the PVA. When it is switched toward the right, it cuts the circuit, but the controller may drift due to the possible magnetic effects of other electronic devices on the control box.

The right switch selects the method of PVA control between analog (leftward) and manual (rightward). When it is set to manual, the user adjusts the speed and direction of the piston of the PVA by using the knob. When it points to analog, it adjusts the pressure to converge to the target voltage (*section 5.1.1.1.6*) that was previously set on the voltage supply.

The four-pin socket on the back connects to the servomotor of the PVA. Of the two banana plugs on the right side of the box, the one on the top connects to the witness transducer and the one on the bottom connects to the target voltage set by the wired outlet of the voltage supply.

5.1.1.1.5. Pressure-Volume Actuator

The device has safety switches at the top and bottom extremes of the stroke of the piston. If the piston touches either of these switches, then the servomotor shuts down in order to prevent equipment damage. To turn the system back on, the motor should be turned from the

little flag (the topmost point of the PVA, see *Figure 4.5*) by hand, so that the piston is pulled away from the safety switch.

After every pressurization, the piston ends up being further inside the cylinder (i.e. the PVA has less water). If the piston is too close to being completely inside the cylinder (i.e. too close to the bottom safety switch), it means there is very little water left in the chamber, so the PVA needs filling.

1. To fill the piston, connect it to the deaerator.
2. Deair (*Section 5.1.1.1.3*) the water.
3. Connect the deaerator to the atmosphere.
4. Connect the deaerator to the PVA.
5. Withdraw the piston using the manual setting (*Section 5.1.1.1.4*).

Normally, the piston moves, at most, a couple of centimeters during pressurization. If it moves more, it means that there is air in the piston. In this case, the PVA must be evacuated and refilled.

1. Before refilling, empty the remaining water in the PVA by pushing the piston as far into the cylinder as possible without triggering off the safety switch,
2. For refilling, the PVA should be connected to both the oil vacuum pump and the deaerator through a three-way valve.
3. Connect the oil vacuum pump to the PVA and the centrifugal vacuum pump to the deaerator.
4. Evacuate both the PVA and deaerator for half an hour. The deaerator disc should be operating throughout this time.
5. Turn off the dearator disc and open the deaerator to the atmosphere. The centrifugal vacuum pump may be shut down.
6. Connect the PVA to the deaerator without turning off the oil pump. The oil vacuum pump may be disconnected and shut down.
7. Withdraw the piston.

The operator should keep in mind that with the huge combined mechanical advantage of the ball screw actuator and the servomotor, the PVAs are able to generate tremendous magnitudes of pressure, and are capable of destroying any equipment connected to them if used improperly.

5.1.1.1.6. Target Voltage

The saturation of the tensiometer approaches 100% with increasing saturation pressure, so the tensiometer should be saturated at the highest pressure possible. The saturation pressure should also be greater than the air entry pressure of the porous interface of the tensiometer. However, it may not exceed the yield pressure of the pressure transducer within the tensiometer (which is two times the linear range for the Data Instruments transducers), or the linear range of the witness transducer on the PVA (the current transducer is 1000 psi = 70 kgf/cm^2). Thus the saturation pressure should be as high as possible, and also less than these two limits with some safety margin. To impose the selected pressure, follow the procedure below:

1. Connect the PVA to the atmosphere to obtain zero (gage pressure) of the witness transducer.
2. Convert the saturation pressure into a target voltage, using the calibration factor and zero of the witness transducer (see *equation 4.2* in *section 4.7.2*).
3. Multiply by 100 to account for the voltage divider on the power supply (*section 4.2.5*).
4. Adjust the proper channel of the power supply to set it to 100 times target voltage. For low-capacity tensiometers (or any other case that requires precision), connect a voltmeter and read from it at much greater resolution than the dial gage of the power supply.

This adjustment is not necessary if the tensiometer is the same as the one that was last saturated. So, along the course of a series of tests with a single tensiometer, the target voltage needs to be set only once before the first test, provided that the saturation setup is not used for any other task throughout this period.

5.1.1.1.7. Tensiometer Placement

MIT tensiometers of version 7 and later can be fixed to a triaxial base (which is also the base of the saturation chamber) by tightening the nut from under the base (*Figure 4.2*). The triaxial base has four legs for support and two male 9-pin electrical sockets for internal transducers, making it impossible to use a wrench or similar tool to tighten the nut. In order to tighten it by hand sufficiently, pressure must be applied to the top of the tensiometer with the other hand at the same time. This compresses the o-ring under the tensiometer and locks stress that is otherwise unachievable by finger-tightening the nut.

5.1.1.2. Preliminary Checks and Adjustments

- Dry the surface of the porous ceramic of the tensiometer.
- Check if the water in the tank of the centrifugal pump is recycling.
- Check if the deaerator has enough water to fill the pressure chamber.
- Check if there is sufficient volume of water in the PVA for pressure saturation. There should be at least one inch of stroke available into the cylinder.
- Check if the oil of the oil pump is at operating level.
- Check if all o-rings are clean, in place and not notched, as well as the cleanliness of the places the o-rings fit into.
- Check the magnitudes of voltages (input voltage of 5.5 V and target voltage) from the power supply.
- Check if all pipes are connected as necessary. If they are connected after evacuating the chambers, air may enter the pipes. To check this, the operator needs to go through the saturation procedure up to the pressurization beforehand, and must connect the pipes as appropriate. The steps of the procedures below telling the operator to "connect" two components of the setup mean that the pipes are already connected, but the valves on them that are closed shall be opened.

5.1.1.3. Saturation in the Triaxial Saturation Chamber

The PVA, deaerator and the oil vacuum pump start connected to the saturation chamber, with all valves closed. The PVA starts at atmospheric pressure and its control box turned off.

1. Fix the tensiometer into the base of the saturation chamber as described in *section 5.1.1.1.7*. The data acquisition cable passes through the hole in the base (If monitoring is desired during saturation, it can be done through this connection).
2. Place the upper half of the saturation chamber on top and tighten its bolts.
3. Connect the chamber to the oil vacuum pump (*section 5.1.1.1.2*) and start evacuation.
4. Start deairing the water in the deaerator (*section 5.1.1.1.3*). These two processes will take about the same amount of time (at least half an hour) with both vacuum pumps operational.
5. Stop the deaerator, disconnect it from the centrifugal vacuum pump and open it to the atmosphere. Turn off the disconnected centrifugal vacuum pump (*section 5.1.1.1.1*).
6. Disconnect the chamber from the vacuum and connect it to the deaerator. Turn off the disconnected oil vacuum pipe.
7. The chamber will be full of water from the deaerator in less than a minute. After two minutes, check if it is filled successfully by opening the top (ventilation) outlet of the chamber very slowly. If it makes a hissing sound by air flowing either in or out, the chamber did not fill properly, so proceed with steps 15, 16, dry the inside of the chamber and the tensiometer with paper towel, then repeat steps 2 through 7. If water comes out of the outlet immediately, the chamber was filled properly, procees to step 8.
8. Disconnect the chamber from the deaerator and connect it to the PVA.
9. Turn the PVA control on and to analog. The piston should rapidly compress, bringing the pressure asymptotically to the saturation pressure.
10. Wait for 24 hours.
11. Perform other preparatory tasks (material preparation, cell preparation).
12. Turn the PVA control to manual and set the rate to decrease at about 0.1 atm/sec.
13. Monitor the witness transducer reading. Turn the PVA off when the pressure inside is close to atmospheric.
14. Open the valve of the topmost outlet to the atmosphere (i.e. not the one that connects with the PVA).
15. Place a container under the lowest outlet and drain the chamber through there.
16. Unscrew the bolts and take off the upper half of the chamber.
17. Take the tensiometer out of the chamber. While it is not in use for short periods (carrying, installing into the triaxial setup), the top face of the tensiometer should always be fully covered with water. Putting a plastic sleeve around the tensiometer to act like a container to store additional water on the surface is also helpful for unattended waiting times longer than a few hours.

5.1.2. Sample Preparation

There are two types of glass spheres (detailed in *section 6.1*). Type 1 spheres were obtained by sieveing mixed-size glass spheres. A Type 1 sample consists of the portion passing #120 (125μm) and retained on #140 (106μm) sieves after one cycle of sieveing. Coarser sieves

were stacked above those two sieves, to better distribute the material over the sieves of interest, and to prevent overloading of these finer sieves by limiting the rate particles pass through the sieve system.

The procedure was modified to process the Type 2 spheres. The same sizes of sieves were used, but the fraction retained on the #140 sieve was repeatedly sieved, until only negligible amounts of material passed through it. This usually involved 7 to 10 cycles, and resulted in 30 grams of sample material. As one cycle took close to 10 minutes, and one test requires 120 grams of Type 2 material, several hours of sieveing was necessary for one test. This led to the development of the retrieval procedure described in *section 5.3.3*.

5.1.3. Cell Preparation

5.1.3.1. Maintenance

5.1.3.1.1. Cleaning

The primary problem against cleanliness is the cell fluid (oil). An efficient way to clean oil is with toilet paper. Both before and during the setup procedure, any oily surface (including the operator's hands) must be wiped with toilet paper, repeatedly if necessary. In unsaturated tests, any contamination can affect the results by changing interfacial characteristics.

Sample materials themselves create major cleaning problems. It is difficult to clean wet glass beads, and extremely difficult to clean oily glass beads off any surface. As glass has the same hardness as steel, glass beads can cause damage if they get into metal moving parts. Therefore, it is essential to keep the workspace clean of the glass beads. If possible, designate on the laboratory bench a "clean area", where operators shall put only clean things, and an "unclean area" where items that have glass on the surface are placed (for example after the test). The latter may also be divided into "oily" and "non-oily" sections.

If sample materials get into the pipes, connections, or transducer sockets, the setup will have to be cleaned. The procedure is itemized below:

- A pressurized water jet is used for cleaning. For this purpose, a hose that narrows down to an opening of less than a millimeter diameter is fitted to a tap in the laboratory.
- All pipes (including the standpipe for top cap connection) and valves in the lower half of the setup are flushed with turbulent water. Valves are flushed a separate time for each dirrection they can point. All o-ring grooves are also cleaned with the water jet.
- The excess water is dried with a paper towel.
- A pressurized air jet is used to blow away the remaining water, which must be completely removed from all oil pipes. If an oil compressor is used then the air jet must be applied to the water pipes and pedestal surface for a minimum possible duration, because there are airborne oil molecules in the jet. Do not use the air jet on the tensiometer.

Another threat to cleanliness is pieces of wire. In time, silicon oil disintegrates the plastic insulation of the electrical wires. Small pieces of exposed ground wire may break off and fall on the base. These can disrupt a test if they fall on the load cell connector or an o-ring. The connector of the load cell inside the triaxial cell must be clean, especially of any wire pieces.

5.1.3.1.2. O-ring Maintenance

Before each test, all o-rings and surfaces contacting them must be clean of grain, wire, hair, or any other tiny object. An o-ring and its contact surfaces can be cleaned by wiping with a clean finger, cloth or paper towel (not cotton or cleenex). Afterwards, grease is applied with a finger. Note the following:

- O-rings in grooves don't usually get dirty inside the groove, so cleaning the open surface is sufficient, unless the setup is being cleaned with pressurized jets.
- O-rings lose ductility over time when repeatedly exposed to silicon oil. This can be prevented by an occasional check involving twisting and bending them while examining closely for cracks.

5.1.3.1.3. Tensiometer Maintenance

Pure water in the tensiometer must not be contaminated by any fluid or solute, as these will change the interfacial tension and introduce unknown inaccuracies to the device, permanently. The only viable way to wash the tensiometer's surface is by holding it under flowing distilled water. If contamination occurs, the tensiometer has to be cleaned piece by piece after separating it into all of its components (steel body, pressure transducer, copper seal, porous interface), among which the copper seal and porous interface can not be reused.

5.1.3.2. Setting up for Specimen Constitution

1. Check if all pieces of equipment are ready. These are:
   - All pieces of the triaxial cell setup (*section 4.3.1*). The load cell and top cap start attached to the steel structure and the piston. The whole assembly will be called the "*superstructure*" for the rest of the procedure description. The water line that goes from the base to the top cap is a separate piece of metal standpipe. The base starts without the pressure transducers, not connected to either PVA, with all valves closed to all flow, and on a workspace accessible to the operator from different angles (table or laboratory bench).
   - The load frame with sufficient stroke (see *section 5.2.1.5*),
   - Preparation equipment (*section 4.5*), calipers, sharp and thin scissors, toilet paper,
   - Carbon dioxide tank with flow regulator (for saturated tests only),
   - Oil vacuum pump with regulator and associated tubing (including a double-outlet T-pipe to connect to the mold). See instructions in *section 5.1.1.1.2* for operation of the pump,
   - 2 thick, 3 thin o-rings and o-ring grease,
   - 2 porous stones and nylon filters (only one of each for modified setup),
   - 3 rubber sleeves, one cut to fit the pedestal, one for the top cap, and one 1-1.5 cm long for the mold,
   - An impermeable membrane, whose tip has been cut off,

- Piston clamp,
- Various necessary sizes of wrenches and hexagonal keys,
- One 250 ml glass beaker, two 250 ml flasks,
- A syringe (for modified setup).

2. Warm the transducers up:
   - Plug all transducers and input voltage of 5.5 V to their sockets (to which they will be connected to during the test). This will require a female-to-female 9-pin extension cable for the load cell, which is a part of the superstructure.
   - For the modified setup, install the saturated tensiometer into the triaxial base and plug it in as well. The surface of the tensiometer must have water on it at all times.

3. Prepare the top cap (this can be done anytime between stages 1 and 7 of this procedure, but it was generally done at this point):
   - In sealed tests, a piece of foil wrap was used to cover the hole on the top cap.
   - Figure out the best orientation of the superstructure to be placed on the base. Find the orientation considering the location of the hole that the water pipe from the top cap will connect, and the orientation of the spiral tubing of the top cap. Rotate the piston relative to the superstructure if necessary.
   - Move the piston to the highest position and clamp it.
   - Put the shorter rubber sleeve around the top cap with very little grease, such that its lower end is 3 mm (i.e. the thickness of the porous stone) lower than the rim of the top cap.
   - Fold the lowermost portion of the sleeve up onto itself (*Figure 5.2.a*).

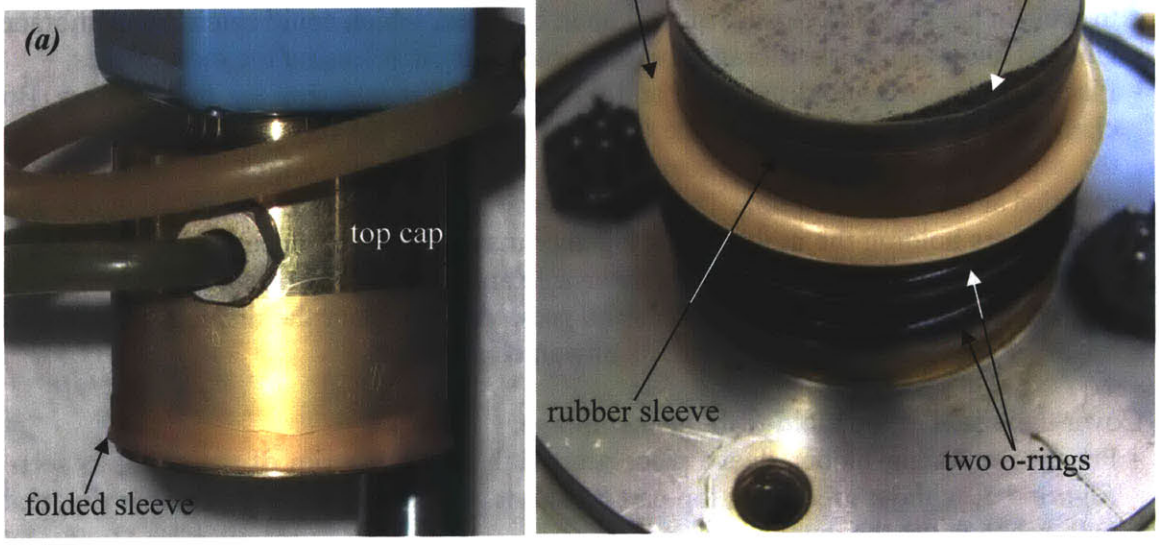

Figure 5.2. Prepared ***(a)*** top cap and ***(b)*** pedestal.

4. Prepare the pedestal:
   - In sealed tests, a piece of foil wrap was used to cover the holes on the pedestal.
   - Put the longer rubber sleeve around the pedestal (or tensiometer for modified setup) with very little grease, such that its upper end is 3 mm (i.e. the thickness of the porous stone) higher than the rim of the pedestal. For the modified setup the sleeve needs to be only a fraction of a millimeter above the tensiometer's upper rim.
   - For standard setup only, place a porous stone on the pedestal, into the sleeve.
   - For standard setup only, place a nylon filter on the stone. If it curls, apply a droplet of water between the filter and the porous stone.
   - Hold the impermeable membrane from the inside with two index and two middle fingers pointing down, hands facing out, cut-end to the bottom, rolling end to the top and outside. Stretch and put it around the rubber sleeve on the pedestal (or tensiometer).
   - Straighten all wrinkles on the membrane by pulling or pushing the cut-end downwards (collecting the wrinkles at the very bottom is acceptable, the aim is having most of the height of the pedestal or tensiometer wrinkle-free).
   - Put the two thick o-rings on a regular stretcher (described in *section 4.5.4*) after greasing them. Drop both of them on the membrane. Final state is *Figure 5.2.b*.

5. Mount the mold:
   - Roll the membrane up about 5 cm off the top rim of the pedestal assembly. For the standard setup hold the porous stone and filter down.
   - Place the two halves of the mold, bottom first, touching the base on both sides of the pedestal (or tensiometer). The gaps on the bottom of the mold halves must be aligned to the 9-pin connectors on the base. One of the mold halves has pieces that fit into the other half's holes. The half with holes must be on the side where the top cap water pipe connects to the base.
   - Hold the membrane up and twist it axially. There should be just enough tension on the membrane to keep it as a vertical cone (as held in *Figure 5.3* for illustrative purposes), because pulling it too much will displace the o-rings and the sleeve around the pedestal (or tensiometer).
   - Slowly close the halves of the mold with care so as not to squeeze any part of the membrane in between. Once closed, keep the two halves pressed together with one hand to prevent opening and closing of the gap in between, which could catch the membrane.
   - Untwist and stash the membrane into the mold, without releasing the mold halves.
   - Place the clamps around the mold and tighten, without releasing the mold halves. Both clamps must be placed on the side opposite to the hole on the base, which connects to the top cap water pipe. The bottom clamp is the one with edges of one of its faces rounded at the middle section. The rounded face faces downward.
   - The fingers holding the mold halves together may be released once one of the clamps is tightened. From this point on, whenever a lateral or upwards force, or torsion will be applied to the mold assembly, it must be pressed down from the diametrically opposite ends of the upper clamp, to prevent its unwanted motion.

6. Cover the inside of the mold with the membrane:
   - Put the remaining rubber sleeve piece around the top outer rim of the mold, as seen in *Figure 5.3*, without grease. Its top part must not go inwards beyond the inner rim, and it only has to cover the outer rim.

- Grease and place a thin o-ring around the mold, on the rubber sleeve, 6-9 mm below the top of the mold. If the regular stretcher is large enough, it can be used. Otherwise, use the new stretcher described in *section 4.5.4*. The end of this step is illustrated in *Figure 5.3*.
- Apply some grease on the inner rim of the mold.
- Cover the inner walls of the mold, as well as the outer o-ring and the parts above the o-ring with the membrane, by stretching it slightly and placing the rolled portion lower than the o-ring, as in *Figure 5.4*. If there are any axial wrinkles or twist, the entire membrane can be moved by holding it from the rolled part. Propagate the movement to the rest of the membrane by pushing with fingers. The purpose of the o-ring is to prevent the membrane from coming off the mold.
- Connect the double outlet pipe to both sides of the mold (as seen in *Figure 5.4*), finger tight, while pressing on the mold (as mentioned at the end of 5th stage of this procedure).
- Connect this pipe to the vacuum regulator. Apply a very slight vacuum (reducing the pressure between the mold and the membrane by a few kPa should suffice). If this does not result in a smooth membrane, vent the pipe to the atmosphere, and move the membrane as described in the step above. The end of this step is shown in *Figure 5.4*.

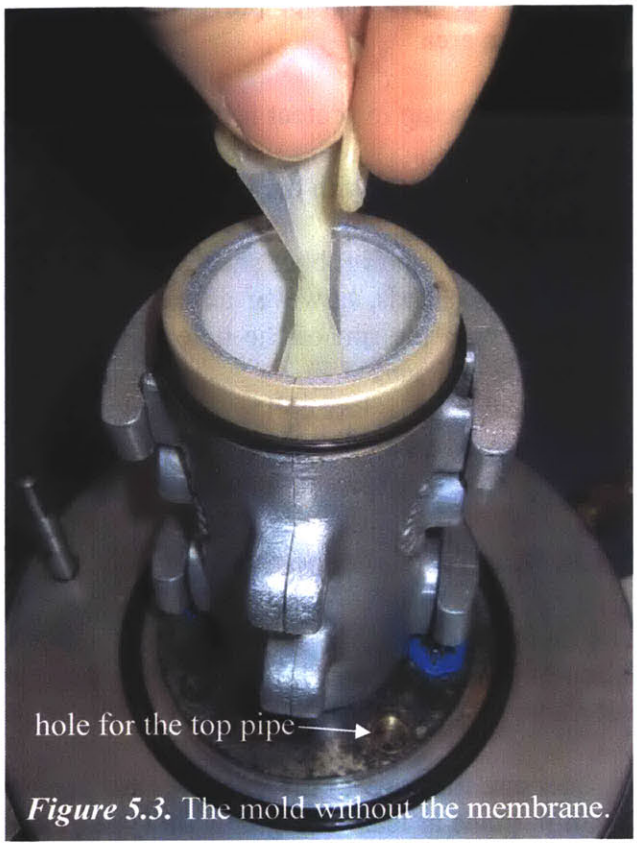

Figure 5.3. The mold without the membrane.

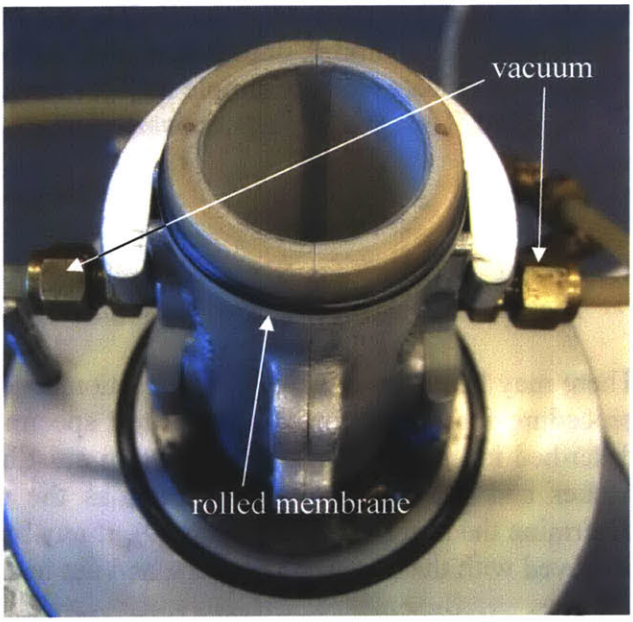

Figure 5.4. The mold with the membrane.

7. Measure the specimen height (H_o) from the top of the mold to the nylon filter using the caliper, making care that its metal tip and corners do not puncture the membrane.

8. For the modified setup, put enough distilled water into the mold to cover the entire specimen area.

9. Cover the setup to protect it from spilling grains (the coverings can be seen in *Figures 5.5* and *5.7*):
   - Cover the setup with the large rubber sheet with the large hole, the mold passing through the hole.
   - Stretch the small rubber sheet with the small hole in four directions (this is possible with only two hands, however an extra pair of hands is an easier option). Place it over the mold with the rim of the hole immediately above the o-ring, folding upwards (this is visible in *Figure 5.7*).
   - Place the plexiglass collar on top of the mold. If the collar rests on the o-ring instead of the top surface of the mold, the o-ring was placed too high, and it must be lowered by pushing it down without the collar, and even without the small sheet if necessary.

5.1.4. Specimen Preparation

The method of specimen preparation is important, because the characteristics of the initial fabric of granular materials are determined not only by the shape of the constituting particles, but also by the manner in which they were deposited (Oda, 1972[2]).

1. Measure the mass of the scoop + glass beaker as [1].
2. In it, place at least 150 grams of Type 1 sample or 120 grams of Type 2 sample. Record the mass of scoop + beaker + dry sample as [2].
3. Mix with a few grams of water (1-3%) in a beaker, to bring the sample to the consistency of snow. Keep mixing until it becomes homogeneous (10 to 20 minutes). Record mass of scoop + beaker + moist sample as [3], immediately before starting to put the sample into the mold. Then the preparation water content (w_p) is

$$w_p = \frac{[3]-[2]}{[2]-[1]} \qquad \textit{Eq. 5.1.}$$

4. For the modified setup, record the input voltage and zero reading of the tensiometer. Then, use the syringe to remove as much water as possible from the tensiometer surface.

There may be different ways of compaction. The important thing here is having a repeatable procedure for the compaction of all test specimen. The procedure used for this research is described in the next steps. Extreme care must be taken not to spill any material outside the beaker and the mold in this process, as the remaining mass will be measured later to determine the specimen mass (step 10). If any material spills on the rubber sheets, it must be retrieved with the scoop or tweezers, and put back into the beaker.

5. Compaction is done in 7 layers, 25 tamps per layer. For the first time this is done with a new material, it may take one or two trials to establish the amount of material to put per layer.

6. A pocket penetrometer with the large shoe is used for compaction (*Figure 5.5*), because it has a spring to keep the applied force constant for a given spring displacement, which is easier to control than force.
   - Before compacting, flatten the surface just by releasing the weight of the pocket penetrometer on the material to make it a uniform layer rather than chunks of material sticking together.
   - Press the penetrometer on the center of the specimen until it starts sinking in. This counts as the first tamp.
   - Put one tamp to the top, bottom, right, left, top-right, bottom-left, top-left and bottom-right of the surface (the path in *Figure 5.6*), touching the inner edge of the retaining ring with the penetrometer at each tamp. Each of these tamps should be enough to initiate a bearing capacity failure in the specimen, but without sinking it into the specimen more than a few millimeters. Each tamp should touch the mold walls (with glass spheres, this will never damage the membrane) in order to push down the material that climbed up the walls as a result of the previous tamps.
   - Repeat the cycle in the previous step twice more. However, since by now the specimen is somewhat compacted, higher pressures will be required to displace the glass spheres.
   - Scrape the top 1 mm of the layer with the tip of the scoop. The loosened material remains inside.

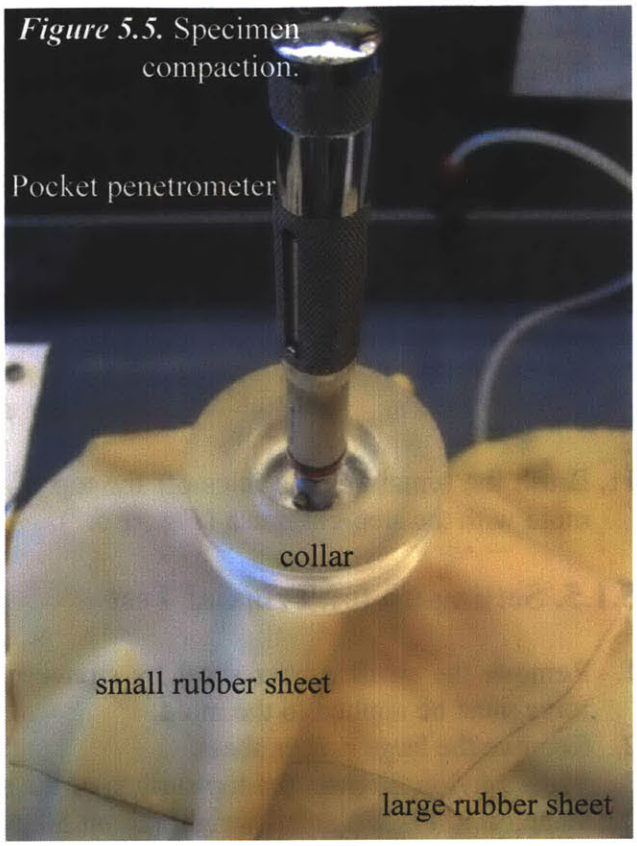

Figure 5.5. Specimen compaction.

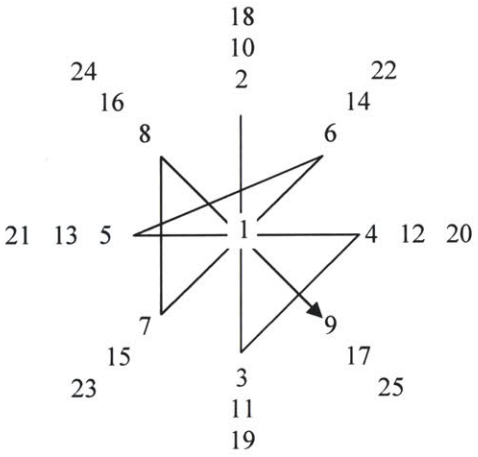

Figure 5.6. Tamping sequence used in this research

7. Put six more layers of material and repeat the entire step 6 for each of the remaining six layers. This should result in a final height less than 5 mm above the top of the mold. If the final amount of material compacted after 7 layers is below or too far (more than 5 mm) above the height of the mold, the specimen can be scooped out back into the beaker to go back to step 3.
8. Twist and remove the plexiglass collar. Clean any grains off the collar and put them into the beaker.

9. Use the straight edge of the scoop (or any other straight tool) to remove the excess material on the top of the specimen, a small amount at a time. Put all recovered material into the beaker.
10. Record the weight of scoop + beaker + remaining moist material as [10]. From the amounts advised in step 2, very little material is left in the beaker. If the water loss from this little amount of material due to evaporation is neglected, the dry mass of the specimen is:

$$m_{dry} = \frac{[3]-[10]}{1+w_p} \qquad \textit{Eq. 5.2.}$$

11. Brush the remaining particles off the top of the mold with the step-cut brush (*Figure 5.7*).

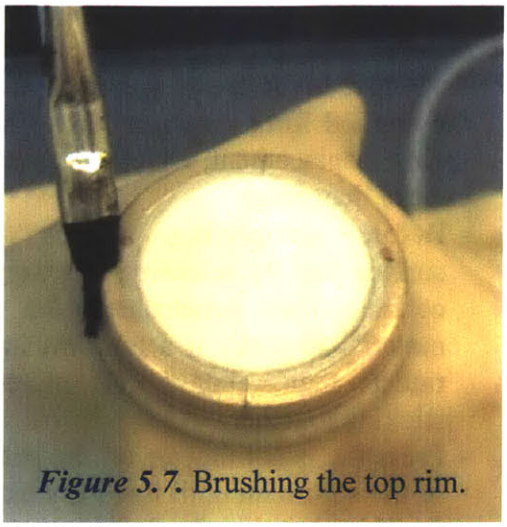

Figure 5.7. Brushing the top rim.

5.1.5. Setting up for Triaxial Test

1. Remove the small rubber sheet by stretching it in 4 directions evenly. Minimal lateral force must be applied to the mold.
2. Remove the large rubber sheet.
3. Place a nylon filter on the top surface of the specimen, convex side down. Place a porous stone on it. Place a small weight (about 50 grams) on the filter and the stone to minimize specimen disturbance in steps 4 and 6.
4. For the standard setup, the standpipe that connects to the top cap is affixed to the base at this stage. Pay attention to the connection orientations on the standpipe and the spiral pipe of the top cap.
5. Record the input and output voltage of the load cell as its zero.
6. Disconnect and remove the vacuum pipes from the sides of the mold.
7. Remove the weight on the specimen.
8. Place the superstructure on the base (for the standard setup, top cap connections aligned). Tighten the nuts on the bolts.
9. Stretch two thin o-rings onto the new stretcher. Place it around the mold as shown in *Figure 5.8*.

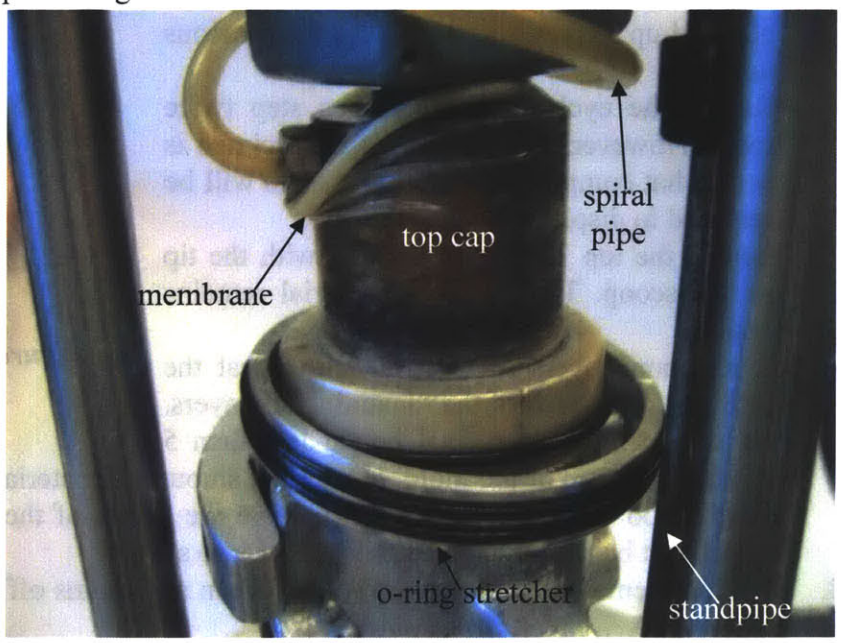

Figure 5.8. Membrane on top cap.

10. Set the top cap height.
    - Release the piston clamp.
    - Lower the piston very slowly, by pressing from the top end with one hand while applying an upward counterforce from under the load cell, until the top cap touches the porous stone. This can be done by watching exactly from the same level as the gap closes between the top cap and porous stone.
    - Clamp the piston.
11. Unfold the fold of the sleeve on the top cap to cover the perimeter of the porous stone. Adjust it by sliding it around the top cap so that it covers the entire lateral area of the stone and digs into the specimen a fraction of a millimeter.
12. Connect the standpipe to the spiral pipe
13. Cover the top cap with the membrane:
    - Move the entire rolled section of the membrane from below the o-ring to immediately above it.
    - Pull the membrane up onto the top cap, symmetrically. This pull must not be too strong, or else grains will come up, stick onto the sleeve, and disrupt sealing.
    - Pull the membrane up with radial motions to straighten the wrinkles. Place the rolled portion above the top cap (*Figure 5.8.*)
14. Drop the two o-rings on the stretcher onto the lateral face of the top cap, to seal. Move the pieces of the o-ring stretcher out of the setup.
15. For saturated tests, a vacuum much less then the intended confining stress can be applied to the specimen by connecting the vacuum pump regulator to the specimen through the pore PVA pipe (see *Figure 4.9*). Use a long extension pipe/hose in order not to be limited in measurement while moving the cell. Both the top and bottom valves connect the specimen to the back pressure junction for applying the vacuum. For unsaturated specimen, the vacuum can not be applied, as it would evaporate the water in the specimen. The confinement provided by the membrane, combined with the strength increase due to suction, is found to keep the specimen intact through the preparation process.
16. Remove the mold with no movement of the specimen.
    - Cut the o-ring around the mold with scissors.
    - Pull the rubber sleeve section around the mold down, so that all of it is on the lateral surface of the mold.
    - Cut the rubber sleeve. This is the stage illustrated in *Figure 5.9*.
    - Remove the clamps.

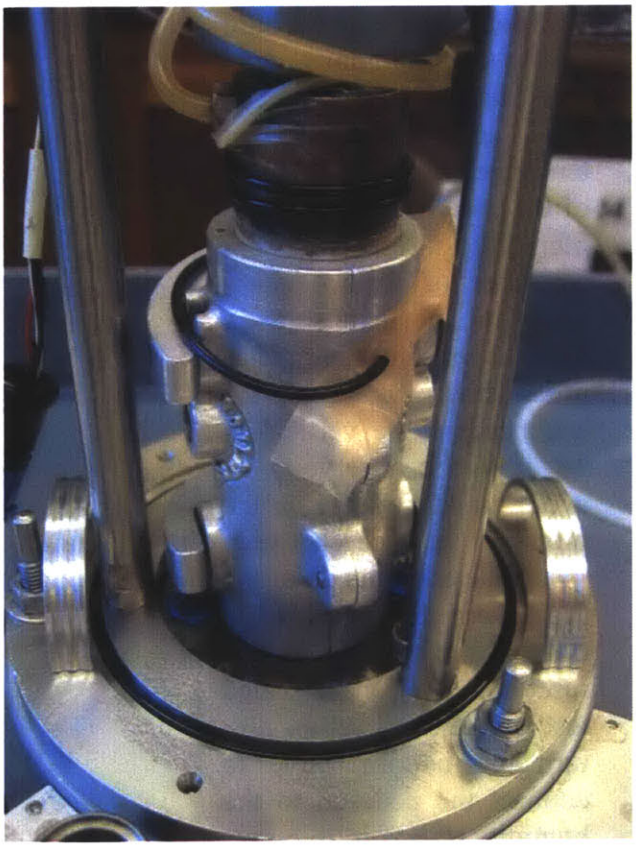

Figure 5.9. The mold is about to be removed.

- Separate the mold halves carefully and remove them without touching the specimen.

17. Plug the load cell to its plug on the base.
18. Determine the initial specimen area (A_o) by the use of optical vernier (see *section 5.3.1* for the optical profiling procedure; photograph in *Figure 4.15*). Obtain two diameter measurements at each one of three different levels and average these three cross-sectional areas to determine A_o.
19. Place the plexiglass cylinder (make sure both o-ring surfaces are clean) around the cell.
20. Place the cell in the loading frame.
    - Lift the cell carefully and rest the edge of its base on the loading platform.
    - Plug the outer cable (not the cable inside the triaxial cell), that connects the load cell to the data acquisition system, into the socket immediately below the 9-pin socket inside the cell, where the load cell is already plugged.
    - Slide the triaxial cell on the loading platform and align it. There is a recess of a few millimeters deep under the base, into which the loading platform fits. When everything is aligned, the triaxial cell will fall into its place, so keep the entire weight of the triaxial cell supported in order to prevent a hard fall (as vibrations may restructure the specimen).
21. For an unsealed or tensiometer test, put the end of the pore PVA pipe into a humidity reservoir (a container of water that is open to the atmosphere). Keep as much of the pipe as possible horizontal (only the end needs to be vertical to go into the reservoir) to avoid gravity effects on the pressure balance between the inside and outside of the pipe. Turn the top valve to connect the top cap to this reservoir. For an unsealed test on standard setup, also turn the bottom valve to connect the pedestal to the humidity reservoir.

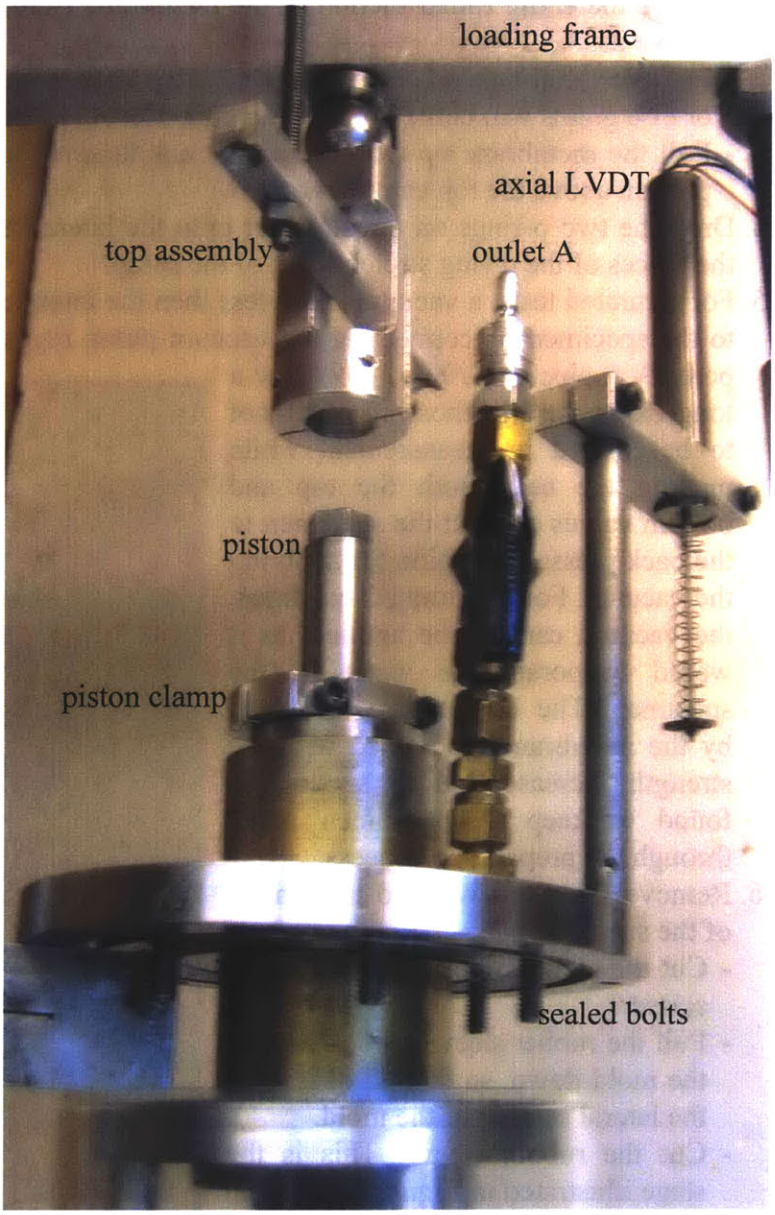

Figure 5.10. Upper components of the triaxial cell.

LVDT structure on top in an orientation that will leave enough open space to work with keys on the front side of the piston (make sure all o-ring surfaces, including those of the bolts, are clean). Tighten the sealed bolts.

23. Put the hole of the LVDT crossbar over the piston. Let the bar rest loosely on the piston clamp.
24. Fix the top assembly and the loading frame (*Figures 4.9* and *5.10*) to the piston and tighten its bolts.
25. Insert the LVDT core. Fix the LVDT crossbar to the piston as high as possible, and with proper the orientation so that it carries the LVDT core. The LVDT crossbar may touch the top assembly.
26. Check if the LVDT is in the proper part of its range; adjust its height if necessary, as described in *section 5.2.1.3.*
27. Connect the cell PVA and oil tank to the triaxial base in their designated places (*Figure 4.9*).
28. Open the cell PVA valve, to fill the cell pressure transducer socket from the reservoir of the cell PVA by gravity (it may take 1-2 minutes).
29. Affix the cell pressure transducer.
30. Turn the cell valve to the PVA to fill the pipe between the valve and the triaxial cell from the cell PVA reservoir by gravity. Then, close the cell valve.
31. Fill the cell:
    - Open the vent valve to the atmosphere.
    - Connect the oil tank to the compressed air pipe and pressurize.
    - Open the tank valve and start filling the cell with oil. Fill upto the mid-level of the specimen.
    - Connect the cell pressure transducer to the cell through the cell valve, monitoring its output voltage reading while tightening it. Record its input and output voltage for its zero reading.
    - Close the cell valve, open the tank valve, and continue filling the cell.
    - Partially close the tank valve when the cell is almost full. Completely close it when oil outflows through outlet A.
    - Depressurize the oil tank and disconnect its compressed air pipe.
    - Close the vent valve.
    - Open the cell valve to connect the cell to the PVA reservoir.
32. If adjusting the cell PVA's stroke (*section 5.1.2.4*) before the test is needed, it should be done at this point.
33. Record the input voltage and output voltages of the LVDTs as their zero readings.

5.2. Triaxial Testing Procedures

5.2.1. Operation of Individual Components

Operation of electrical equipment (voltmeters, switches, plugs) will not be explained in this thesis, because they differ from laboratory to laboratory, and thus some laboratories will not have to be the same electrical equipment as that used in the MIT Geotechnical Laboratory.

5.2.1.1. Controller Interface Box

The user interface of the control box is very simple as 4 switches and one knob (*Figure 5.11*) control all functions. The on-off switch turns the box on/off (the box consumes some electricity to run its cooling fan).

The remaining 3 identical switches are for axial, cell and pore pressure control, and each have options of manual, off or computer that select how each servomotor is controlled. *Off* is the default position. Switches should be turned to *computer* only when the computer control software is running, otherwise it will send uncontrollable signals to the servomotors. The knob is a 10-turn potentiometer that controls the speed of the servomotor, whose switch points to *manual*. The numbers, if there are numbers, on the knob may not reflect the control rate.

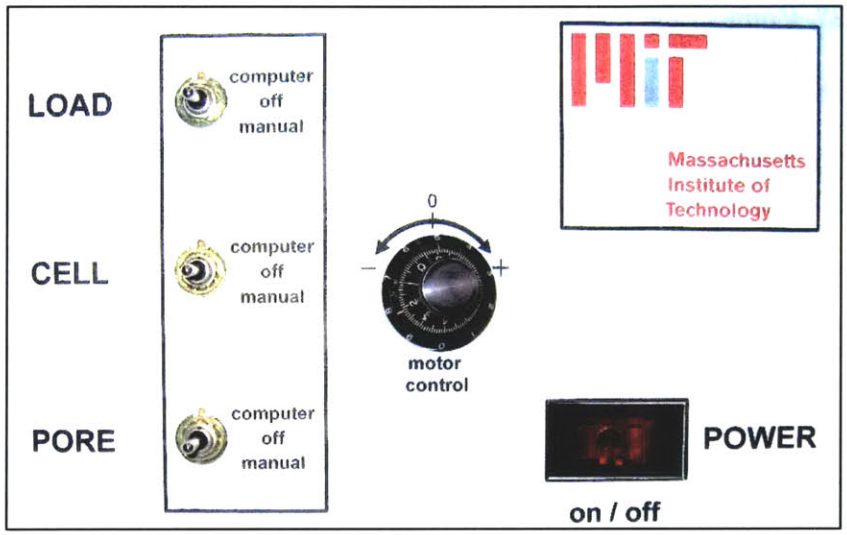

Figure 5.11. Front panel of the control interface box.

At most, one switch may be on *manual* at any given time. Before a switch will be turned to *manual* for the first time by an operator in a day, it must first be turned to *manual* for a fraction of a second and then brought back to the *off* position while watching the corresponding servomotor. This is done because the potentiometer might have been left at any rate or direction during the previous use. If it has been left at a very fast rate, turn it to a slower value. Repeat the process of briefly switching it to *manual* and back to *off*, until the rate is slow. Then, it can be left on *manual* and the final adjustment to the rate can be made. To be safe for the next use, slow the rate down to stationary before turning the switch to *off*.

The back of the controller interface box has sockets for cables from all servomotors, the control computer, and power.

5.2.1.2. Affixing Pressure Transducers

Two issues are important when affixing a pressure transducer to its socket for fluid pressure measurement:

- Air should not be trapped in the transducer socket. Air can be let out if the transducer is inserted at a slight angle into a socket full of fluid.
- A transducer should not be screwed in or out unless it is open to an air-fluid interface (or it will be destroyed).

- A transducer should be tightened by hand only, not by tools (wrench, etc.). While tightening, its voltage reading must be monitored through a voltmeter, because when the other end of the pipe is mistakenly closed (as opposed to the previous step), even tightening by hand can destroy the transducer.

5.2.1.3. Adjusting LVDTs for Linear Range

Check the LVDT reading; it must be in the linear range (±2 V). For the volume measurement, start from about the middle of the range (0 volts) when testing a material for the first time, preferably from the side of the zero that has the PVA piston more out of its cylinder than in, as, on average, the total flow will be from the specimen to the PVA (due to consolidation). The materials used in this research don't have large volume deformations in any case.

For the axial measurement, the initial LVDT reading should be close to one end of the range (either 1 to 2 V or -1 to -2 V). Check which way the reading changes when the core is moved into the LVDT. It should be moving toward the closer boundary of the linear range. If these conditions are not satisfied, loosen the bolt holding the LVDT and adjust its height. (during the test the core will move out of the LVDT, so this check ascertains that the LVDT has most of its range available for the measurement of axial deformation of the specimen).

If either LVDT runs out of its linear range during the test,
- Stop the test
- Record the last LVDT reading
- Make the necessary adjustment to the LVDT position (the axial LVDT was described in the previous paragraph, the volume LVDT is described in the next section)
- Record the new LVDT reading
- When processing the data, subtract {normalized new reading minus normalized old reading} from all readings after the adjustment.

5.2.1.4. PVAs of the Triaxial Setup

The reservoirs above the PVAs must always have fluid in them. They can be filled using a funnel through the hole on their top surface.

When pressurizing, the PVAs constantly push fluid toward the setup. This eventually results in the pore PVA running out of the linear range of the volume LVDT, or more often, the cell PVA running out of the stroke of its piston. To continue operation, the PVA that is close to the end of its stroke should be adjusted as follows, while the pipe connecting to the triaxial cell is connected only to closed valves (i.e. cell, or top and bottom valves of the triaxial base must be closed):
- Connect the piston to the reservoir by opening the PVA valve.
- Use manual control (*section 5.2.1.1*) to draw the piston to the other end of its stroke.
- Turn off the manual control (preferably at zero rate).
- Close the PVA valve.

If the stroke runs out during a test, the procedure is more complicated for both pore and cell PVAs. For the pore PVA, resetting the piston requires moving the volume LVDT, so the following process written for both PVAs needs to proceed in parallel to the steps for the volume LVDT in *section 5.2.1.3* for pore PVA.

- Stop the test by turning all three control switches to *off* simultaneously.
- Record the voltage reading of the cell/pore pressure transducer. In the case of the pore PVA, the pore pressure transducer must be connected to the back pressure junction through the transducer valve. In the case of the pore PVA, also record the volume LVDT reading.
- Close the cell valve for the cell PVA, or top and bottom valves for the pore PVA.
- Connect the piston to the reservoir by opening the PVA valve.
- Use manual control (*section 5.2.1.1*) to draw the piston to the other end of its stroke.
- Turn off the manual control at zero rate.
- Close the PVA valve.
- Use manual control to bring the voltage reading of the cell/pore pressure transducer back to the reading recorded before the adjustment.
- Open the cell valve for the cell PVA, or top and bottom valves for the pore PVA. For the pore PVA, record the new reading from the volume LVDT. When processing the data of a test in which the pore PVA had been reset, subtract {normalized new reading minus normalized old reading} from all readings after the adjustment..
- Resume a test by turning all three control switches to *computer* simultaneously.

5.2.1.5. Loading Mechanism

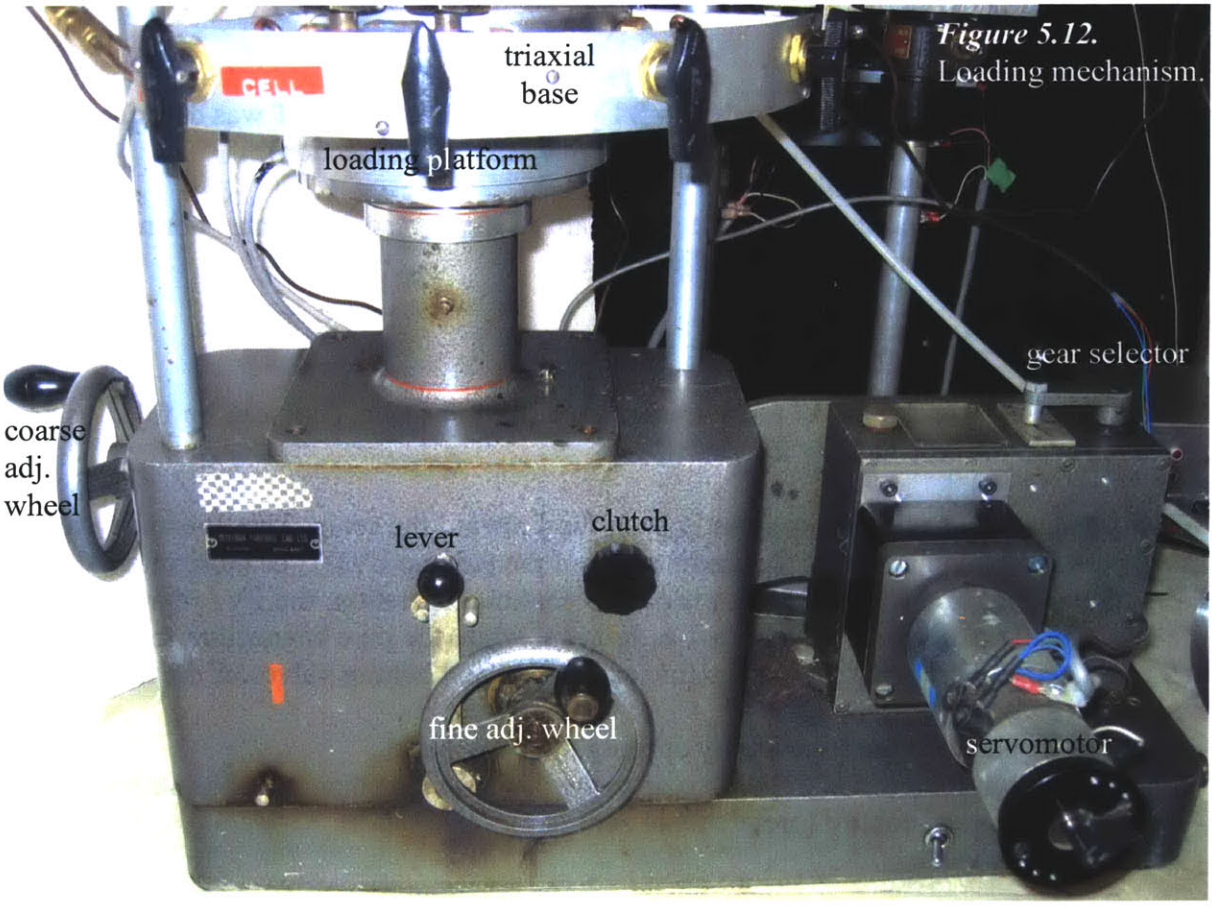

Figure 5.12. Loading mechanism.

The gear configurations of the loading frame transmission are marked with letters A to E on the gear selector. The gear ratio used in all tests is C.

In its pushed-in position, the clutch gives control of the mechanism to the two manual adjustment wheels. A lever selects which wheel is in control. In the pulled-out position, the clutch connects the mechanism to the servomotor and therefore, automation. For the automated system to run, the lever also has to point at the fine adjustment wheel (the position in *Figure 5.12*). Being a geared system, when a new control option is selected, sometimes the gears don't align properly and don't engage. If this happens, move related pieces back and forth a bit while trying to engage the desired control.

The loading ploatform can move vertically through a stroke of 10 cm. Before any test, it must be checked whether at least half of this stroke is available. If more stroke is needed, push the clutch to engage the wheel control, lower the lever to coarse control, and lower the platform using the coarse adjustment wheel. When this is done, put the lever and the clutch back to their original positions. The level of the cross-bar of the loading frame might need adjustment as a result of this process.

5.2.1.6. Computer Control Software

The input module of the program (named `QBSETUP.BAS`) requires the operator to input calibration factors and normalized zeros for all transducers, as well as specimen dimensions. Other information, such as date, operator's initials, membrane and piston type, may also be entered for record keeping. The module program directs the user to the main program (named `QBMIT04.BAS`).

The main program offers a variety of automated loading schemes:

1. Undrained Hydrostatic Initial Stress
2. Drained Hydrostatic Stress Change
3. Hold Current State of Stress
4. Measure "B" Value
5. K_o Consolidation
6. Stress Path Consolidation
7. Undrained Shear

In each of these schemes, it asks for self-explanatory inputs - for example, "`Enter target axial effective stress (ksc)`". It also gives some instructions as to what must be changed, if anything, in the triaxial setup, when necessary – for example, "`Close pore pressure valves and press ENTER`".
Scheme 3 is for keeping the stresses and pressures constant, so it must be used if, for some reason, the process has to pause while in between schemes. The program automatically reverts to scheme 3 if the target of any other scheme is reached.

One issue of note is the absence of a separate scheme for Drained Shear. This is because scheme 6 runs as a drained shear test, if a very large number is entered as the target axial effective stress.

5.2.1.7. Carbon dioxide Tank

The carbon dioxide is kept in a pressurized tank, which can act as a powerful rocket in the case of an accident. This has important safety directives. The carbon dioxide is needed only for the saturated tests.

- The tank must be kept vertical to minimize the risk of an accident.
- Except during transportation, the tank must be fixed to an immobile object (laboratory benches are appropriate) with a belt and clamp.
- For transportation, the regulator valves and gages must be removed and the tank's steel cap must be tightly screwed on the top.
- The tank must not be transported by rolling, carrying, pushing or dragging. The only safe mode of transportation is securing it to a wheeled cart specifically designed for transporting pressurized gas tanks.

5.2.1.8. Piston Clamp

The piston clamp is a two piece doughnut shaped metal component, with two bolts holding it together. To clamp the piston, place the pieces around the piston at the lowest possible point, touching the piston guide (the metal cylinder with ball bearings). Then tighten its bolts.

The clamp prevents the piston from moving down into the triaxial cell, but not up. When tightening or loosening the bolts of the clamp, or axial LVDT crossbar, or the top assembly, the piston should be held down by holding the clamp.

5.2.2. Saturation

The procedure in this section (entire *5.2.2* with all of its subsections) is used only for saturated tests, and is completely skipped for unsaturated tests. Saturation is achieved by first displacing the pore air with carbon dioxide, then replacing carbon dioxide with water. Any remaining pockets of CO_2 are dissolved in water (carbon dioxide's solubility in water is much higher than air's) through pressurization. This is done using the following procedure:

5.2.2.1. Initial Effective Stress

In order to preserve the integrity of the specimen, the initial effective stress, which was applied by lowering the air pressure in the pore space during setup, must be maintained during saturation. But this can no longer be done through the pore air. The initial effective stress will be provided by applying a small magnitude of hydrostatic total stress.

- Start the setup module of the computer program.
- Input the information except pore pressure zero (pore pressure transducer is not yet connected to the triaxial cell). The setup module will route the user to the main program.
- Remove the vacuum within the specimen by disconnecting the vacuum pump from the pore PVA pipe. With the piston clamped and the fluid in cell under about 0.04 kgf/cm^2 pressure from the elevation of the cell PVA reservoir, it is possible to have a stable specimen with zero pore pressure.

- Choose option 1 (undrained hydrostatic initial stress) in the main program. Apply a small initial stress (0.2 – 0.25 kgf/cm^2 was used in all tests of this research).
- Switch the cell pressure control to *computer.*
- Take the piston clamp off.

5.2.2.2. Carbon dioxide Flushing

- In order to judge whether the gas is flowing properly, dip the end of the tub or hose connected to the gas tank into a container of water and observe the CO_2 outflow as bubbles. Use the valves of the regulator on the tank to adjust the flow to 1-2 gas bubbles per second.
- Connect the CO_2 at this flow rate to the pore PVA pipe on the triaxial base
- Fill pore pressure transducer socket with distilled water
- Connect outlet B to an open container (a flask works best) with some water inside, through a flexible tube whose end is submerged in this water.

Carbon dioxide is heavier than air. Therefore the pore space and all connected pipework must be flushed upwards from the bottom (this will be called *directive 1*). One end must open to the atmosphere through a body of water, in order to prevent the gas pressure from building up (*directive 2*). The next four steps are designed to flush the system while satisfying these two directives. If two valves are to be turned between consecutive steps, they are turned simultaneously. *Figure 4.9* can be referred to, for tracing the pipes that are being flushed.

1. Turn the transducer valve to connect the back-pressure junction to the pore pressure transducer socket. Bubbles should start to come out through the socket, satisfying *directive 2*. Wait for a minute to get all air in the transducer socket – back pressure junction – pore PVA line replaced by CO_2.
2. Read this step and the next step. Turn the transducer valve to connect the pedestal to the pore pressure transducer socket, and turn the top valve to connect the back-pressure junction to the top cap. This will flush the line between the back-pressure junction and the top valve, while pushing the excess air downwards through the specimen and out of the transducer socket. As this will operate against *directive 1* once the CO_2 reaches the top cap, this step of flushing must not last more than 5 seconds (proceed to step 3 after 5 sec.).
3. Open the bottom valve, and close the top valve to all flow. This flushes the back pressure junction – pedestal line, the lower porous stone, and pedestal – transducer valve line. The dispersed flow through the porous stone, and getting the CO_2 into all of its pores, may take some time. So wait for 5 minutes in this step.
4. Close the transducer valve to all flow, and turn the top valve to connect the top cap to outlet B (i.e. the flask of water). This flushes the specimen, upper porous stone, and the top cap – top valve line. In order to fill as many specimen pores as possible, leave it at this step for 20-30 minutes.

To finish;
- seal the CO_2 in the system by closing all three water valves (transducer, top and bottom valves) on the base,
- bend the (copper) pore PVA line upwards,
- disconnect it from the CO_2 tank, and connect it to the PVA,

- close the regulator valves on the CO_2 tank.

5.2.2.3. Water Flushing

- Fill the PVA reservoir with water. This will be the source of water for the flushing stage, and the flow will be by gravity.
- Have an additional empty water container ready with flexible tubing.

For the purpose of flushing the system with water, *directive 1* holds because water is heavier than CO_2. *Directive 2* holds because most of the CO_2 will have to leave the system through a vent (the remaining amount will dissolve). As the criteria are same as those for CO_2 flushing, the procedure is very similar to that of CO_2 flushing.

1. Turn the transducer valve to connect the back-pressure junction to the pore pressure transducer socket. Bubbles should start to come out through the socket, satisfying *directive 2*. Wait until the bubbles stop, which indicates all CO_2 in the transducer socket – back pressure junction – pore PVA line is replaced by water.

2. Read this step and the next step. Turn the transducer valve to connect the pedestal to the pore pressure transducer socket, and turn the top valve to connect the back-pressure junction to the top cap. This will flush the line between the back-pressure junction and the top valve, while pushing the excess CO_2 downward through the specimen and out of the transducer socket. As this will operate against *directive 1* once the water reaches the top cap, this step of flushing must not last more than 5 seconds (proceed to step 3 after 5 sec.). Any sign of water at the top of the specimen at this stage will disrupt the procedure, and force the operator to first drain the pores (*section 5.2.4.1*) and then go back to *section 5.2.2.2*.

3. Open the bottom valve, and close the top valve to all flow. This flushes the back pressure junction – pedestal line, the lower porous stone, and pedestal – transducer valve line. The specimen, which has seemed translucent until this point, becomes opaque at the lower end due to wetting. Wait in this step until the bubbles of CO_2 are seen coming out of the pore pressure transducer socket stop.

4. Close the transducer valve to all flow, and turn the top valve to connect the top cap to outlet B (i.e. the flask of water). This flushes the specimen, upper porous stone, and the top cap – top valve line. The opaqueness of wetting in the specimen will progress upwards. In order to fill as many specimen pores as possible, the specimen is flushed with several volumes of water. During this time, the pore PVA reservoir may need refilling, and the flask connected to outlet B may need emptying. The rate of flow can be controlled by changing height of the flask. This step takes about one hour.

At this stage, the only missing component is the pore pressure transducer, which must be affixed while regarding the rules in *section 5.2.1.2*, by the following procedure:
- Bring the flask to a level so that the water level in the flask is a few centimeters higher than the pore pressure transducer socket,

- Stop the flow of water by closing the bottom valve,
- Turn the transducer valve to connect the pore pressure transducer socket to the pedestal. Water will start to flow slowly from the flask to the socket, through the specimen. The level of water in the socket will start to rise (if the flow is unobservably slow, raise the flask).
- Affix the pore pressure transducer into its socket, monitoring its output voltage.
- Raise the flask so that its water level is at the mid-height of the specimen.
- Record the input and output voltages of the pore pressure transducer as its zero reading.

5.2.2.4. Back-Pressure Saturation

In order to dissolve the remaining pockets of air or CO_2, the pore pressure will be kept at a high value (3 kgf/cm^2) throughout all saturated tests. An equal increment of cell pressure must be applied to keep the effective stress positive.

- Close the pore PVA valve.
- Turn the cell switch on the control box to *off*.
- Record the outputs of all transducers.
- On the control computer, go back to the setup module and enter the pore pressure zero.
- In the main program select scheme 2 (drained hydrostatic stress change).
- Enter a pressurization schedule that will elevate the pore pressure (called "back pressure" in the program) by 1 to 5-minute increments of 0.5 kgf/cm^2, while keeping the effective stress at 0.2 kgf/cm^2. This results in *Table 5.2*, which is how the schedule appears on the computer screen while being input.

Table 5.2. Back-pressure saturation increments.

Increment #	Cell (ksc)	Back (ksc)	Time (min)
1	0.7	0.5	5
2	1.2	1.0	5
3	1.7	1.5	5
4	2.2	2.0	5
5	2.7	2.5	5
6	3.2	3.0	5

- Turn both the top and bottom valves to connect the specimen to the back-pressure junction.
- Turn the transducer valve to connect the pore pressure transducer to the pedestal.
- Turn all control switches to *computer* and wait. (It must be noted that each increment takes much longer than its specified duration, so the scheme above may take over one hour.)

5.2.2.5. B Value Check

In order to check if saturation was successful, Skempton's B value (Skempton, 1954) is measured. The B value is the change in pore pressure in an undrained specimen in response to a unit increase in isotropic stress, and is close to 1 for completely saturated materials. Scheme 4 of the computer program does this by applying several separate increments of user-defined stress (in the case of this research, 0.25 kgf/cm^2). The program also prompts the

operator to close the top and bottom valves to flow at the beginning, and to open them back to the junction when the increment is reversed. In the end, the program computes the B value and displays it. B values higher than 0.95 are considered acceptable for a triaxial test, and the procedure can be continued. If it is lower, Scheme 3 (hold current state of stress) is run for 24 hours, and then the B value is checked again.

5.2.3. Loading

After starting each of the phases of loading described in the next three subsections (*5.2.3.1* to *5.2.3.3*) the operator should stay for a few minutes to observe if everything is running properly. The unsaturated tests skipped the previous section (*5.2.2*). Resuming the procedure for all test types.

5.2.3.1. Initial Total Stress

For unsaturated tests only, this section is to make sure everything is working with low stresses, before proceeding to higher stresses. Saturated tests already had an equivalent section in *5.2.2.1*.

- Start the setup module of the computer program.
- Input the information. The setup module will route the user to the main program.
- Take the piston clamp off.
- Choose option 1 (undrained hydrostatic initial stress) in the main program. Apply a small initial stress (0.2 – 0.25 kgf/cm^2).
- Switch the cell pressure control to *computer.*

5.2.3.2. Isotropic Compression

- Record the values on the control computer screen onto the datasheet.
- Select scheme 6 (stress path consolidation).
- Enter the intended confining stress (σ_c for unsaturated test, or σ_c' for saturated test), when prompted for both of the target radial effective stress and the target axial effective stress. This will not exactly be equal to the applied confining stress, as will be explained in *section 5.4.3.1.*
- Enter 0.1 to 0.3 %/hr for axial strain rate. The actual strain rate will not match this, and will not stay constant.
- Start collecting readings from all 4 to 6 channels (input voltage, axial load, axial displacement, cell pressure for *sealed* and *unsealed* tests; plus the pore pressure which is tensiometer in *tensiometer* tests; plus volume change LVDT for *saturated* tests) with the Central Data Acquisition computer, at a rate of one reading per five seconds, set for 2000 readings.
- Start applying the scheme from the control computer, and turn all related control switches (cell pressure and axial load for unsaturated; plus pore pressure for saturated) to *computer.*
- This scheme lasts less than two hours, and the computer reverts to scheme 3 (hold current state of stress).

5.2.3.3. Shearing

- Record the values on the control computer screen onto the datasheet. Also record the number of data points in the data acquisition computer, or start a new data acquisition task. In order to preserve accuracy in the data, the strain values at this stage will act as the zero readings when processing the data (*section 5.4.1*).
- Select scheme 6 (stress path consolidation).
- Enter the intended value of σ_c for unsaturated test, or σ_c' for saturated test, when prompted for the target radial effective stress.
- For the target axial effective stress, enter a number larger than the expected strength at this confining pressure. In this research 20 kgf/cm^2 was entered, whereas no specimen withstood any axial stress greater than 10 kgf/cm^2.
- Enter 1 %/hr for axial strain rate. The actual strain rate will not match this, and will not stay constant.
- Start the scheme.
- Add several thousand readings to the Central Data Acquisiton computer.
- After 2 - 3 hours, increase the reading rate to 15 or 20 seconds. Add enough thousands of readings for the next 24 hours.

5.2.4. End of Test

- Earlier the next day, stop the shearing if the axial strain has exceeded 15%. Turn all control switches to *off*, and stop the data acquisition.

5.2.4.1. Draining the Pore Water

For saturated tests only, follow this procedure before continuing, for unsaturated tests, skip to *section 5.2.4.2*;

- Close the bottom and transducer valves to all flow.
- Turn the top valve to connect the top cap to outlet B.
- Open the cell PVA valve.
- Detach the pore PVA from the triaxial cell.
- Connect both the vacuum pump regulator and pore PVA outlet of the cell, to a watertrap. A watertrap is a flask that has two holes through its stopper, through which flexible tubes connect it to other components. The watertrap, in this case, will accommodate the pore water without letting it into the vacuum pump.
- Open the bottom valve and turn on the vacuum pump at a small vacuum. This will drain the specimen in a few minutes. A Visible color difference will progress throught the specimen. When the bulk pore water is completely drained, water stops flowing into the watertrap and the hissing sound of air flow through the specimen begins.
- Close the top valve to all flow.
- Close the bottom valve. This seals the vacuum in the specimen.
- Turn the transducer valve to connect the pore pressure transducer to the back-pressure junction.
- Remove the pore pressure transducer. Water in its socket will be sucked out into the watertrap immediately.

- Disconnect the vacuum from the setup.
- Close the cell valve to all flow.

5.2.4.2. Emptying and Dismantling the Cell

- Open the vent valve.
- Open the tank valve.
- The cell fluid starts to drain very slowly. It can be left as it is, and it will drain completely by gravity in 20-30 minutes. Or, if faster drainage is desired, the compressed air pipe (not shown in *Figure 4.9*) that pressurizes the oil tank may be connected to outlet A with pressure, to generate a larger head difference.

Dismantling the cell is mostly the reverse procedure of assembling it (*section 5.1.5*). The following steps can be carried out while waiting for the cell to empty:
- For the modified setup, unplug the tensiometer.
- Disconnect the pipe of the cell PVA from the triaxial cell.
- Close the cell PVA valve.
- Bend the end of the pipe that was connected to the cell PVA on the triaxial cell, such that its end is at the same level as the cell pressure transducer.
- Remove the cell pressure transducer.
- Put the piston clamp on.
- If air pressure was used to accelerate the drainage, then disconnect the compressed air pipe from outlet A.
- Release the bolts of the top assembly.
- Raise the cross-bar of the loading frame, and the top assembly, off the piston.
- Remove the reference bar and the core of the axial LVDT.
- Unscrew six bolts of the top plate. Remove the top plate with the LVDT.
- Disconnect the pipe that goes to the oil tank.
- Lift the triaxial cell and rest it on the edge of the loading platform.
- Unplug the load cell cable from underneath the base.
- Put the triaxial cell on a workable space with operator access from all directions.
- Remove the plexiglass cylinder.
- Use toilet paper to dry as much fluid as possible from transducer sockets, outlets and base.
- Use the optical vernier (as described in *section 5.3.1*) to take diameter measurements of the deformed specimen at various levels, in two directions. In the majority of tests the measurements were taken at every 0.5 or 1 cm, with an extra measurement at the widest cross-section.

5.2.4.3. Specimen Retrieval and Recycling

As described in *section 5.1.2*, sample processing procedure is impractically long for Type 2 material. Any material that touches oil is deemed unusable, as oil may affect the friction angle. Moreover, it certainly changes the mechanics by adding oil-water surfaces to all tests, and oil-air surfaces to unsaturated tests. The following procedure was developed to recycle upto three-quarters of each specimen without oil contamination. On average, the missing amount can be replaced by repeating the procedure in *section 5.1.2* only once.

The equipments for this part of the procedure are:

- scoop,
- spatula,
- sharp, thin scissors,
- a glass plate of about 25-30 cm on each side,
- a roll of toilet paper,
- a container to collect contaminated material,
- 3 very clean water content tares, with known weights for unsaturated tests.

Use toilet paper to dry as much oil as possible from the ceiling of the superstructure, load cell, top cap, and the membrane surface, from top to bottom.

- Wipe the superstructure and the load cell.
- Wipe the gap between the top cap and the load cell. Wrap and leave some toilet paper in the gap, as oil retained within the load cell can continue oozing down for several hours.
- Fold the rolled part of the membrane down, over the o-rings. Dry the exposed oily surfaces (rubber sleeve, inner surface of the membrane) with toilet paper.
- Wipe the oil off the outer surface of the membrane around the specimen.
- Set a clean glass plate on the laboratory bench or table.

5.2.4.3.1. Opening up the Specimen in the Standard Setup

For the standard setup only;

1. Increase the distance between the o-rings around the pedestal by sliding them apart.
2. Hold and pull the lower o-ring radially with fingertips to make a gap between the o-ring and the pedestal. Pull the membrane up out of this gap with the other hand.
3. Repeat the step above from several directions until the end of the membrane is free of the o-ring.
4. Slide the upper o-ring on the pedestal downwards. Repeat the previous two steps for this o-ring as well, to free the lower end of the membrane from both o-rings.
5. Turn both top and bottom valves to the back-pressure junction to release the vacuum.
6. Place the rolled section of the membrane immediately above both o-rings.
7. Push the upper o-ring on the top cap down and slide both o-rings on the top cap down to a level between the upper porous stone and the surface of the top cap.
8. Hold both porous stones from outside the membrane and pull them horizontally while keeping the specimen intact.
9. Lay the specimen on its side onto the glass plate.
10. Collect the porous stone and nylon filter at the bottom end (the end without the rolled section of the membrane).
11. Cut the membrane along the length of the specimen, with minimal disturbance to the specimen. Start the cut from the bottom end, and cut to a little above the top porous stone.
12. Peel the membrane from this cut to the sides.
13. Collect the remaining porous stone, nylon filter and o-rings (*Figure 5.13* is at the end of this step).

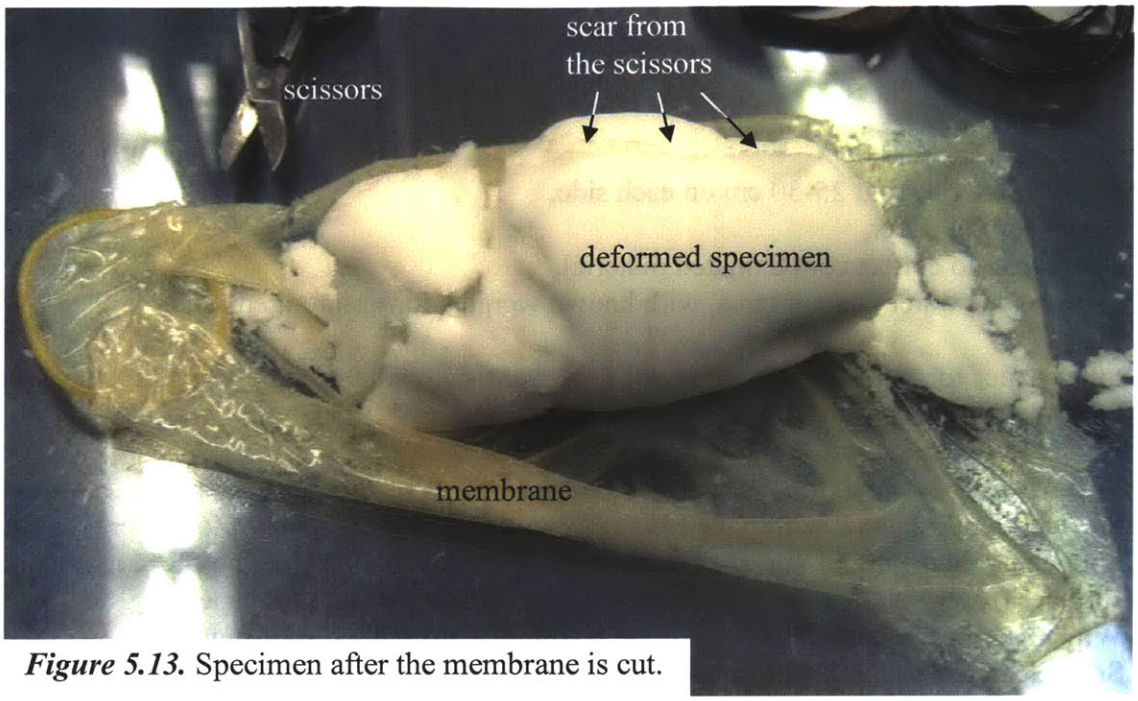

Figure 5.13. Specimen after the membrane is cut.

5.2.4.3.2. Opening up the Specimen in the Modified Setup

For the modified setup only;

1. Disconnect the connection between the standpipe and the spiral tube of the top cap.
2. Slide the o-rings around the tensiometer down, but not off the membrane.
3. Place and tighten a second piston clamp at the tip of the piston shaft.
4. Turn the entire triaxial cell upside down and balance it on the newly placed piston clamp. For the steps in which the cell is upside down, the instructions will use "towards the base" and "away from the base" instead of "up" and "down", to avoid confusion. The help of a second operator will be required for some of the following steps.
5. Remove the toilet paper in the gap between the top cap and the load cell.
6. Unfold the rolled portion of the membrane away from the base, over the two o-rings, and into the gap between the top cap and the load cell.
7. Slide the o-ring further from the base into the gap between the top cap and the load cell. Pass the rolled portion of the membrane through this o-ring toward the base.
8. Repeat the process with the second o-ring on the top cap, freeing the top cap – end of the membrane from both o-rings.
9. Unscrew and remove the nuts of the bolts fixing the superstructure to the base.
10. Unscrew and remove the nut of the tensiometer.
11. One operator holds the tensiometer body with one hand, the top cap with the other. The other operator lifts the base with one hand while guiding the tensiometer's cable through the hole in the base with the other. The result of this step is removal of the base while everything else remains in place.

12. The second operator holds the superstructure with the hand that was holding the base. The first operator holds the porous stone of the top cap from outside the membrane with the hand that was holding the top cap.
13. The first operator pulls out the stone, the specimen and the tensiometer while keeping the specimen intact, and lays them on their side onto the glass plate.
14. Collect the porous stone and nylon filter.
15. Cut the membrane along the length of the specimen, with minimal disturbance to the specimen. Start from the rolled portion, and cut all the way to the o-rings around the tensiometer. Then cut it around most of the circumference of the tensiometer, parallel to the o-rings.
16. Peel the membrane from this cut to the sides.

5.2.4.3.3. Separating Potential Contamination

The potentially contaminated material comprises the parts that have touched the membrane, nylon filters, or the scisors. The scoop and the spatula should be wiped with toilet paper after every step in which they are used on potentially contaminated material.

1. Cut off the 5 mm that was closest to the top cap off the specimen.
2. For the standard setup, repeat the previous step for the bottom end. For modified setup, pull and separate the tensiometer from the specimen.
3. Use the scoop to collect the material immediately around the trace made by the scissors. Put it into the container of potentially contaminated material.
4. Scrape 1-2 mm off the lateral surface of the specimen using the spatula or the scoop (*Figure 5.14*). Do not roll the specimen. For the side it lies on, use the spatula to carve as much as possible under it.

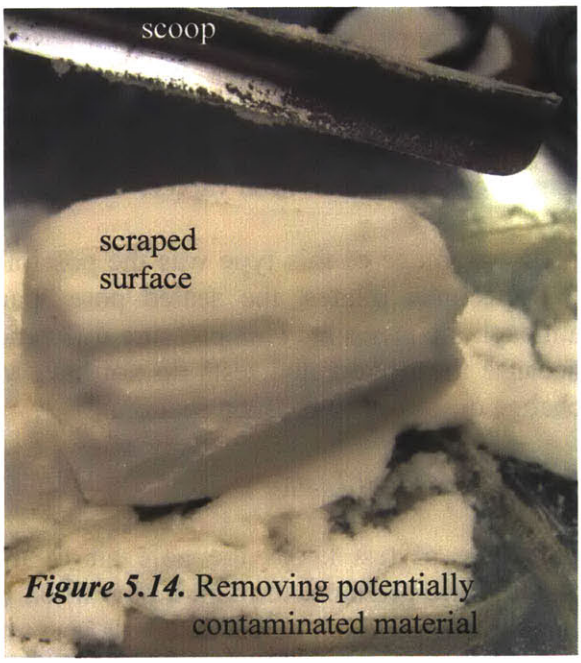

Figure 5.14. Removing potentially contaminated material

5.2.4.3.4. Collect Clean Material

1. Slice the remaining part into three using the spatula.
2. Place each portion into a tare. For the modified setup, scrape the material that was stuck to the face of the tensiometer into the same tare as the bottom portion.
3. For unsaturated tests, label and determine the mass of each of them.
4. Put the tares into the laboratory oven (110 °C). Wait for 24 hours.
5. Take the tares out of the oven and into a dessicant jar. Wait for 30-60 minutes so that the tares cool down to room temperature.
6. For unsaturated tests, determine the mass of the tares and calculate water contents for the top, middle, and bottom parts of the specimen.

7. Check each tare for contamination. Using the scoop, shuffle the material in the tare and destroy any structure caused by oven-drying. Then, shake the tare gently (without spilling out the material). If the material has a planar top surface and particles are freely flowing or rolling around, it is considered clean and can be reused. If the particles stick together and exhibit snow-like behavior as if they are moist, pendular rings of oil are holding them together, therefore they are contaminated and should be discarded.

5.2.5. Summary of Procedure Differences Among Test Types

For this section, the *saturated* tests will be the basis to which the procedures of other test types are compared, because the saturated setup has the most complicated procedure and uses almost all components of the triaxial testing equipment. The setup illustrated in *Figures 4.8* and *4.9* is the setup for *saturated* tests.

5.2.5.1. Sealed Tests

This was the procedure for the earliest unsaturated tests. Surfaces of the top cap and pedestal are covered with nylon wrap, sealing the specimen. This also removes all parts of the setup that are associated with the pore water from the procedure. These parts include: all water pipes to the top cap and the pedestal; the pore pressure transducer; the pore PVA; and transducer, top and bottom valves.

A disadvantage of this type was the possibility of inaccuracy with volume deformations. If the specimen dilates, the sealed pore space will have smaller pressure then the initial atmospheric pressure. This pressure difference would be unaccounted for in the calculations, because the unsaturated tests do not have volume measurement. This led to the procedure change described in the next section.

5.2.5.2. Unsealed Tests

This type of test keeps the pore air of the specimen connected to a water reservoir at atmospheric pressure, through a pipe filled with air. This connection is through both the top cap and the pedestal, as the reservoir is connected to the pipe that connects to the pore PVA in *saturated* tests. In this type of test, the pore PVA, pore pressure transducer and the transducer valve are not used at all. The possible disadvantage of the *sealed* tests was negated by "sealing" the pore air with a phreatic water reservoir.

5.2.5.3. Tensiometer Tests

These tests use the modified setup, in which a generation 7 MIT tensiometer replaces the pedestal, the bottom porous stone and nylon filter, pore pressure transducer, transducer valve, and bottom valve. These tests use the "sealing" method of the *unsealed* tests, which means that the pore PVA is replaced by an open water reservoir, connected to the top cap through a pipe filled with humid air.

5.3. Measurement Procedures

5.3.1. Optical Profiling

An optical vernier is used for the cross-section area measurements before and after a test. Both vertical and horizontal axes have a fixed scale with markings every 0.02 inches (0.5 mm). Across each scale there is a set of 20 markings, which move with the vernier, distributed over the span of 19 markings of the fixed scale. This provides the measurements on both axes with a resolution of 0.001 inches (25 μm). The number on the fixed scale immediately before the "0" mark on the moving gradations is the coarse part of the reading. Whichever of the moving gradations match any marking on the fixed scale is the fine part of the reading (*Fig.5.15*). The resulting measurement is:

$$measurement = coarse + fine \qquad Eq.5.3.$$

The procedure for mapping the specimen geometry using this instrument is as follows:

1. Set the instrument so that its objective lens is about 10 cm away from the specimen, aiming at its edge.
2. Pull the eyepiece to its full length. Focus the hairlines in the view by rotating the eyepiece.
3. Looking through the eyepiece, move the entire instrument to focus the view (it must be noted that the lenses invert the image in both directions, so up in the eyepiece view is down on the specimen, and left in the view is right on the specimen). First, move sideways to locate sight of the side of the specimen. Then, move toward or away from the specimen to focus it into view. With good lighting, the image can be focused enough to distinguish the outline of individual grains. The very

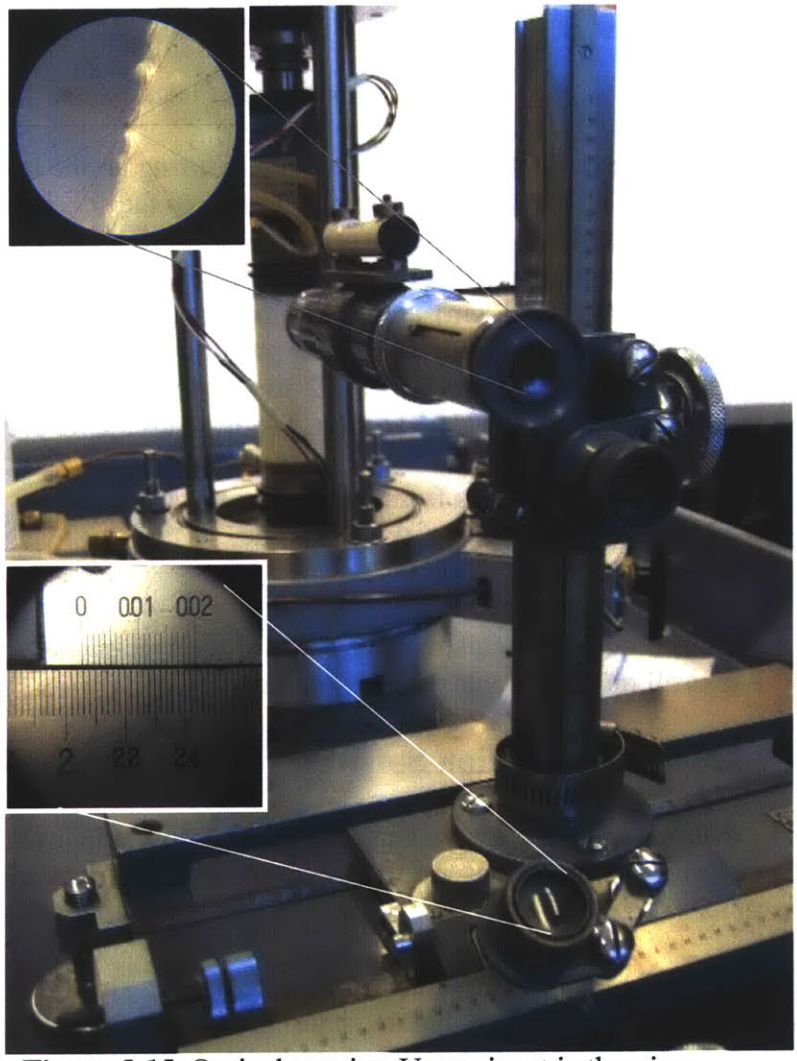

Figure 5.15. Optical vernier. Upper inset is the view throught he eyepiece, lower inset is the view through the monocle on the ruler - reading 2.04 + 0.017 = 2.057.

edge of the specimen is the target of focusing. If any other point on the specimen is targeted, the edges of the specimen will be fuzzy because the edges are farther away from the instrument, compared to the rest of the specimen surface.

4. Bring the instrument to level by adjusting the height of the four screw-legs and watching the circular water gauge on the base platform. The weight of the instrument should rest equally on all four legs (which is tricky compared to a three-leg setup).
5. Level the optical tube, watching the water gauge on it.
6. Looking through the eyepiece, traverse the length of one side of the specimen. Locate the top and bottom ends of the specimen and note their elevations.
7. A point measurement at a given level is taken by aligning the cross-hairs exactly to the edge of the spcimen and recording the lateral measurement. The diameter measurement at a level is the difference between the point measurements from each side of the specimen at the same level. The area measurement at a level is taken by the use of two diameter measurements at the same level, from two different orientations that are perpendicular to each other on the horizontal plane. From the equation for the area of an ellipse, the area measurement is:

$$Area = diameter1 \times diameter2 \times \frac{\pi}{4} \qquad Eq.5.4.$$

   It should be noted that, as opposed to measuring at one level at a time, it is much easier to first collect all measurements from one side of the specimen and then the other, and finally move the vernier to change the orientation.
8. For the measurement before the test, area measurements at three levels are taken: 0.2 to 0.4 inches (0.5 to 1 cm) below the top end, 0.2 to 0.4 inches (0.5 to 1 cm) above the bottom end, and the middle. For the profiling of the deformed shape, measurements were taken at elevation intervals of 0.2 to 0.4 inches (0.5 to 1 cm), possibly with an extra measurement at the widest section. For measurements at multiple elevations like these, it is more convenient to:
   - take all measurements from one side of the specimen,
   - take all measurements of the other side,
   - rotate the triaxial cell by 90°,
   - refocus the view,
   - take all measurements from one side of the specimen,
   - take all measurements of the other side.

5.3.2. Data Acquisition Software

The data acquisition program runs under Microsoft Windows, and is user friendly. Among its capabilities, the ones that are useful for an ordinary data acquisition task will be explained here.

The "Tasks" menu has an option to "Create Task". This brings out an input window in which task name, waiting time before starting, number of readings (upto 1000), time interval between readings and data channels to be read (all data sockets in the labs have numbers on them indicating their number) are entered. Entering this information and clickking OK starts a task of data acquisition from the selected channels.

The main screen lists all current tasks. For each task, it displays name, status (running, standing by, or completed), channels, time interval, "missed/read/total" number of data points. Double-click on the last column of a task displays upto 1000 readings in tabular form in a new window. Double-click on the "time interval" column brings out an input box asking the waiting time before starting, number of additional readings and time interval between readings – in case the data collection scheme needs to be changed while the task is running. Double-click on the "channels" column opens a window in which each channel number is displayed with its current reading, updated once per second, to act as a voltmeter.

In order to save data while the task is still running, select the task in the main screen, and click on the "S" button at the lower right corner of the screen. If a task is no longer needed (because the experiment is completed), selecting the task in the main screen, and selecting "Retire Task" form the "Tasks" menu saves the data and closes the task. The data saved by either means is stored in tabular form in a ".dat" file with the same name as the task, in the program's directory. This file can be opened in MS Excel and the data can be processed.

5.4. Data Processing

Data acquisition and conversion of the acquired data into engineering units was discussed in *section 4.6*. As mentioned earlier in *section 2.8.1.1*, lengths are in cm, forces are in kgf; therefore pressure and suction terms are in kgf/cm^2. For each data point, this results in the raw measurement of the following set of quantities:

- Time
- Axial displacement (ΔH).
- Volume change (ΔV), in saturated tests only.
- Axial load reading (F_{read}).
- Cell pressure (σ_{cell}).
- Pore pressure (u), in saturated tests only.
- Matric suction ($u_a - u_w$), in unsaturated tests with tensiometer.

Additionally, measurements that were described in prior sections of this chapter are:
- Initial specimen height (H_o).
- Initial diameter (D_o) and area (A_o).
- Initial volume (V_o).
- Dry mass of specimen (m_{dry})
- Final deformed profile of the specimen, in which the height with the maximum cross-section area is considered as the final area of the specimen (A_f).

The apparent final volume of the specimen $(V_f)_a$ can be calculated using the final deformed profile measurements. The specimen is approximately composed of slices in the shape of truncated cones, each slice being between two levels of optical measurement (see *Appendix 5.1* for the derivation of relevant equations).

The initial void ratio (e_{ini}) is calculated from the phase relations and using the specific gravity of the specimen (G_s) as:

$$e_{ini} = \frac{m_{dry} \cdot V_o}{G_s} - 1 \qquad \textit{Eq. 5.5}$$

5.4.1. Strains

All strains used in the calculations are Eulerian (engineering) strains. These are

$$\varepsilon_x = \Delta H / H_o \qquad \varepsilon_v = \Delta V / V_o \qquad \textit{Eqs. 5.6}$$

where ε_x is axial strain and ε_v is the volumetric strain. For consolidation, H_o and V_o are the initial values; for shear, they are the values at the start of shearing (a.k.a. pre-shear values).

5.4.2. Corrections

For the calculation of stresses from the measurements listed above, area and membrane corrections must be applied. There is no piston correction because the load cell is below the piston in MIT triaxial setups, as opposed to the commercially widespread external load sensors.

5.4.2.1. Standard Area Correction

The area of a specimen decreases during isotropic compression. The relevant measured quantities are axial force, specimen volume and height. Calculation of stress in the axial direction requires re-computation of the cross-sectional area at each data point because, for isotropic compression (as well as other types of consoidation loading), the specimen is assumed to remain a cylinder. With this assumption, the area of the specimen (A_c for cylindrical) can be calculated through geometry as follows:

$$A_c = \frac{V}{H} = \frac{V_o \cdot (1-\varepsilon_v)}{H_o \cdot (1-\varepsilon_x)} = A_o \cdot \frac{1-\varepsilon_v}{1-\varepsilon_x} \qquad \textit{Eq. 5.7}$$

During shearing, a triaxial specimen bulges and increases its cross - sectional area. Similar to the case of isotropic compression, during shearing the area must be re-calculated for every data point. To approximate the bulging, the specimen is assumed to be the rotational body of a parabola. By equating the rotational integral of such a parabola to the volume of the specimen, the maximum cross-sectional area (A_p for parabolic) at any given strain can be calculated as:

$$A_p = \frac{A_o}{16} \cdot \left(\sqrt{30 \cdot \frac{1-\varepsilon_v}{1-\varepsilon_x} - 5} - 1 \right)^2 \qquad \textit{Eq. 5.8}$$

The derivation of *Eq.5.8* is *Appendix 5.2.* Changing the area in this manner always results in a significantly larger area and smaller axial stress, compered to the uncorrected case.

5.4.2.2. Modified Area Correction

After the first few tests, it became clear that the specimen does not deform as a parabola during shearing. As asserted by Oda (1972[1]) and discussed in *section 6.2.1.2*, the bulging concentrates in the center. The parabolic area correction (*Eq.5.8*) uses the total volume and height in its calculations, therefore, it underestimates the maximum cross-sectional area by being unable to consider the concentration of deformation in the center of the specimen.

The final measurements of an experiment include optical measurement of specimen diameter. The area (A) at each data point is calculated by proportionally increasing the areas calculated by the parabolic correction, as follows:

$$A = A_p \cdot \frac{A_f}{A_{pf}} = area\ multiplier \times A_p \qquad Eq.\ 5.9$$

where A_{pf} is the area calculated with the parabolic correction for the end of the test, and A_f is the maximum cross-sectional area measured after the test. The ratio, which is named "area multiplier" was between 1.24 and 2.43 through all tests conducted during this research (*Table 6.2*).

5.4.2.3. Standard Membrane Corrections

The impermeable membrane that separates the specimen from the cell fluid adds some resistance to applied forces and pressures. Therefore, all the computed stresses are stresses carried by the specimen plus the membrane. Hence, they must be corrected to account for the contribution of the membrane, which must be subtracted from them.

In the following equations, $\boldsymbol{K_m}$ is the stiffness of the membrane, which is the product of the modulus of elasticity of latex and the area of membrane's cross-section. For a single thin membrane used in this research, its magnitude is ***1.3 kgf***, as noted earlier in *section 4.3.5*. It is also worth reminding the reader that the strains are positive in compression, negative in extension.

In the axial direction, the membrane is assumed to act as an elastic material, carrying more force with increasing strain. The force carried by the membrane (F_m in *Eq.5.10*) must be substracted from the measured axial load.

$$F_m = K_m \,.\, (\varepsilon_x + 2/3\ \varepsilon_v) \qquad Eq.5.10$$

In the radial direction, the membrane provides additional confinement, resisting the radial displacement more as the specimen expands. This translates into a radial pressure as an addition to the cell pressure, which is

$$\sigma_m = \frac{K_m}{A} \cdot \frac{-\varepsilon_v}{3} \qquad Eq.5.11$$

As volume change is not measured in unsaturated tests, ε_v is assumed to be zero for the purpose of membrane correction, in the light of the minuscule volumetric strains measured in the saturated experiments.

5.4.2.4. Axial Modification to Membrane Correction

While setting up the equipment in preparation for an experiment, the operator is bound to stretch the membrane. This stretching in the axial direction imposes an additional axial stress, unique to the preparation procedure used for this research. The membrane corrections should be modified in accordance.

The initial axial strain of the membrane is measured by the following procedure:

- Follow the setup procedure upto the point of stretching the membrane over the mold.
- Mark the membrane from the inside with an inkpen, at the top edge of the mold (top of the specimen) and the top edge of the bottom porous stone (bottom of specimen).
- Take the membrane out of the setup.
- Measure the distance between the markings. This is the initial membrane height (H_{mo}).
- For each operator, repeat the process multiple times and take the average for a more representative assessment.
- In the tests by a particular operator, the mebrane is prestressed (in tension) by

$$\varepsilon_{mx} = 1 - \frac{H_o}{H_{mo}} \qquad \textit{Eq. 5.12}$$

which is a negative quantity, as compression is in the positive direction. This is a novel correction factor.

Initial axial strain of the membrane during setup (ε_{mx}), which depends on the operator, is between 3% (for the author) and 7% (for Naeem Abdul-Hadi). 5% was used for the tests with uncertainity of which operator stretched the membrane during a setup. For more discussion on operators and a list of which test was done by which operator, see *section 6.1.2*.

Finally, the axial strain in *Eq 5.10* is replaced by ($\varepsilon_x + \varepsilon_{mx}$) for the calculation of membrane correction onto the axial force. This is a simplified solution; the exact version would require calculating the strains for all data points using H_{mo} instead of H_o, but doing so only when calculating the membrane correction. Compared to the ±1 mm precision of each pen marking on the membrane, this simplification is sufficiently accurate.

It should be noted that this modification is applicable only to the experiments prepared by the procedures described in this chapter. Standard clay testing (and some sand testing) procedures roll the membrane over the specimen, rather than stretching it, eliminating ε_{mx}.

5.4.2.5. Radial Modification to Membrane Corrections

The diameter of the membrane is smaller than that of the specimen. This results in a built-in increase in the confining pressure for all types of triaxial cells. In order to incorporate this in

the calculations, the perimeter of the membrane (P_m) is measured (10.6 cm), and the initial volume strain of the membrane (ε_{mv}) is described by the ratio of the areas of the specimen and a circle bound by the membrane, resulting in the following expression

$$\varepsilon_{mv} = 1 - \frac{A_o}{\left(\frac{P_m^{\,2}}{4\pi}\right)} \qquad \textit{Eq. 5.13}$$

which is a negative quantity for all experiments conducted in this research. This correction was also proposed by Berre (1985).

Similar to the axial modification, the volumetric strain in *Eq 5.11* is replaced by ($\varepsilon_v + \varepsilon_{mv}$) for the consideration of membrane correction in the radial stress calculations. This, too, is a simplified solution in comparison to the more exact alternative of using $P_m^2/4\pi$ instead of A_o for calculating the membrane correction.

Even though ε_v is deemed negligible in the unsaturated tests, membrane correction due to ε_{mv} is still applied because it is a known and significant magnitude.

5.4.3. Stress Calculations

Applying the membrane correction to the axial force, modified as described in the previous section, results in the following corrected axial force:

$$F = F_{read} - F_m = F_{read} - K_m \cdot \left[\left(\varepsilon_x + \varepsilon_{mx}\right) + \frac{2}{3} \cdot \left(\varepsilon_v + \varepsilon_{mv}\right) \right] \qquad \textit{Eq. 5.14}$$

where ε_{mx} and ε_{mv} are described by the equations *5.12* and *5.13*, respectively. In order to calculate the axial stress, the corrected axial force is divided by the specimen area that is also corrected (in accordance to *section 5.4.2.2*). Cell pressure, which acts hydrostatically on everything (even the load cell), is added for the axial stress:

$$\sigma_x = \frac{F}{A} + \sigma_{cell} \qquad \textit{Eq. 5.15}$$

As mentioned in *section 5.4.2.3*, stress in the radial direction is the cell pressure, with a membrane correction. From *Eq.5.11* and *section 5.4.2.5*, the corrected stress can be expressed as such:

$$\sigma_r = \sigma_{cell} + \sigma_m = \sigma_{cell} - \frac{K_m}{A} \cdot \frac{\left(\varepsilon_v + \varepsilon_{mv}\right)}{3} \qquad \textit{Eq. 5.16}$$

In the form expressed above, both axial and radial stresses are total stresses. They are used for the results of unsaturated tests. In the case of saturated tests, they are converted into effective stresses via Terzaghi's effective stress principle:

$$\sigma'_x = \sigma_x - u \qquad \sigma'_r = \sigma_r - u \qquad \textit{Eqs. 5.17}$$

In the rest of this chapter, formulae are written in total stresses, but they all can be converted into effective stresses by changing all (σ)s to (σ′)s.

The stress space of choice is octahedral or mean stress (σ_{oct}) vs. shear (2q, so that it is not confused with q of p-q space). These can easily be calculated from the principal stresses of σ_x , σ_r , σ_r .

$$\sigma_{oct} = \frac{\sigma_x + 2 \cdot \sigma_r}{3} \qquad \textit{Eq. 5.18}$$

$$2q = \sigma_x - \sigma_r \qquad \textit{Eq. 5.19}$$

5.4.3.1. Confining Stress

The confining stress (σ_c) is an input to the triaxial control program. However this control is not as accurate as the measurements, because the computer uses more simplified versions of correction formulas. A more exact value of σ_c can be inferred at this point in calculations. Once the stress path of the experiment is plotted in σ_{oct} – 2q space, the intersection of the loading path (or its extrapolation) with the σ_{oct} axis is marked as the true σ_c (*Fig.6.2*). For comparison between tests at different stress levels, σ_{oct} and 2q are normalized by dividing them by the true σ_c.

5.4.3.2. Smoothening of Deviatoric Stress

When sheared, uniform glass spheres tend to undergo cycles of stress relaxation and rebuild-up (Anthony & Marone, 2005) as in *Fig.6.3*. When this happens, the stress-strain curve is "smoothened" by joining only the top portions of each cycles. This is explained and discussed in greater detail in *sections 6.2.1.1*, *6.2.2.1* and *7.1*.

5.4.4. Locating the Yield Stress and Strain

A common comparison between tests is based on the yield stress. The stress strain curves (see next chapter) have more or less elastoplastic overall behavior, without peaking at yield and with strain hardening upto a peak stress. As with other stress hardening materials, it is difficult to unambiguously define the yield stress. For this research, the maximum curvature point on the stress-strain curve (smoothened – see *Fig.6.3*) was used as a unique definition of yielding. The relative scale of the axes is recognized as important to the application, so it was necessary to unify all stress axes into normalized shear stress to remove the effects of stress level. More importantly, all axial strain scales are magnified by a factor of 20, without which maximum curvature would occur at the peak stress rather than the yield stress. This number is chosen to bring the strain axis to similar magnitudes as the normalized shear axis; it gives the same (or similar) scale on both axes of the stress-strain curves in *Chapter 6*.

To summarize, in this thesis, the yield stress is defined as the point with maximum curvature in the plotting of "normalized shear versus twenty times axial strain". For the remainder of

this section, the selected horizontal (transformed strain) and vertical (normalized shear) axes will be denoted by x and y for convenience. This means

$$x = 20 \cdot \varepsilon_x \qquad y = {}^{2q}/_{\sigma_c} \qquad \textit{Eqs. 5.20}$$

The test results are made up of the discrete points. Curvature calculations will require making finite difference approximations of partial derivatives. The approximations of

$$y_x = \frac{y_{i+1} - y_{i-1}}{x_{i+1} - x_{i-1}} \qquad y_{xx} = \frac{\dfrac{y_{i+1} - y_i}{x_{i+1} - x_i} - \dfrac{y_i - y_{i-1}}{x_i - x_{i-1}}}{\dfrac{x_{i+1} - x_{i-1}}{2}} \qquad \textit{Eqs. 5.21}$$

will be used in *Eq.3.1*, which is repeated here as *Eq.5.22*.

$$\kappa_{xy} = \frac{y_{xx}}{\sqrt{1 + y_x^{\,2}}^{\,3}} \qquad \textit{Eq.5.22}$$

Even though the curve is already a smoothened form of the actual data, there are some local perturbations. At those points, this approximation will give unrealistically high curvatures.

Figure 5.16. Locating yield strain for TX680.

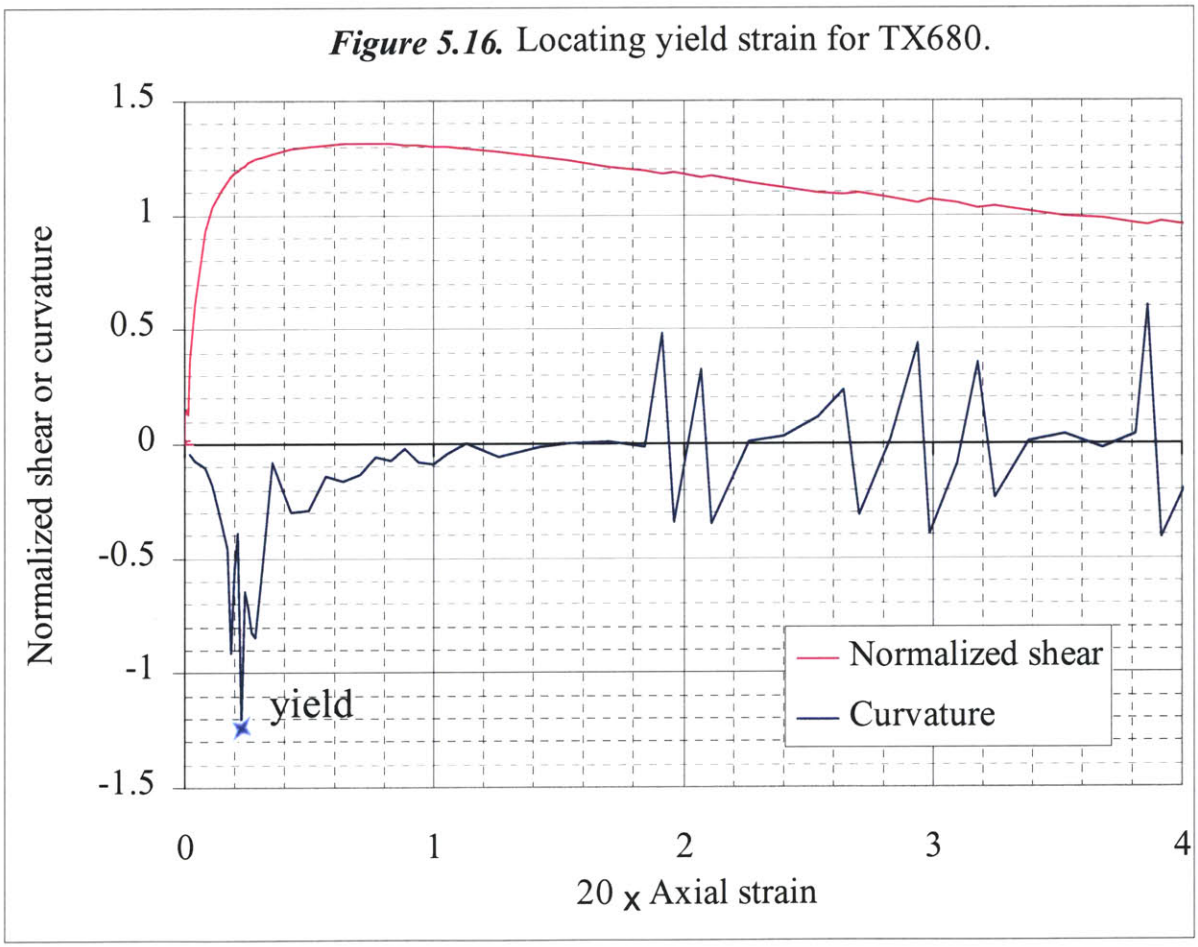

One way of avoiding this problem is basing the aproximation on more points than just the neighboring two points. Let the curvature obtained above be labeled $\kappa_{i\pm1}$, as it is solved using the i-1, i and i+1 th data points. For $\kappa_{i\pm2}$, only i-2, i and i+2 are used, while i-1 and i+1 are ignored. Averaging multiple such approximations to a single point's curvature should give a better result. Averaging 4 curvature approximations at each point is deemed enough for the purposes of this research. The smoothened curvature (κ_s) is therefore

$$\kappa_s = \frac{1}{4} \cdot \sum_{j=1}^{4} \kappa_{i\pm j} \qquad \textit{Eq.5.23}$$

The lowest (highest but with negative magnitude) curvature in the earlier stages of shearing is at the yield strain. There may be other large curvatures at large strains (*Fig.5.16*), but these signify localized fluctuations. The stress corresponding to the yield strain is the yield stress.

5.4.5. Work Calculations

Work done on the specimen is calculated separately as work done by axial load or deviatoric stress, and work done by radial stress. Both are calculated by numerically integrating axial force vs. axial displacement, and radial stress vs. volume change. The stress relaxations (*sections 5.4.3.2, 6.2.1.1, 6.2.2.1* and *7.1*) return energy into the system, therefore they must be included in the calculations. For this reason, the work integrations are on the entire data, not the smoothened curve.

$$W_x = \sum_i \left[\frac{F_i + F_{i+1}}{2} \cdot \left(\Delta H_{i+1} - \Delta H_i \right) \right] \qquad \textit{Eq. 5.24}$$

$$W_r = \sum_i \left[\frac{(\sigma_r)_i + (\sigma_r)_{i+1}}{2} \cdot \left(\Delta V_{i+1} - \Delta V_i \right) \right] \qquad \textit{Eq. 5.25}$$

Appendices

Appendix 5.1. Truncated cone slice volumes

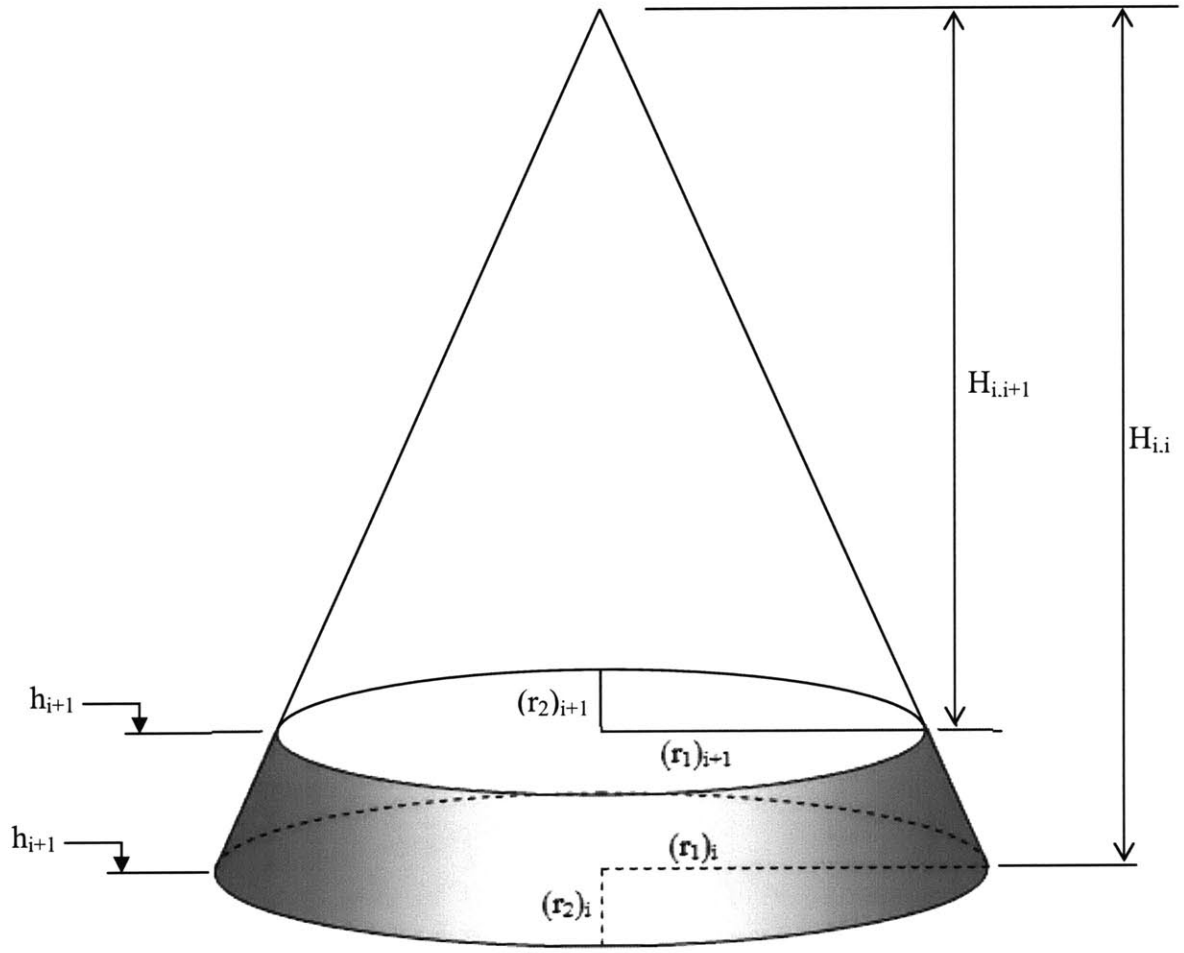

For i^{th} slice, where i is the index for elevaion of optical measurement of specimen diameter;

$r_i = \sqrt{(r_1)_i \cdot (r_2)_i}$, where r_1 and r_2 are optically measured radii in two orthogonal alignments;

$H_{i,j} = \left| \frac{h_{i+1} - h_i}{r_{i+1} - r_i} \right| \cdot r_j$, where j is either i or i+1, and h_i is the elevation of i^{th} measurement;

$V_i = \frac{\pi}{3} \cdot \left| {r_{i+1}}^2 H_{i,i+1} - {r_i}^2 H_{i,i} \right| = \frac{\pi}{3} \cdot \left| \frac{h_{i+1} - h_i}{r_{i+1} - r_i} \cdot \left({r_{i+1}}^3 - {r_i}^3 \right) \right|$, where V_i is the slice volume.

The sum of slice volumes give the apparent final volume $(V_f)_a$ as:

$\left(V_f\right)_a = \sum_{i=1}^{n-1} V_i$, where n is the number of optical measurement elevations.

Appendix 5.2. Parabolic area correction

$$x = f(y) = \sqrt{A/\pi} - 4y^2 \cdot \frac{\sqrt{A/\pi} - \sqrt{A_o/\pi}}{H^2} = \frac{\left(H^2 - 4y^2\right)\cdot\sqrt{A/\pi} + 4y^2\sqrt{A_o/\pi}}{H^2}$$

$$\pi x^2 = \frac{\left(H^2 - 4y^2\right)^2 \cdot A + 8y^2 \cdot \left(H^2 - 4y^2\right)\cdot\sqrt{A\cdot A_0} + 16y^4 A_0}{H^4}$$

$$\pi x^2 = \frac{16}{H^4} y^4 \left(A + A_0 - 2\sqrt{A\cdot A_0}\right) + \frac{8}{H^2} y^2 \left(\sqrt{A\cdot A_0} - A\right) + A$$

Volume expressed in terms of initial dimensions = volume of the rotational body

$$\frac{H_0 A_0}{2}(1-\varepsilon_v) = \int_0^{H/2} \pi x^2 dy = \frac{16H}{160}\left(\sqrt{A} - \sqrt{A_0}\right)^2 + \frac{H}{3}\left(\sqrt{A\cdot A_0} - A\right) + A\cdot\frac{H}{2}$$

$$A_0 \frac{(1-\varepsilon_v)}{(1-\varepsilon_a)} = \frac{1}{5}\left(\sqrt{A} - \sqrt{A_0}\right)^2 + \frac{2}{3}\left(\sqrt{A\cdot A_0} - A\right) + A$$

$$0 = A\cdot\left(\frac{1}{5} - \frac{2}{3} + 1\right) + \sqrt{A\cdot A_0}\left(\frac{2}{3} - \frac{2}{5}\right) + A_0\left(\frac{1}{5} - \frac{(1-\varepsilon_v)}{(1-\varepsilon_x)}\right) = \frac{8}{15}A + \frac{4}{15}\sqrt{A\cdot A_0} + A_0\left(\frac{1}{5} - \xi\right)$$

where $\xi = \dfrac{(1-\varepsilon_v)}{(1-\varepsilon_x)}$

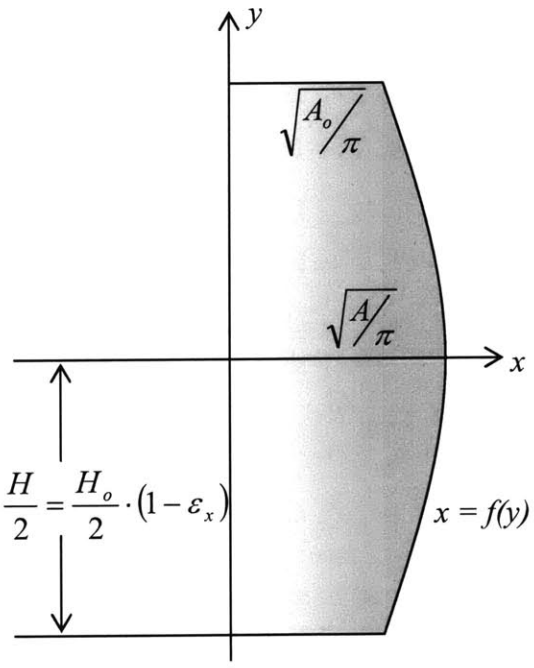

$$\sqrt{A} = \frac{-\frac{4}{15}\sqrt{A_0} + \sqrt{\frac{16}{225}A_0 - \frac{32}{15}\left(\frac{1}{5} - \xi\right)A_0}}{16/15}$$

$$\sqrt{A} = \frac{\sqrt{A_0 - 6A_o + 30\xi A_0} - \sqrt{A_0}}{4}$$

$$\sqrt{A} = \frac{\sqrt{A_0}}{4}\left(\sqrt{-5 + 30\xi} - 1\right)$$

$$A = \frac{A_0}{16}\left(\sqrt{30\xi - 5} - 1\right)^2$$

$$D = \frac{D_0}{4}\left(\sqrt{30\xi - 5} - 1\right) \quad \text{where} \quad \xi = \frac{(1-\varepsilon_v)}{(1-\varepsilon_x)}$$

6

EXPERIMENTS and RESULTS

6. EXPERIMENTS and RESULTS

This chapter details results of the experiments and observed effects of various procedurial parameters. There is no attempt to make connections between the results or to provide any interpretations with regards to the main ideas of the research. Nevertheless, the chapter contains essential information for the following chapters of interpretation and conclusion.

The naming convention of the ***model*** (for analytically estimating the effective stress increment due to suction - *sections 3.2* and *3.3*) and the ***hypothesis*** (inferring the effective stress increment due to suction, from the saturated and unsaturated shear strength envelopes – *section 3.4.2*) will continue in this chapter.

6.1. Specimen Properties

6.1.1. Sample Materials

In order to have the experiments closer to the calculations with spherical uniform particles in *chapter 3*, glass spheres were selected as the material to be tested. Two types of glass spheres were tested. These will be designated as Type 1 and Type 2 for the remainder of this thesis. Through an optical microscope, both materials were observed to contain smooth spheres. Moreover, post-experimental observations show that they preserve their shape and smoothness through testing, and do not undergo crushing, plastic deformation, or flattening of contacts (*Appendix 6.1*).

Drying SMC curves for both materials (*Appendix 6.2*) were obtained by the MIT technique (*section 2.2.2*) and fit the normal behavior of uniform glass sphere samples (Toker, 2002). As any other uniform material, the SMC curves distinctly show saturated, bulk drainage, and pendular regimes. In the low water content range (pengular regime), suction is highly sensitive to variations of water content, as expected of uniform materials. According to the model, unlike matric suction, effective stress and shear strength shall not have large sensitivity to water content.

6.1.1.1. Type 1 Glass Spheres

This material was processed from a mixture of glass spheres of various sizes and origins, found in the MIT Geotechnical lab from past research projects. A specific gravity of 2.43 (Sjoblom, 2000) indicate the composition to be a mixture of borosilicate (G_s=2.2) and soda-lime glass (G_s=2.57). The size range of 106-125 μm diameter was separated by sieving in the standard manner (ASTM-D6913), and was used as *Type 1* glass spheres in the tests.

Examination of the microscope photographs (*Appendix 6.1a* and *6.1b*), as well as additional sieving through 106 μm sieve, showed that the grains are not uniform and that there are particles smaller than the sieve size in the sample. This is speculated to happen due to the fact that the material was sieved through consecutive sieves (...180 μm, 150 μm, 125 μm, 106 μm,...). All particles that are supposed to be retained on a particular sieve are only slightly

larger than the sieve size. Such a particle can easily get stuck in the holes of the sieve, thus blocking the passage of smaller partices. This results in a significant amount of finer particles retained on every sieve.

6.1.1.2. Type 2 Glass Spheres

As the limited amount of Type 1 material was used up, a new batch of glass beads was purchased from MO-SCI Corporation. These are borosilicate glass beads with specific gravity of 2.2. The company used sieves of 125 μm and 80 μm size for separation of the purchased batch. Note that, due to the sieving problem mentioned above, this still did not mean all particles are larger than 80 μm. This material was repetitively sieved as described in *section 5.1.2*. The resulting 106-125 μm fraction is designated as *Type 2* glass spheres in the tests. The microscope photographs of this material (*Appendix 6.1c* and *6.1d*) show it to be a lot more uniformly sized than the *Type 1* spheres.

6.1.2. Specimen Repeatability

The preparation method described in *section 5.1.4* results in specimens of similar, but not always the same initial relative density and void ratio (these are interchangeable as noted in *section 2.8.3*). Even with a constant number of compaction layers and blows, the initial void ratio depends on both the initial moisture content and the operator. This is documented in

Table 6.1. Variability in specimen preparation.

Material	Test Type	Test No	compacting operator	wc_{ini} (%)	e_{ini}
Type 1	saturated	TX653	NKT	1.00	0.593
		TX654	NKT	1.00	0.568
		TX669	NKT	1.00	0.578
	sealed	TX663	NKT	1.00	0.604
		TX664	NKT	1.20	0.602
		TX674	NAH	0.98	0.581
		TX678	NAH	0.91	0.57
	unsealed	TX676	NAH	1.33	0.599
	incomplete	TX661	NKT	1.50	0.582
Type 2	saturated	TX680	NAH	1.54	0.652
		TX685	NAH	1.41	0.654
		TX692	NAH	3.03	0.628
		TX684	*NKT*	*1.20*	*0.691*
	Tensiometer	*TX686*	*NKT*	*2.50*	*0.688*
		TX687	NAH	1.76	0.656
		TX688	*NKT*	*3.05*	*0.669*
		TX690	*NKT*	*3.50*	*0.632*
	sealed	TX681	NAH	1.16	0.662
	unsealed	TX682	NAH	1.08	0.653
		TX683	NAH	1.35	0.666

The two operators who have prepared the specimens are Naeem Abdul-Hadi (NAH) and the author (NKT). Colors and fonts are coded in parallel to *Figure 6.1*.

Table 6.1 and illustrated in *Figure 6.1*. In all cases, the void ratios are within the boundaries of the densest and loosest possible uniform configuration, which have void ratios of 0.35 and 0.91, respectively (*Table 3.1*).

Table 6.1 lists the triaxial shear tests, including one (namely TX661) that did not produce any useful shear results, in order to document the variability in specimen preparation. The procedures of the four main test types are detailed in *section 5.2* (see *section 5.2.5* for summary of differences).

Without any other consideration, void ratios of Type 1 glass spheres has an average of 0.586 and standard deviation of 0.014; whereas for Type 2, the average is 0.659 and the standard deviation is 0.020. Most of the experiments on Type 1 are the early tests when the procedure was being devised and the operators were learning, so some scatter is expected. Type 2, on the other hand, shows a clear dependency of the initial void ratio to the operator and a trend of densification with increasing preparation water content (*Fig.6.1*). Variation in the void ratio can affect the results significantly, by changing both the saturated material strength, and the contribution of suction to it. The effects of initial void ratio variation will be discussed later in the thesis.

Fig. 6.1. Variability in specimen preparation

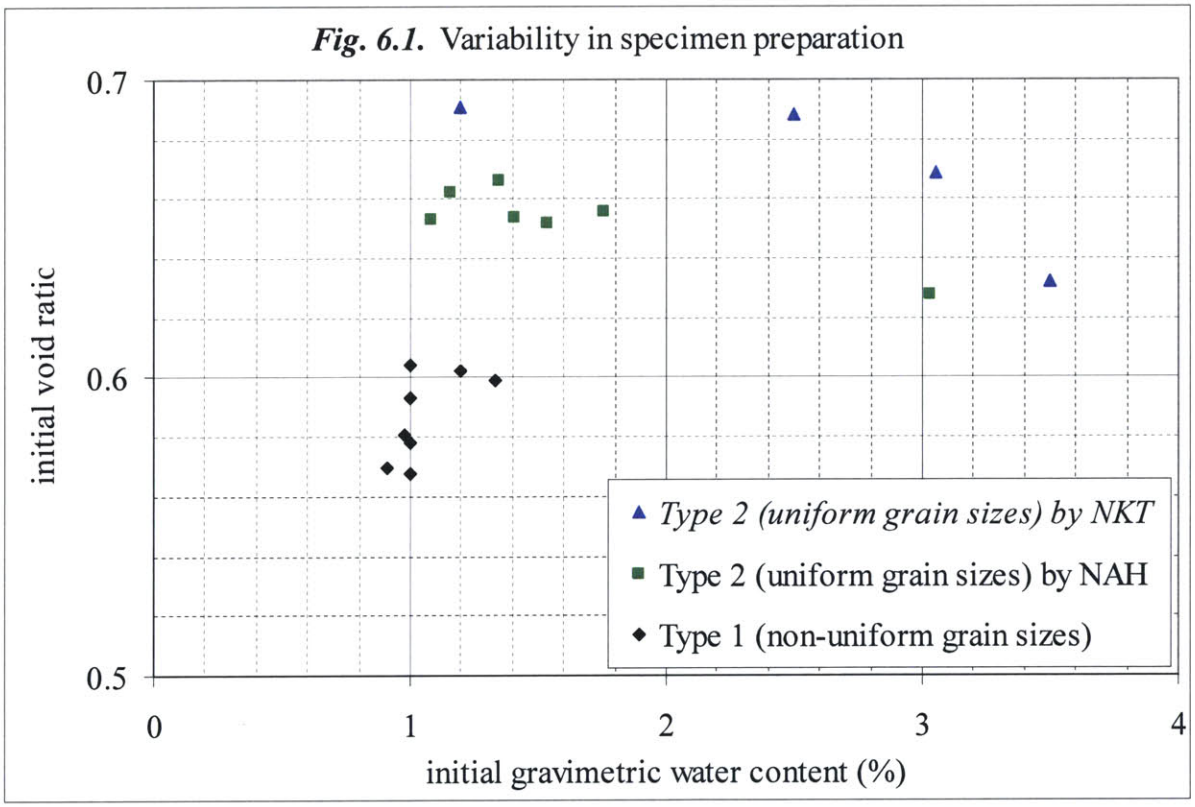

6.1.3. Estimate for the Effective Stress Increment due to Water Forces

For the materials described above, the effect of suction on effective stress can be estimated before the experiments, within the framework discussed in *Chapter 3*. Comparing the void

ratios of the specimens of both types of materials to those listed in *table 3.1*, the packings are inferred to be between body-centered cubic and cubic, but are much closer to the body-centered cubic. From *figures 3.12* and *3.13*, this gives a $(\sigma'-\sigma).r$ of about 120 Pamm. When divided by the average particle radius of 0.058 mm, the resulting effective stress increment is 2000 Pa, which is approximately equal to 0.02 kgf/cm^2. Note that this value may be slightly higher in Type 1 material (0.02 to 0.025 kgf/cm^2) because of a greater coordination number due to variation of sizes of this material's grains.

6.2. Triaxial Test Results

The samples were subjected to CIDC (isotropically consolidated drained) triaxial compression tests under both saturated and unsaturated conditions. In each test, the specimen was first isotropically consolidated, and then sheared by increasing axial load (see *Appendix 6.3* for stress paths). All stress quantities, indicated as "normalized" in the rest of the thesis, denote division by the total radial stress, which is also the total isotropic consolidation stress. Deviatoric stress (2q), sometimes normalized, is used as the measure of shearing, complementing the axial strain axis in the stress-strain curves.

Table 6.2. is a list of all triaxial tests, with corresponding measurements of quantities that are not observable in the graphs presented throughout this chapter. The tests are divided into four types: saturated, sealed, unsealed, tensiometer. The three latter types are all for unsaturated tests.

A ***confining pressure*** is specified by the operator in every test, as an input to the triaxial control computer program. However, the cell pressure control is not very precise without correct area and membrane corrections, missing the desired value by upto 0.05 kgf/cm^2. As an additional effect, this minor imprecision slightly disturbs the isotropy of the initial compression. The real confining pressure (σ_c) values are inferred from the extrapolation of measured stress path to the horizontal axis (as in *Figure 6.2*), rather than direct control (see *section 5.4.3.1* for more detail). ***Initial void ratio***s are determined from the solid mass and initial volume, each of which are determined as described in *sections 5.1.4* and *5.3.1*. ***Apparent final volumetric strain*** is calculated from the apparent final specimen volume, which is obtained (beginning of *section 5.4* and *Appendix 5.1*) by optically profiling the post-shear deformed geometry in two directions (*section 5.3.1*). The difference between the apparent and measured final volumetric strains is less than 1% in all cases of saturated tests (unsaturated tests don't have volumetric strain measurements). The ***area multiplier*** is the ratio of maximum cross sectional area of the deformed specimen to the maximum specimen area estimated by the parabolic approximation at the end of the test (the area multiplier is always greater than 1, as bulging is concentrated to the center - see *sections 5.4.2.2* and *6.2.1.2* for details). Area multipliers of tests without reliable post-shear profile measurements were assigned by averaging within their group of tests (e.g. the area multiplier for TX680 is the arithmetic average of TX 684, 685 and 692). ***Final void ratio*** is computed using the final measured volumetric strain, which is measured by the change in pore water volume in saturated tests.

Table 6.2. List of triaxial tests.

Material	Test Type	Test No	σ_c (kgf/cm^2)	Optically measured			PVA LVDT		final water contents (gravimetric, %)		
				$e_{initial}$	ε_{vfinal} (%) (apparent)	Area multiplier	ε_{vfinal} (%) (measured)	e_{final}	top	middle	bottom
Type 1	saturated	TX653	0.97	0.593	1.99	1.2796	1.78	0.621			
		TX654	1.64	0.568	1.58	1.2422	1.85	0.597			
		TX669	2.61	0.578	-0.29	1.7904	0.69	0.589			
	sealed	TX663	1.01	0.604	5.36	1.6310				0.28	
		TX664	1.64	0.602	3.57	1.6595				0	
		TX674	2.50	0.581		1.64*				0.46	
		TX678	0.486	0.57		1.64*				1.43	
	unsealed	TX676	1.60	0.599	3.45	1.5942				1.11	
	incomplete	TX661		0.582						0.85	
Type 2	saturated	TX680	1.01	0.652		1.31*	2.62	0.695			
		TX685	1.74	0.654	2.05	1.2547	2.83	0.701			
		TX692	2.53	0.628	0.75	1.3739	-0.36	0.622			
		TX684	2.49	0.691	2.57	1.3015	1.98	0.724			
	Tensiometer	TX686	1.72	0.688	10.8 #	2.427 #			4.4	2.48	2.62
		TX687	3.48	0.656		1.77*			1.24	1.32	1.47
		TX688	1.73	0.669	2.4	1.3118			2.69	2.69	2.88
		TX690	1.73	0.632	4.4	1.5710			3.39	3.38	7.49
	sealed	TX681	0.96	0.662	4.57	1.5047					
	unsealed	TX682	0.99	0.653	4.66	1.5884				0.78	
		TX683	2.47	0.666	1.09	1.2951					

*: Because the specimen was unintentionally disturbed while dismantling the setup, optical profiling at the end of test was not possible. Therefore area multipliers were assigned to be equal to the mean value within the same type of tests on the same material

#: Possibly erroneous optical measurement due to unnoticed specimen disturbance in the end. specimen. Differences in the experimental procedures of these types of tests are summarized in *section 5.2.5*. There is also a test designated as "incomplete", which did not succeed beyond the preparation phase due to some electrical problems.

Yield stress and strain are identified as the point of maximum curvature in a plot of normalized deviatoric stress vs. 20 times axial strain, as detailed in *section 5.4.4*. Both yield and peak values are based on deviatoric stress. Deviatoric stresses and axial strains at both yield and peak are tabulated in *Appendix 6.4*.

6.2.1. Saturated Tests

There are some features and aspects of behavior that are common in all saturated tests. These will be examined within the context of the results of one of the tests (TX653), but they occur similarly in all tests.

As shown in *Figure 6.2*, first the confining stress of $\sigma_2 = \sigma_3 = \sigma_c$ is applied, sometimes (as is the case in this example) with slight deviatoric stress. Both types of materials can carry shear stresses upto large fractions (more than half) of their strength without much deformation (*Figure 6.3*). Yield strains are in the range of 0.56-1.13 % (*Appendix 6.4*). After yielding, the material behaves plasticly and the general stress level does not vary much, except for the

cycles of stress drops (see *section 6.2.1.1*). A little strain-hardening occurs after yielding up to a peak stress, and then continues its plastic behavior with slight softening. The axial strain at which peak stress is observed varies a lot, depending on the material and whether it is a saturated test or not (*Appendix 6.4*). For saturated tests on Type 1 material it is 5.93 to 7.35 %, whereas in for Type 2 it varies between 2.11 and 5.43 %.

Figure 6.2. Stress path for TX653

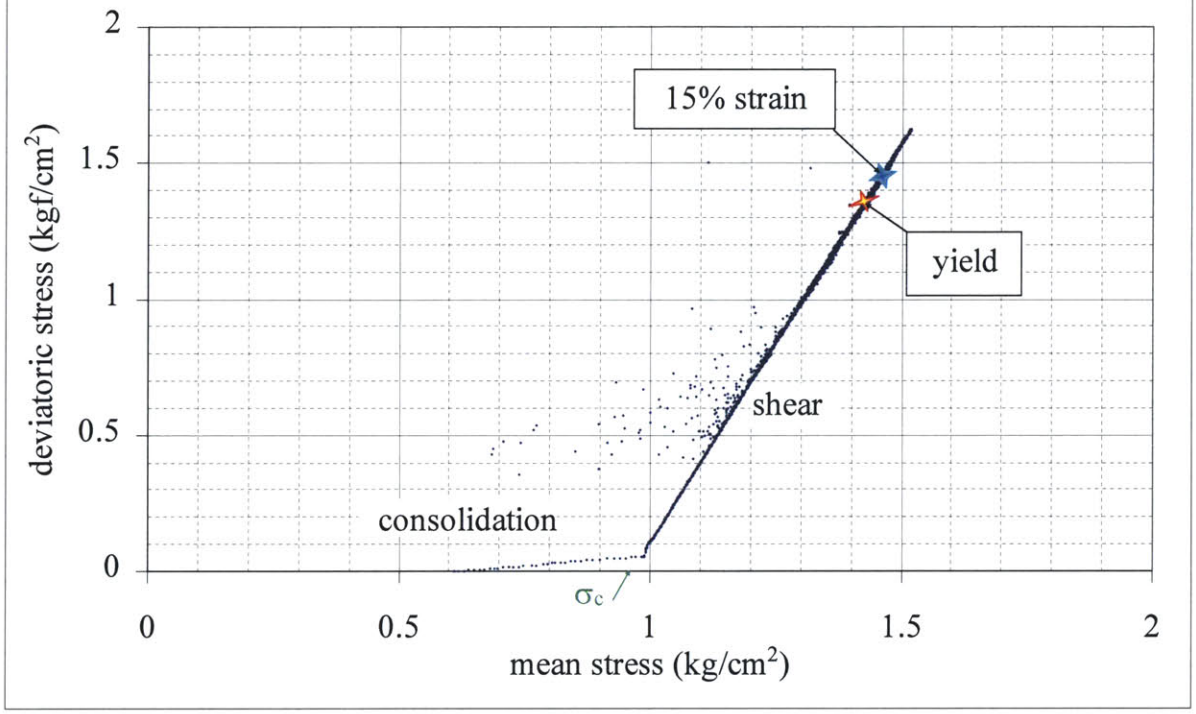

6.2.1.1. Stress Drops

According to *Figure 6.3.a*, starting from around - but not necessarily exactly at - the yield point, the specimen undergoes cycles of sudden relief of deviatoric stress every 0.2 to 0.3 % of axial strain (less than two times the particle diameter). From a point of view, such a loss of strength at its first occurence could have been assumed as the yielding point. However, such a definition of yielding would not be consistent through the tests, given that on several tests the stress drops started after significant plastic deformation.

A closer examination of the stress drops (*Fig.6.4*) reveals that they each resemble a miniature elastoplastic stress-strain curve. The data points corresponding to low stresses during a stress drop cycle constitute a scatter of points on the left side of the stress path in *Figure 6.2*. Each sterss drop causes the stress state to jump from the imposed stress path (solid line with slope of 3:1 in the *Fig.6.2*) to one of the scattered points.

The stress drops are drastic enough for the specimen to emit audible crunching sounds. At the time of each stress drop, a momentary excess pore pressure of 0.02 to 0.5 kgf/cm^2 was recorded (*Fig.6.4*), as well as a sudden drop of 0.02 to 0.1 % in volume (*Fig.6.5*). It must be noted that the pore pressure measurements at exactly the jump are probably inaccurate, because the data acquisition system was not designed to record such rapid changes.

Figure 6.3.(a) Stress-strain curve for TX653

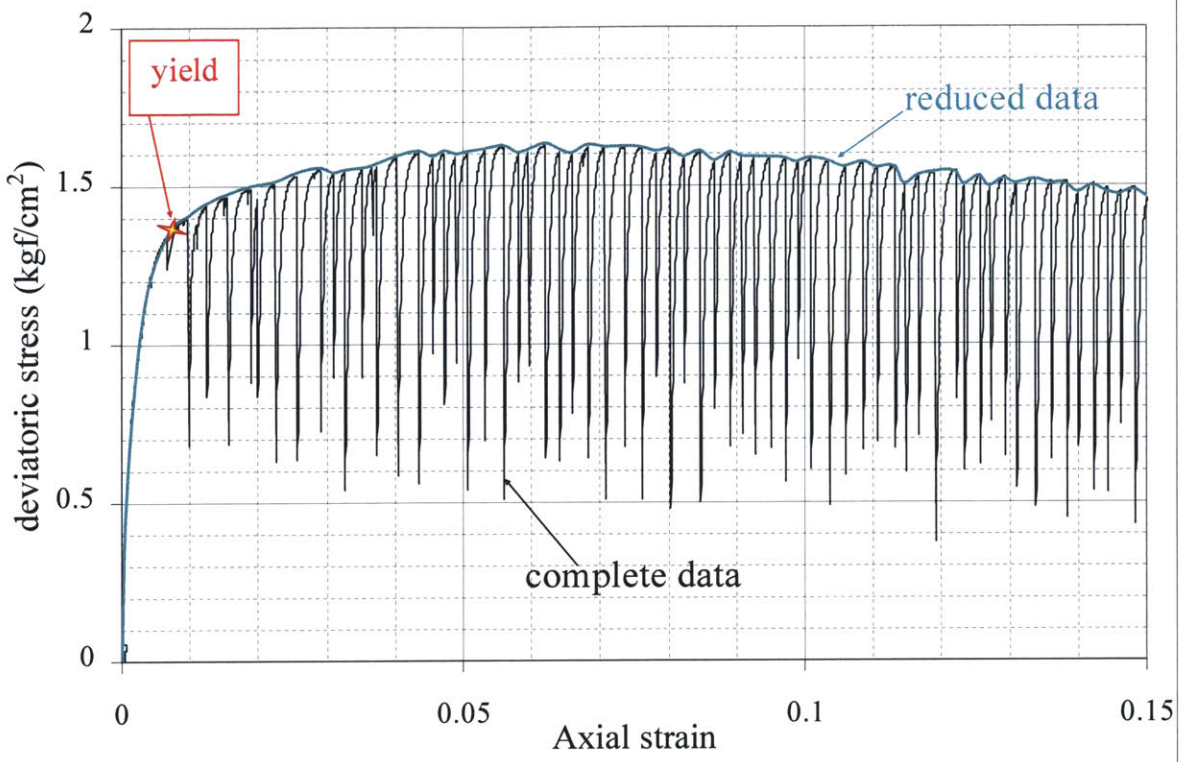

Figure 6.3.(b) Stress-strain curve for TX653 (small strain range).

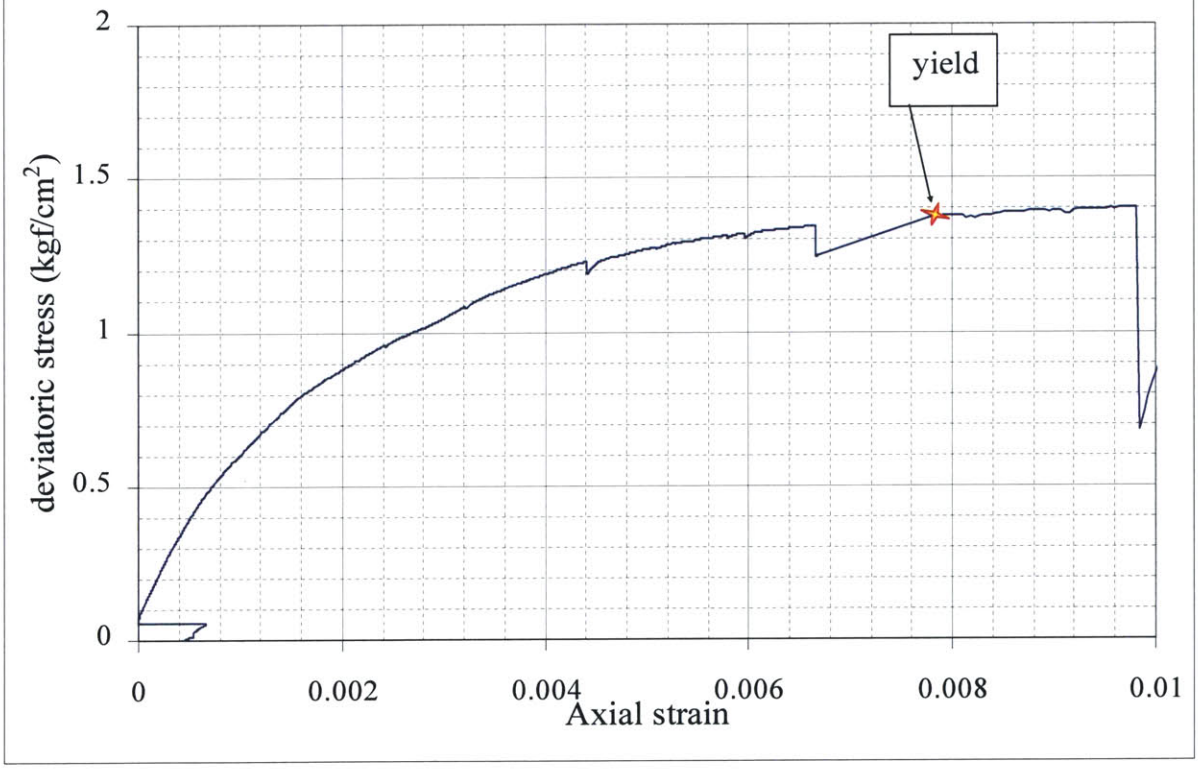

It should be noted that these numbers may err on the low side, as the data acquisition and control systems are not designed to record instantaneous changes in data, and do not respond fast enough to monitor sudden discontinuities.

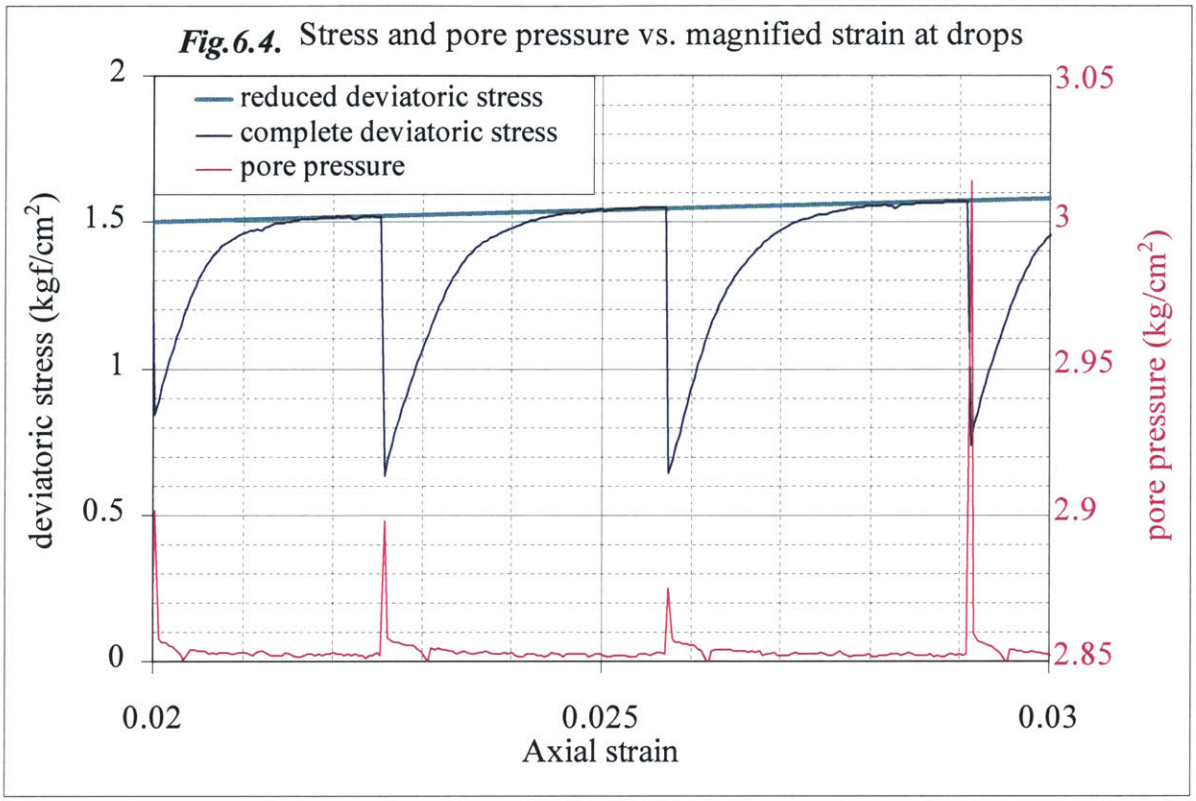

Fig.6.4. Stress and pore pressure vs. magnified strain at drops

In the post-yielding portion of any stress-strain relationship, the stress is (supposed to be) the maximum that the material is able to withstand following its strain history. Immediately after a stress drop, the material is no longer at its momentary strength. Therefore, only the plastic portion of each cycle belongs to the true stress-strain relationship, while the rest are random disturbances in stress. Because of this, as well as to clarify figures, all tests have been reduced by plotting only one (or a few) high stress data points from each cycle for almost all of the figures throughout the rest of the thesis, as examplified with the light colored line in *Figures 6.3* and *6.4*. This results in intelligible graphs with data from multiple tests, like those in *Appendix 6.5* as opposed to plots like multiple *Figure 6.3*s overlapping each other. The reduced graphs of normalized deviatoric stress vs. axial strain and volumetric strain vs. axial strain of all saturated tests are included in *Appendix 6.7*.

6.2.1.2. Deformation

As expected from compacted granular materials, the glass spheres dilate throughout shearing after a little compression at the beginning, in all tests but one (except TX692, which did not exhibit dilation – see *Appendix 6.7.b*), sharing the deformation behavior of most dense granular materials. However, the dilation does not seem to converge to unique critical state void ratios for either sample material, as can be seen from the scatter of the final void ratios reported in *Table 6.2* (especially for Type 2 spheres). This is somewhat expected given the non-uniform deformation of the specimen.

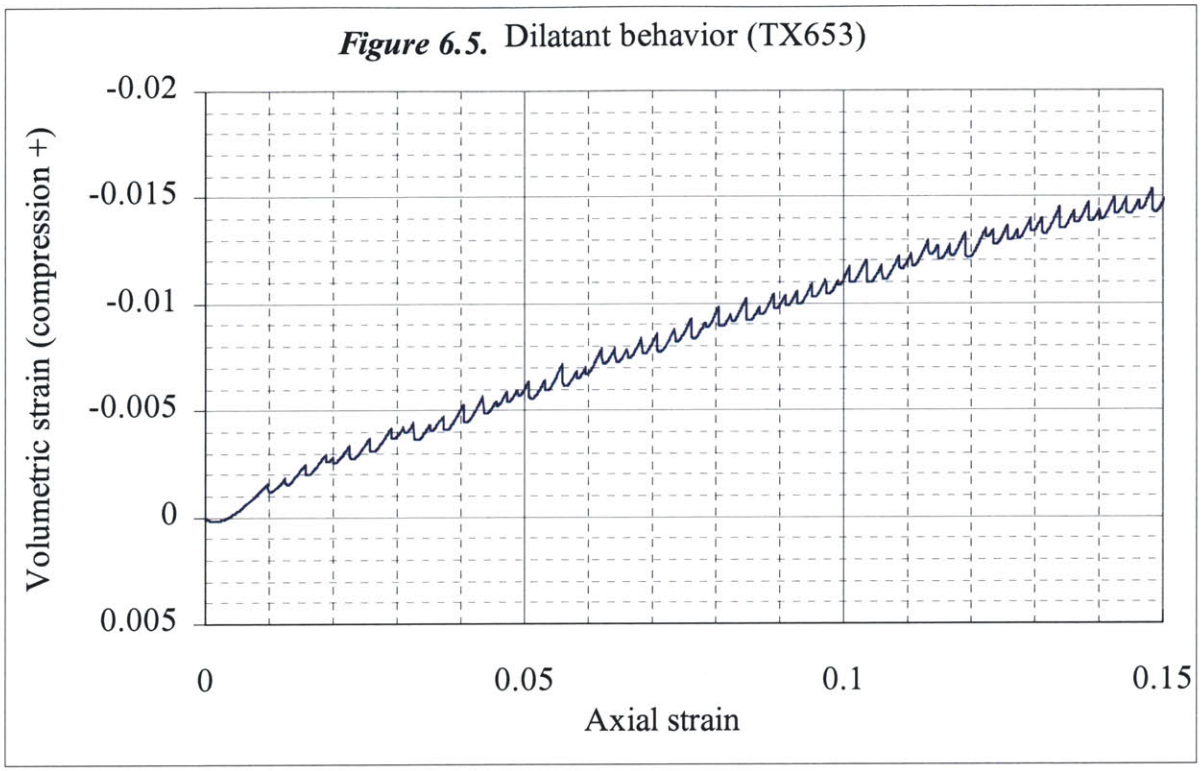

Figure 6.5. Dilatant behavior (TX653)

During shearing, the specimen's profile deforms more like a bell curve (*Fig.6.6*; *Appendix 6.6* shows similar profiles from other tests) than a parabola, which is an often assumed shape. This means the center of the specimen bulges more than usual for triaxial tests. This is in parallel to the findings of Oda (1972[1]), who had observed volume expansion due to dilatancy to concentrate in the center third of a uniform granular specimen.

The irregular geometry heavily affects the results at large strains, because the parabolic area correction (*section 5.4.2.1*) is not formulated for the unusual deformed geometry. The area correction is modified to accommodate the localized bulging in *section 5.4.2.2*.

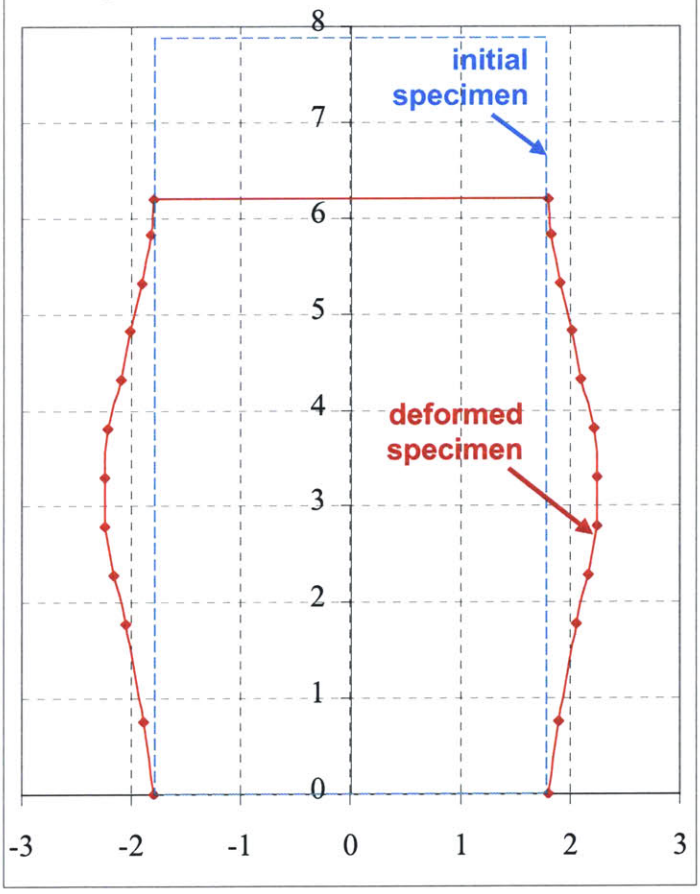

Figure 6.6. Deformed TX653 specimen (cm)

6.2.2. Unsaturated Tests

Pores of the specimen in a sealed unsaturated test are completely sealed from the outside throughout the test. The pore gas phase of an unsealed specimen is connected only to a water reservoir at atmospheric pressure through a very narrow pipe, which allows pressure equilibrization but not too much water transfer. In the tests designated "tensiometer", the specimen is sealed from the outside, but is in physical contact with an MIT tensiometer that forms the pedestal in the triaxial cell. The reduced graphs of normalized deviatoric stress vs. axial strain and of all unsaturated tests are included in *Appendix 6.8*.

6.2.2.1. Stress Drops

Stress drops in unsaturated tests are similar to those observed in the saturated tests, as far as the shape is concerned (i.e. a miniature elastoplastic stress-strain curve shape). The stress drops in unsaturated tests may

- happen insignificantly or not happen at all. (TX678, TX681, TX686, first half of TX682, first half of TX687. See *Figure 6.7* for an example)
- happen infrequently (irregular intervals of upto 1% axial strain), with minuscule stress drops and oscillations in between. (TX663, TX676, first half of TX664, second half of TX682, second half of TX687. See *Figure 6.8* for an example)
- occur as frequently as in the saturated tests, i.e 0.2-0.3%. (TX674, TX683, TX688, TX690, second half of TX664. See *Figure 6.9* for an example)

Figure 6.7. Stress-strain graph of TX681

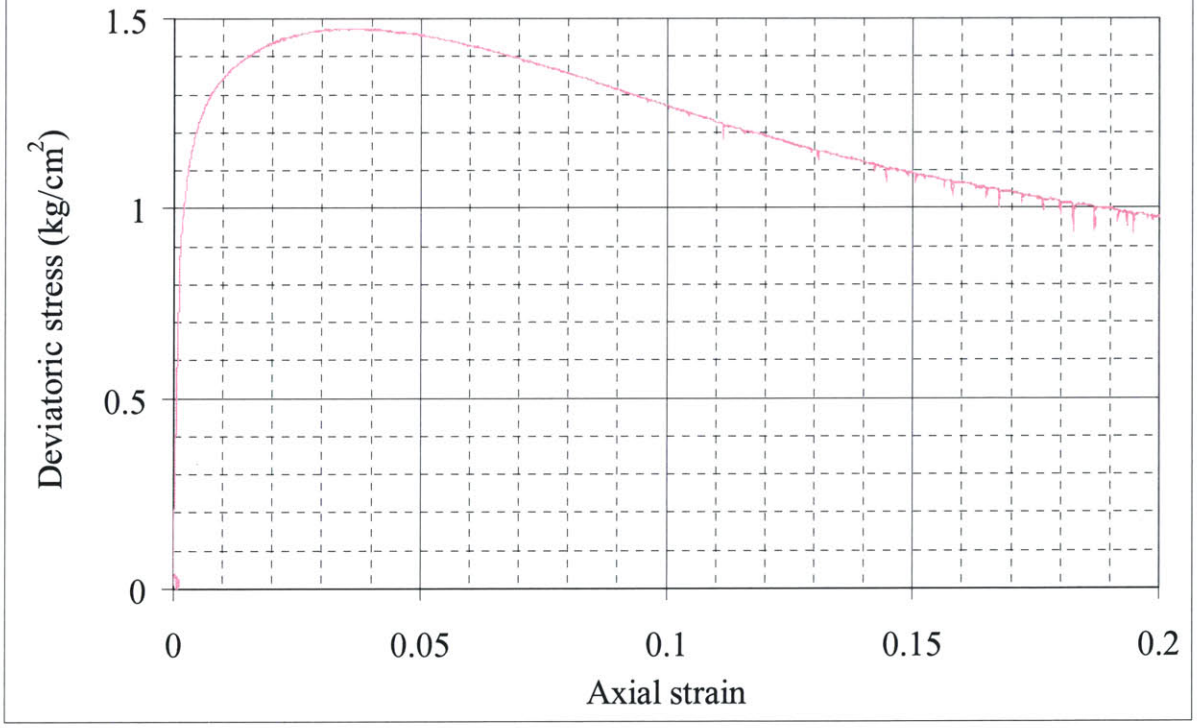

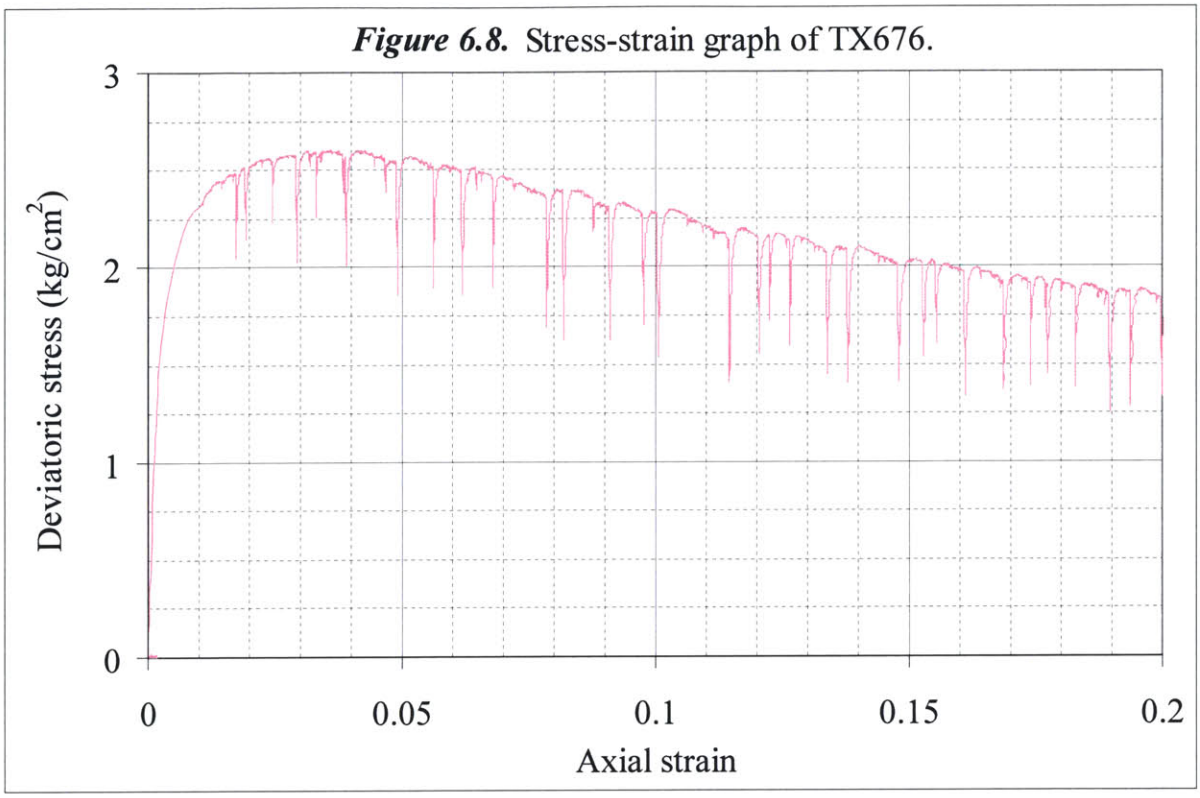

Figure 6.8. Stress-strain graph of TX676.

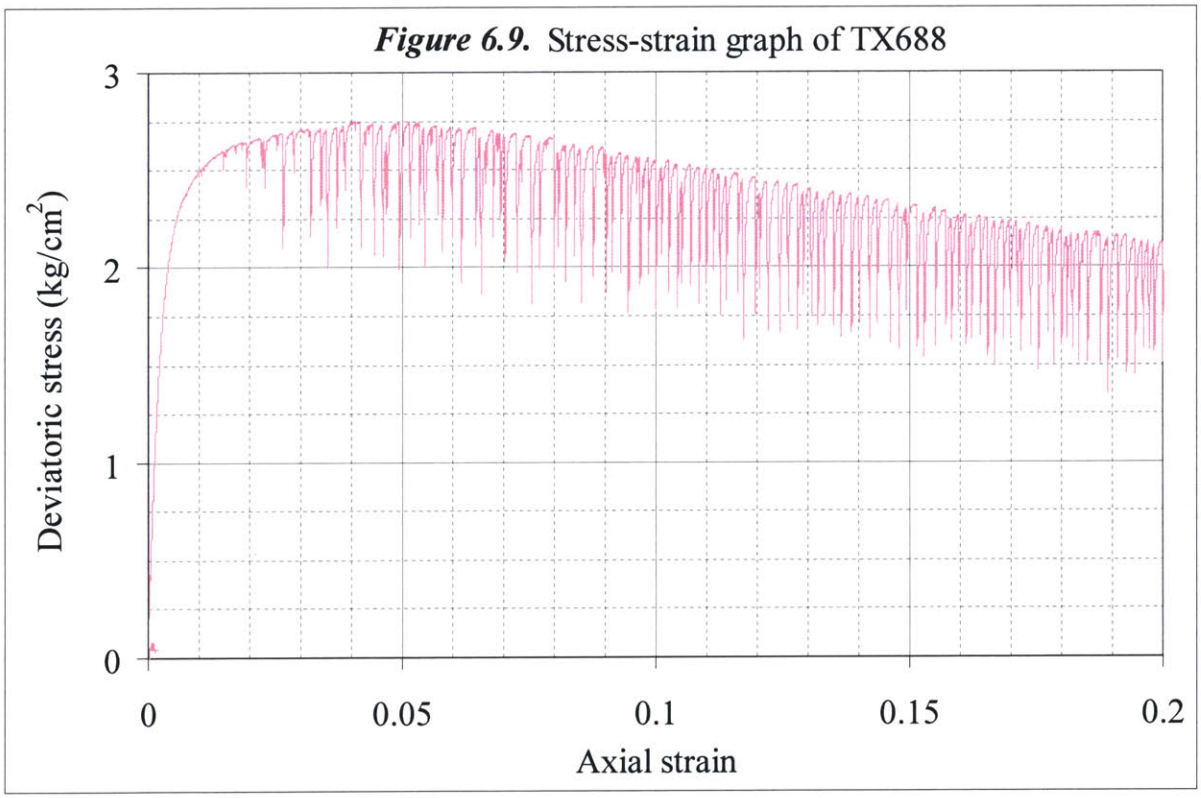

Figure 6.9. Stress-strain graph of TX688

As can be deduced from the tests listed above for each type of behavior, in some tests the stress-strain curves start with one of the former two (of the three) patterns and continue with one of the latter two (of the three). The stress drops in the unsaturated tests are much smaller than the saturated tests in magnitude (0-30% of the deviatoric stress in unsaturated tests as opposed to 40-80% in the saturated tests). This is most likely associated with the lack of pore pressure generation (reduction in effective stress) in the unsaturated tests. Stress-strain plots of the rest of the triaxial tests mentioned in this section are given in *Appendix 6.5*.

6.2.2.2. Tensiometer Measurements

Four tests were carried out in the triaxial cell that is modified to accommodate the MIT tensiometer. The progression of matric suction in these tests is plotted in *Appendix 6.9*, versus time. Values of interest from those plots are summarized in *Table 6.3*. The high-capacity tensiometer (v.7.1) was utilized in test TX687, instead of the high-resolution tensiometer (v.7.0) that was employed in the rest of the tests.

The magnitudes of matric suction throughout the tests vary greatly, as expected within the pendular regime. The following observations were made from the suction measurements presented in *Appendix 6.9*:

- The suctions that were measured immediately after setting up the specimen are in descending order with increasing water contents, as the SMC curves suggest.
- At the start of the 24-hour equilibration period, the suction decreased (except in TX687), but remained in the same descending order.
- Suction equilibrium was successfully sustained for one day in tests except TX687, which sustained it for 6 hours (see footnote in *Table 6.3*).
- Isotropic compression caused the suction to decrease monotonically, except in TX687. In the case of this exception, the rapid increase of suction with time stopped during consolidation, and although not monotonic, it had an overall decrease.
- During secondary compression, the suction increased slightly.
- Shearing caused an increase in suction in all of the tests, but by different magnitudes. In two of the tests, the suction exceeded the capacity of the tensiometer.

Table 6.3. Suction measurements and other relevant data for the tensiometer tests.

Test	Initial water content (%)	Final water content at the bottom (%)	Initial matric suction (kgf/cm^2)	Equilibrated matric suction (kgf/cm^2)	Matric suction at the end of shearing (kgf/cm^2)
TX687	1.76	1.47	0.115	0.115 - 3 *	>4.3
TX686	2.5	2.62	0.044	0.029	0.047
TX688	3.05	2.88	0.026	0.023	>0.8
TX690	3.5	7.49	0.017	<0 ?	0.046

* : Stayed constant at 0.115 kgf/cm^2 for 6 hours. Afterwards the suction reading started to increase. By the start of consolidation, it was 3 kgf/cm^2.

? : possibly error in the transducer zero in this test

6.2.2.3. Deformation

There were no volume change measurements in the unsaturated tests. The post-shear optical measurements show the deformed shapes of the unsaturated specimen to be similar to the saturated case. In parts of tests that did not have stress drops, the volumetric strain – axial strain curve was smooth as well.

6.2.3. Parametric Sensitivity

Section 5.4.2 proposed two new corrections for the processing of data from triaxial tests. The next two sub-sections (*6.2.3.1* and *6.2.3.2*) show the effects of these corrections on the deviatoric stess. As earlier, TX653 is selected as an example to demonstrate the differences.

6.2.3.1. Modifications to the Membrane Correction

The conventional way of correcting for membrane stiffness is modified to account for the initial axial and radial stretching of the membrane, which happens during the process of setting up the glass sphere specimen. As was noted in *Section 5.4.2.4*, and can be seen in *Figure 6.10*, modifications to the membrane correction in the axial direction result in higher axial and deviatoric stresses by 0.003-0.004 kgf/cm^2. It must be noted that the modification on the membrane correction in the axial direction varies with the operator, because it depends on how much the membrane is stretched during the setup process. This effect is taken into account in the results. Modification to the axial correction for TX653 (*Fig.6.10*) is actually one of the smallest in magnitude; some other tests have this modification with more than twice the magnitude.

The radial modification increases axial stress as well, but the increase in radial stress is higher, making the overall effect on deviator stress a decrease of 0.005-0.006 kgf/cm^2. A large portion of this correction is due to the initial radial stretching of the membrane. Modification to the radial correction is of similar magnitude in all tests, because neither membrane perimeter nor specimen area vary significantly from one test to another.

These modifications result in measuring more correct and lower deviator stress values, but the overall difference from the unmodified corrections is within a mere ±0.002 kgf/cm^2.

6.2.3.2. Modification to the Area Correction

The difference between stresses corrected with respect to the specimen area and uncorrected stresses increases as the shearing progresses (*Figure 6.11*), because the area correction directly depends on the strains. For this research, this dependence is dominated by the axial strain, because volumetric strains are small. It should be noted that the area correction to stress is actually in terms of a fraction of the stress, so in the tests of this research the area correction would appear to be directly proportional to the confining pressure as well.

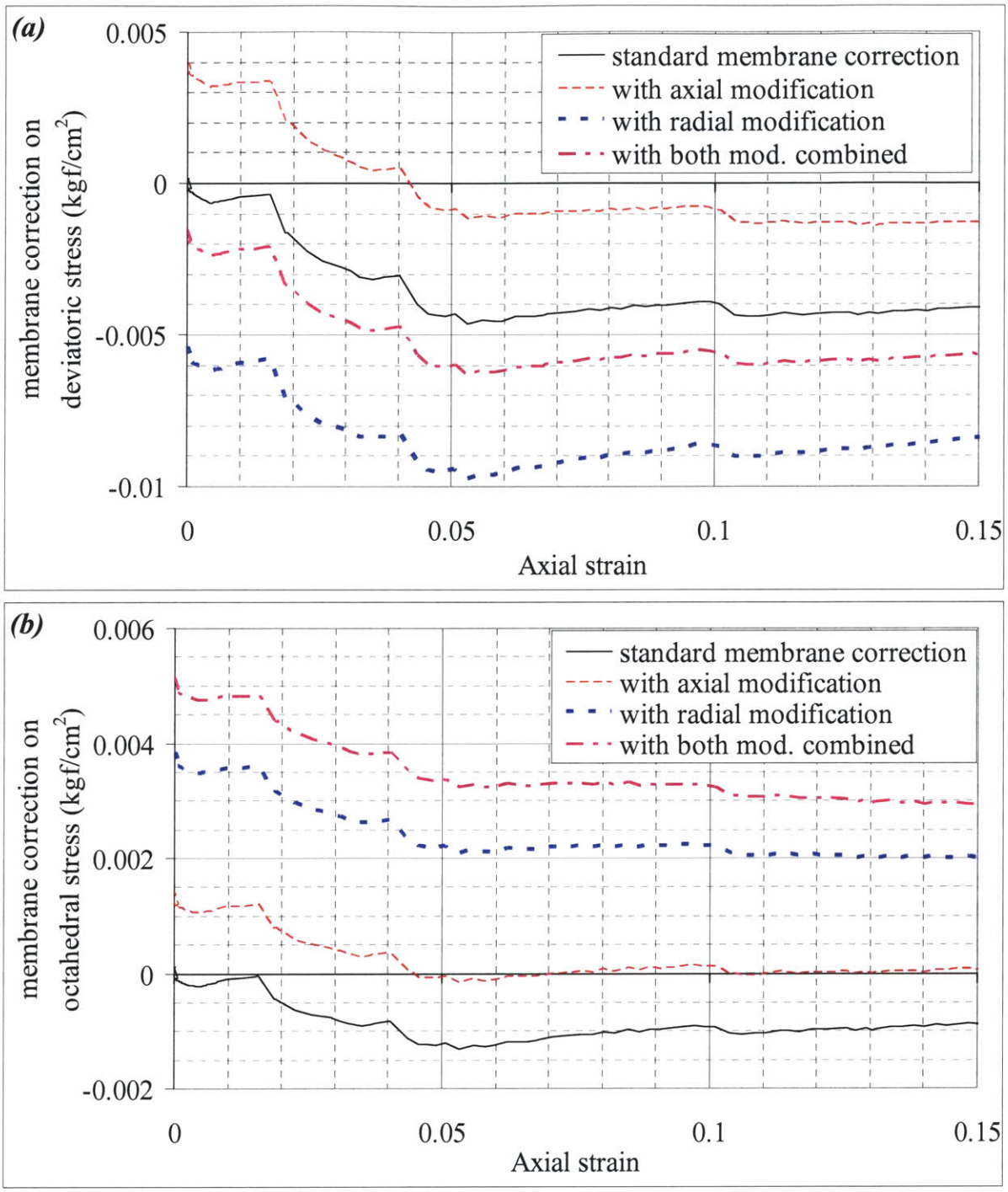

Figure 6.10. Effect of membrane correction and its modifications on the stresses in experiment TX653: ***(a)*** on deviatoric stress, ***(b)*** on octahedral stress.

The modification to the area correction affects only the axial stress. It results in negligible difference in deviator stress at smaller strains (such as the yield strain). By the time the axial strain reaches 15%, the modification may diminish the deviator stress by as much as $0.1\sigma_c$, compared to the usual parabolic correction. In other tests with a specimen more dramatically

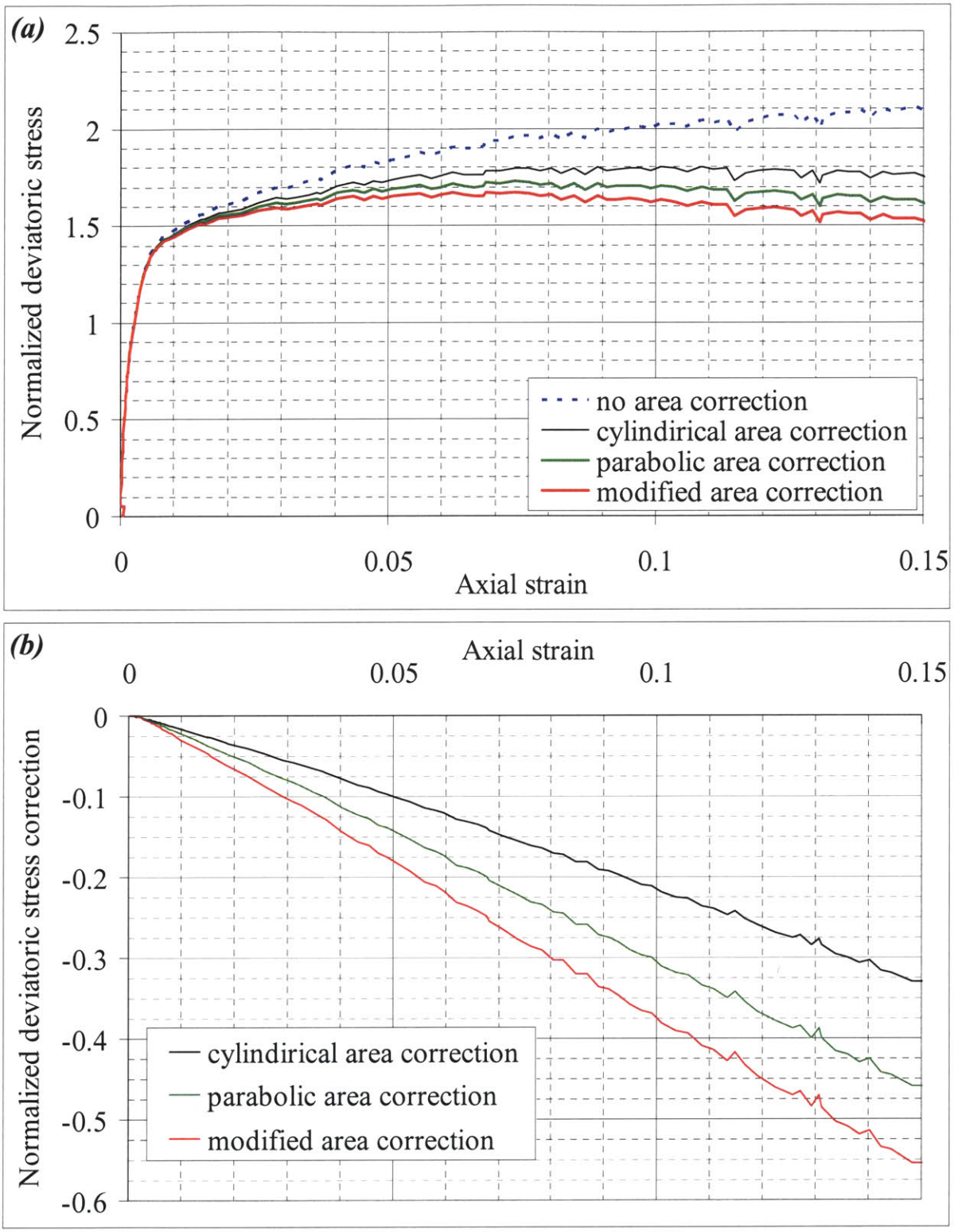

Figure 6.11. Results of TX653 (σ_c = 0.97 kgf/cm^2) with modifications to area correction. ***(a)*** Absolute deviatoric stress. ***(b)*** Deviatoric stress relative to the uncorrected measurement.

bulged at the center, this difference is observed to be as high as $0.27\sigma_c$. The column named "area multiplier" in *Table 6.2* is a direct indicator of the magnitude of the stress change due to the modification of area correction.

For the final values of axial and radial stress, both membrane and area corrections are modified. At smaller strains, this results in higher stresses as the membrane correction is more prevalent. As the shearing progresses, the area correction dominates the magnitude of total correction, drawing the stress down. This introduces significant uncertainity to the large-strain results collected at the peak stress and 15% strain, compared to the yield stresses. Hence, this research gives precedence to the results obtained from smaller strains, such as the yield strain, for the interpretation of data.

When comparing results of a group of tests, differences in area multipliers between individual tests can result in misleading appearance trends where there were none (or disappearance of existing trends) at large strains. Because of this, the area correction must be employed with care, especially if large strain behavior is an area of interest. The effects of different area corrections on interpreting the results of a group of tests is visible in *Figure 6.12.*

Note that even at 1% axial strain, which is the approximate yield strain in many tests, the total of area and membrane corrections to deviatoric stress is -0.03 kgf/cm^2 in TX653, which has a σ_c of 0.97 kgf/cm^2. Compared to the prediction of 0.02 kgf/cm^2 for the increment in effective stress due to suction by the model (*section 6.1.3*), the corrections are significant, therefore such a detailed study and improvement of standard corrections was necessary.

6.2.3.3. Initial Water Content / Void Ratio

Some of the tests on Type 2 samples (namely TX686, 688 and 690) were repeated at the same radial stress but different initial water contents. This group of tests was originally intended as a way to investigate the effects of varying the matric suction on the strength and effective stress. The matric suction measurements until the start of shear (i.e. through the moisture equilibration and consolidation) are of the order expected from the initial water contents. As described in *section 6.2.2.2*, matric suctions generally increase during shearing, but the magnitude and rate of this increase does not exhibit any trends with respect to other parameters of the test.

However, the direct effects of suction on strength and effective stress were not perceivable in this set of tests, because the results were under the greater influence of variations in void ratio. As mentioned in *section 6.1.2*, the void ratio is affected by the initial water content. Within the water content range under consideration, better compaction (i.e. smaller void ratio) is achieved by increasing the initial water content. The shear strength of these specimen is greatly affected by the initial void ratio, as illustrated in *Figure 6.12*. A similar comparison can be made between the saturated tests of TX684 and TX692, whose results are included in *Appendix 6.7.b*.

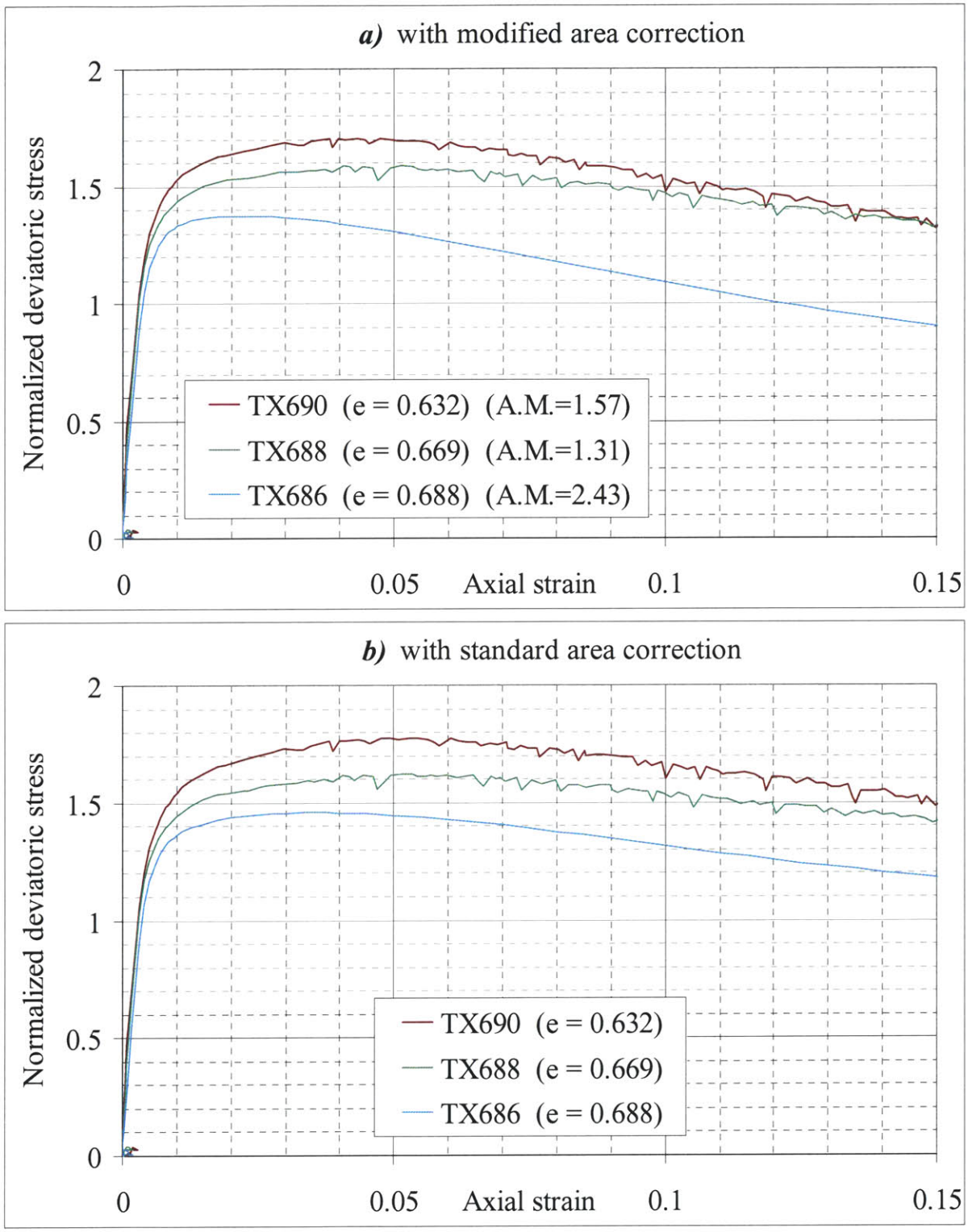

Figure 6.12. Comparison of unsaturated tests with the same σ_c and different void ratios and different area multipliers.

It should be noted that the behavior at higher strains probably do not match because of the different area correction multipliers (a test with an unrealistically large area multiplier, such as TX686, has its stress reduced faster than other tests as axial strain increases). Because the area multipliers are too different in this group of tests, results with parabolic (unmodified) area correction are also included as *Figure 6.12.b.*

Appendices

Appendix 6.1. Photographs of the two specimen materials through optical microscope.

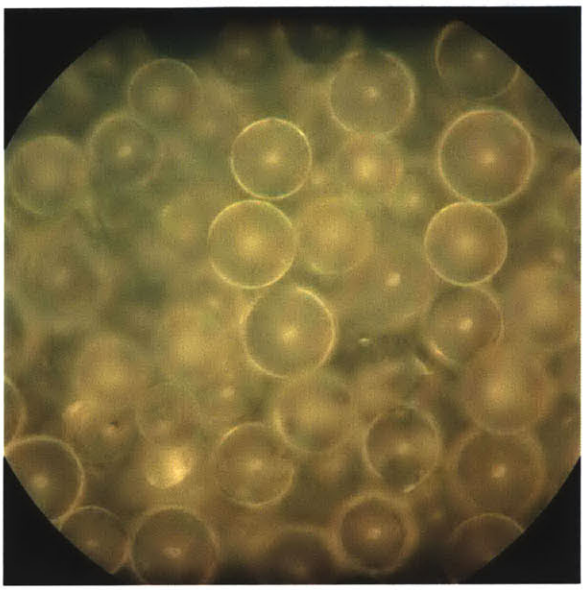

(a) Type 1 spheres before test (200x)

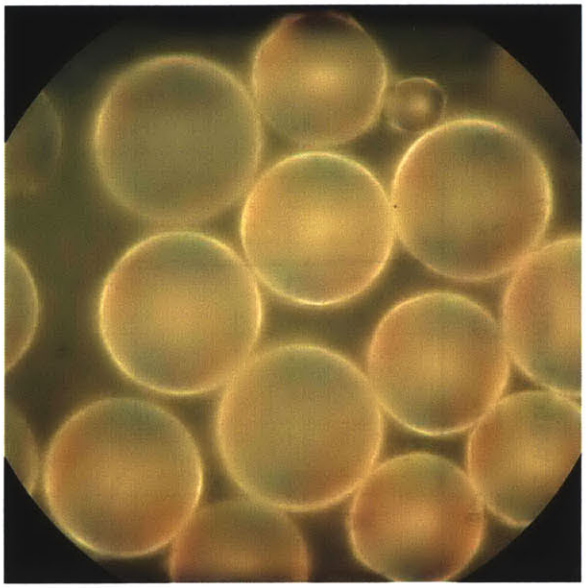

(b) Type 1 spheres after test (400x)

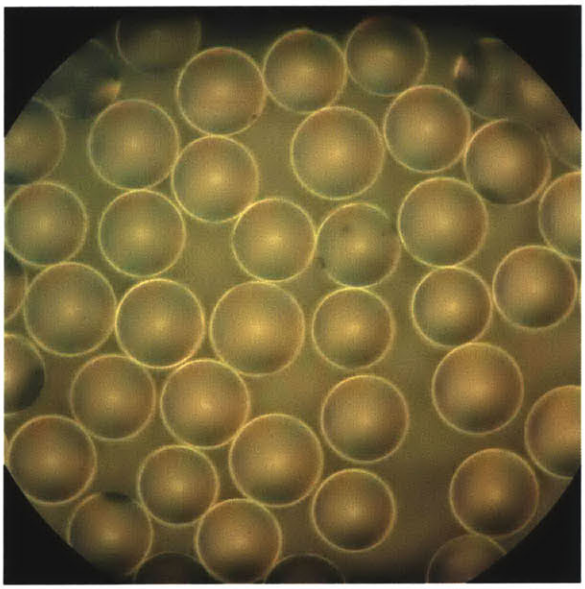

(c) Type 2 spheres before test (200x)

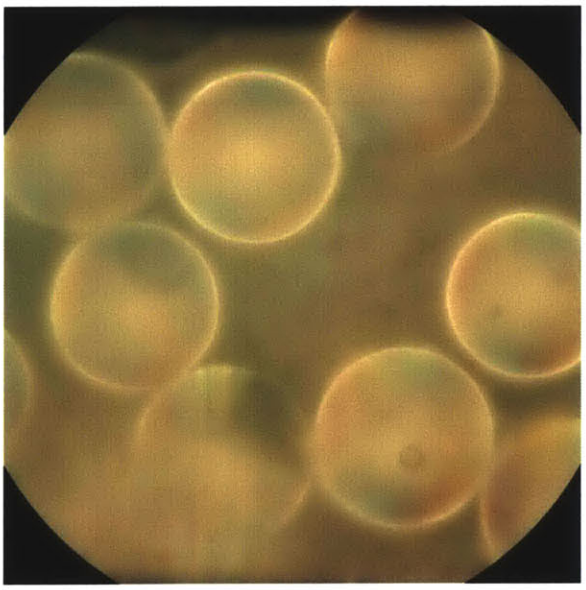

(d) Type 2 spheres after test (400x)

Appendix 6.2. Soil-moisture characteristic curves of the two specimen materials.

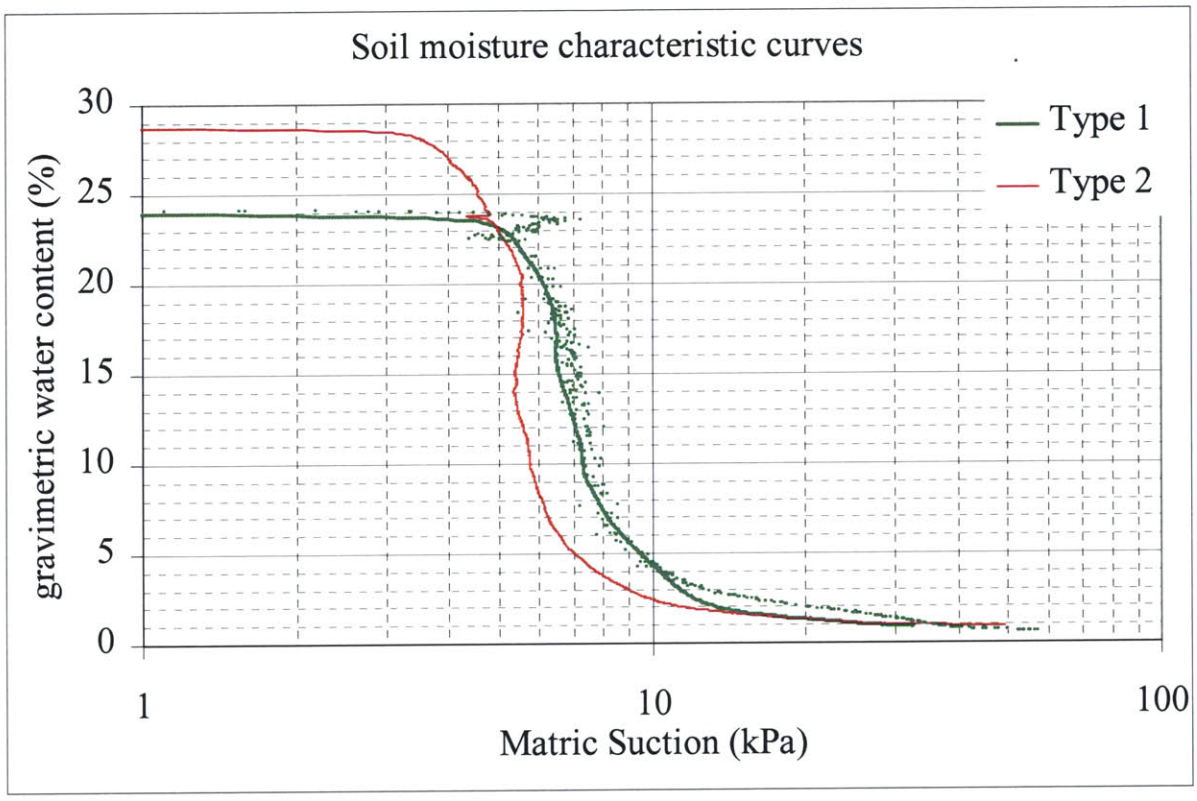

Appendix 6.3.a. Stress paths for Type 1 material.

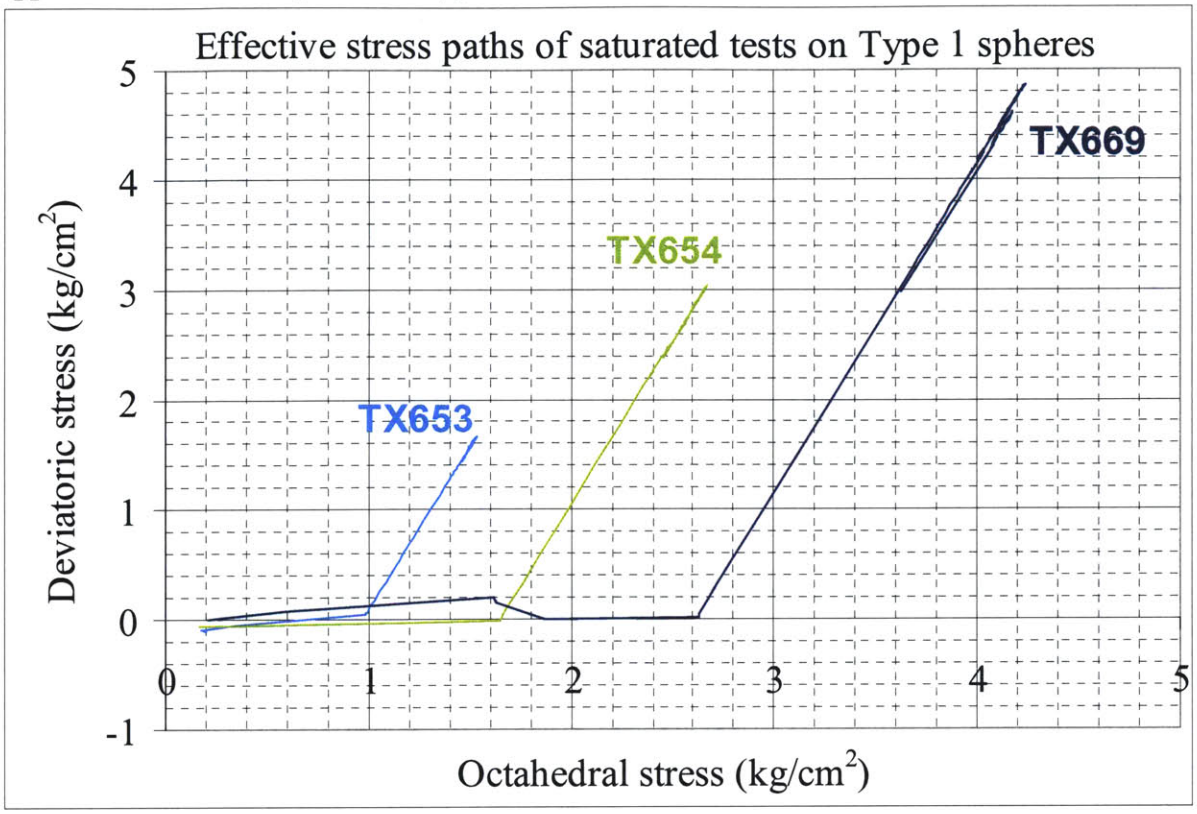

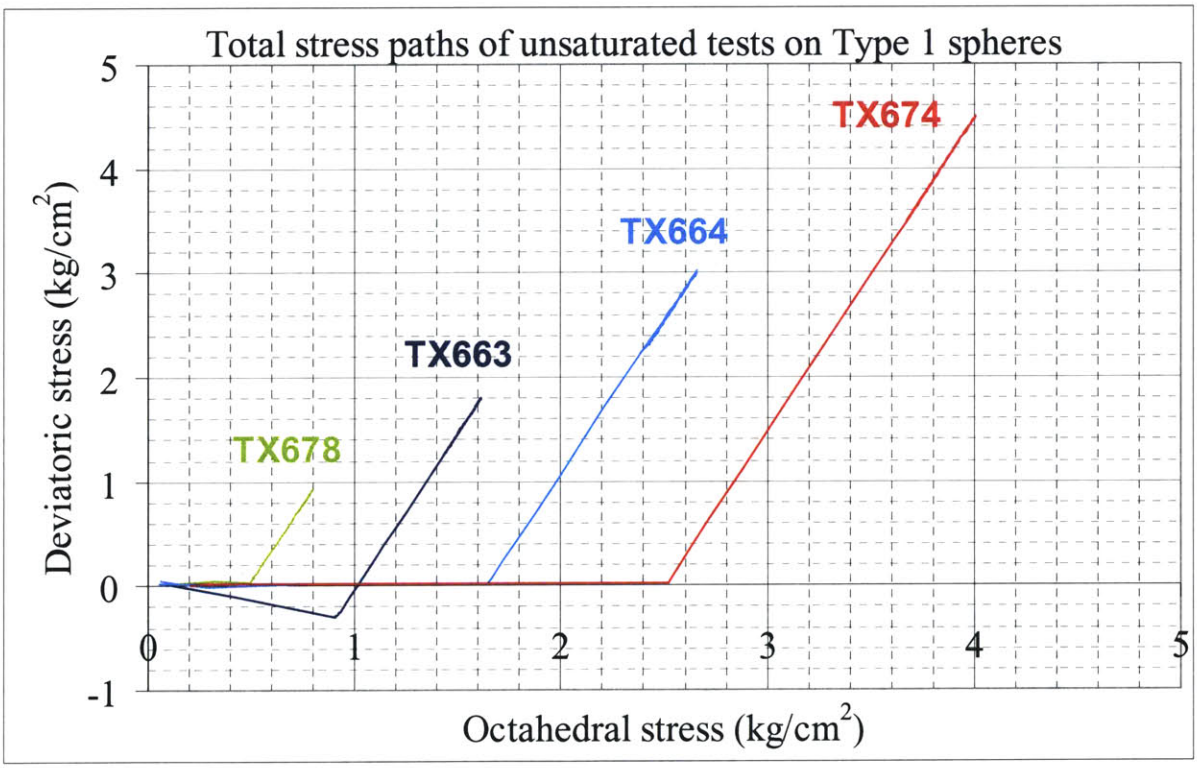

Appendix 6.3.b. Stress paths for Type 2 material.

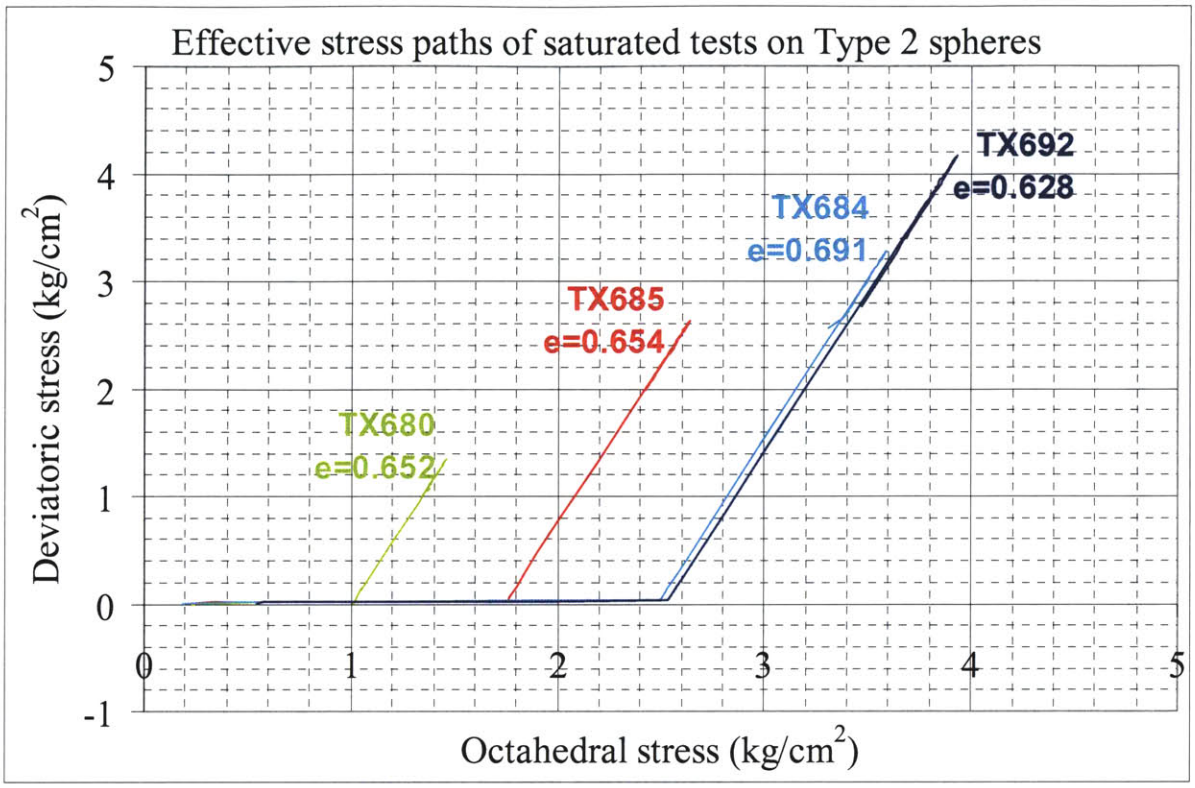

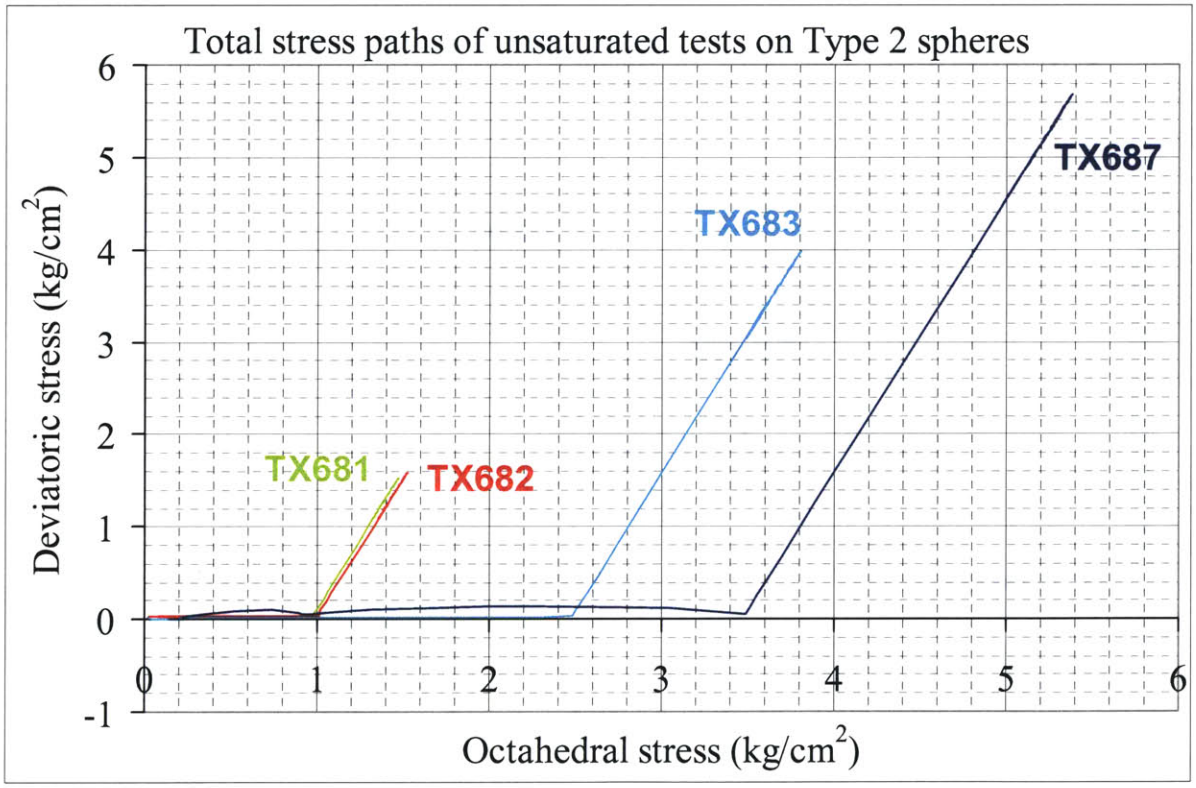

Appendix 6.4. Axial strains at yield and peak stresses.

Material	Test Type	Test No	ε_{axial} (%) at yield	ε_{axial} (%) at peak
Type 1	saturated	TX653	0.56	7.35
		TX654	0.77	5.93
		TX669	0.69	5.96
	sealed	TX663	0.86	3.48
		TX664	0.55	3.52
		TX674	0.76	2.33
		TX678	1.06	4.24
	unsealed	TX676	1.09	3.60
Type 2	saturated	TX680	1.13	3.52
		TX685	1.06	5.43
		TX692	0.99	4.14
		TX684	0.64	2.11
	Tensiometer	TX686	1.00	2.00
		TX687	0.80	2.50
		TX688	1.00	4.07
		TX690	0.95	3.98
	sealed	TX681	1.20	3.81
	unsealed	TX682	0.92	2.82
		TX683	1.27	4.67

Appendix 6.5. Deviatoric stress – axial strain raw data except TX653. Darker (blue) colored graphs belong to saturated tests and light (pink) colored graphs belong to unsaturated tests.

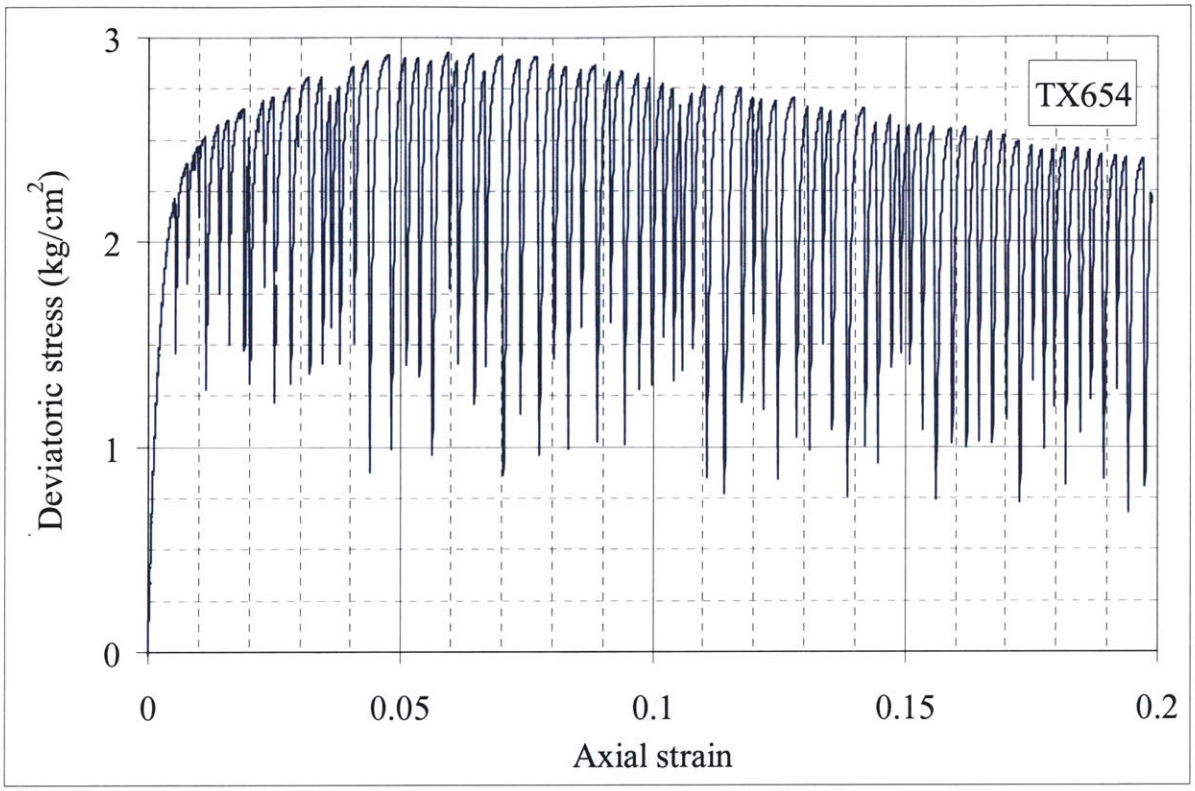

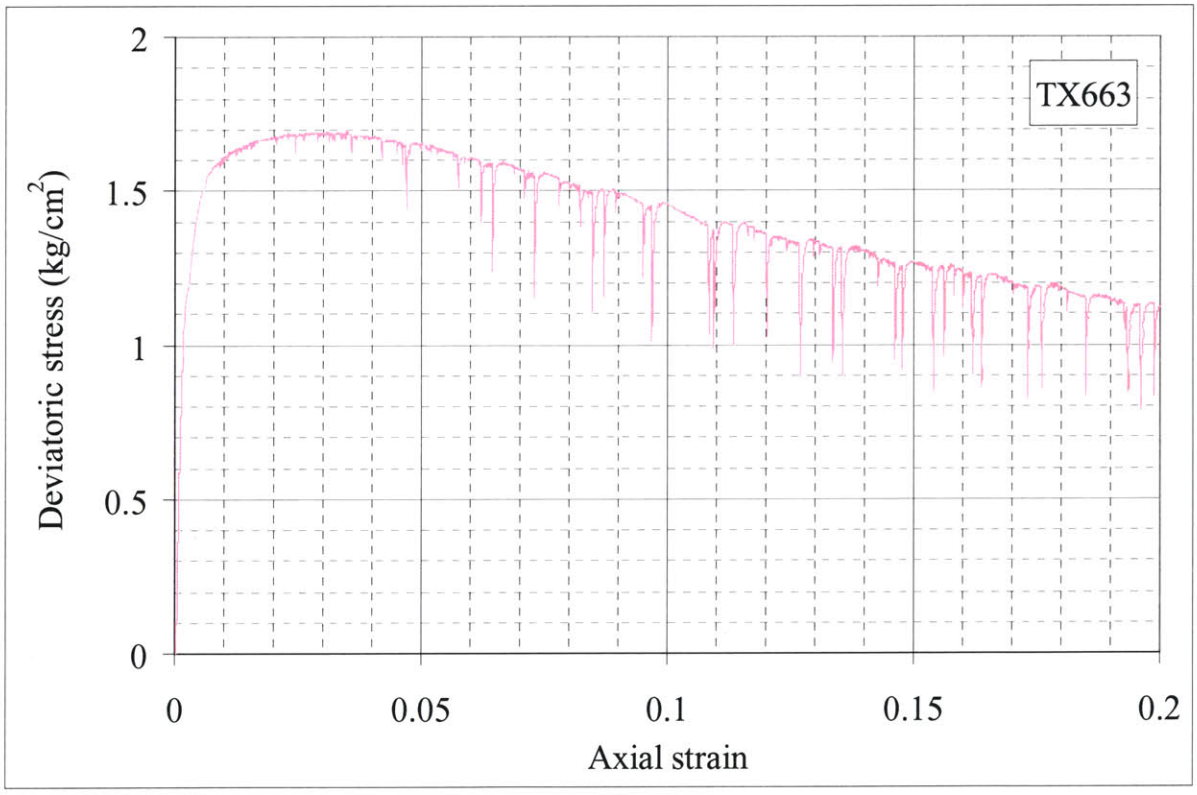

Appendix 6.5. continued

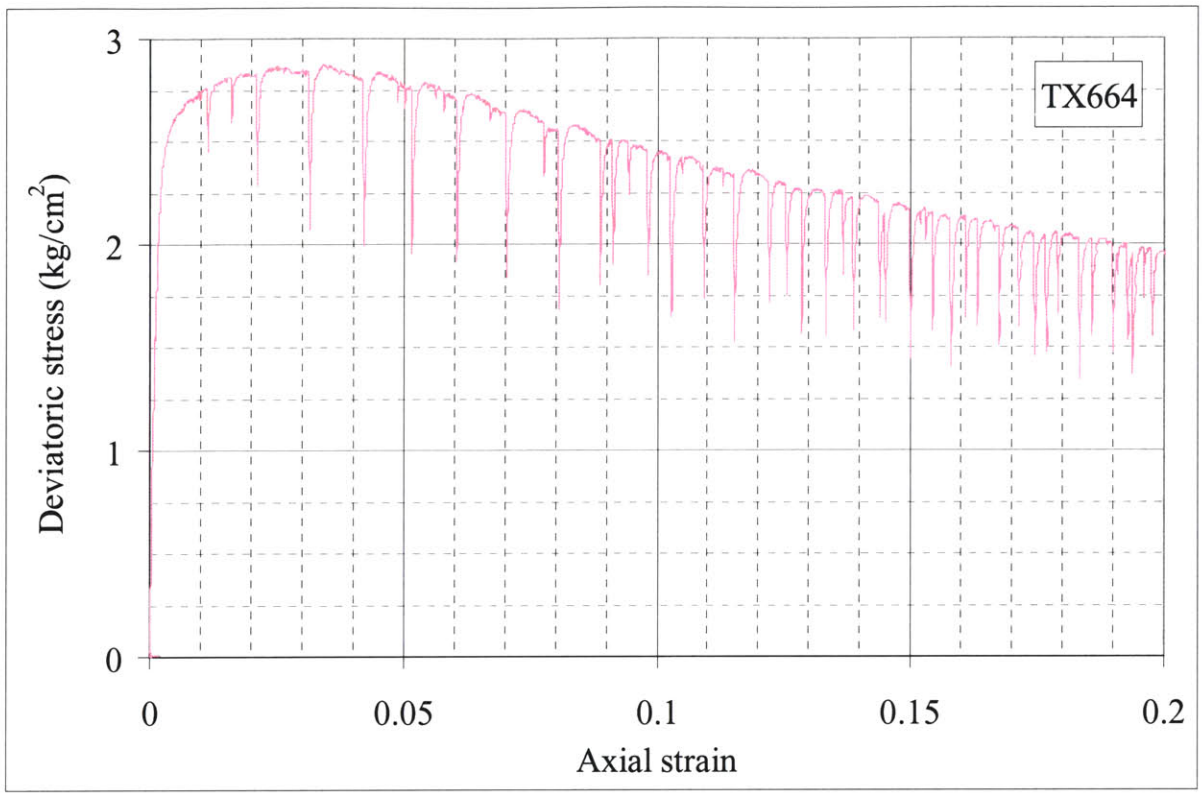

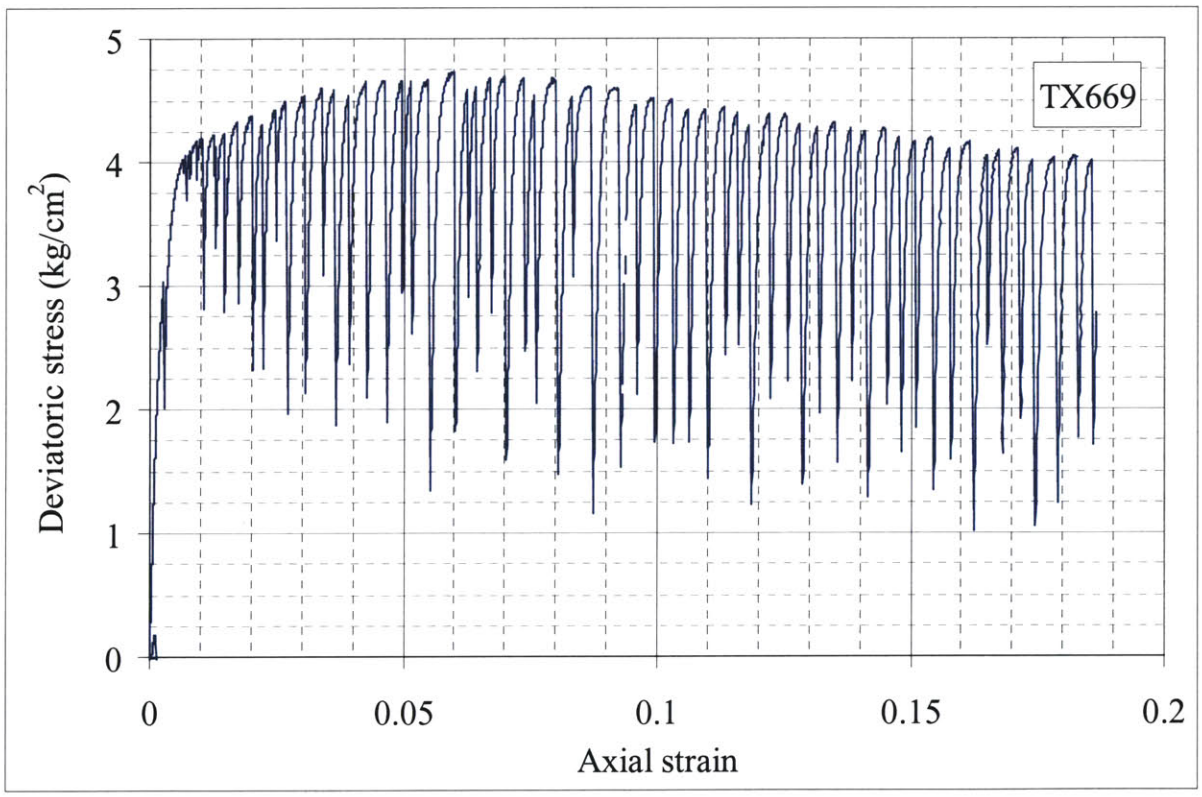

Appendix 6.5. continued

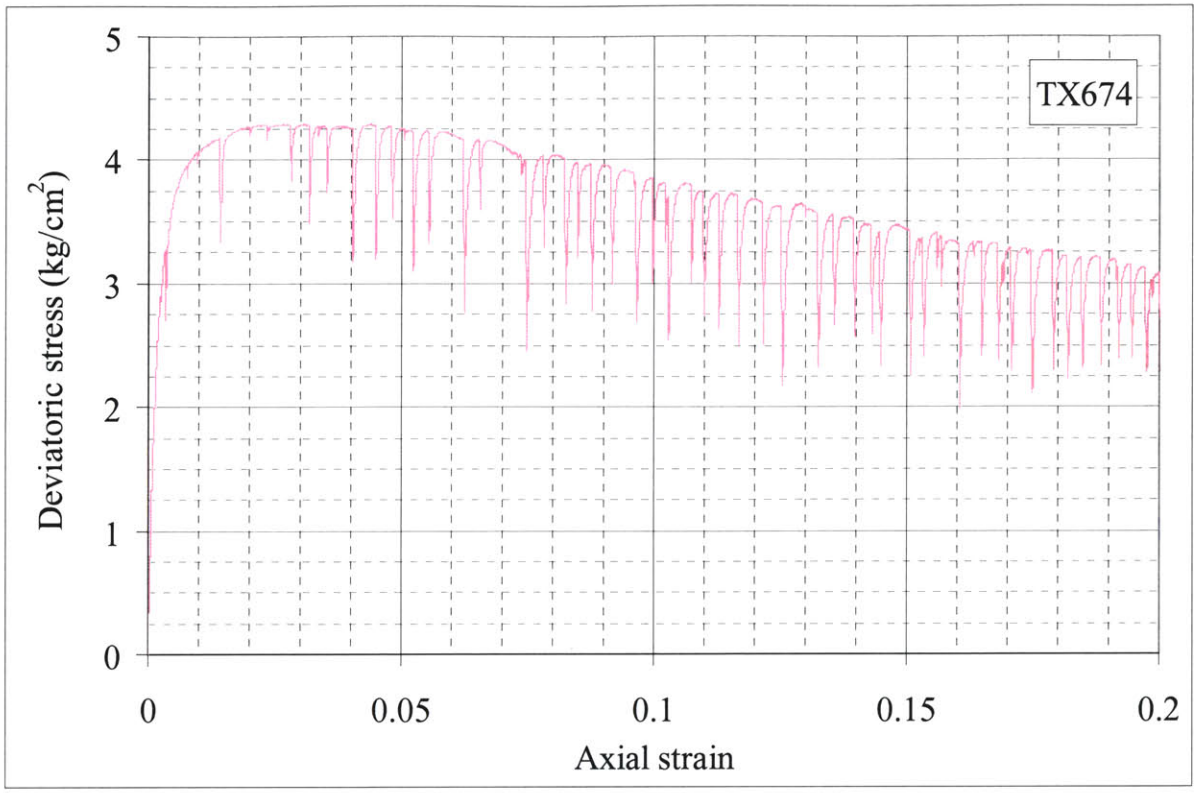

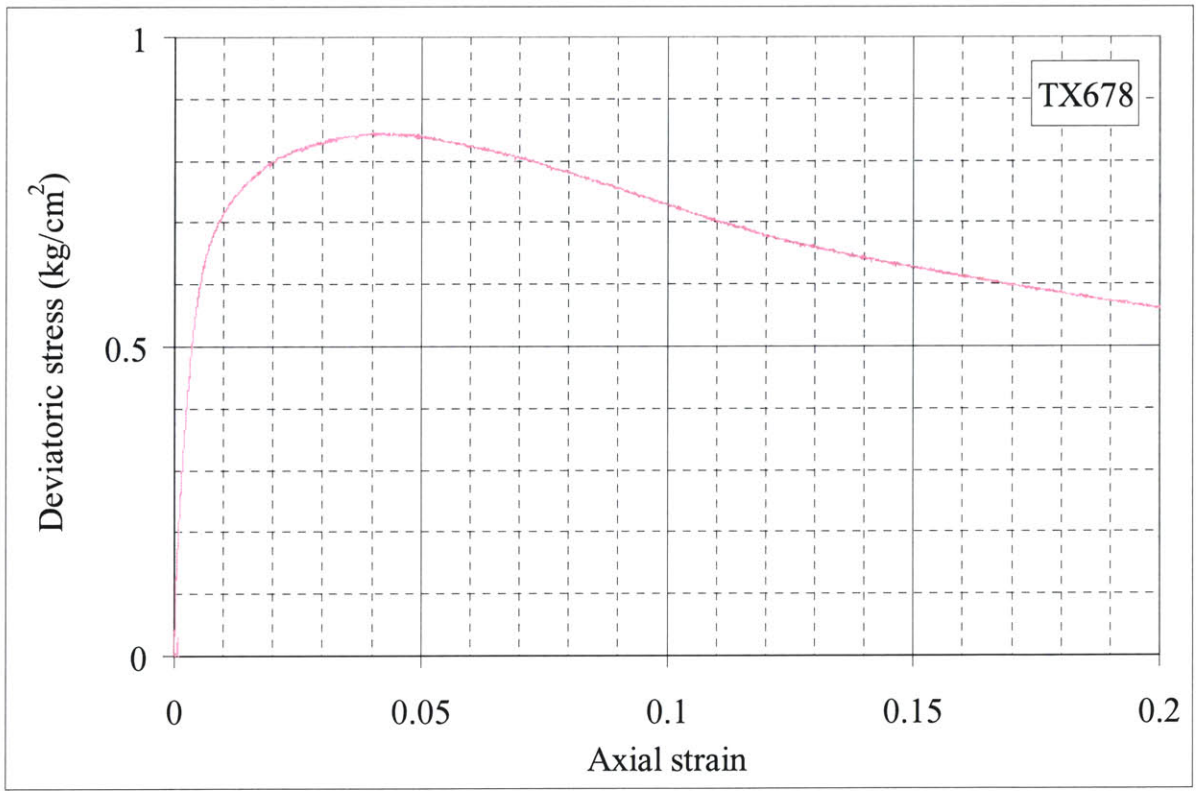

Appendix 6.5. continued

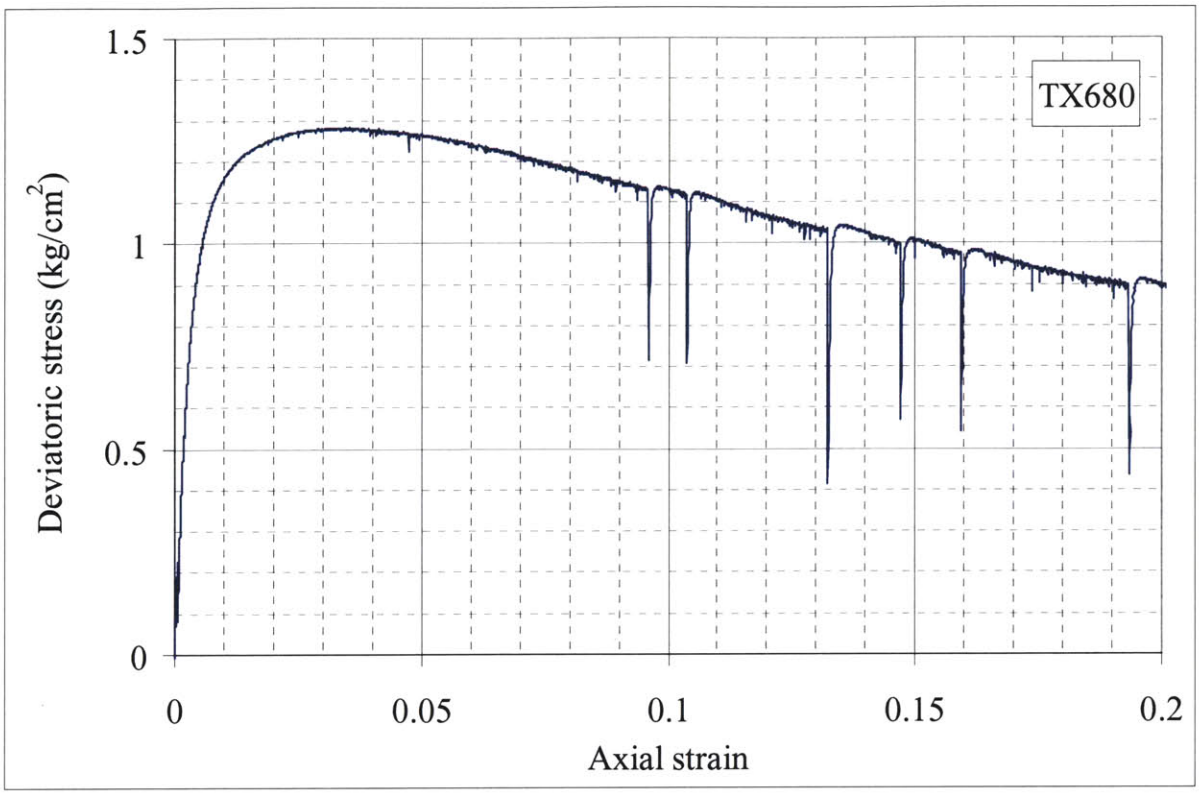

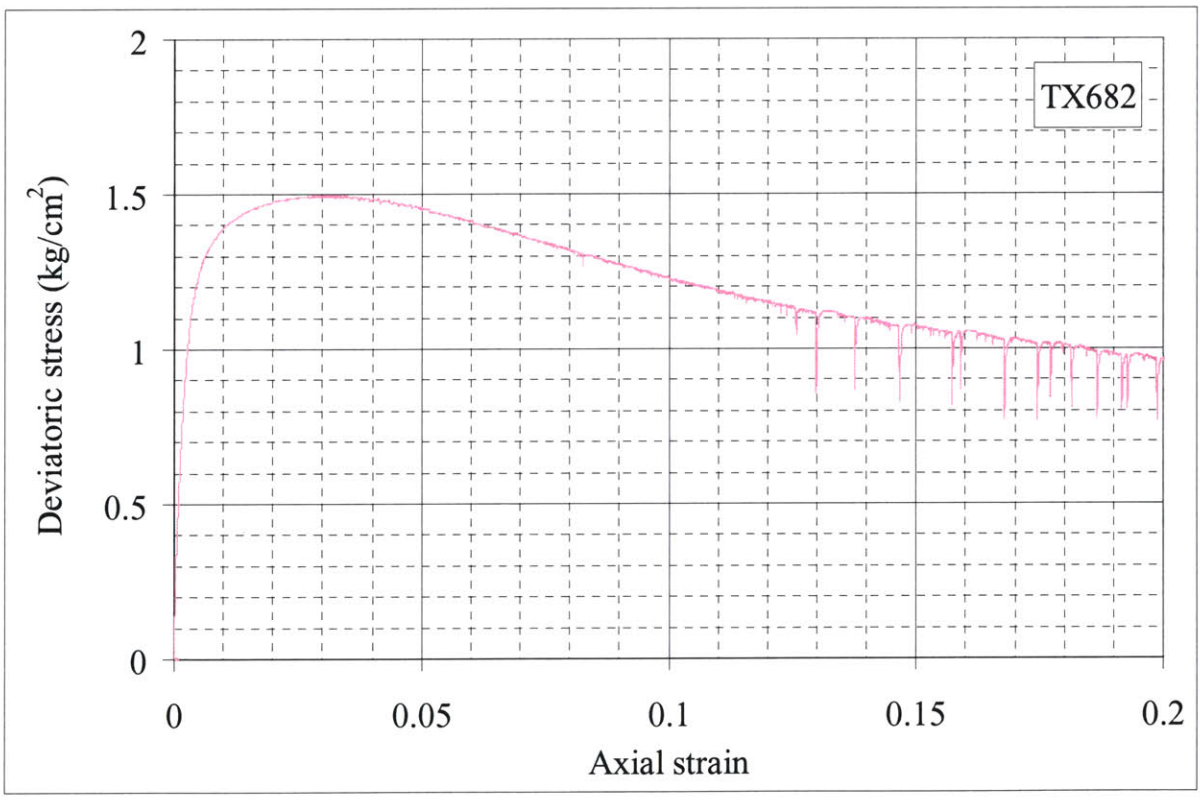

Appendix 6.5. continued

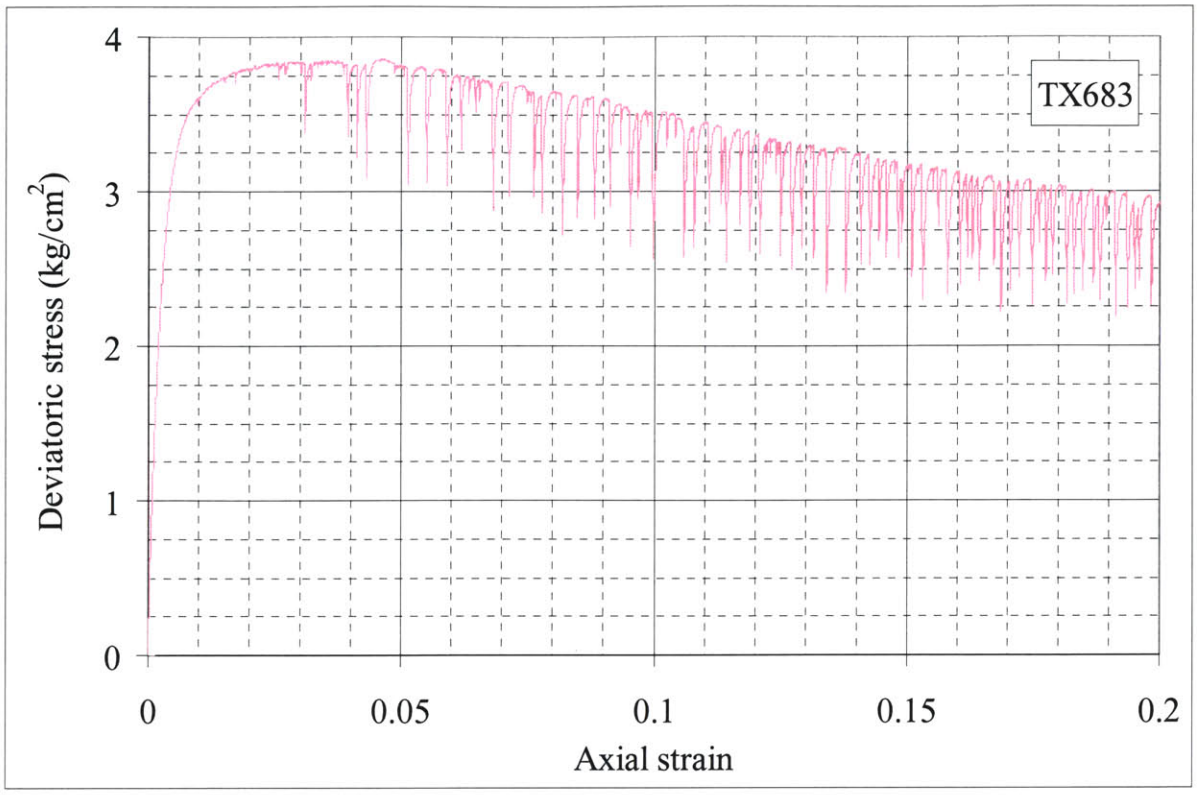

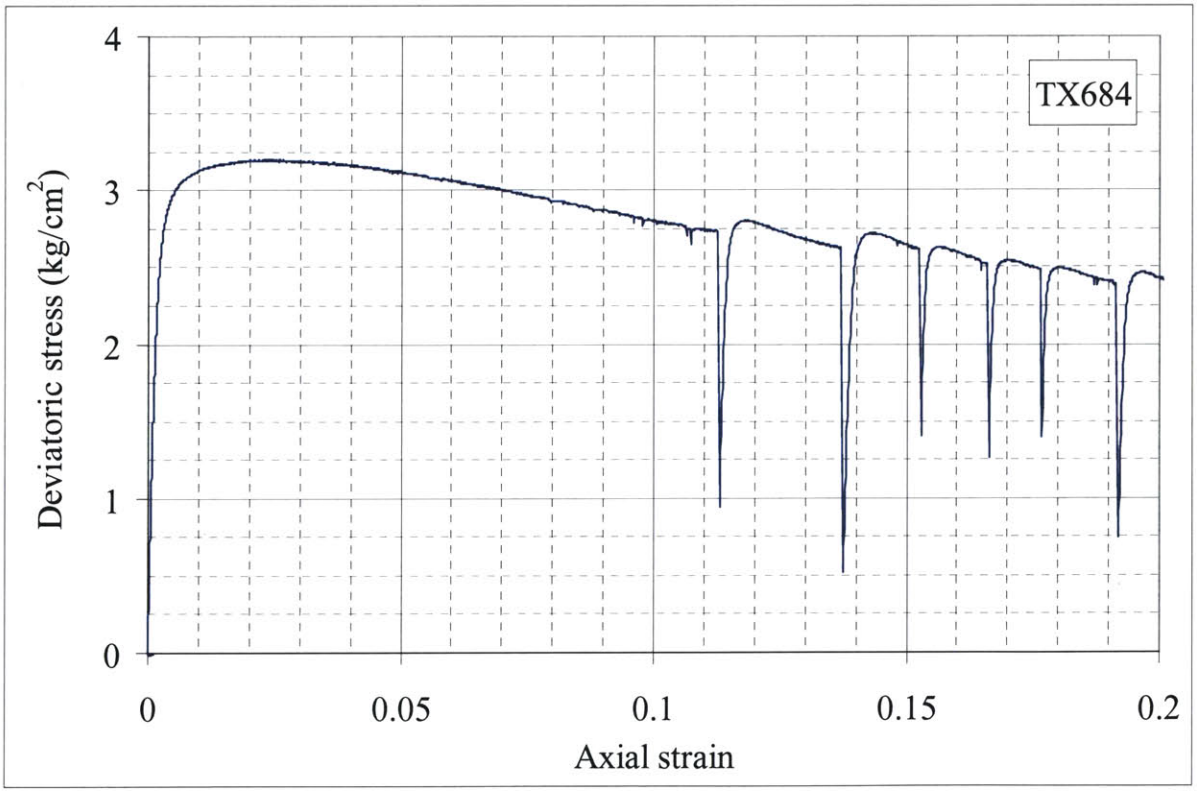

Appendix 6.5. continued

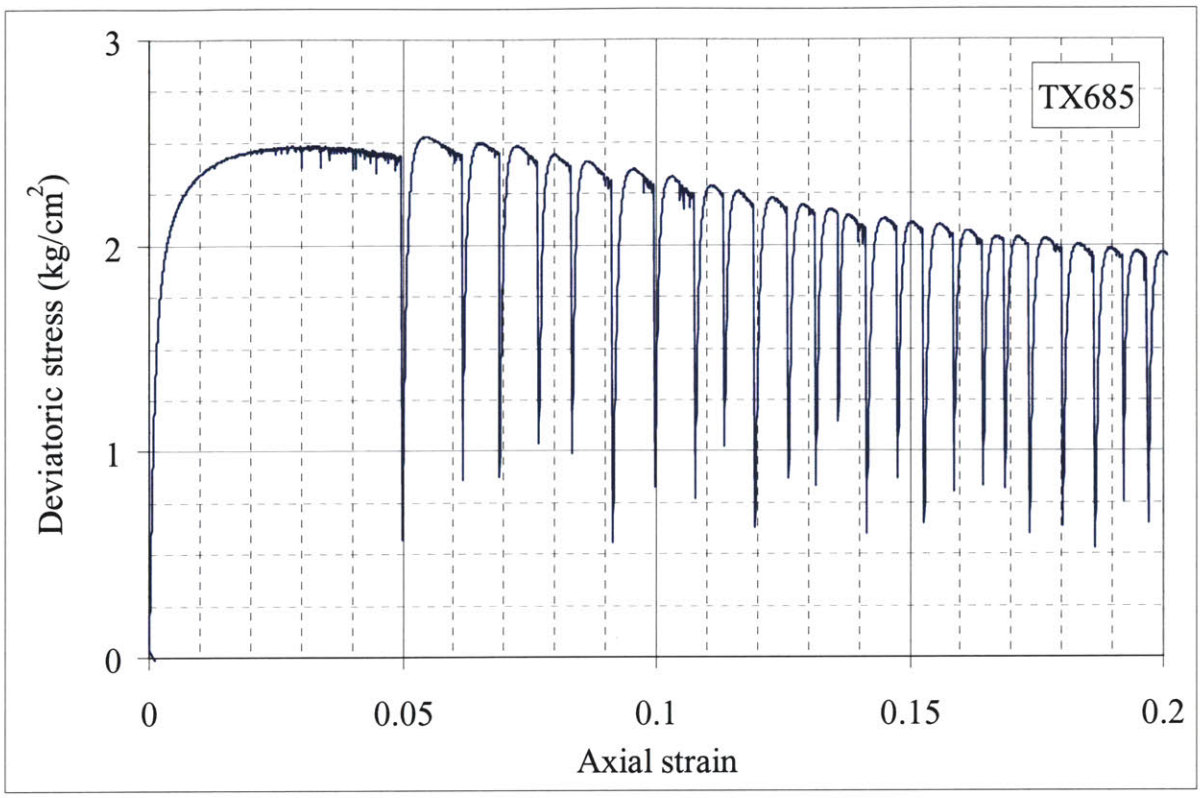

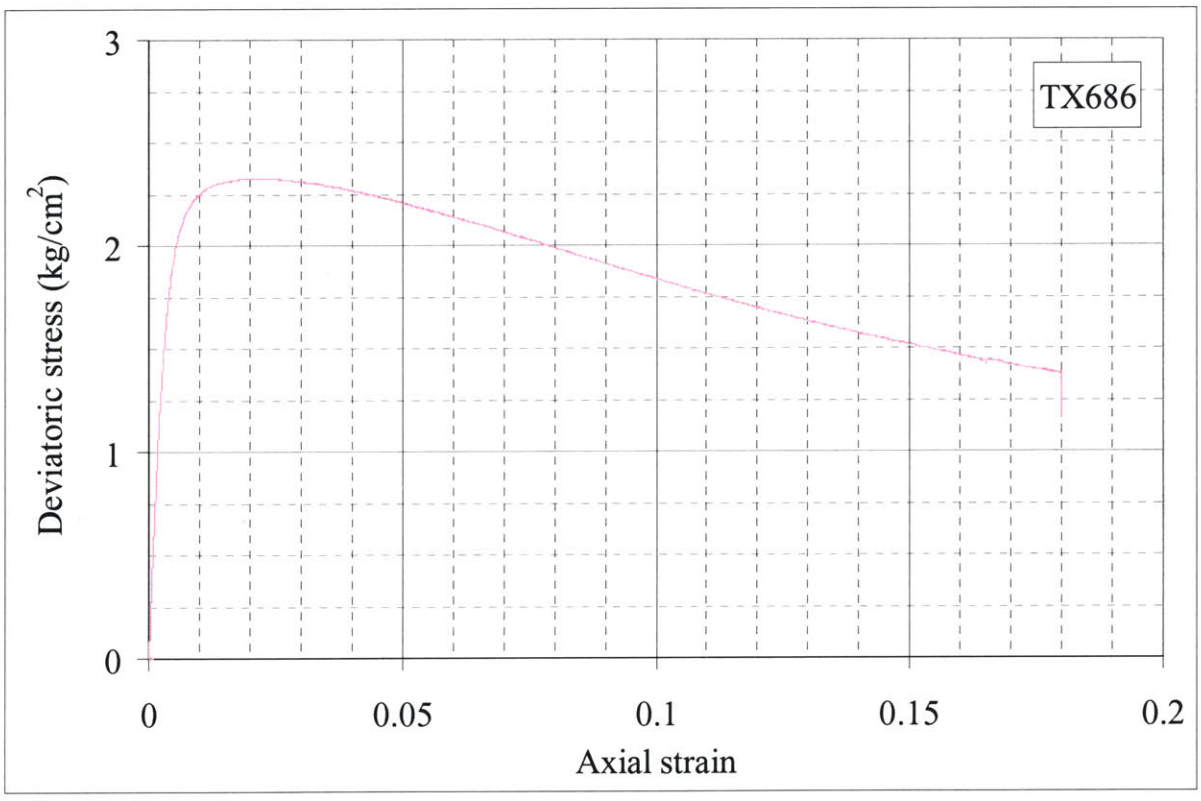

Appendix 6.5. continued

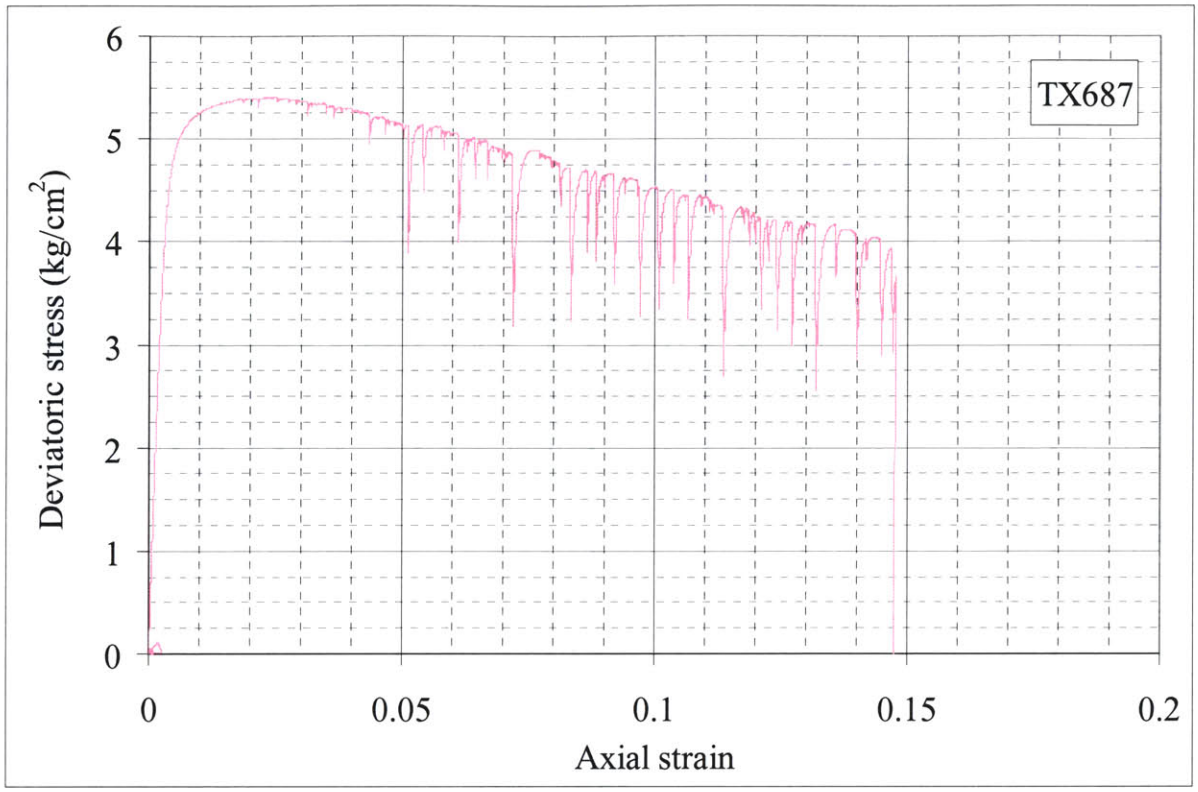

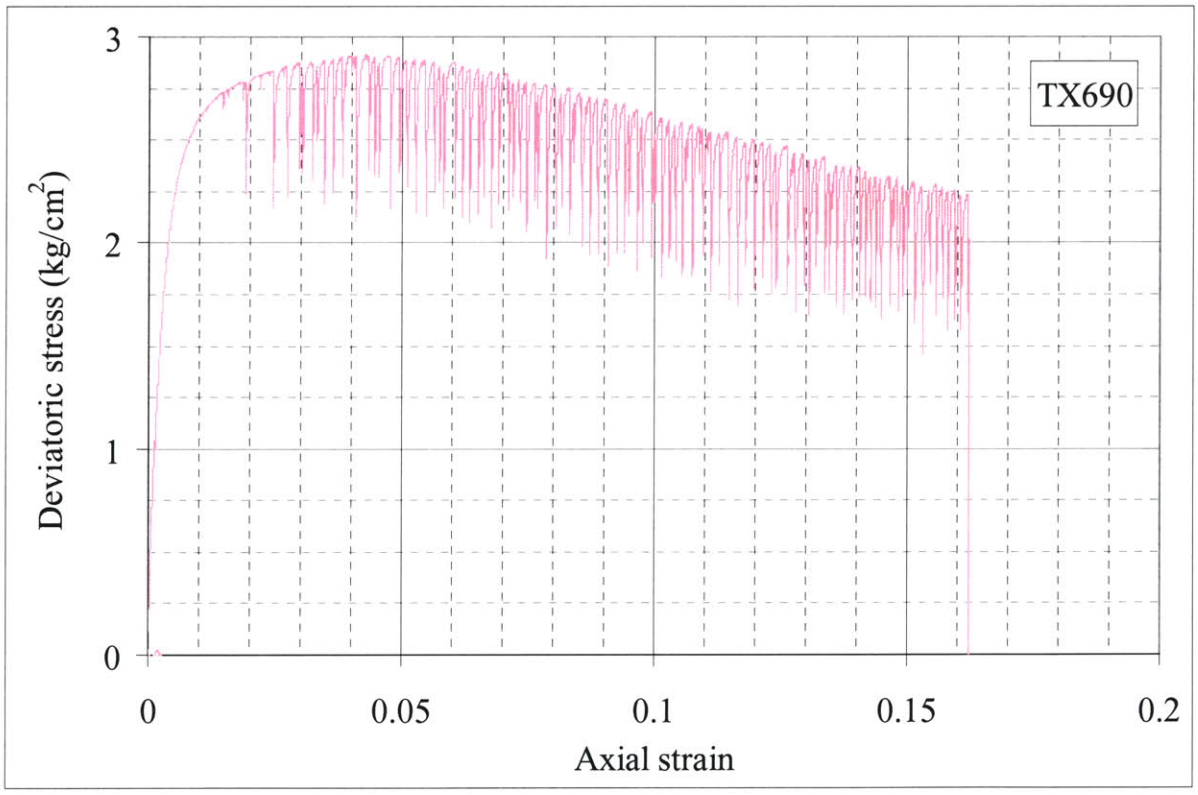

Appendix 6.5. continued

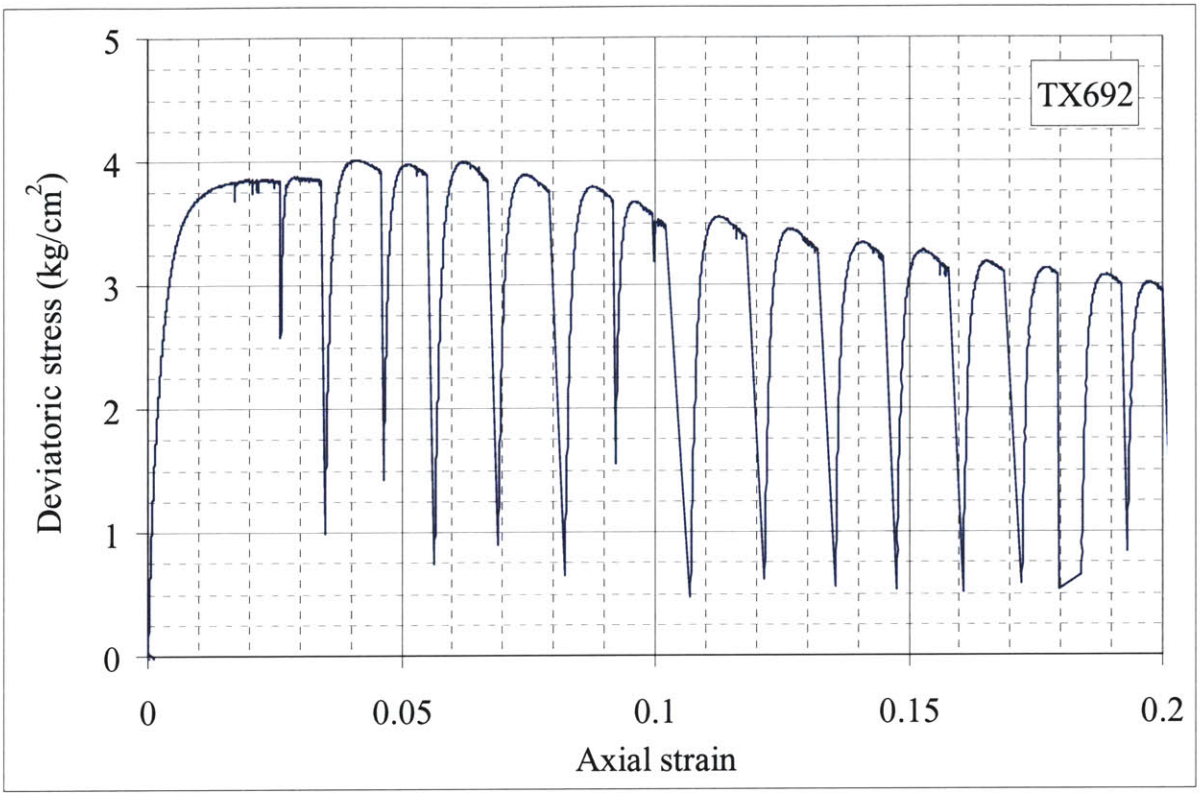

Appendix 6.6. Post-shear deformed shapes. Dash-lines show initial specimen geometry.

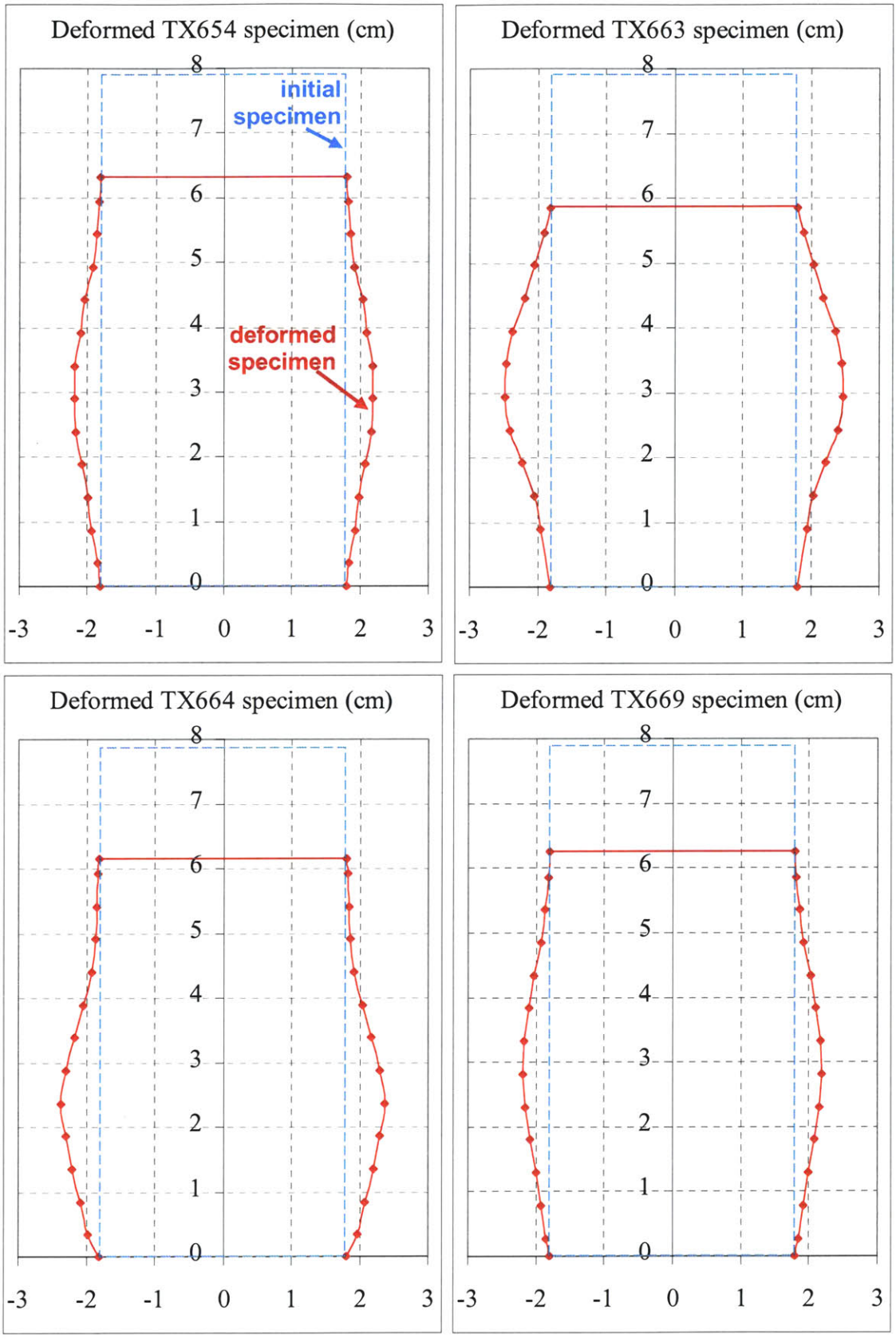

Appendix 6.6. continued

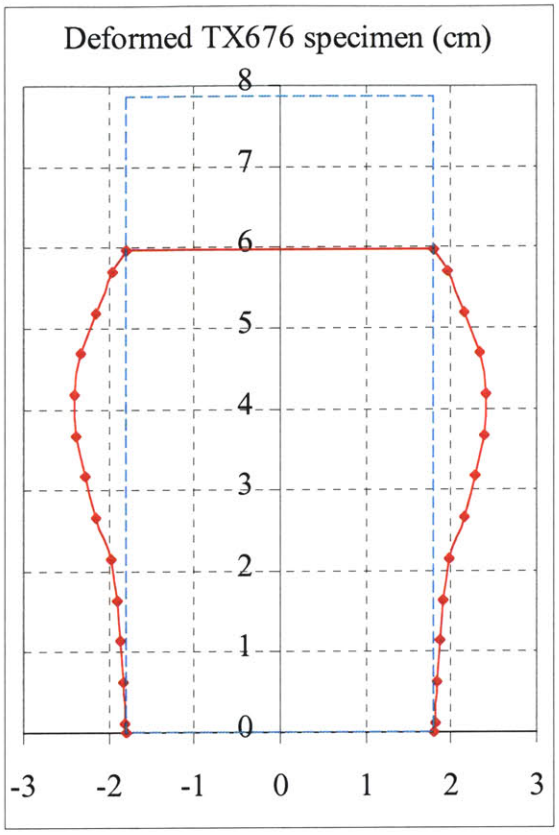

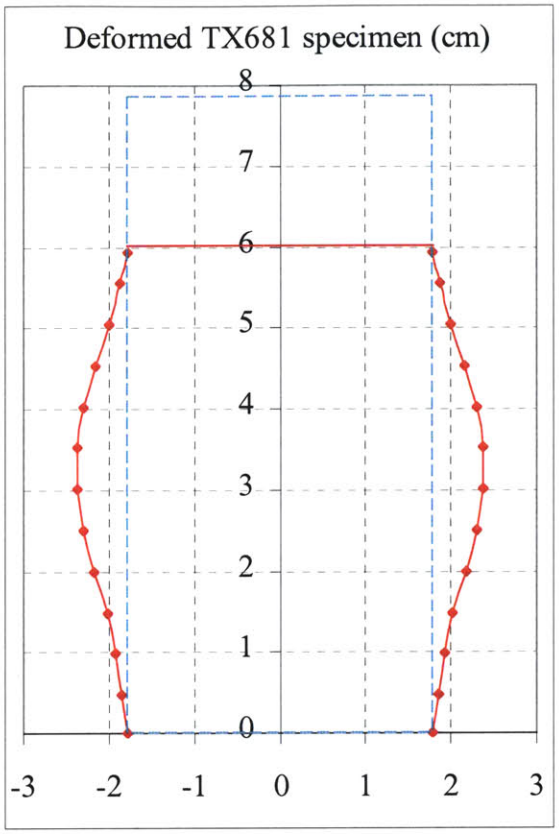

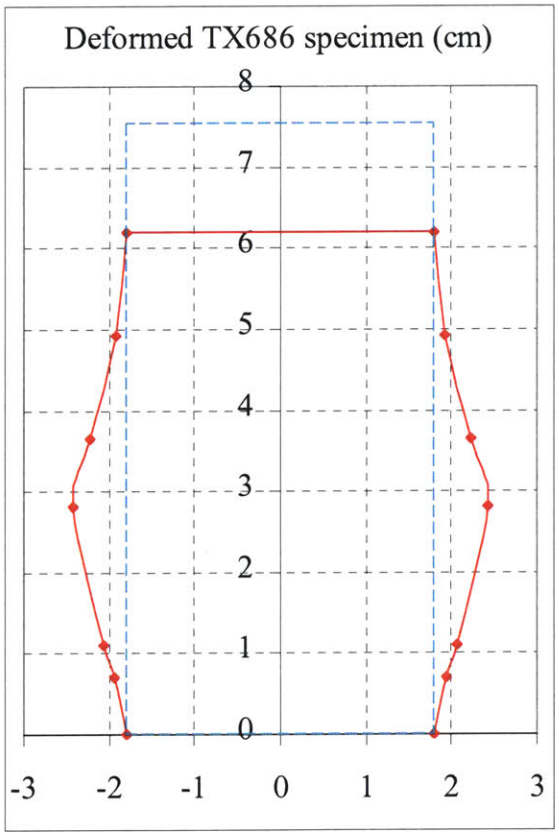

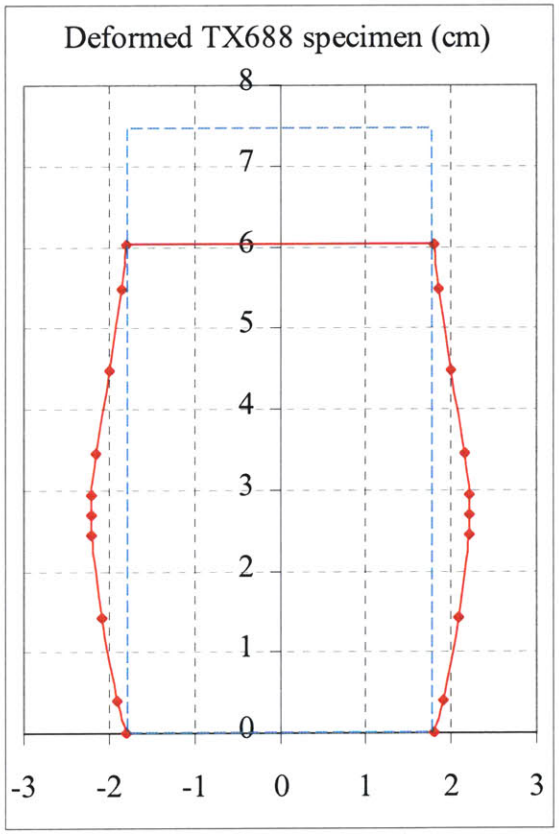

Appendix 6.6. continued

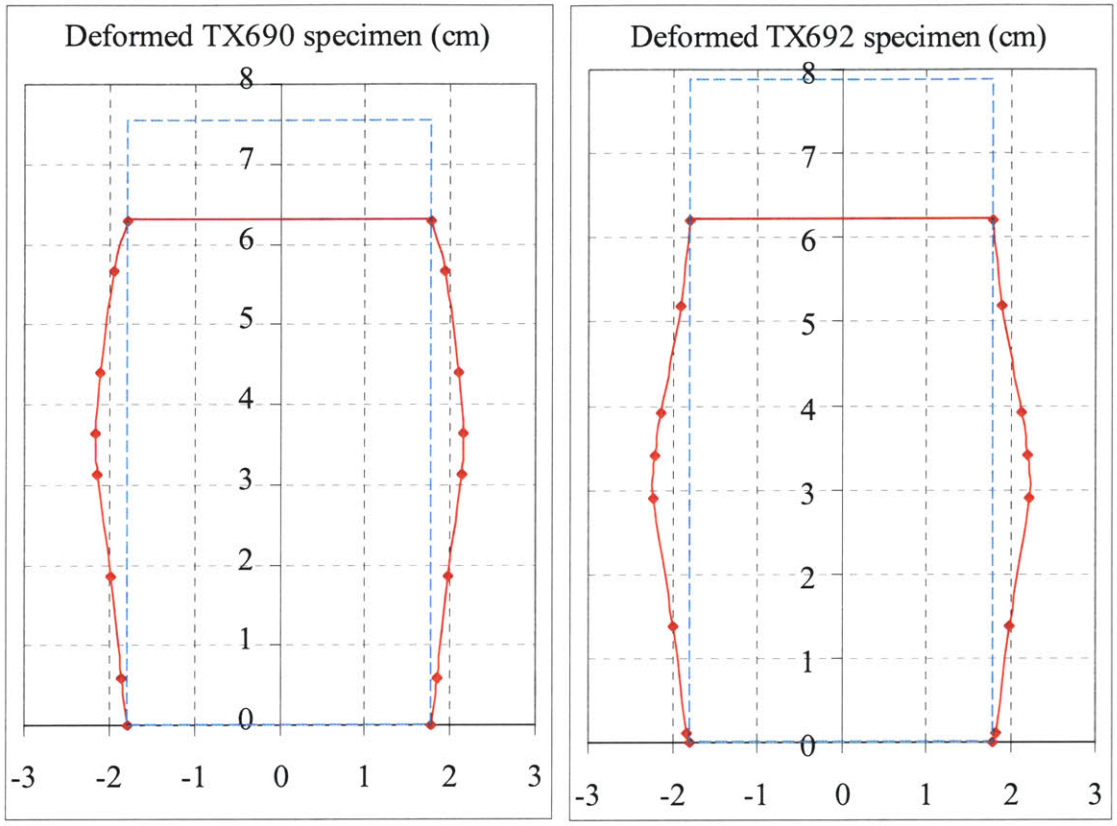

Appendix 6.7.a. Reduced curves for saturated tests on Type 1 material.

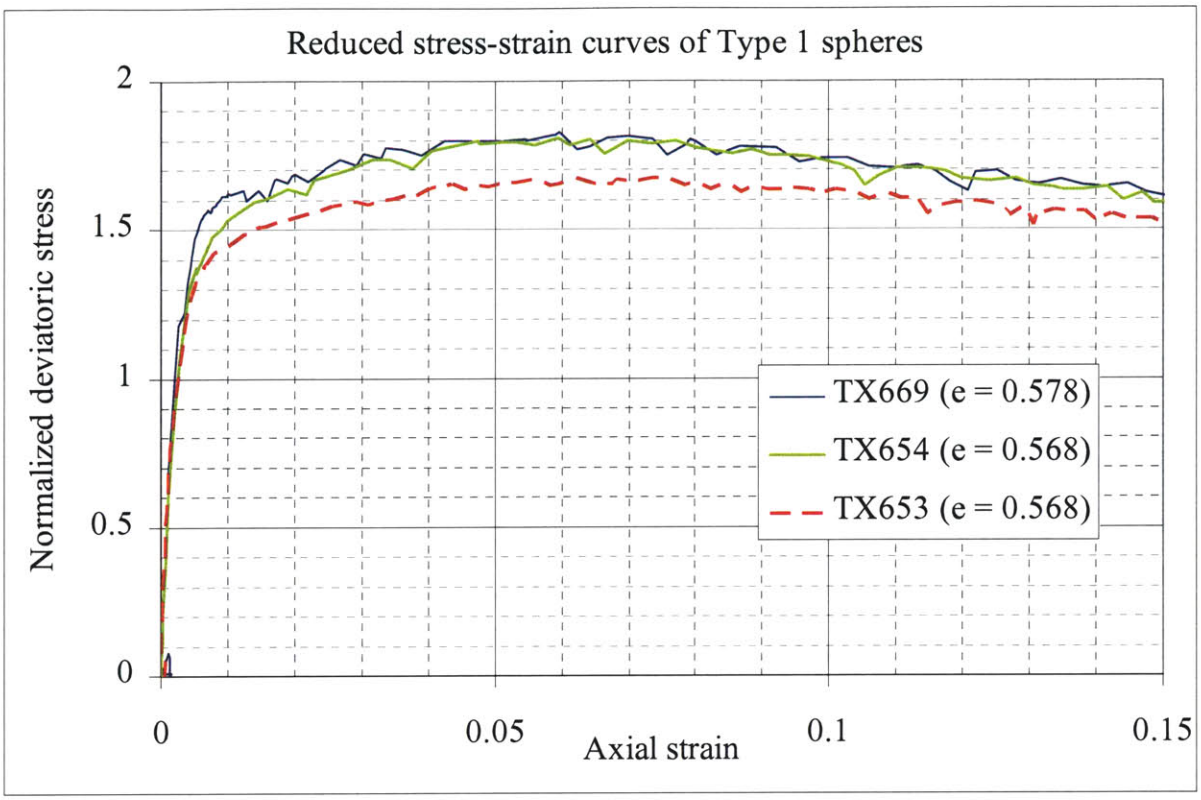

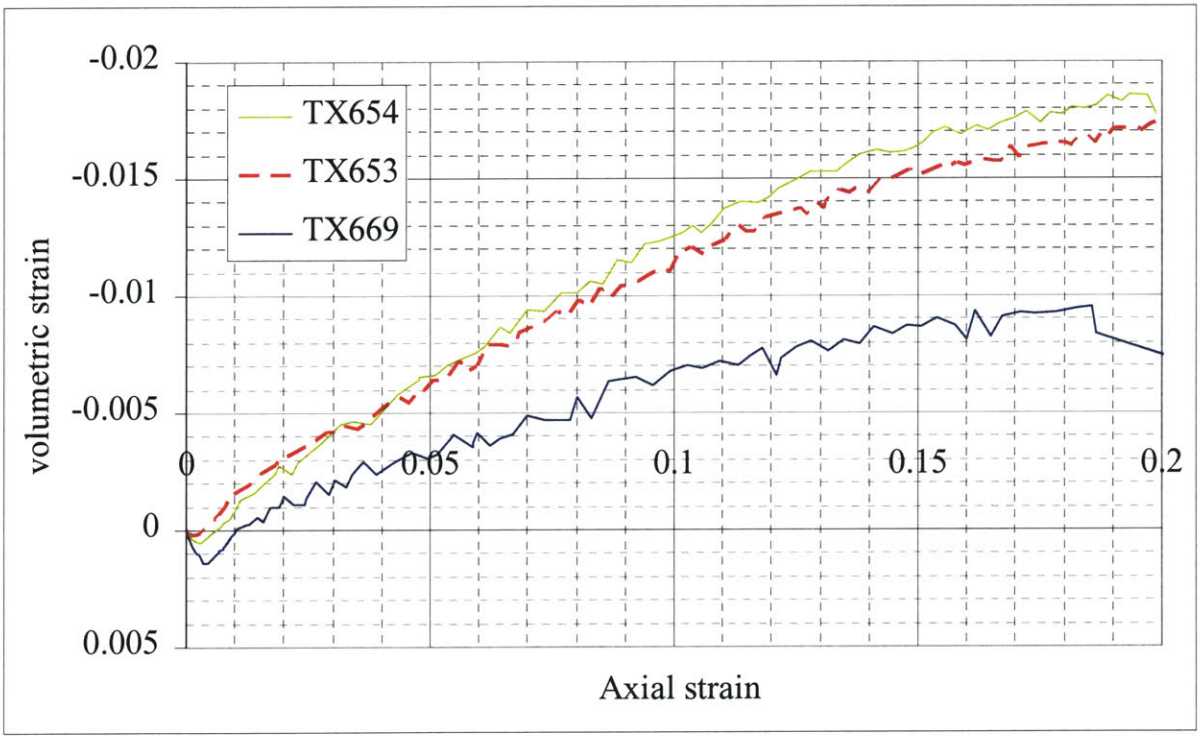

Appendix 6.7.b. Reduced curves for saturated tests on Type 2 material.

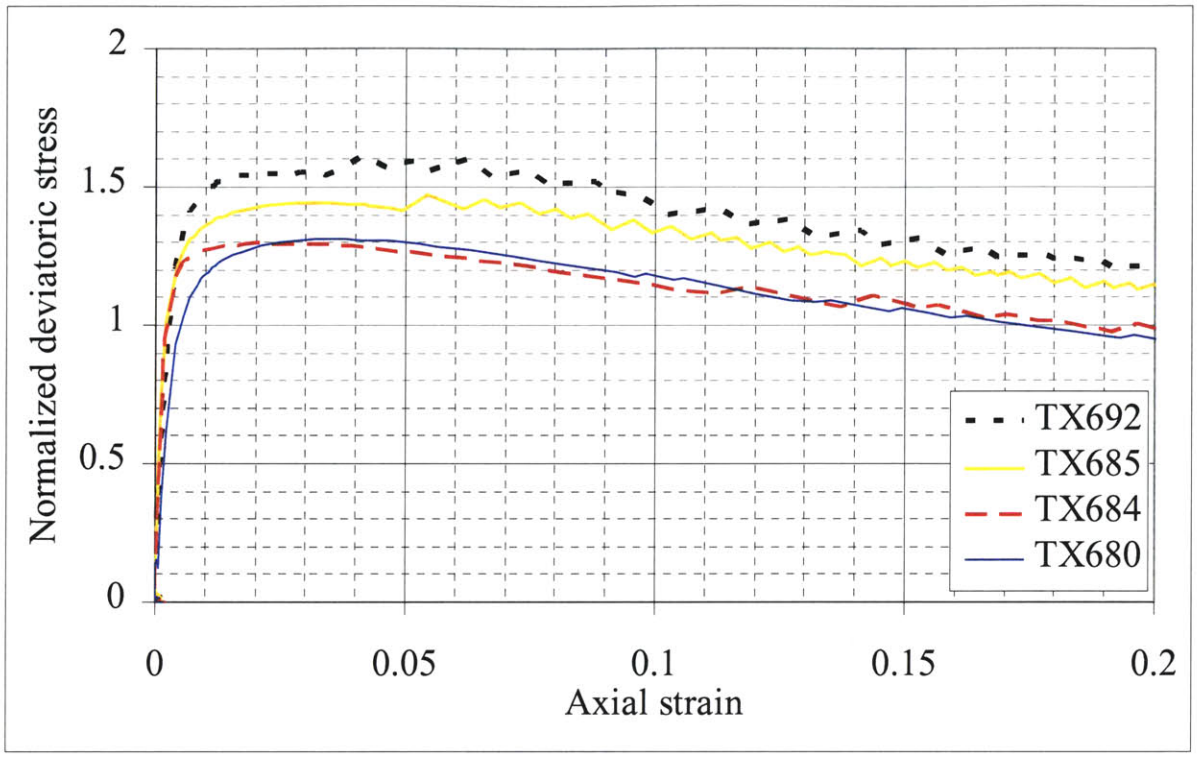

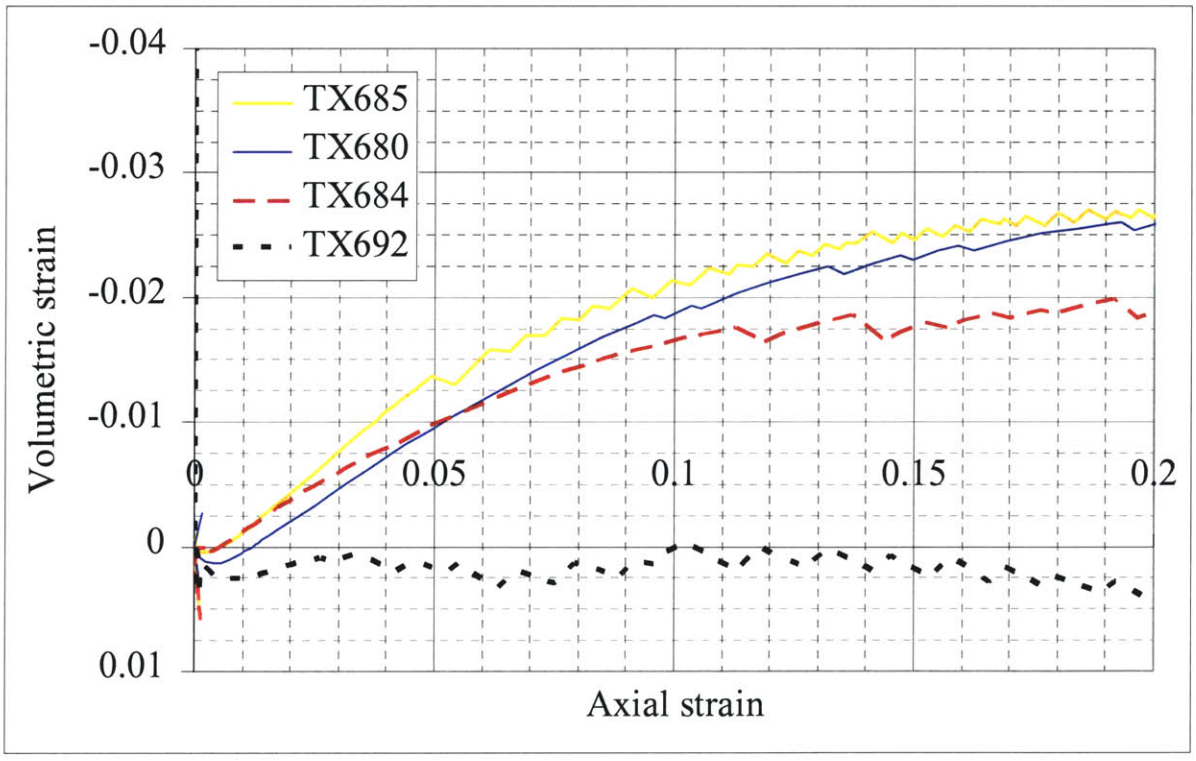

Appendix 6.8.a. Reduced stress-strain curves for unsaturated tests on Type 1 material.

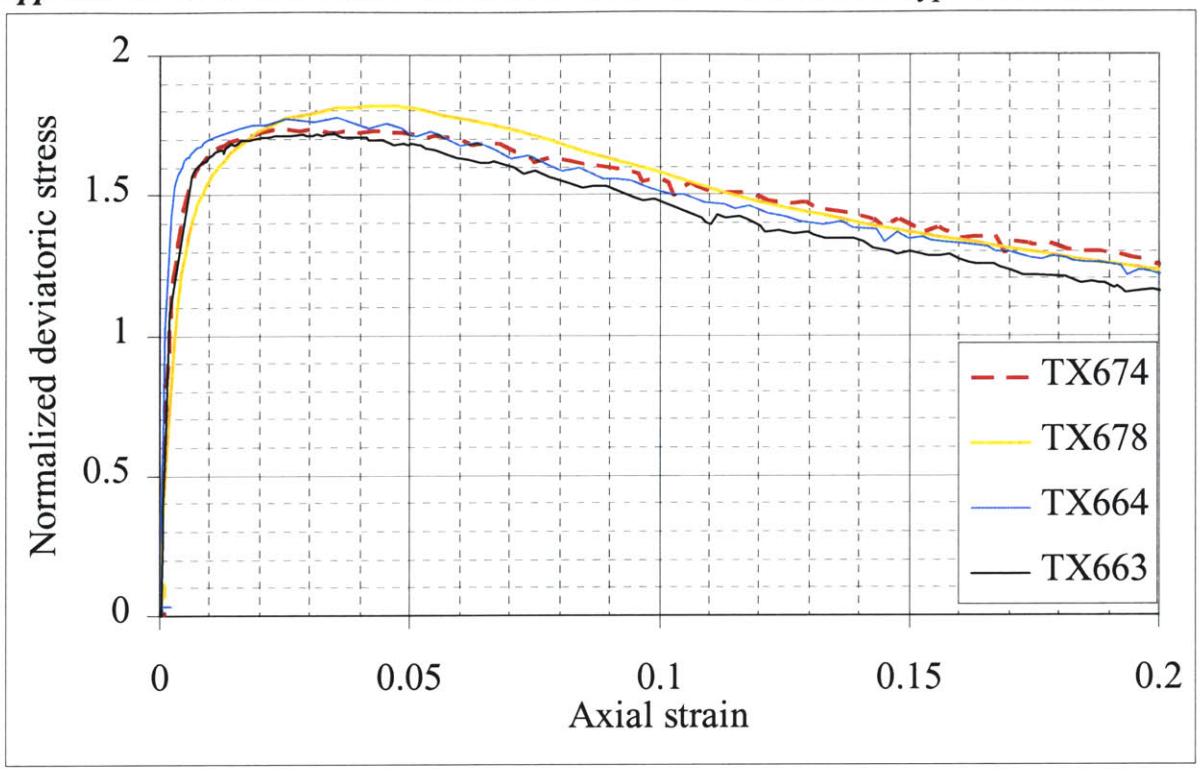

Appendix 6.8.b. Reduced stress-strain curves for unsaturated tests on Type 2 material.

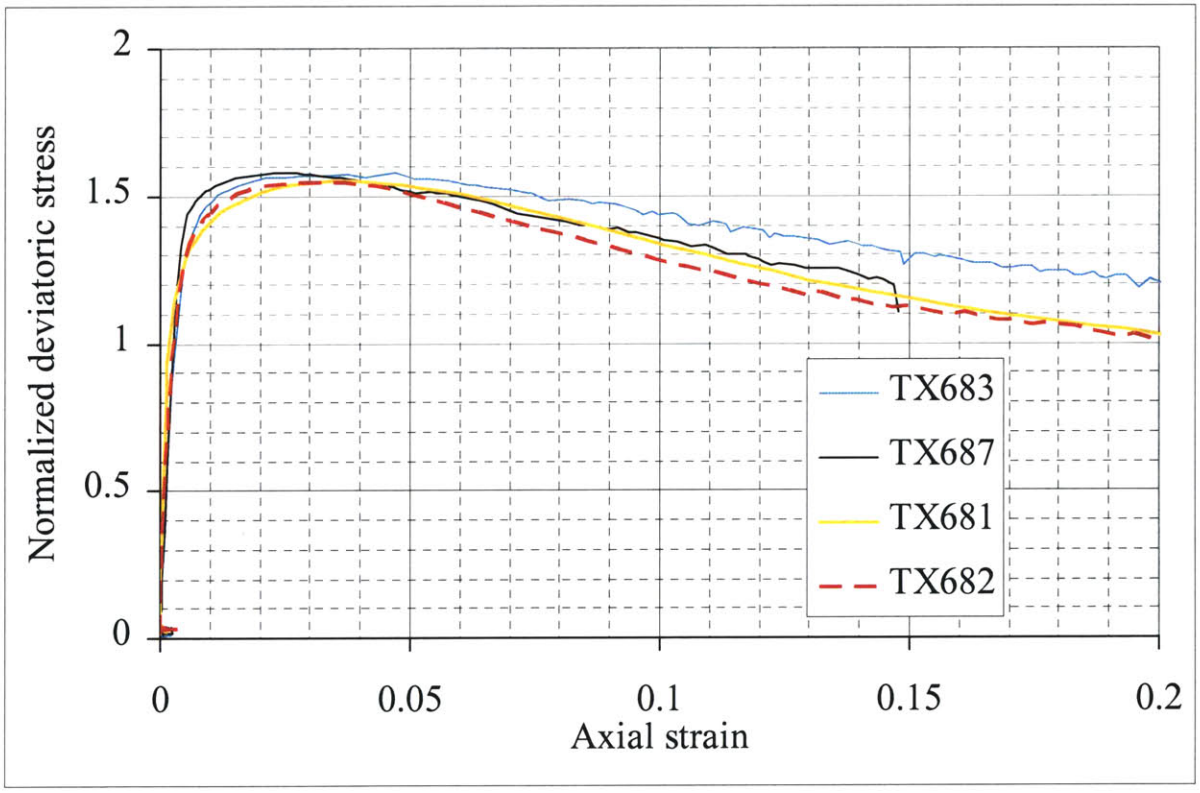

Appendix 6.9. Tensiometer measurements. Time periods marked "c" indicate isotropic compression, those marked as "2" indicate secondary compression, and those marked "s" indicate shearing.

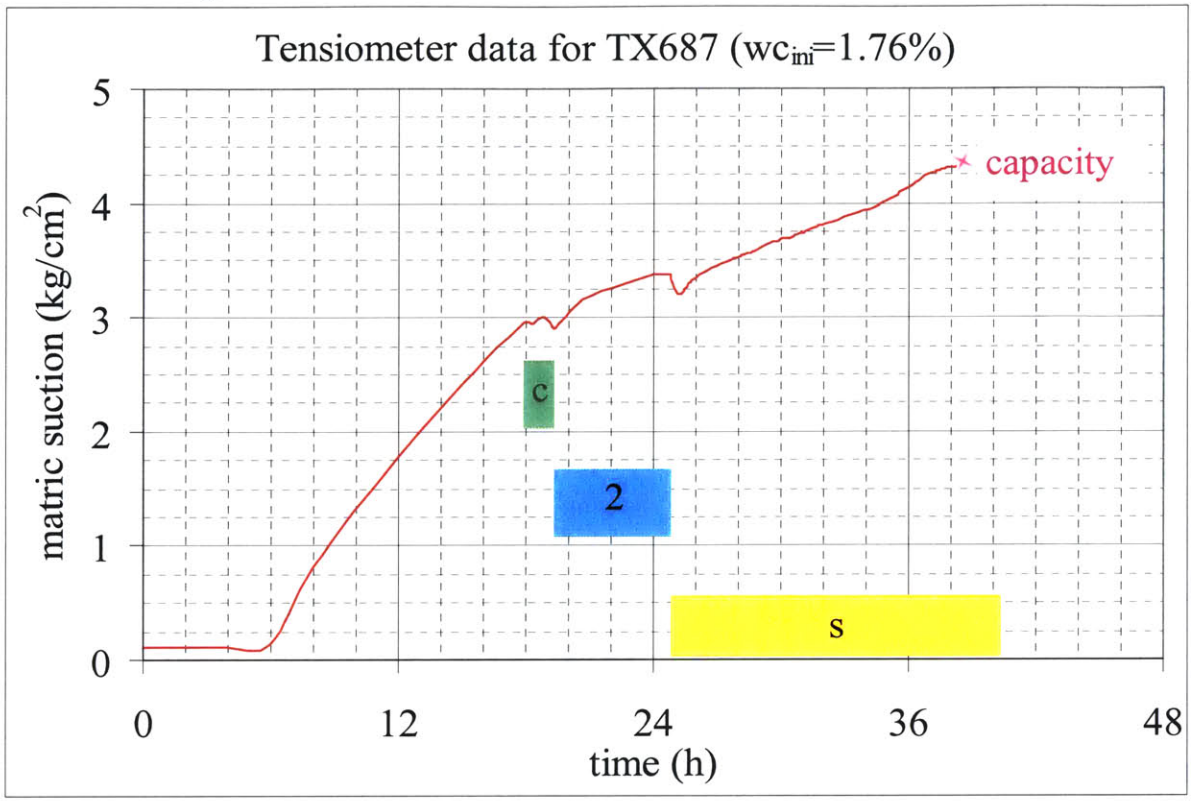

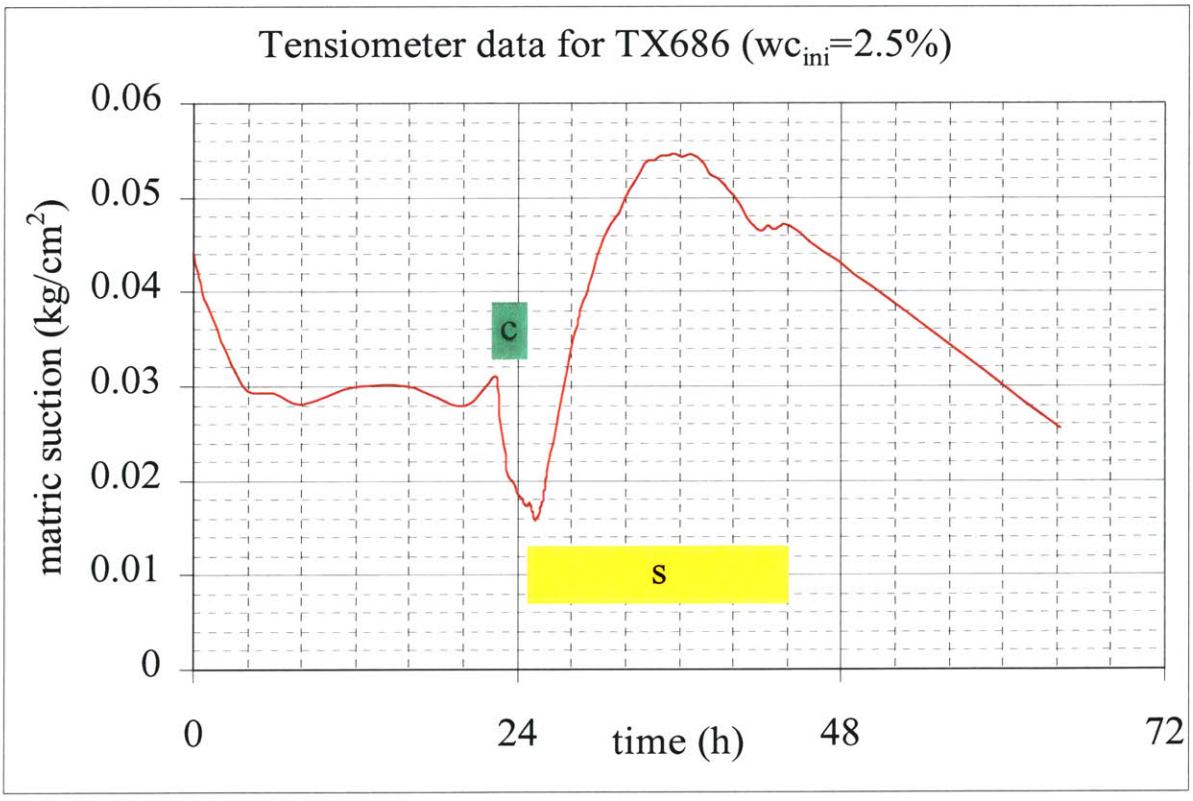

Appendix 6.9. continued

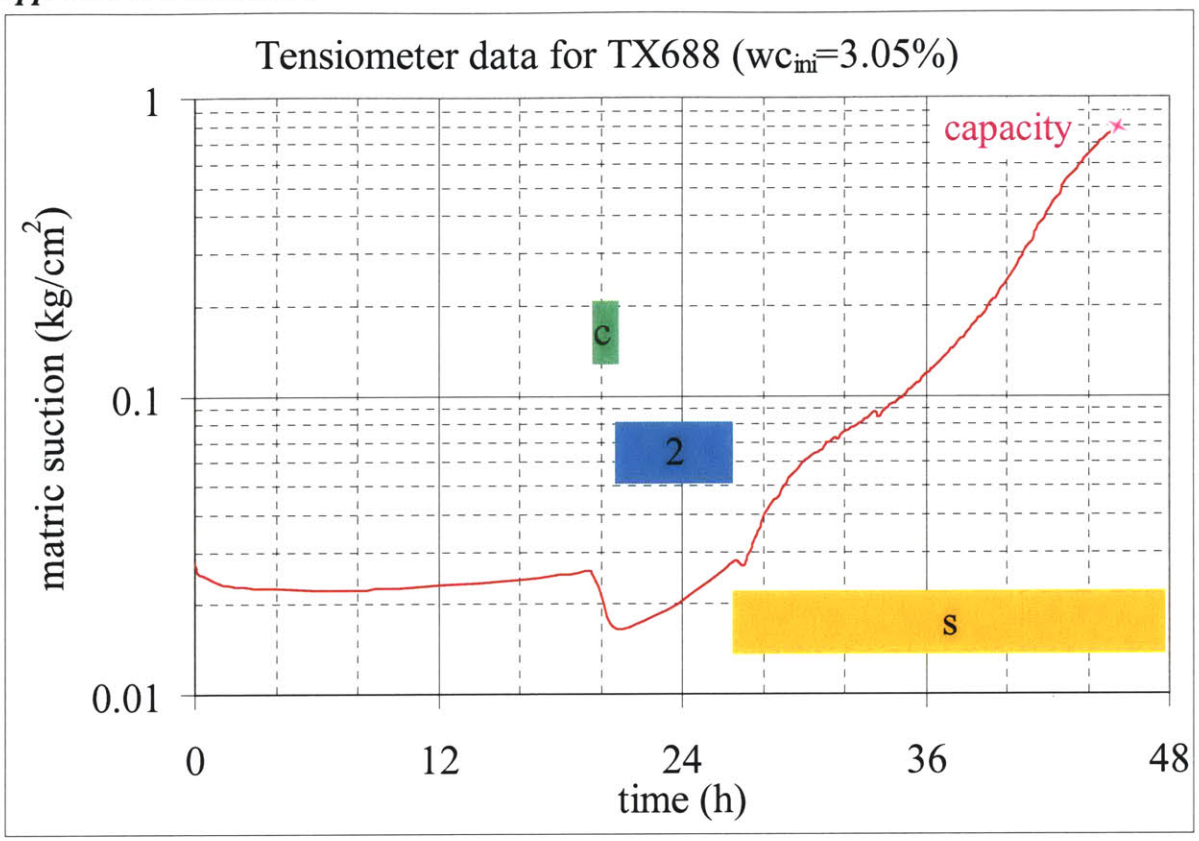

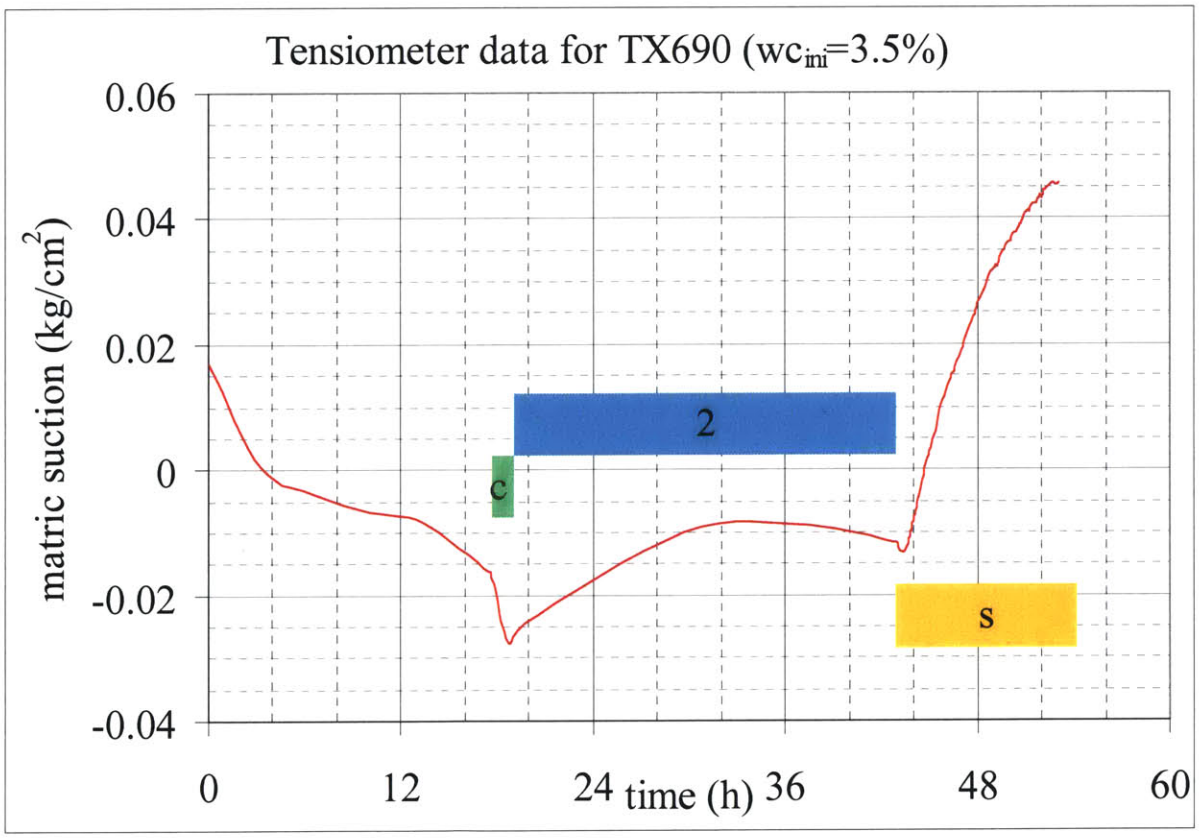

7

INTERPRETATION of RESULTS

7. INTERPRETATION of RESULTS

This chapter complements *Chapter 6* by providing an in-depth analysis of the important findings of the test program and detailed comparison of saturated and unsaturated behavior, Finally, the results are assembled in the framework of the hypothesis described in *section 3.4.2* for comparison between analytical and experimental results for the increment in effective stress due to suction.

The naming convention of the ***model*** (for analytically estimating the effective stress increment due to suction - *sections 3.2* and *3.3*) and the ***hypothesis*** (inferring the effective stress increment due to suction, from the saturated and unsaturated shear strength envelopes – *section 3.4.2*) will continue in this chapter.

7.1. Stand-Alone Interpretations

7.1.1. Stress Drops

The cycles of stress drops that were observed throughout most of the experiments, were introduced in *section 6.2.1.1*. Seemingly random stress drop cycles in tests on uniform round particles have also been measured by other researchers (Ting, 1981; Ovando-Shelley, 1986; Anthony & Marone, 2005). A plausible explanation for the stress drops is a mechanism involving a layer of particles suddenly moving outwards from one gap to the other over another layer of particles, followed by a totally different layer moving in a similar pattern. Such a mechanism would not only exhibit stress drop cycles, but also lead to concentated strain in the center of the specimen.

Contrary to the apparent randomness of the stress drop cycles, the local peaks of cycles seem to follow an elastoplastic stress-strain curve, which represents the overall behavior of the material, as discussed in *section 6.2.1.1*. This may be a reflection that continuum response represents the aggregate behavior of many force chains - and gives an overall envelope on the behavior (making and breaking) of individual force chains (apparent stick-slip). Effects of individual force chains become more apparent in glass spheres due to the uniformity of particle size, shape and surface roughness

Occurrence and magnitude of the stress drops show large differences between the tests. The table below (*7.1*) reports the amplitude ranges and average intervals (of axial displacement) of the measured stress drops. For comparison, the average grain size of the materials is about 0.11 mm. It is followed by *Table 7.2*, which shows the average values of amplitudes and intervals over groups of tests, separated by material and saturated/unsaturated distinctions.

From these results, the following observations can be made about stress drops:
1. They always occur in saturated tests.
2. They are larger in magnitude in the saturated tests, compared to unsaturated tests.
3. The interparticle attraction in the form of pendular rings in unsaturated material may prevent some of the particles from moving away from each other suddenly when they

move around other particles. This would remove the discontinuous behavior for some of the particles in the specimen, reducing the overall appearance of the stress discontinuities in unsaturated tests.

Table 7.1. Amplitude ranges and average intervals of stress drops. Drops that are smaller than 10% of the deviatoric stress (2q) are ignored for the average interval calculations.

				Stress drops	
Material	Test Type	Test No	σ_c (kg/cm^2)	Amplitude (% of 2q)	Av.Interval (mm)
Type 1	saturated	tx653	0.97	40 - 70	0.17
		tx654	1.64	40 - 75	0.20
		tx669	2.61	30 - 75	0.27
	sealed	tx663	1.01	0 - 30	0.43
		tx664	1.64	0 - 30	0.37
		tx674	2.50	10 - 40	0.33
		tx678	0.486	None	None
	unsealed	tx676	1.60	0 - 35	0.47
Type 2	saturated	tx680	1.01	35 - 60	1.56
		tx685	1.74	45 - 75	0.59
		tx692	2.53	60 - 90	0.94
		tx684	2.49	50 - 85	1.25
	Tensiometer	tx686	1.72	None	None
		tx687	3.48	0 - 40	0.37
		tx688	1.73	20 - 30	0.13
		tx690	1.73	20 - 35	0.12
	sealed	tx681	0.96	None	None
	unsealed	tx682	0.99	15 - 30	0.50
		tx683	2.47	0 - 30	0.21

Table 7.2. Averages of amplitudes and intervals of the stress drops for groups of tests. Test without stress drops aren't included in the averaging.

Material	Test type	Average amplitude (% of 2q)	Average interval (mm)
Type 1	saturated	55	0.22
	unsaturated	18	0.40
Type 2	saturated	64	1.09
	unsaturated	22	0.27

4. They are more frequent in saturated tests on Type 1 material, compared to unsaturated tests on the same sample. For Type 2 material, the opposite is true for the frequency of the drops. There are a few unsaturated tests whose results were continuous, and therefore were exceptions to this observation.
5. With the exception of saturated Type 1 samples, larger and more frequent stress drops occur at higher stresses. All continuous tests (i.e. tests without stress drops) are tests that are run under lower confining stresses, among the tests of the same type. A possible

explanation for this is microscopic indentations occuring at the contacts between the glass spheres under higher stresses. This may then cause shear behavior to be in the form of a stick-slip mechanism.

6. Stress drops appear to be more pronounced in test setups with a smaller load frame stiffness. Although the numbers in *Table 7.1* do not directly support this speculation, very close examination of the drops in some later tests (especially TX692 – see last graph in *Appendix 6.5*) show that each stress drop is accompanied by a sudden positive strain increment in the axial strain.

In summary, the materials being poorly graded and with very round particle geometry somehow allows infinitesimal but widespread plane slips. While the details listed above seem rather random, it is clear that the water forces of the pendular rings act in opposition to this brittlely erratic stick-slip phenomenon and reduce the magnitudes of drop in stress. Although not directly relevant to the research, it is an additional revelation about the inner workings of pendular rings.

7.1.1.1. Excess Pore Pressure Cycles

As seen in *Figure 6.4*, each stress drop was accompanied by a jump in the pore pressure (for saturated tests only), hinting at some sort of undrained behavior. This is reasonable, because any particulate material reacts to sudden stress changes by temporarily developing excess pore pressures (i.e. undrained behavior). The magnitudes of pore pressure jumps corresponding to similar magnitudes of stress drops appear to show no trend or similarity to each other, but this is very likely due to measurement inaccuracy (A system can not accurately record a change of a few seconds while it is reading a data point every 15 seconds). Theoretically, the jump in the pore pressure would be momentarily equal to the drop in mean total stress (σ_{oct}).

7.1.2. Effects on Suction

The observations made by matric suction measurements were listed in *section 6.2.2.2*. Two of those are relatively more important and deserve deeper interpretation.

The first observation is that matric suction decreases under isotropic compression. This may be due to elastic compression of the specimen matrix, probably concentrated at particle contacts at the micro-scale. When two particles are pressed together in this fashion, the pendular ring between them will have to expand (without change in water volume), reducing its surface curvature and matric suction.

Secondly, matric suction was observed to increase during shearing. The process of shearing breaks many particle contacts, and the engulfing pendular rings as two particles of the matrix move away from each other. A portion of the water that had been contained in such a pendular ring might evaporate and leave the system (to the humidifying reservoir), as it no longer has the low energy of a stable pendular ring. This would leave less water (more suction) for a new pendular ring that would be formed at a newly formed contact.

7.2. Comparison between Saturated and Unsaturated Tests

The consistency within each set of saturated and unsaturated tests provided the ability to observe the differences associated with suction (i.e. differences between the results of saturated and unsaturated tests). The two materials are observed to have slight differences regarding the effect of suction on shear behavior. There is no significant behavioral difference among types of unsaturated tests (i.e. sealed, unsealed, tensiometer).

7.2.1. Generalized Comparisons

7.2.1.1. Axial Strains at Yield and Peak Deviatoric Stress

Unsaturated specimen reach a higher yield stress at similar axial strain in comparison to the saturated specimen. The axial strains at yield are between 0.55 and 1.27 %. Type 1 spheres have significantly lower yield strains. Afterwards, the unsaturated tests reach peak deviatoric stresses at lower strains than their saturated counterparts. For Type 1 spheres, this difference is more pronounced: the strains at peak stresses range from 2.33 to 4.24 %, which is approximately half of the saturated case on average. In the case of Type 2 spheres, the peak stress occurred between 2 and 4.67% axial strain, which on average is 0.4 % less than the strains in saturated tests. *Table 7.3* demonstrates these results by comparing the average yield and peak strains of unsaturated versus saturated tests on both materials.

Table 7.3. Averages ± standard deviations of axial strains at yield and peak stresses from all tests.

Material	Test type	axial strain at yield (%)	axial strain at peak stress (%)
Type 1	saturated	0.67 ± 0.11	6.42 ± 0.81
	unsaturated	0.81 ± 0.21	3.43 ± 0.69
Type 2	saturated	0.96 ± 0.22	3.80 ± 1.38
	unsaturated	1.02 ± 0.16	3.41 ± 0.97

7.2.1.2. Work

Work, as the product of *force* (or stress) and *displacement* (or strain), directly depends on both of these variables. In order to see any trend outside the stress and strain trends, effects of stress and strain variation from test to test must be eliminated. For the stress aspect, work terms will be normalized by the confining stress for comparison. For the strain aspect, the work quantities calculated with the equations above can only be compared if they are upto the same strain. For instance, comparing work upto the peak stresses will not be viable, as the axial strains corresponding to the peak stresses vary between 2 and 7.35 %. Consequently, the comparison will be made for a specific axial strain, namely 1%, 2% and 15%. This means the work summations in *Eqs. 5.20* and *5.21* will include the data only upto these specific axial strains.

Full listing of the work done on the specimen by deviator stress upto 1%, 2% and 15% axial strains, and in the case of saturated tests, work done by the confining stress can be found in *Appendix 7.1.* Work done by the deviator stress and the total work done in the experiment TX653 are plotted in *Figure 7.1.* Work done by the confining stress is the difference between the two graphs, and it is negative. Work by the confining stress can not be calculated for the unsaturated tests due to the absence of volume change measurement. As mentioned in *sections 6.2.1.2* and *6.2.2.3*, the volumetric deformations are low compared to the axial for all kinds of tests performed in this research. Therefore, a comparison of work done by the deviator stress alone would reflect the majority of the total work.

Figure 7.1. Work done on the specimen of TX653

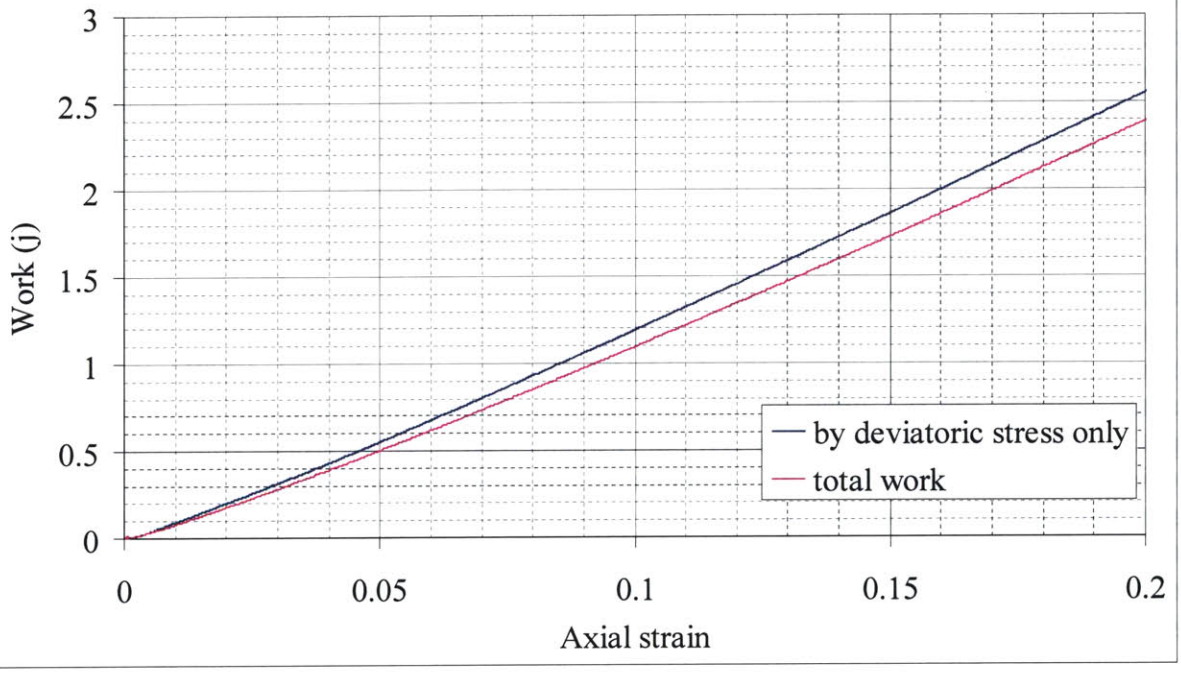

Table 7.4. Averages ± standard deviations of work by deviator stress, normalized by σ_c.

Material	Test type	Work done on the specimen by deviator stress, normalized by σ_c, (cm^3), upto		
		1% axial strain,	2% axial strain,	15% axial strain,
Type 1	saturated	0.093 ± 0.004	0.209 ± 0.009	1.946 ± 0.034
	unsaturated*	0.104 ± 0.011	0.241 ± 0.014	2.190 ± 0.054
Type 2	saturated	0.082 ± 0.010	0.191 ± 0.018	1.690 ± 0.081
	unsaturated	0.084 ± 0.008	0.202 ± 0.013	1.863 ± 0.087

*: calculated by ignoring the test TX676, which had less strength, possibly due to moisture equilibrium problems.

There is no trend within groups of tests (each of the four lines in *Table 7.4* are the groups for this purpose). Between different types of tests, two results are observed:

1. In all cases, unsaturated tests require more work than saturated tests to shear. This is speculated to be because moving and breaking pendular rings require additional energy.
2. In all cases, Type 1 material requires more work than Type 2 to shear. The extra energy is speculated to be spent on
   a) the pendular rings, which are more in number for Type 1 specimen,
   b) overcoming a slightly greater overall shear strength (see *section 7.3*).

7.2.2. One-to-One Comparisons

As described in *section 6.2.3.3*, results of both saturated and unsaturated tests are affected by void ratio. Therefore, results of a test can not be compared to another test unless their void ratios are close. If a particular test condition was run multiple times at the same stress level but with different void ratios (none of which match the rest of the tests), a virtual result can be interpolated between tests, such that its void ratio would have been acceptably close to other tests. Such an interpolation was deemed necessary in two cases, as described in the next two paragraphs.

In the case of Type 2 material, the unsaturated test, designated as TX683, does not have a saturated counterpart with the same void ratio. Instead there is the pair of TX684 and TX692, which were prepared at different initial water contents, and then tested at the same confining stress as TX683. The specimen of TX684 is looser and that of TX692 is denser, in comparison to the specimen of TX683. Through linear interpolation of stresses (at yield, peak, or large axial strains) between the two saturated tests, weighted with respect to their void ratios, the stresses at the corresponding strains can be estimated for an imaginary saturated test on a specimen with the same void ratio of the rest of the tests. This brings the too dense or too loose specimen to the relatively more consistent void ratios around 0.653 and 0.654, which are the average values for the rest of the saturated and unsaturated specimen, respectively.

A similar interpolation, this time between results of the unsaturated tests TX688 and 690 was necessary to approximate a counterpart to the saturated test TX685. Results of these two interpolations are used to generate further results in *Section 7.3*, rather than the individual results of the pairs of experiments contributing to each interpolation.

Appendix 7.2 shows comparisons between pairs of saturated and unsaturated tests of similar confining stress and initial void ratio. According to these plots, axial stresses at yield are higher in the unsaturated tests. As the shearing progresses, the stress carrying capacities of the unsaturated specimen decrease at a faster rate, compared to the saturated tests.

These interpolations are made only for the few quantities (yield stress, peak stress, etc.) necessary for the final plots of the *Section 7.3*, not the entire stress-strain curve. Thus the interpolated results are not presented graphically in *Appendix 7.2*.

7.3. Stress Space and the Effective Stress Increment due to Water Forces

The stress increment due to water forces was estimated to be around 0.02 kgf/cm^2 in *section 6.1.3*, based on the model for effective stress. This corresponds to the horizontal difference between the total stresses from the unsaturated tests and the effective stresses from the saturated tests, when plotted in mean stress space (*section 3.4.2*). *Figures 7.2* and *7.3.a* show such plots, created with yield stresses for both materials. *Appendix 7.3* contains similar plots for peak stresses as well as stresses at large (15%) strain. It should be remembered that with increasing strain, reliability of the results decreases, mainly because of the area correction. Therefore, the results at high strains have less weight than the results at yielding, which are the only plots included in the main text.

Figure 7.2. Yield stresses for Type 1 samples.

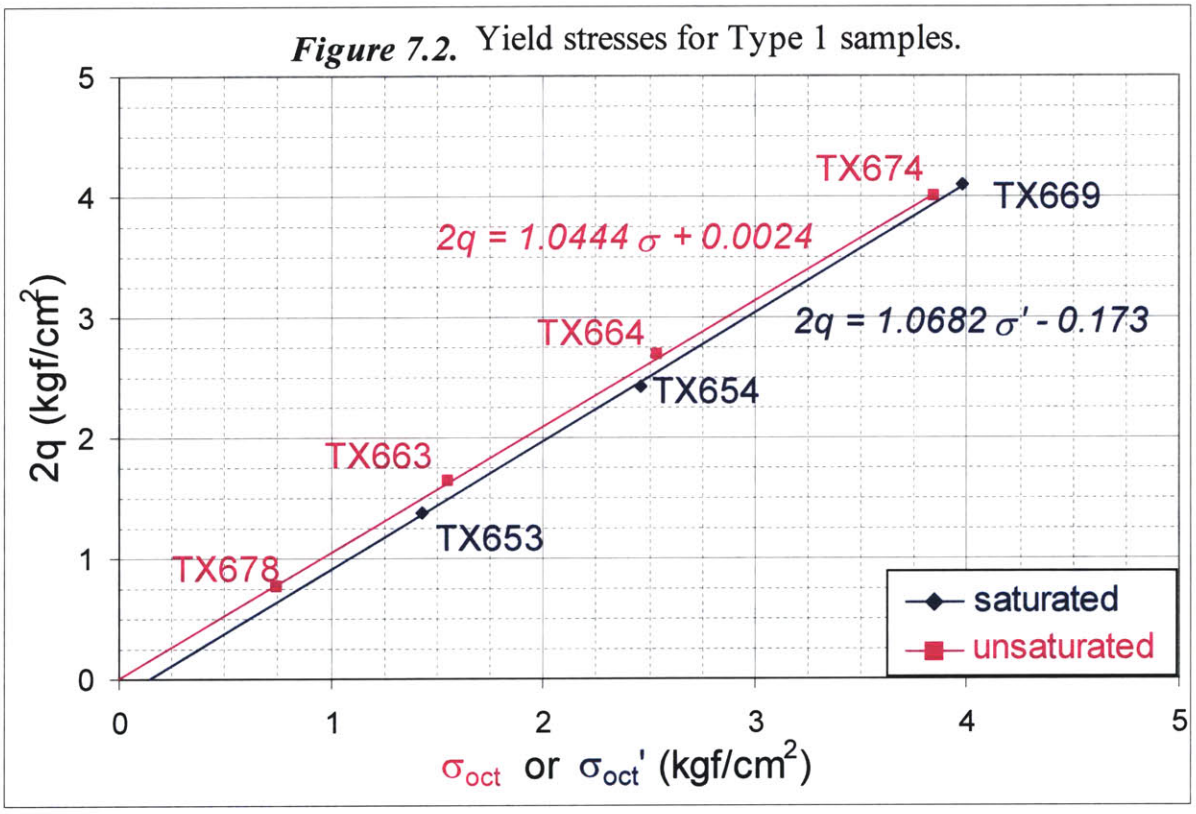

All results appear to form linear envelopes. However, there are two unexpected results that contradict the normal behavior of granular materials:

- In the two plots for the larger strains (peak and 15%) of Type 1 material (*Appendix 7.3*), the saturated envelopes appear stronger than the unsaturated. Given the unreliability of results at large strains, this aspect is not detrimental to the research – the main focus will be the most reliable results, i.e. the ***yield*** strength envelopes.

- Almost all of the envelopes seem to intersect the deviatoric stress axis on the negative side, if they are extended linearly. This will be discussed in greater detail in *section 7.3.1*.

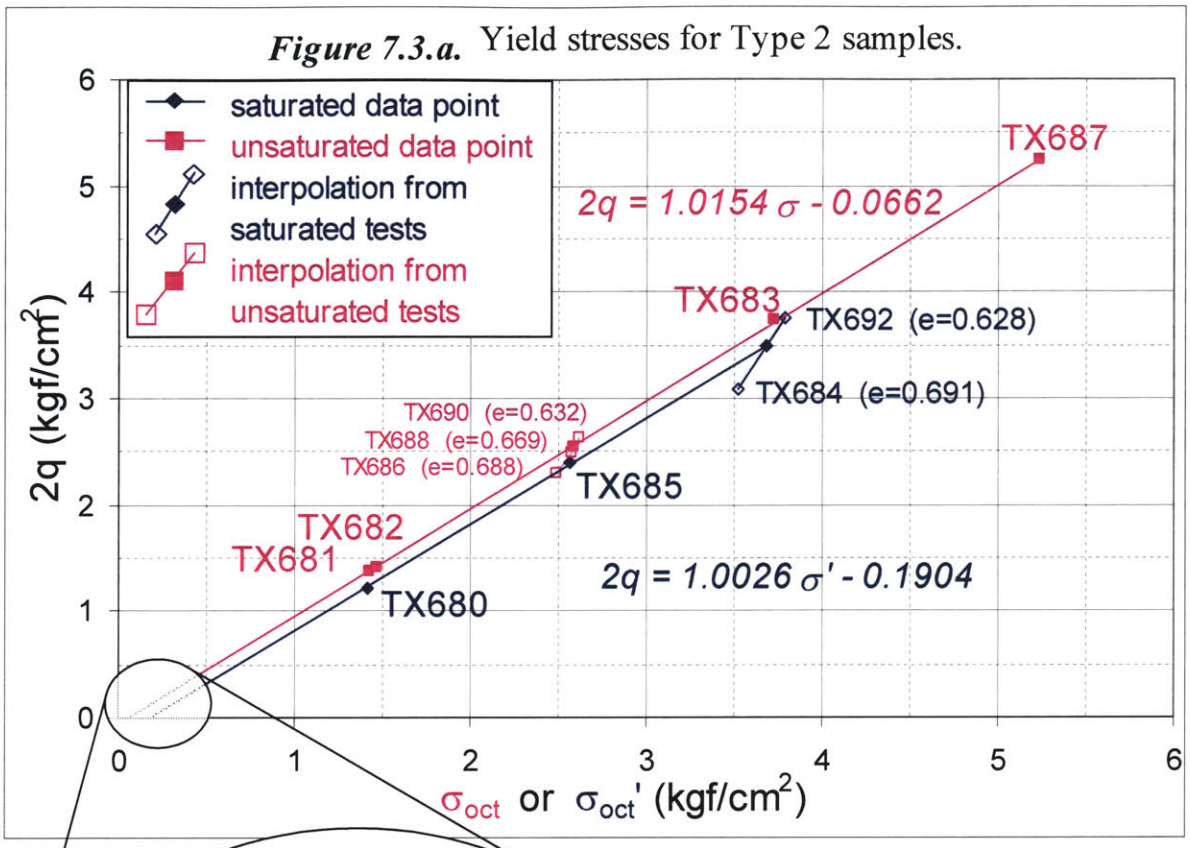

Figure 7.3.a. Yield stresses for Type 2 samples.

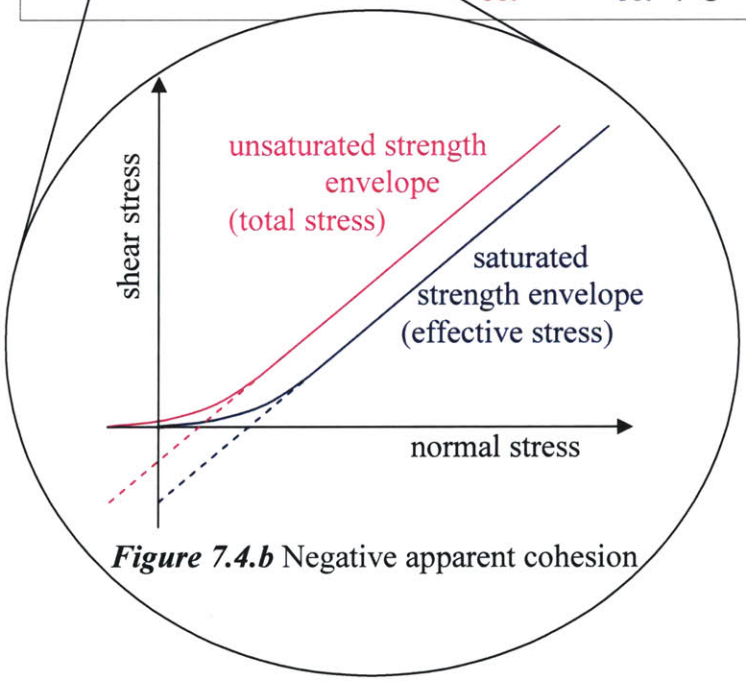

Figure 7.4.b Negative apparent cohesion

As for the main purpose of these plots in mean stress space, *Table 7.5* lists the horizontal differences between saturated and unsaturated envelope, when applicable. These numbers are far greater than the 0.02 kgf/cm^2 that was originally predicted by the model before the experiments (*section 6.1.3*). Therefore, a mechanism that is not accounted for in this research must have significant influence on strength in partially saturated granular materials.

This result may mean that introducing pendular rings into the system is not equivalent to applying additional isotropic effective stress. Pendular rings increase the normal force at particle contacts without adding shear force, because the water force acts perpendicular to the particle surface. Therefore, increasing shear resistance of the contact. Increasing the isotropic effective stress also increases shear strength. These two increases in shear strength need to be different for ($\sigma'-\sigma$) values in *Table 7.5* to be so high.

Table 7.5. Magnitude of the differences between effective and total stresses (i.e. effective stress increment due to water forces. N/A entries occur when the quantity is zero or less, which is not expected as far as unsaturated soil mechanics is concerned.

	Ranges of $\sigma' - \sigma$ (kgf/cm^2)			ϕ, ϕ' (°)	
Material	yield	peak stress	15% strain	saturated	unsaturated
Type 1	0.07 to 0.12	N/A	N/A	29.2	28.5
Type 2	0.14 to 0.18	0.16	0.09 to 0.18	27.3	27.6

If applying effective stress on a dry material creates shear forces at some of the particle contacts, increase in the capacity for extra shear force (i.e. shear strength) would be smaller in comparison to the shear capacity increase due to the pendular rings (*Figure 7.4*). Since the hypothesis for effective stress increment - shear strength relationship (*section 3.4.2*) is based on macroscopic effective stress, it underpredicts the strengthening effect of pendular rings.

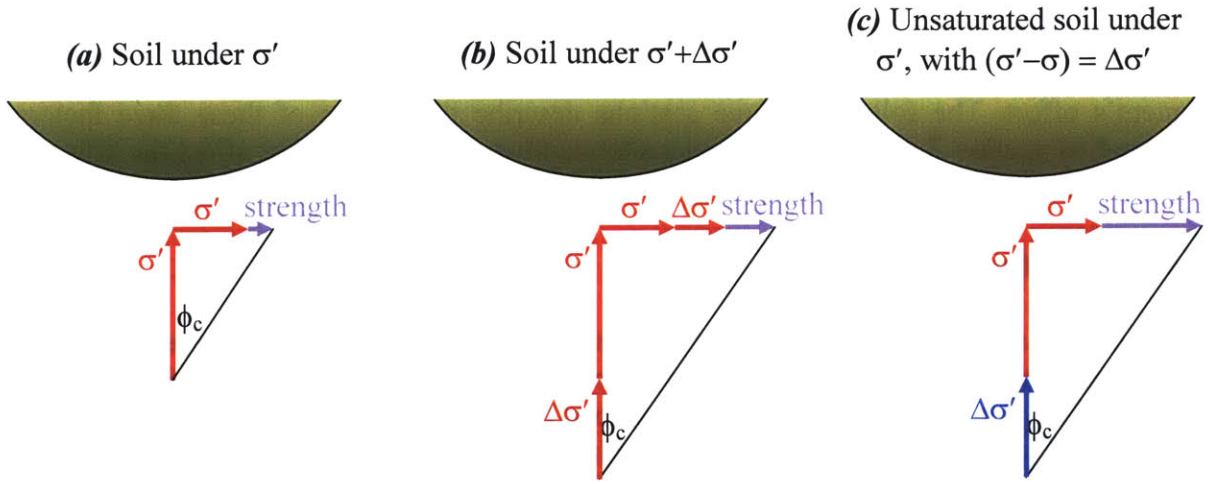

Figure 7.4. Possible difference between a regular effective stress increment and the increment in effective stress due to suction. ϕ_c is the friction angle at the contact, associated to the solid plane – on – solid plane friction, not to be confused with the internal friction angle, or angle of repose, of the granular matrix.

7.3.1. Strength Parameters

Table 7.5 also reports friction angles, calculated from the slope (M) of the envelopes in *Figures 7.2* and *7.3* through the following equation:

$$\phi = \arcsin\left(\tan\left(\frac{3 \cdot M}{6 + M}\right)\right) \qquad \textit{Eq. 7.1}$$

The friction angles calculated above are very similar to the experimentally determined angle of repose of 28.6° for glass beads, reported by Jaeger et al. (1989). This is the friction angle of glass as a granular material, and must not be confused with the friction angle between two glass surfaces.

As mentioned earlier, the cohesion strangely seems to be negative. However, glass spheres under zero stress simply roll around with no angle of repose, as opposed to the friction angles observed under confining stress (reported in *Table 7.5*). Since the glass spheres do not stick together when dry (they are cohesionless), the envelope for the saturated case must start from the origin. These two boundary criteria for the saturated envelope dictate non-linearity at very low stresses, as illustrated in *Figure 7.4.b*. Following the hypothesis, unsaturated strength envelope in total stress space would still be a copy of the saturated envelope in effective stress space, shifted by the effective stress increment due to suction along the normal stress axis.

7.4. Parameters Affecting the Effective Stress Increment

According to the model presented in *Chapter 3*, the increment in effective stress due to suction is affected mainly by the grain size and particle packing. Suction and water content affect it very little, as shown in *section 3.3.4*. Grain size distribution of the two materials were not different enough to create observable differences. Among the remaining three factors, the effect of suction and that of void ratio are found to be intertwined with the water content's effect. The following three sections describe the effects of these three factors, followed by *section 7.4.4*, which will characterize three mechanisms that affect the effective stress increment and/or shear strength.

7.4.1. Effect of Suction

The model in *section 3.3.4* suggests that no matter how much the suction is varied, its effects on effective stress (and behavior) shouldn't change by more than 30% (*Figure 3.12*). This is ***supported*** by the suction readings from the four tests (TX686, 687, 688 and 690) with an incorporated tensiometer. These suction measurements spread over two orders of magnitude (0.04 or less to 4 kgf/cm^2 – see *Appendix 6.9*), and yet the behavior in the triaxial test results are not visibly affected by this variation. Three of the four tests (except TX687) were specifically aimed to observe effects of suction and water content differences, but did not encounter any trend that can be a result of suction variation. Instead, a reverse trend (more strength at smaller suction or larger water content) of the results was observed. This is not attributable to the effect of suction, but it is to ***void ratio*** (see *sections 7.4.2* and *7.4.3*).

7.4.2. Effect of Preparation Water Content

In the two groups of tests in which every aspect of preparation and testing other than the water content was kept constant (saturated tests TX684, 692; and unsaturated tests TX686, 688, 690), the results were significantly affected. According to these results, as the preparation water content increases, the strength increases. This would also indicate greater effective stress, which clearly is the opposite of not only the calculations presented in this thesis (*section 3.3.4*), but also the widely accepted characteristics of partially saturated soils (Fredlund & Rahardjo, 1993).

These three unsaturated tests by themselves do not point to any explanation, as their differences are not justifyable solely by the effect of water content. However, further investigation of the results of these tests show that their initial void ratios are different as a result of preparation with different water contents.

The saturated pair has the same trend of strength with preparation water content. If everything else was identical, saturated tests shouldn't have been affected by initial water content, since the specimen gets saturated at the start of the test. The only other difference between TX684 and 692 is the initial ***void ratio***, so it must be the factor affecting the results. Therefore, the preparation water content affects the results indirectly, not through suction or pendular ring size, but through compaction of the specimen (see *section 7.4.3*).

7.4.3. Effect of Void Ratio

Among the tests prepared with different water contents (listed in the previous section above), another consistent observation was the dependency of void ratio to the water content. As the specimen are constituted with a standardized method, the energy put into their compaction is (in theory, with the same operator) the same. Similar to compaction of coarse grained soil, it is observed that the material becomes denser (void ratio decreases) with increasing water content in preparation. This is observable in Type 2 specimen plotted in *Fig.6.1.*

Similar to the behavior of any other granular material, denser glass sphere samples have greater strength in the triaxial tests, compared to looser packings. This effect on strength outweighs the reverse effect of the decreased effective stress due to decreased suction and increased water content.

7.4.4. Mechanisms Influencing the Results

Within the pendular regime, each of the following mechanisms is caused by, or result in, changes in one or more of suction, water content and void ratio. The first two mechanisms exist only in unsaturated materials, whereas the third takes effect regardless of saturation. *Figure 3.13* was redrawn as *Fig. 7.5*, for the average particle radius of the tested materials, in order to assist this section.

1- If a pendular ring grows because of decreasing suction and increasing water content, with no change in solid matrix, the effective stress decreases. This effect is very small (water content changes by adding or removing water in a given granular matrix are along a single curve in *Fig. 7.5*).
2- Increasing the preparation water content results in denser packing of particles (smaller void ratio), therefore increased number of contacts and pendular rings. This increases the effective stress. This mechanism has much larger effect than mechanism 1, and it corresponds to changing from curve to curve in the direction opposite of mechanism 1 in *Fig. 7.5*.
3- Densifying a granular material increases its strength drastically, without increasing the effective stress. The effect of densification on shear strength is much larger than the effects of the previous two mechanisms. The hypothesis that links the shear strength to

the effective stress increment due to suction does not consider strength changes due to void ratio variations. Nevertheless, the hypothesis remains applicable provided the void ratios of all tests are kept constant.

Fig. 7.5. Two mechanisms of water content's effect on the calculated values of effective stress increment due to suction

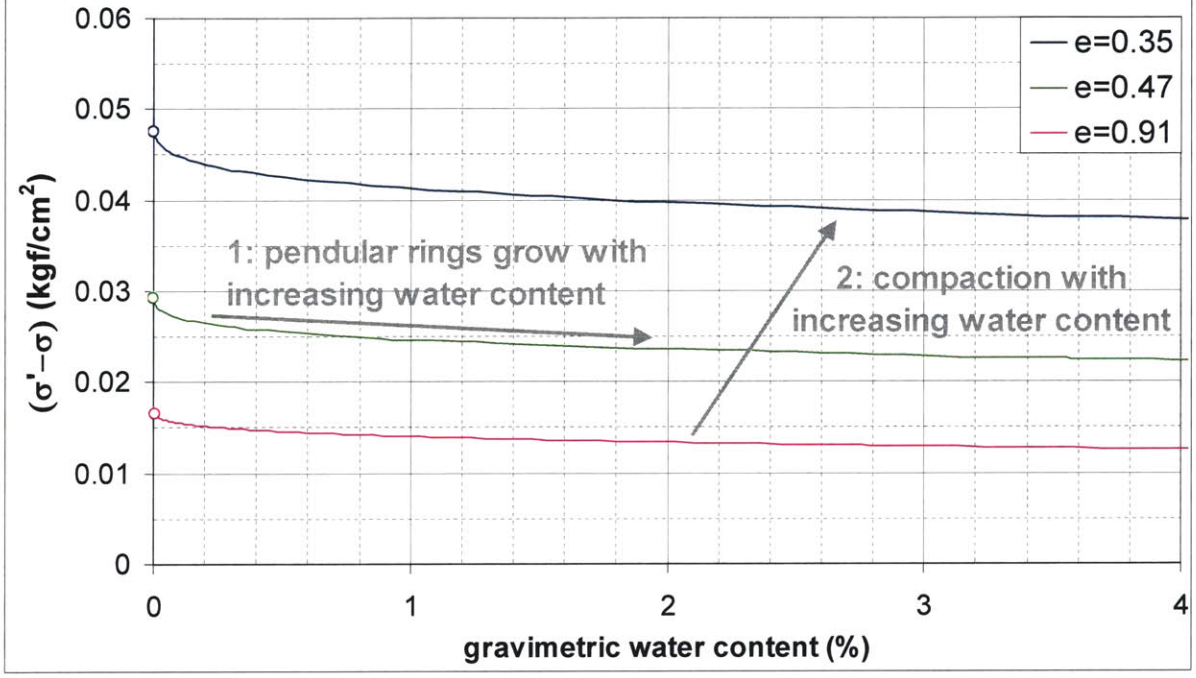

Appendices

Appendix 7.1. Table of work done on the specimen by deviator and confining stresses, until 1%, 2% and 15% axial strains.

Material	Test Type	Test No	σ_c (kgf/cm^2)	Work done (j) on specimen by ***deviator*** stress until the axial strain of			Work done (j) on specimen by ***confining*** stress until the axial strain of			***Total*** work (j) until the axial strain of			Work done by ***deviator*** stress, ***normalized*** by σ_c, (cm^3) until the axial strain of		
				1 %	2 %	15 %	1 %	2 %	15 %	1 %	2 %	15 %	1 %	2 %	15 %
Type 1	Saturated	tx653	0.97	0.087	0.196	1.849	-0.009	-0.022	-0.130	0.078	0.174	1.719	0.090	0.202	1.906
		tx654	1.64	0.148	0.337	3.229	-0.010	-0.033	-0.213	0.138	0.304	3.015	0.090	0.205	1.969
		tx669	2.61	0.255	0.573	5.124	0.001	-0.030	-0.178	0.256	0.543	4.946	0.098	0.220	1.963
	Sealed	tx663	1.01	0.105	0.244	2.167							0.104	0.242	2.145
		tx664	1.64	0.194	0.425	3.622							0.118	0.259	2.209
		tx674	2.50	0.258	0.596	5.367							0.103	0.239	2.147
		tx678	0.486	0.045	0.109	1.097							0.092	0.225	2.258
	Unsealed	tx676	1.60	0.085	0.333	1.849							0.053	0.208	2.006
Type 2	Saturated	tx680	1.01	0.069	0.169	1.643	0.004	-0.016	-0.182	0.072	0.153	1.461	0.068	0.167	1.627
		tx685	1.74	0.156	0.353	3.123	-0.015	-0.059	-0.367	0.140	0.294	2.756	0.089	0.202	1.784
		tx692	2.53	0.222	0.527	4.373	0.049	0.030	0.014	0.271	0.557	4.387	0.088	0.208	1.729
		tx684	2.49	0.210	0.468	4.031	-0.023	-0.072	-0.356	0.187	0.395	3.674	0.084	0.188	1.619
	Tensiometer	tx686	1.72	0.132	0.318	2.898							0.077	0.185	1.685
		tx687	3.48	0.316	0.739	6.496							0.091	0.212	1.867
		tx688	1.73	0.145	0.347	3.204							0.084	0.200	1.852
		tx690	1.73	0.151	0.363	3.390							0.087	0.210	1.959
	Sealed	tx681	0.96	0.067	0.176	1.801							0.069	0.183	1.876
	Unsealed	tx682	0.99	0.091	0.211	1.862							0.091	0.213	1.880
		tx683	2.47	0.222	0.525	4.752							0.090	0.213	1.924

Appendix 7.2.a. Comparisons between saturated and unsaturated tests at ~1 kgf/cm^2 consolidation stress. Type 1 material.

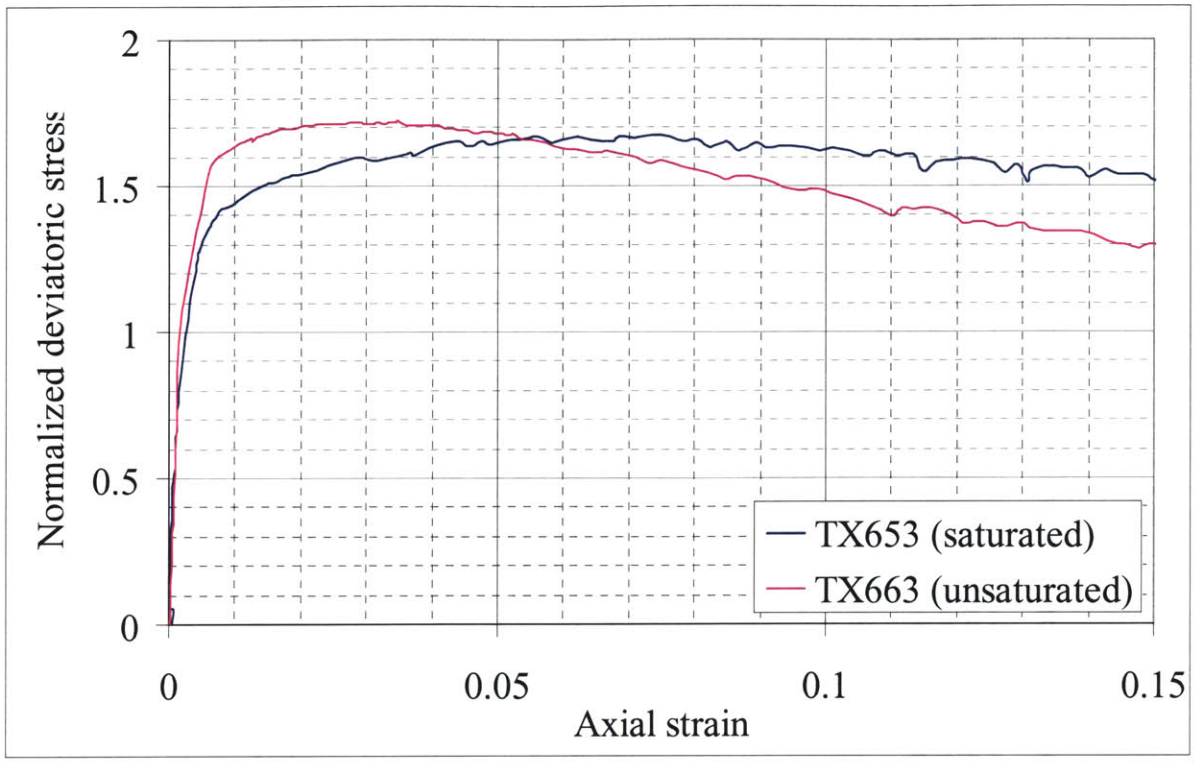

Appendix 7.2.b. Comparisons between saturated and unsaturated tests at ~1.6 kgf/cm^2 consolidation stress. Type 1 material.

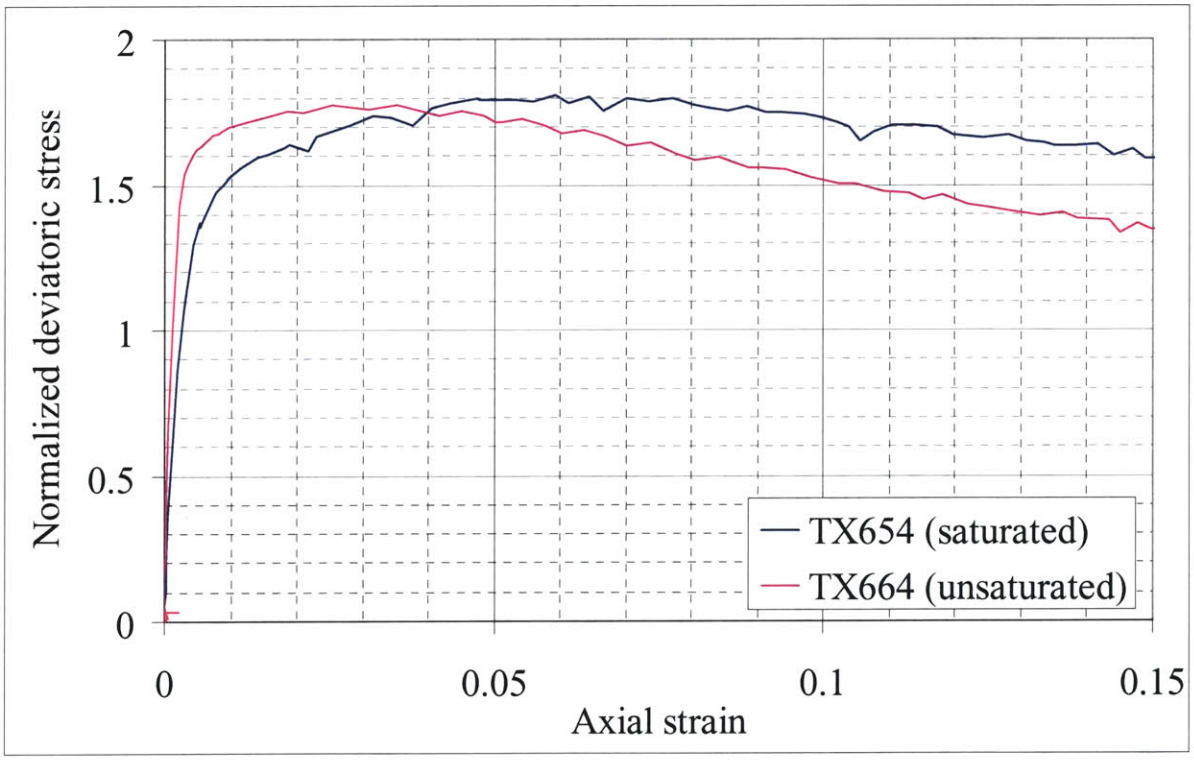

Appendix 7.2.c. Comparisons between saturated and unsaturated tests at ~2.5 kgf/cm^2 consolidation stress. Type 1 material.

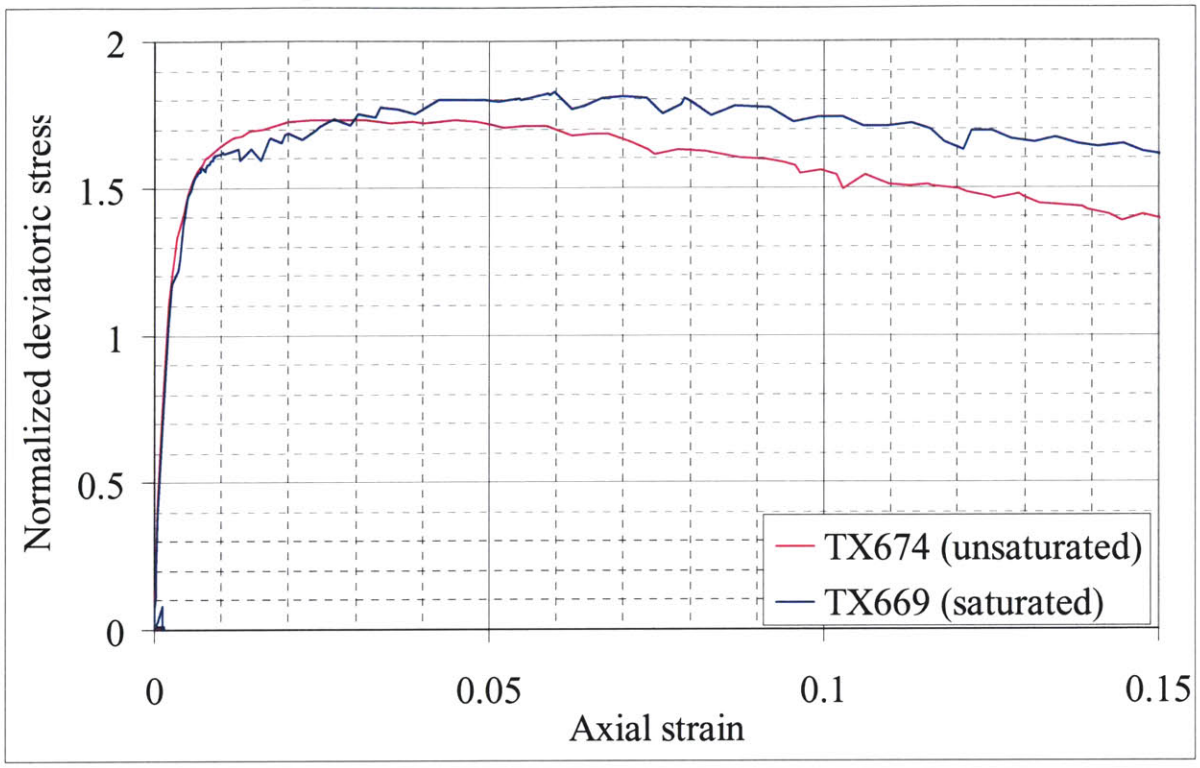

Appendix 7.2.d. Comparisons between saturated and unsaturated tests at ~1 kgf/cm^2 consolidation stress. Type 2 material.

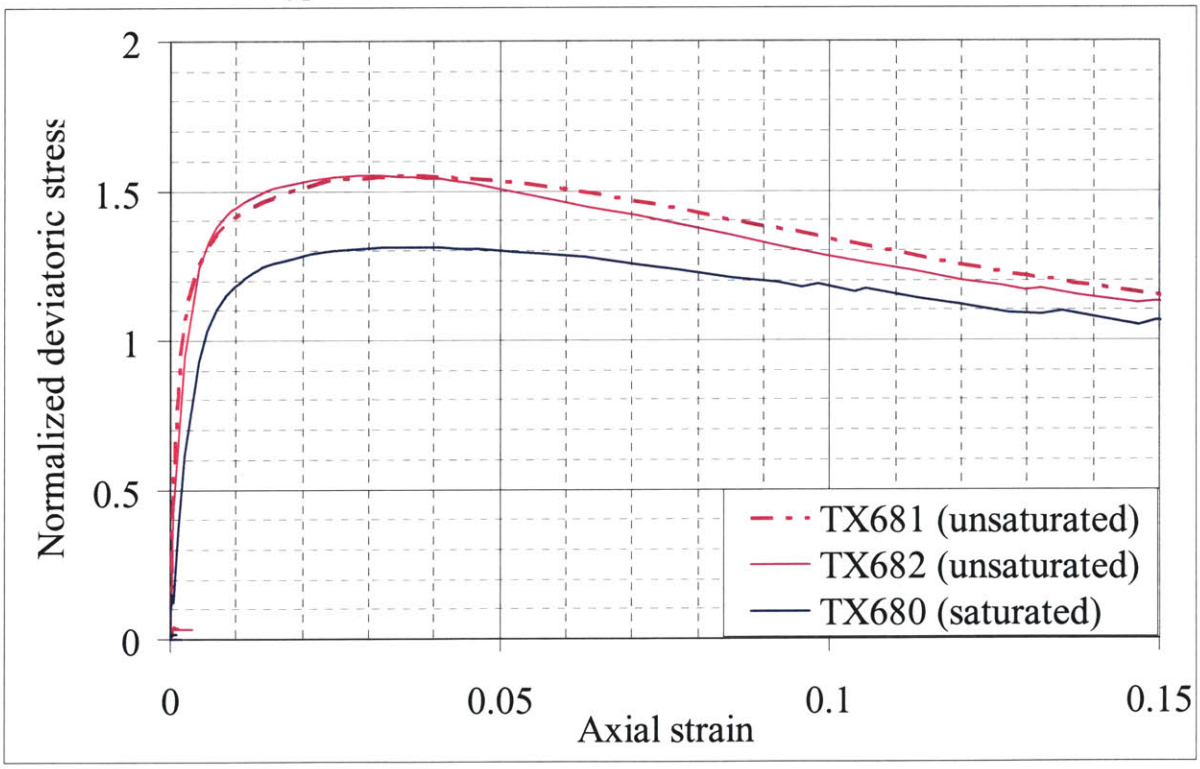

Appendix 7.3.a. Peak stresses.

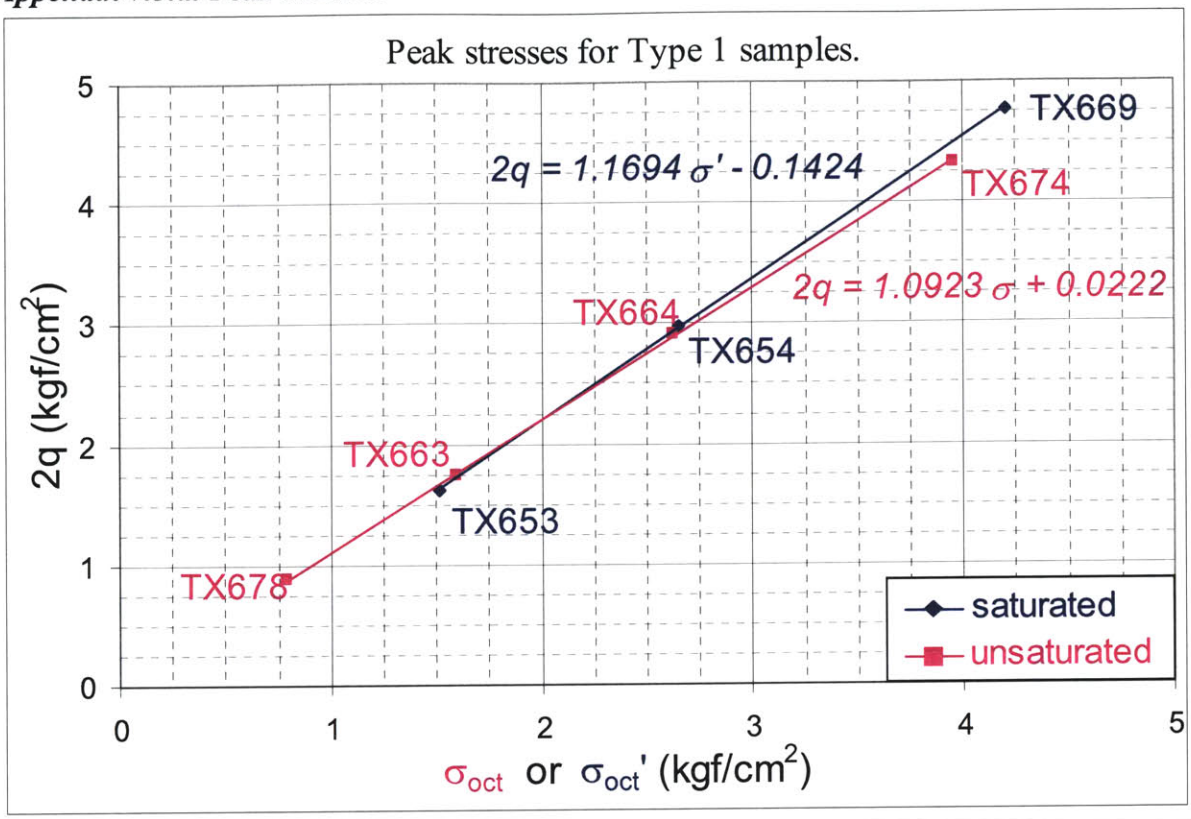

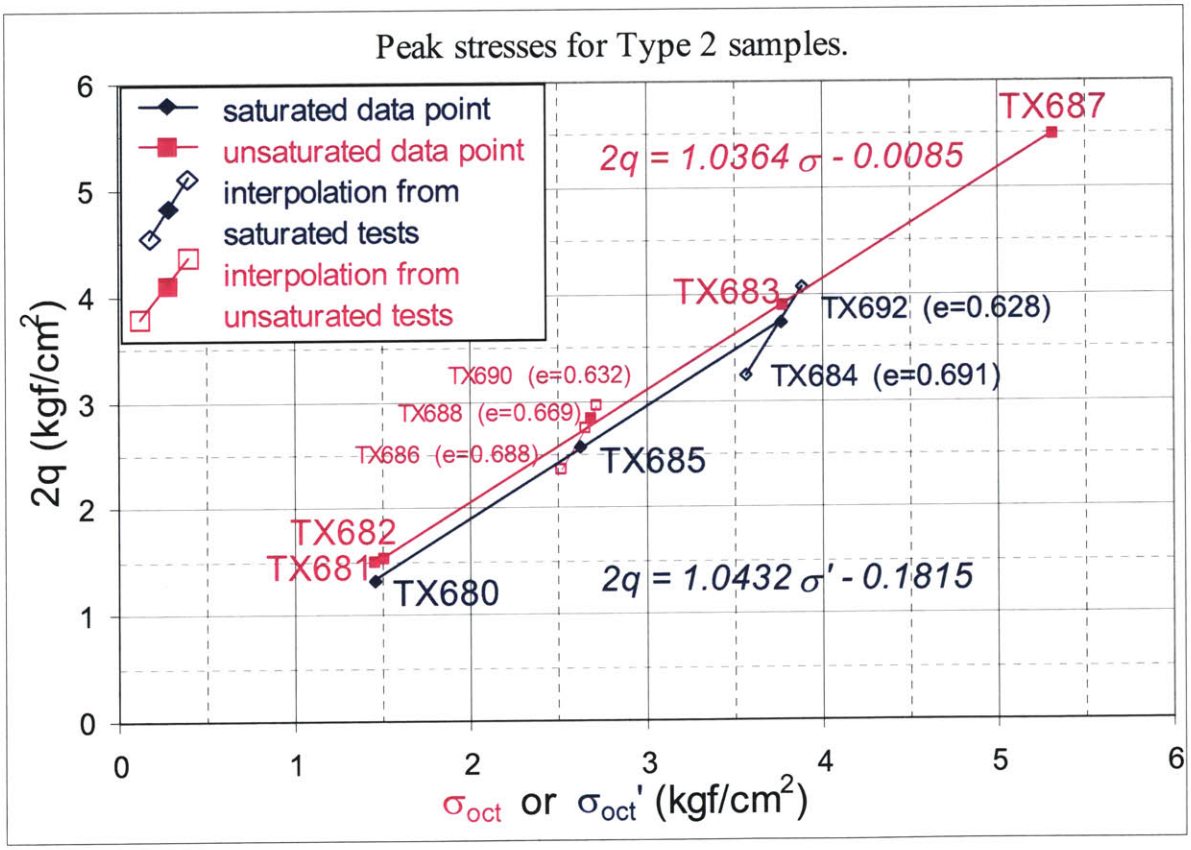

Appendix 7.3.b. Stresses at 15% axial strain.

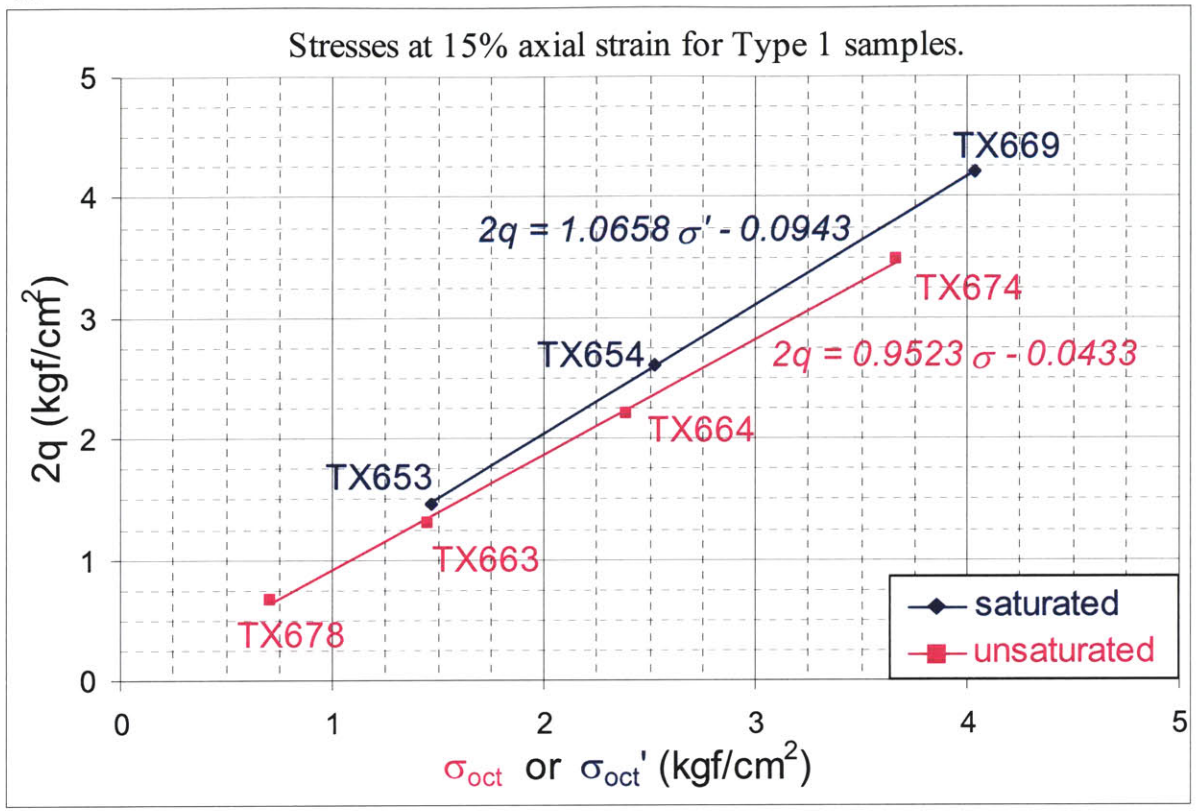

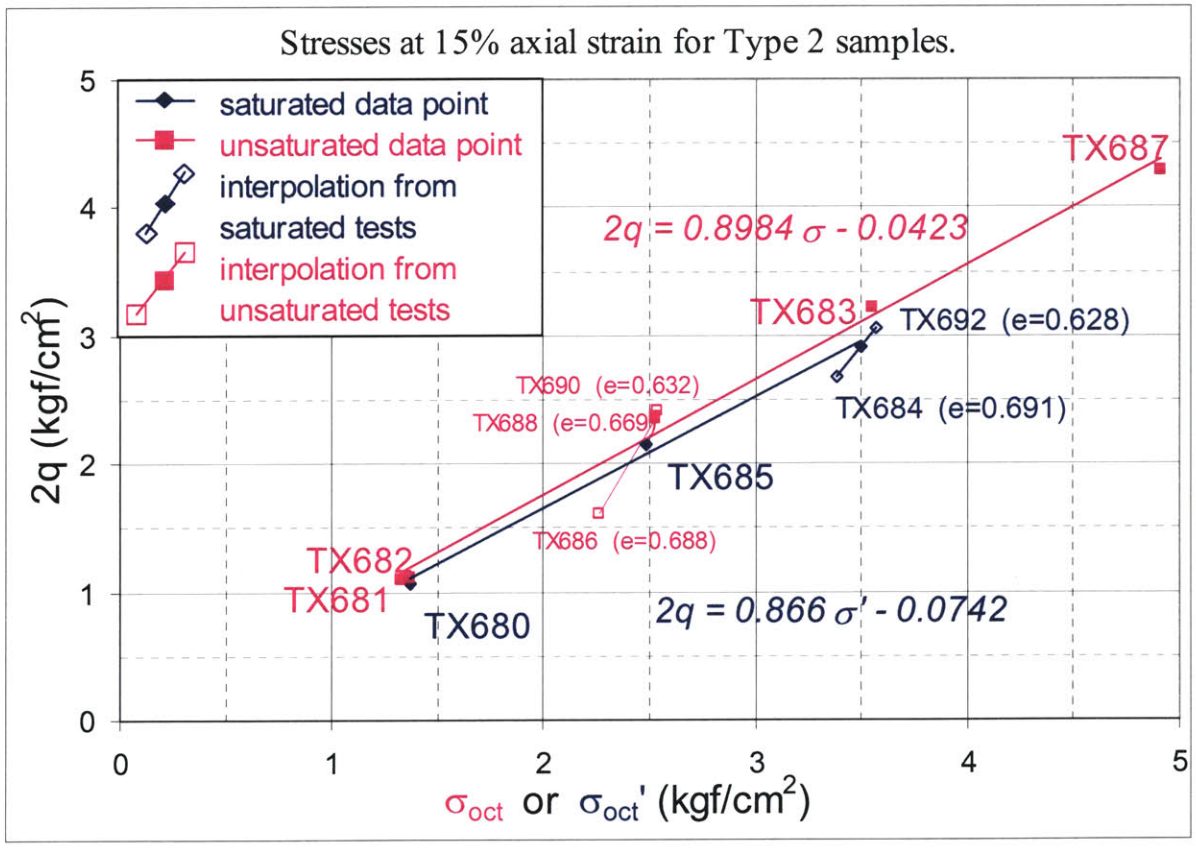

8

CONCLUSIONS and RECOMMENDATIONS

8. CONCLUSIONS and RECOMMENDATIONS

Among the objectives that were set forth in *section 1.2*, some were achieved along the course of this research and some were not. This chapter examines the extent to which each of the theorethical and experimental research objectives have been achieved. This chapter also summarizes the interpretations of the results from *Chapters 3, 4, 5* and *7* in an organized manner, and provides some recommendations for future research.

The naming convention of the ***model*** (for analytically estimating the effective stress increment due to suction - *sections 3.2* and *3.3*) and the ***hypothesis*** (inferring the effective stress increment due to suction, from the saturated and unsaturated shear strength envelopes – *section 3.4.2*) will continue in this chapter.

8.1. Achievements

8.1.1. Theoretical

8.1.1.1. Model for Effective Stress Increment due to Suction

A theoretical model for calculating the effective stress in unsaturated granular media using a microscopic model of uniform, rigid, inert, spherical grains was developed (*Chapter 3*). The primary elements of the model include analytical formulation of water geometry and forces at the particle contact scale. The change in effective stress due to soil suction is estimated from this micromechanical scale, involving particle packing in the estimation.

The model applies to the pendular domain where water contents are low. It incorporates surface tension into the calculations, which is never done in mainstream unsaturated soil mechanics. The model takes grain size, void ratio, and suction or water content into account as parameters that influence the increment in effective stress due to a material being partially saturated. It predicts the influences of grain size and void ratio on the increment in effective stress to be much larger than the influences of suction and water content (*Fig.3.12* and *3.13*).

8.1.1.2. Hypothesis to Infer the Effective Stress Increment from Shear Strength

Since effective stresses can not be measured directly in unsaturated materials, the result of the model had to be linked to a measurable quantity - in this case, shear strength. As a means of testing the theoretical model, a hypothesis for inferring the effective stress increment in an unsaturated soil from strength test results is proposed. Basically the effective stress increment due to suction is postulated to be the difference in mean effective stress between the saturated and partially saturated strength envelopes in mean shear – mean stress space (*section 3.4.2*).

8.1.2. Experimental

8.1.2.1. Developments in Tensiometer

During this research four new versions of the MIT tensiometer were built (*section 4.1.4*). Precursors to these tensiometer designs had been described by Toker (2002) and Sjoblom (2000). Tensiometer Version 6.2 was used to measure the Soil Moisture Characteristic Curves of the sample materials.

The utility of Vycor® porous glass, which has never been used as the porous interface of a tensiometer before, was investigated with the purpose of increasing the suction capacity of MIT Tensiometers. Tensiometer V6.2 recorded a matric suction of 2.4MPa before its Vycor glass cracked under the pressure difference (*section 4.1.4.1*). This is the highest value by any MIT Tensiometer, and a close second in the world after 2.5MPa by Tarantino et al. (2000). Glass with a different geometry was used in V7.2 to have higher resistance to cracking, but other problems were encountered (*section 4.1.4.2*). As the experimental research objectives focused on the verification of the effective stress model, this line of research was abandoned.

Versions 7.0 (*section 4.1.4.3*) and 7.1 (*section 4.1.4.4*) were designed and built to be implemented in triaxial tests. These two devices were utilized in some of the unsaturated tests, and also provide technology for further study. So far, the implementation of tensiometers into triaxial tests provided observations of the changes in matric suction during isotropic compression and shearing.

8.1.2.2. Triaxial Technology

The geometry of the standard MIT triaxial test setup was modified in order to accommodate the MIT tensiometer versions 7.0 and later. With this modification, the tensiometer replaced the pedestal on the triaxial test setup. Continuous measurements of water tension were recorded throughout some of the triaxial tests. Although other researchers have used tensiometers in triaxial tests before, this is the first time an MIT tensiometer is used in such manner.

A procedure for triaxial testing of cohesionless materials of extreme weakness was developed. The main procedure was modified into three separate variations in order to perform saturated tests and unsaturated tests in the standard MIT triaxial setup, and unsaturated tests in the modified setup. In the case of unsaturated tests, pore air of the specimen was either sealed from the outside, or connected to a water reservoir at atmospheric pressure. Each of these procedures are detailed in *Chapter 5*.

Various pieces of preparation equipment were modified to complement the newly devised procedures. These are detailed in *section 4.5*.

8.1.2.3. Improvements on Triaxial Test Calculations

Novel area and membrane corrections for triaxial testing were derived and applied to all data. These are detailed in *sections 5.4.2.2* and *5.4.2.4*, respectively. The area correction takes localized bulging of the specimen into account, whereas the membrane corrections incorporate initial stretching of the membrane in axial and radial directions while setting up the specimen. The effects of both unmodified and modified versions of area and membrane corrections on the test results were investigated.

A method to identify the yield stress and strain uniquely and repeatably was devised. The method determines the yield point by examining the maximum curvature of a scaled version of the stress-strain graph.

8.1.3. Greater Understanding of Spherical Particle Behavior

The behavior of materials composed of rigid spheres was examined through experimentation. In some aspects the glass spheres behaved like any other particulate material. Shear strength is highly affected by void ratio. Unique features that are specific to specimen of spherical particles, such as stress drop cycles due to stick-slip type shear deformation behavior, were observed. Trends of this behavior with test type and stress level were investigated. The concentration of shear deformation in the middle of the specimen was noted. Friction angles (using yield stresses) for the Type 1 and Type 2 glass bead samples were measured as 29° and 27°, respectively, without observable difference due to suction. Suction is observed to increase cohesion as expected. The cohesion intercept appears to be negative at first glance, but as discussed in greater detail in *section 7.3.1*, this is probably due to the curving of the strength envelope by its boundary conditions at the origin of the stress space.

8.2. Conclusions

8.2.1. Model Assessment

8.2.1.1. Verification of the Model and Hypothesis

The model successfully represented some aspects of effective stress in partially saturated granular materials. The trends of the experimental results (*section 7.4*) with respect to matric suction fit well into the dependency described in *section 3.3.4*, and hence support the model for the effective stress. Key aspects that are successfully represented are:

- Based on the observation that the shear strength increased equally in tests in which the measured suction spanned over two orders of magnitude, the effective stress increment due to suction is concluded to be independent of the stress level. This means pendular rings do not change the friction angle of a particulate material, but they shift the strength envelope (in total stress space) in a way that amounts to an apparent cohesion.

- Changing matric suction or water content within the pendular regime has very little to no effect on the effective stress increment, and thus strength of granular materials. This implies that any unsaturated model based on suction or water content alone is unrealistic at low water contents of pendular regime.

The test results did not match the predictions of the model with respect to the magnitude of increment in effective stress due to suction. The partially saturated tests indicate greater increase in shear strength - and therefore effective stress - than predicted by the model. The increment in effective stress due to suction that the hypothesis inferred from the experiments (*section 7.3*) is 4 to 9 times larger than that estimated by the model (*section 6.1.3*). However, this does not disprove the model for the effective stress, because it is also possible that the misrepresentation causing this discrepancy is in the verification procedure (through the hypothesis for stress-strength relationship) rather than the effective stress model itself.

8.2.1.2. Speculation for the Explanation of the Discrepancy

This discrepancy in measured and predicted increase in shear strength may indicate that introducing pendular rings into the system is fundamentally different than applying additional isotropic effective stress. If isotropic boundary stress on a dry material creates shear forces in some of the particle contacts, adding pendular rings, which increases normal contact stresses but not contact shear stresses, would result in heightened shear resistance of these contact locations. This would create greater overall shear strength of the specimen, in comparison to the strength of an identical saturated specimen subject to an additional increment of effective stress equivalent to the water forces in accordance to the model. (see *Figure 7.4* in *Section 7.3*)

8.2.2. Equipment and Procedures

The experimental developments within the framework of this research, which were summarized in *section 8.1.2*, also results in the following conclusions:
- It is possible to employ the MIT tensiometers as the base of a triaxial test setup. The tensiometer is able to monitor sustained suction in the triaxial specimen.
- It is within researchers' capability to perform triaxial tests on absolutely cohesionless and low strength materials, such as glass spheres. This suggests that it is also possible to perform other tests on such materials.
- Utilizing Vycor® porous glass in high capacity tensiometers has potential to measure unprecedented magnitudes of suction directly. However, it also has potential problems of saturation difficulty and slower response time.
- In unsaturated tests, having the sample sealed or unsealed did not make noticeable difference as the volumetric deformations are small.
- The specimen preparation procedure affects all results, because the idealized material used for the tests has a small range of formation conditions. Void ratios of the specimen of any set of strength tests on unsaturated materials must be the same, or else the effect of void ratio on strength of the material dominates the results, as elaborated in *section 7.4*.

8.2.3. Suction Behavior

Matric suction in the pendular rings is affected by stresses applied on a specimen. During isotropic compression, suction is reduced slightly, probably because particles are pressed closer as they elastically deform at the contacts. During shearing, matric suction increases. This is speculated to happen because the water that is freed from the contacts between particles moving away from each other does not have enough time to move into the new contacts. In that case it is hypothesized to move out of the system, through pore air, into the humidifying reservoir.

These variations in the magnitude of matric suction do not appear to affect overall behavior, as mentioned in *sections 7.4.1* and *8.2.1.1* above.

For another perspective of interpretation of the unsaturated tests, the work done on specimen was calculated and found to be more than the work done for the saturated case. This energy difference is probably spent in breaking pendular rings.

8.3. Recommendations for Future Research

The increase in effective stress predicted by the model does not match the difference inferred from the experiments. Some aspect may be amiss from either the effective stress model or the method of verification using the hypothesis. Therefore, improving either with modifications that will not change the results drastically (calculating elastic contact deformations, distributing the contacts over the particles statistically, etc.) will result in calculations that are bound to fail in closing the large gap between the results of the model and the interpretation of experiments by the hypothesis. Consequently, attempts at such improvements will not be beneficial to this research. Instead, future efforts should focus on understanding various aspects, mechanisms or phenomena in unsaturated soils that haven't been properly described by the model or the hypothesis.

8.3.1. Analytical Aspects

8.3.1.1. Strength

To investigate whether the speculation for the explanation of the discrepancy (*section 8.2.1.2*) between the model and test results is true, some form of micromechanical modelling that links the contact forces to macroscopic shear strength better than was done in this research could be implemented. In parallel to the calculations proposed in this thesis, an existing micromechanical simulation or statistical solution could be run to obtain more realistic contact forces and represent the effective stress – shear strength relation more realistically. This would help verify the ideas underlying the model.

8.3.1.2. Particle Packing

The model can only be used for repeatable elements in its current form. If the granular matrix is simulated in a realistic manner (i.e. more randomly), a mechanism that is lost in the idealization of the material may be found to exist. A good way to achieve this might be by investigating contact forces on individual particles of random particle assemblies. This task would require using ***D***iscrete ***E***lement ***M***ethods in conjunction with pendular ring equations.

In such a random assembly of particles, the pore area associated to each grain (*sections 3.2* and *3.3*) would not be identical or repetitive. But since DEM would already be making calculations for each individual grain, it could also calculate non-repetitive elements of the pore space by dividing it according to Voronoi separation of the matrix based on particle centers.

One fact, which is neglected by the model presented in this thesis and various other approaches that simulate unsaturated micromechanics in the literature, is that pendular rings do not require particle to particle contact to exist. A more detailed simulation, be it analytical or numerical, would include pendular rings between close but non-contacting particles.

8.3.1.3. Water Surface Analysis

Even though the geometry of the pendular ring is well established, the pendular regime represents only the lower end of the saturation scale. Mechanisms of air entry and bulk drainage, which are valid for the remaining majority of saturation values, are never modelled beyond a simple capillary tube analysis. More detailed approximations might increase the understanding of the phenomenon of air entry, as well as the transition from bulk water to pendular water. It is even possible to numerically simulate the exact geometry of air-water interface in the pores by utilizing finite difference approximations to curvature and suction.

8.3.2. Narrowing Down the Experimental Factors

The first two subsections (*8.3.2.1 and 8.3.2.2.*) are suggestions applicable to experiments regardless of saturation, whereas the third subsection (*8.3.2.3*) is specific to triaxial tests on unsaturated samples.

8.3.2.1. Increase Reliability at Large Strains

At larger strains (above 5%), results of the triaxial tests are highly affected by changes in the specimen geometry. Even if the deformed geometry is known, how to compute stress conditions is unclear. Moreover, membrane and area corrections become too large to deem the results to be reliable. Better understanding of the stress-strain behavior of triaxial specimen at large strains would contribute to more accurate representation of the failure envelope, as well as evolution of suction effects with shearing.

Developing new technology for frictionless ends for the triaxial test would also improve the results by resisting the specimen's tendency to bulge, and making its geometry more reliably calculable.

8.3.2.2. Compaction Variability

The behavior of granular materials is known to depend on relative density (or void ratio). The ability to constitute a specimen at a desired void ratio would diminish one of the largest causes of variation in the results.

The void ratio is observed to be significantly affected by the water content at preparation. A study of compaction characteristics of the materials before the testing program would ensure more consistent void ratios, even with different initial water contents (by changing the compaction energy). Some of the observed effects are possibly unique to, or magnified in case of, uniform glass spheres.

It was also noted that the void ratios resulting from the current preparation procedures are different from one operator to the other even at the same water content. The standard specimen preparation needs to move away from energy-based compaction to a density-based method. This might be done by developing a more precisely repeatable compaction procedure, for example, by undercompaction method (Ladd, 1978), or by modifying the compaction energy applied by each operator according to the efficiency at which they perform the compaction procedure.

8.3.2.3. Water Content and Suction

When specimen were prepared with different amounts of water to investigate effects of water content, void ratio was unavoidably affected as well. In order to observe the direct effects of changing the amount of water in the pendular rings, the void ratio must be kept constant among tests prepared at different water contents. This can be achieved only by changing the energy put into the compaction for each different water content, perhaps in line with the previous subsection (*8.3.2.2*).

Another good way of changing the amount of water is keeping the specimen preparation standardized, but then controlling the suction. This has the additional (and in fact more important) benefit of an ability to keep suction constant through the tests, and investigating behavior under varying suctions and water contents, such as failure induced by loss of suction upon wetting. The main drawback of controlling the suction is that the time of testing will be very long and rate of shear will become important, unless the saturated tests are run at equally slow strain rates. Suction control has been successfully implemented on a few occasions using osmotic equilibrium systems (*section 2.7.2*).

8.3.3. Broadening the Experimental Investigation

8.3.3.1. Testing Different Grain Sizes

Repeating similar testing programs on materials of different particle size, especially smaller, would make the increment in effective stress due to suction more detectable, with better precision. However, it is more difficult to obtain a uniform grain size for smaller sizes, both in the laboratory and commercially.

8.3.3.2. Testing Different Materials

Investigation of the effects of particle shape and angularity is possible by experimenting on materials with angular and/or non-equidimensional particles (such as real sands). Results of tests on different materials can be compared to the results from the idealized material (i.e. results from this research) to characterize effects like particle geometry on the relation between suction and effective stress.

Another aspect that affects unsaturated behavior of granular materials would be particle gradation (a well graded material has significantly more pendular rings than a uniform material of the same average particle size). Tests on well-graded granular materials might shed some light on the effects of the grain size distribution.

8.3.3.3. Increasing Tensiometer Capacity

Studying unsaturated behavior of finer materials is necessary for the practical implications of this work. If the line of research presented in this thesis is to be expanded in that direction, suction measurement methods with higher capacity would be needed. For this purpose, direct measurement of unprecedented magnitudes of matric suction can be pursued, by merging the advantages of tensiometer versions 6.2 and 7.2 (detailed in *section 4.1.4*). This would require the porous interface of the device to be a small (< 1 cm) diameter cylinder cored out of a Vycor® plate.

8.3.3.4. Testing at Low Stresses

Although it is not necessary for research in unsaturated soil mechanics, accurate characterization of the curve of the strength envelope of glass spheres at low stresses might be useful to some other research on mechanics of idealized granular materials. At the very least, this would verify the explanation suggested here (in *section 7.3.1*) for the low-stress portion of the strength envelope.

8.3.3.5. Testing with Different Stress Paths

All triaxial experiments in this research was done under constant confining pressure, while results were investigated in the stress space of mean shear vs. octahedral (mean normal) stresses. Testing under, for example, constant octahedral stress may provide some additional insight, as octahedral stress is a key element of the theorethical approach.

REFERENCES

REFERENCES

Adamson, N. K. (1960). *Physical Chemistry of Surfaces,* Interscience Publishers Inc.

Aitchison, G. D. (1960). "Relationships of moisture stress and effective stress functions in unsaturated soils", *Proceedings of Conference on Pore Pressure and Suction in Soils,* pp.47-52.

Aitchison, G. D. (1965). "Moisture equilibria and moisture changes in soils", *A Symposium in Print Convened by Soil Mechanics Section Commonwealth Scientific and Industrial Research Organization*, Butterworths, Australia.

Alonso, E. E., Gens, A. and Josa, A. (1990). "A constitutive model for partially saturated soils", *Geotechnique*, Vol.40, No.3, pp.405-430.

American Society for Testing and Materials (1997). *Annual Book of ASTM Standards*, American Society for Testing and Materials, West Conshohocken, PA, volumes 04.08 and 04.09.

Anthony, J. L. and Marone, C. (2005). "Influence of particle characteristics on granular friction", *Journal of Geophysical Research*, Vol.110, B08409, doi:10.1029/2004JB003399.

Andersen, G.R. (1991). "Physical mechanisms controlling the strength and deformation behavior of frozen sand", *Doctor of Science Dissertation in Civil and Environmental Engineering,* Massachusetts Institute of Technology, Cambridge, MA.

Anderson, W. F., Goodwin, A. K., Pyrah, I. C. and Salman, T. H. (1997). "Equipment for one-dimensional compression and triaxial testing of undrained granular soils at low stress level", *Geotechnical Testing Journal*, Vol.20, No.1, pp.74-89.

Arya, L. M. and Paris, J. F. (1981). "Physicoempirical model to predict the SMC from particle size distribution and bulk density data", *Soil Science Society of America Journal*, Vol.45, pp.1023-1030.

Berney IV, S. E. (2004). "A partially saturated constitutive theory for compacted fills", US Army Corps of Engineers, ERDC/GSL TR-04-4.

Berre, T. (1985). "Suggested international code of soil engineering practice for triaxial compression tests", Norwegian Geotechnical Institute, Internal Report 56103-30.

Berthelot, M. (1850). "Sur quelques phénomènes de dilatation forcée des liquides / On some phenomena of tensile force of liquids", *Annales de Chimie et Physique*, Vol.30, No.3, pp.232-237.

Bishop, A. W. (1959). "The principle of effective stress", *Teknisk Ukeblad,* Vol.106, No.39, pp.859-863.

Bishop, A. W., Alpan, I., Blight, G. H. and Donald, I. B. (1960). "Factors controlling the strength of partly saturated cohesive soils", *Proceedings of the ASCE Research Conference on Shear Strength of Cohesive Soils,* Boulder, pp.503-532.

Bishop, A. W. and Donald, I. B. (1961). "The experimental study of partly saturated soil in the triaxial apparatus", *5th International Conference on Soil Mechanics and Foundation Engineering*, Paris, Vol.1, pp.13-21.

Bishop, A. W. and Henkel, D. J. (1962). *The Measurement of Soil Properties in the Triaxial Test*, 2nd Ed., Edward Arnold, London.

Blatz, J. and Graham, J. (2000). "A system for controlled suction in triaxial tests", *Geotechnique*, Vol.50, No.4, pp.465-469.

Bohren, C. F. (1987). *Clouds in a Glass of Beer: Simple Experiments in Atmospheric Physics*, John Wiley & Sons, New York, pp.51.

Briggs, L. J. (1897). *The Mechanics of Soil Moisture*, US Department of Agriculture, Division of Soils, Bulletin No.10.

Buckingham, E. (1907). *Studies of the Movement of Soil Moisture*, US Department of Agriculture, Bureau of Soils, Bulletin No.38.

Buisson, M. S. R. and Wheeler, S. J. (2000). "Inclusion of hydraulic hysteresis in a new elasto-plastic framework for unsaturated soils", *Experimental Evidence and Theoretical Approaches in Unsaturated Soils,* Tarantino & Mancuso (eds), Balkema, Rotterdam, pp.109-120.

Burland, J. B. (1964). "Effective stresses in partly saturated soils", discussion of "Some aspects of effective stress in saturated and partly saturated soils" by A.W. Bishop and G.E. Blight, *Geotechnique*, Vol.14, No.2, pp.65-68.

Chang, C. S., Misra, A. and Sundaram, S. S. (1990). "Micromechanical modelling of cemented sands under low amplitude oscillations", *Geotechnique*, Vol.40, No.2, pp.251-263.

Chateau, X., Moucheront, P. and Pitois, O. (2002). "Micromechanics of unsaturated granular media", *Journal of Engineering Mechanics*, Vol.128, No.8, pp.856-863.

Coleman, J. D. and Marsh, A.D. (1961). "An investigation of the pressure membrane method for measuring the suction properties of soil", *Journal of Soil Science*, Vol.12, No.2, pp.343-362.

Cook, B. K., Noble, D. R. And Wiliams, J. R. (2004). "A direct simulation method for particle-fluid systems", *Engineering Computations: International Journal for Computer-Aided Engineering,* Vol.21, No.2/4, pp.151-168.

Coussy, O. (1995). *Mechanics of Porous Continua*, John Wiley & Sons, New York.

Coussy, O. and Fleureau, J. M., (2002). *Mecanique des Sols non Satures*, Hermes Science Publications.

Cundall, P. (1971). "A computer method for simulating progressive, large-scale movements in blocky rock systems, Paper No. II-8", *Proceedings of Symposium of the International Society for Rock Mechanics*, Vol.1.

Dalton, J. (1802). "Experimental Essays", *Memoirs & Proceedings of Manchester Literary & Philosophical Society,* Vol.5, Part.II, pp.535-602.

Donald, I. B. (1960). "Discussion", *Proceedings of Conference on Pore Pressure,* Butterworths, London, p.69.

Einstein, A. (1901) "Folgerungen aus den Capillaritätserscheinungen / Consequences of the observations of capillarity phenomena", *Annalen der Physik,* Vol.4, pp.513-523.

Escario, V. and Juca, J. F. T. (1989). "Strength and deformation of partly saturated soils", *Proceedings of the 12th International Conference on Soil Mechanics and Foundation Engineering,* Rio de Janerio, Vol.2, pp.43-46.

Faatz, M., Cheng, W. and Wegner, G. (2005). "Mechanical strength of amorphous $CaCO_3$ colloidal spheres", *Langmuir: The American Chemical Society Journal of Surfaces and Colloids,* Vol.21, No.15. pp.6666-6668.

Feng, J. Q. (2000). "Contact behavior of spherical elastic particles: a computational study of particle adhesion and deformations", *Colloids and surfaces A: Physico-chemical & Engineering Aspects*, Vol.172, pp. 175-198.

Field, W. G., (1963). "Towards the statistical definition of a granular mass", *Proceedings of the 4th Australian and New Zealand Conference on Soil Mechanics*, pp.143-148.

Fisher, E. A., (1923). "Some factors affecting the evaporation of water from soil", *Journal of Agricultural Science,* Vol.13, pp.121-143.

Fisher, J. C., (1948). "The fracture of liquids", *Journal of Applied Physics,* Vol.19, pp.1062-1067.

Fleureau, J. M., Bouabdallah, A., Maouchi, D. and Taibi, S. (1998). "Mechanical behavior of an unsaturated loam under high stresses and high negative pressures", *Proceedings of the Second International Conference on Unsaturated Soils,* Beijing, Vol.1, pp.37-43.

Fredlund, D. G. and Morgenstern, N. R. (1977). "Stress state variables for unsaturated soils", *Journal of Geotechnical Division, ASCE,* Vol.103, No GT5, pp.447-466.

Fredlund, D. G., Rahardjo, H. and Gan, J. K. M. (1987). "Nonlinearity strength envelope for unsaturated soils", *Proceeding 6th International Conference on Expansive Soils,* New Delhi, Vol.1, pp.49-54.

Fredlund, D. G. and Rahardjo, H. (1993). *Soil mechanics for unsaturated soils*, John Wiley and Sons Inc., New York.

Fredlund, D. G., Vanapalli, S. K., Xing, A. and Pufahl, D. E. (1995)[1]. "Predicting the shear strength function for unsaturated soils using the soil-water characteristic curve" *Proceedings of First International conference on Unsaturated Soils*, Paris, Vol.1, pp.63-69.

Fredlund, D. G., Xing, A., Fredlund, M. D. and Babbour, S. L. (1995)[2]. "The relationship of the unsaturated soil shear strength to the soil – water caharacteristic curve", *Canadian Geotechnical Journal,* Vol.32, pp.440-448.

Fredlund, D. G. (2006). "Unsaturated soil mechanics in engineering practice", *ASCE Journal of Geotechnical and Geoenvironmental Engineering,* Vol.132, No.3, pp.286-321.

Gallipoli, D., Gens, A., Sharma, R. and Vauant, J. (2003). "An elastoplastic model for unsaturated soil incorporating the effects of suction and degree of saturation on mechanical behaviour", *Geotechnique*, Vol.53, No.1, pp.123-135.

Gardiner, B. S. and Tordesillas, A. (2000). "Micromechanical constitutive modelling of granular media: evolution and loss of particle contact in clusters", *Journal of Engineering Mathematics,* Vol.52, pp.93-106.

Gens, A. and Alonso, E. E. (1992). "A framework for the behavior of unsaturated expansive clays", *Canadian Geotechnical Journal*, Vol.29, pp.1013-1032.

Gili, J. A. and Alonso, E. E. (2002). "Microstructural deformation mechanisms of unsaturated granular soils", *International Journal for Numerical and Analytical Methods In Geomechanics,* pp.433-468.

Glasstetter, R., Rickets, C. I., and Wilhelm, J. G. (1991). "Towards modeling the meniscus geometry and volume of capillary water between two contacting microspheres in moist air" *Journal of Aerosol Science,* Vol.22, Supp.1, pp.S196-S198.

Graham, J., Oswell, J. M. and Gray, M. N. (1992). "The effective stress concept in saturated sand-clay buffer ", *Canadian Geotechnical Journal,* Vol.29, pp.1033-1043

Graton, L. C. and Fraser, H. J. (1935). "Systematic packing of spheres, with particular relation to porosity and permeability", *Journal of Geology*, Vol.43, pp.785-909.

Gray, W. A. (1968). *The Packing of Solid Particles*, Chapman and Hall Ltd.

Guan, Y. and Fredlund, D. G. (1997). "Use of tensile strength of water for the direct measurement of high soil suction", *Canadian Geotechnical Journal,* Vol.34, No.4, pp.604-614.

Hauksbee, F. (1709). *Philosophical Transactions.*

Head, K. H. (1986). *Manual of Soil Laboratory Testing, Vol.3: Effective Stress Tests*, Pentech Press, London.

Henderson, S. J. and Speedy, R. J. (1980). "A Berthelot-Bourdon tube method for studying water under tension", *Journal of Physics e – Scientific Instruments,* Vol.13, No.7, pp.778-782.

Hicher, P. Y. and Rahma, A. (1994). "Micro-macro correlations for granular media, application to modeling of sands" *European Journal of Mechanics, A:Solids*, Vol.13, No.6, pp.763-781.

Houlsby, G. T. (1997). "The work input to an unsaturated granular material", *Geotechnique*, Vol.47, No.1, pp.193-196.

Hoyos, L. R. and Macari, E. J. (2001). "Development of a stress/suction-controlled true triaxial testing device for unsaturated soils", *Geotechnical Testing Journal,* Vol.24, No.1, pp.5-13.

Itasca Consulting Group (1999). *PFC2D Users' Guide, Command Reference, FISH Reference, and Theory and Background*, Minneapolis, MN.

Jaeger, H. M., Liu, C. H. and Nagel, S. R. (1989). "Relaxation at the angle of repose", *Physical Review Letters*, Vol.62, issue 1, pp.40-43.

Jennings, J. E. B. and Burland, J. B. (1962). "Limitations to the use of effective stress in partly saturated soils", *Geotechnique,* Vol.12, No.2, pp.125-144.

Jommi, C. (2000). "Remarks on the constitutive modelling of unsaturated soils" *Experimental Evidence and Theoretical Approaches in Unsaturated Soils,* Tarantino & Mancuso (eds), Balkema, Rotterdam, pp.139-154.

Jotisankasa, A., Coop, M. and Ridley, A. (2007). "The development of a suction control system for a triaxial apparatus", *Geotechnical Testing Journal,* Vol.30, No.1, pp.69-75.

Karube, D., Kato, S., Hamada, K. and Honda, M. (1996). "The Relationship between the mechanical behavior and the state of pore water in soil", *Journal of JSCE*, Vol.535, pp.83-92.

Khalili, N. and Khabbaz, M. H. (1998). "A unique relationship for the determination of the shear strength of unsaturated soils". *Geotechnique,* Vol.48, No.5, pp.681-687.

Kim, H., Suresh, P., Rao, C. and Annable, M. D. (1997). "Determination of effective air-water interfacial area in partially saturated porous media using surfactant adsorption" *Water Resources Research,* Vol.33, No.12, pp.2705-2711.

Kim, T. H. and Hwang, C. (2003). "Modeling of tensile strength on moist granular earth material at low water content", *Engineering Geology,* Vol.69, pp.233-244.

Kong, L. W. and Tan, L. R. (2000), "A simple method of determining the soil-water characteristic curve indirectly", *Proceedings of Asian Conference on Unsaturated Soils*, Singapore, pp.341-345.

Ladd, R. S. (1978). "Preparing test specimens using undercompaction", *Geotechnical Testing Journal,* Vol.1, No.1, pp.16-23.

Laplace, P. S. (1806). *Mécanique Céleste*, Supplement to the Tenth Edition.

Laudahn, A., Sonsa, K. and Bohác, J. (2005). "A simple method for air volume change measurement in triaxial tests", *Geotechnical Testing Journal,* Vol.28, No.3, pp.313-318.

Lee, H. C. and Wray, W. K. (1995). "Techniques to evaluate soil suction - A vital unsaturated soil water variable", *Proceedings of First International Conference on Unsaturated Soils*, Paris. Vol.2. pp.615-622.

Lewis, G. M. (1961). "The tensile strength of liquids in Berthelot tubes", *Proceedings of Physics Society*, Vol.78, pp.133-144.

Li, Y., Wu, D., Zhang, J., Chang, L., Wu, D., Fang, Z. and Shi, Y. (2000). "Extension of a model for bulk crushing strength of spheres to solid catalysts of different shapes", *Industrial Engineering and Chemical Research*, Vol.39, pp.838-842.

Li, J. and Mason, D. J. (2002). "Application of the discrete element modelling in air drying of particulate solids", *Drying Technology*, Vol.20, No.2, pp.255-282.

Li, X. S. (2003). "Effective stress in unsaturated soil: a microstructures analysis", *Geotechnique*, Vol.53, No.2, pp. 273-277.

Likos, W. J. and Lu, N. (2004). "Hysterisis of capillary stress in unsaturated granular soil", *Journal of Engineering Mechanics*, Vol.130, No.6, pp.646-655.

Liu, S. H., Sun, D. A. and Wang,Y. (2003). "Numerical study of soil collapse behavior by discrete element modelling", *Computers and Geotechnics*, Vol.30, pp.399-408.

Lu, N., Wayllace, A., Carrera, J. and Likos, W. J. (2006), "Constant Flow Method for Concurrently Measuring Soil-Water Characteristic Curve and Hydraulic Conductivity Function", *Geotechnical Testing Journal*, Vol.29, No.3, pp.230-241.

Mancuso, C., Vassalo, R. and d'Onofrio, A. (2000). "Soil behavior in suction controlled cyclic and dynamic torsional shear tests", *Unsaturated soils for Asia*, Rahardjo (ed), pp.539-544.

Mattox, D. M. (1998). *Handbook of physical vapor deposition (PVD) processing : film formation, adhesion, surface preparation and contamination control*, Noyes Publications, Westwood, NJ, pp.689.

Matyas, E. L. and Radhakrishna, H. S. (1968). "Volume change characteristics of partially saturated soils", *Geotechnique*, Vol.18, No.4, pp.432-448.

Mehrabadi, M. M., Nemat-Nassar, S. and Oda, M. (1982). "On statistical description of stress and fabric in granular materials", *International Journal for Numerical and Analytical Methods in Geomechanics*, Vol.6, pp.95-108.

Mitchell, J. K. (1976). *Fundamentals of Soil Behaviour*, John Wiley & Sons, Inc., New York, NY.

Molenkamp, F. ,and Nazemi, A. H. (2003). "Interactions between two rough spheres, water bridge and water vapour", *Geotechnique*, Vol.53, No.2, pp.255-264.

Muraleetharan, K. K. and Granger, K. K. (1999). "The use of miniature pore pressure transducers in measuring matrix suction in unsaturated soils", *Geotechnical Testing Journal*, Vol.22, No.3, pp.226-234.

Nelson, J. D. and Miller, D. J. (1992). *Expansive Soils, Problems and Practice in Foundation and Pavement Engineering*, John Wiley and Sons Inc., New York.

Oda, M. (1972[1]). "Deformation mechanism of sand in triaxial compression tests", *Soils and Foundations,* Japanese society of Soil Mechanics and Foundation Engineering, Vol.12, No.4, pp.45-63.

Oda, M. (1972[2]). "Initial fabrics and their relations to mechanical properties of granular material", *Soils and Foundations,* Japanese society of Soil Mechanics and Foundation Engineering, Vol.12, No.1, pp.17-36.

Oda, M. (1974). "A mechanical and statistical model of granular material", *Soils and Foundations,* Japanese society of Soil Mechanics and Foundation Engineering, Vol.14, No.1, pp.13-27.

Oda, M. (1977). "Co-ordination number and its relation to strength of granular material", *Soils and Foundations,* Japanese society of Soil Mechanics and Foundation Engineering, Vol. 17, No. 2, pp.29-42.

Oda, M., Mehrabadi, M. M. and Nemat-Nassar, S. (1982). "A statistical study of fabric in a random assembly of spherical granules", *International Journal for Numerical and Analytical Methods in Geomechanics*, Vol.6, pp.77-94.

Ohde, Y., Ikemizu, M., Okamoto, H., Yokoyama, T. and Shibata, S. (1989). "Cavitation history effect of a water-metal Berthelot tube system interpreted by an elaborated gas trapping crevice model", *Journal of Physics D-Applied Physics*, Vol.22, No.11, pp.1721-1727.

Ovando-Shelley, E. (1986). "Stress-strain behaviour of granular soils tested in the triaxial cell", *Doctor of Philosophy Dissertation in Faculty of Engineering,* Imperial College of Science and Technology, London.

Öberg, A. L. and Sällfors, G. (1995). "A rational approach to the determination of the shear strength parameters of unsaturated soils", *Proceedings of First International conference on Unsaturated Soils*, Paris, Vol.1, pp.151-158.

Papadopoulos, J. M. (1986). "Incremental deformation of an irregular assembly of particles in compressive contact", *Doctor of Philosophy Dissertation in Mechanical Engineering,* Massachusetts Institute of Technology, Cambridge, MA.

Petrucci, R.H. (1989). *General Chemistry: Principles and Modern Applications*, Macmillan Publishing Co., New York.

Princen, H. M. (1968). "Capillary phenomena in assemblies of parallel cylinders", *Journal of Colloid and Interface Science*, Vol.30, No.1, pp.69-75.

Restagno, F., Bocquet, L., Crassous, J., Charlaix, E. (2002). "Slow kinetics of capillary condensation in confined geometry: experiment and theory", *Colloids and Surfaces A: Physicochemical Engineering Aspects*, Vol.206, pp.69-77.

Richards, B. G. (1966). "The significance of moisture flow and equilibria in unsaturated soil in relation to the design of engineering structures built on shallow foundations in Australia", *Symposium on Permeability and Capillarity*, ASTM, Atlantic City, NJ.

Ridley, A. M. and Wray, W. K. (1996). "Suction measurement: a review of current theory and practices", *Proceedings of First International conference on Unsaturated Soils, 1995*, Paris, Vol.2, pp.1293-1322.

Ridley, A. M. and Burland, J. B. (1993). "A new instrument for the measurement of soil moisture suction", *Geotechnique*, Vol.43, No.2, pp.321-324.

Rifa'i, A., Laloui, L. and Vulliet, L. (2002). "Volume measurement in unsaturated triaxial test using liquid variation and image processing", *Unsaturated Soils*, Jucá, de Campos and Marinho (eds), Swets and Zellinger, Lisse, pp.441-445.

Roscoe, K. H., and Burland, J. B. (1968). "On the generalised stress-strain behaviour of wet clay", *Engineering Plasticity*, J. Heyman and F.A. Leckie (eds.), Cambridge.

Rumpf, H. (1961). "The strength of granules and agglomerates", *Proceedings of International Symposium on Agglomeration*, Philedalphia, pp.379-418.

Sako, K., Kitamura, R., Yamada, M. (2001). "A consideration on effective cohesion of unsaturated sandy soil", *Powders and Grains*, Kishino (ed.), Swets and Zeitlinger, Lisse, pp.39-42.

Santagata, M. C. (1998). "Factors affecting the initial stiffness and stiffness degradation of cohesive soils", *Doctor of Philosophy Dissertation in Civil and Environmental Engineering,* Massachusetts Institute of Technology, Cambridge, MA.

Sheahan, T. C. (1991). "An experimental study of the time-dependent undrained shear behavior of resedimented clay using automated stress-path triaxial equipment", *Doctor of Science Dissertation in Civil and Environmental Engineering,* Massachusetts Institute of Technology, Cambridge, MA.

Sheahan, T. C. and Germaine, J. T. (1992). "Computer automation of conventional triaxial equipment", *Geotechnical Testing Journal*, Vol.15, No.4, pp.311-322.

Sjoblom, K. J. (2000). "The mechanisms involved during the desaturation process of a porous matrix", *Doctor of Philosophy Dissertation in Civil and Environmental Engineering,* Massachusetts Institute of Technology, Cambridge, MA.

Sjoblom, K. J. and Germaine, J. T. (2001). "Method and apparatus for the direct measurement of moisture characteristics of porous samples of soil, wood, concrete and the like." *U.S. Patent No. 6,234,008.*

Skempton, A. W. (1954). "The pore pressure coefficient A and B", *Geotechnique*, Vol.4, pp.143-147.

Smith, W. O., Foote, P. D. And Busang, P. F. (1929). "Packing of homogeneous spheres", *Physical Review*, Vol.34, pp.1271-1274.

Soulié, F., Cherblanc, F., El Youssoufi, M. S. and Saix, C. (2006). "Influence of liquid bridges on the mechanical behaviour of polydisperse granular materials", *International Journal for Numerical and Analytical Methods In Geomechanics*, Vol.30, pp.433-468.

Subbash, G., Nemat-Nasser, S., Mehrabadi, M. M., Shodja, H. M. (1991). "Experimental investigation of fabric-stress relation in granular materials", *Mechanics of Materials,* Vol.11, pp.87-106.

Tamagnini, R. (2004). "An extended Cam-clay model for unsaturated soils with hydraulic hysterisis", *Geotechnique*, Vol.54, No.3, pp.223-228.

Tarantino, A. and Mongiovi, L. (2000). "Experimental investigations on the stress governing unsaturated soil behaviour at medium to high degrees of saturation", *Experimental*

Evidence and Theoretical Approaches in Unsaturated Soils, Tarantino & Mancuso (eds), Balkema, Rotterdam, pp.3-20.

Tarantino, A., Bosco, G. and Mongiovi, L. (2000). "Response of the IC tensiometer with respect to cavitation", *Proceedings of Asian Conference on Unsaturated Soils*, Singapore, pp.309-314.

Terzaghi, K. (1924). "Die theorie der hydrodynamischen Spannungserscheinungen und ihr erdbautechnisches Anwendungsgebiet", *Proceedings of the international congress for applied mechanics,* Delft, pp.288-294.

Terzaghi, K. (1943). *Theoretical Soil Mechanics*, John Wiley and Sons, Inc., New York.

Ting, J. M-M. (1981). "The creep of frozen sands: qualitative and quantitative models", *Doctor of Science Dissertation in Civil and Environmental Engineering,* Massachusetts Institute of Technology, Cambridge, MA.

Toker, N. K. (2002). "Improvements and reliability of the MIT tensiometer and studies on soil moisture characteristic curves", *Master of Science Dissertation in Civil and Environmental Engineering,* Massachusetts Institute of Technology, Cambridge, MA.

Toker, N. K., Germaine, J. T. and Culligan, P. J. (2003). "Comment on 'Cavitation during desaturation of porous media under tension' by Dani Or and Markus Tuller", *Water Resources Research*, Vol.39, No.11.

Toker, N. K., Germaine, J. T., Sjoblom, K. J. and Culligan, P. J. (2004). "A new technique for rapid measurement of continuous SMC curves", *Geotechnique*, Vol.54, No.3, pp.179-186.

Tordesillas, A., Walsh, S. D. C. and Gardiner, B. S. (2004). "Bridging the length scales: micromechanics of granular media", *BIT Numerical Mathematics*, Vol.44, pp.539-556.

Towner, G. D. (1983). "Effective stresses in unsaturated soils and their applicability in the theory of critical state soil mechanics", *Journal of Soil Science*, Vol.34, pp.429-435.

Trentadue, F. (2004). "An equilibrium-based approach for the micromechanical modelling of a non-linear elastic granular material", *Mechanics of Materials*, Vol.36, pp.323-334.

Trevana, D. H. (1987), *Cavitation and Tension in Liquids*, IOP Publishing Ltd., Philadelphia.

Tuller, M., Or, D. and Dudley, L. M. (1999). "Adsorption and capillary condensation in porous media: Liquid retention and interfacial configurations in angular pores", *Water Resources Research*, Vol.35, No.7, pp.1949-1964.

Urso, M.E.D., Lawrence, C.J. and Adams, M.J. (2002). "A two-dimensional study of the rupture of funicular liquid bridges", *Chemical Engineering Science*, Vol.57, pp.677-692.

Van der Waals, J. D. (1893). "The thermodynamic theory of capillarity under the hypothesis of a continuous variation of density", *Verhandel. Konink. Akad. Weten. Amsterdam*, Sect.1, Vol.1, No.8.

Vanapalli, S. K., Ferdlund, D. G., Puhafl, D. E. and Clifton, A. W. (1996). "Model for the prediction of shear strength with respect to soil suction", *Canadian Geotechnical Journal*, Vol.33, No.3, pp.379-392.

Vanapalli, S. K. and Ferdlund, D. G. (2000). "Comparison of different procedures to predict unsaturated soil shear strength", *Advances in Unsaturated Geotechnics, ASCE 99*, pp.195-209.

Vaunat, J., Romero, E. and Jommi, J. (2000). " An elastoplastic hydromechanical model for unsaturated soils." *Experimental Evidence and Theoretical Approaches in Unsaturated Soils*, Tarantino & Mancuso (eds), Balkema, Rotterdam, pp.121-138.

Wapner, P. G. and Hoffman, W. P. (2002). "Partial wetting phenomena on nonplanar surfaces and in shaped microchannels", *Langmuir: the American Chemical Society Journal of Surfaces and Colloids*, Vol.18, No.4, pp.1225-1230.

Wheeler, S. J. and Sivakumar, V. (1992). "Critical state concepts for unsaturated soils", *Proceedings of 7th International Conference on Expansive Soils*, Dallas, Vol.1, pp.167-172.

Wheeler, S. J. and Sivakumar, V. (1993). "Development and application of a critical state model for unsaturated soil", *Predictive Soil Mechanics*, G.T. Houlsby & A.N. Schofield (eds), pp.709-728.

Wheeler, S. J. and Sivakumar, V. (1995). "An elasto-plastic critical state framework for unsaturated soil", *Geotechnique*, Vol.45, No.1, pp.35-53.

Williams, J. R. and O'Connor, R. (1995). "A linear complexity intersection algorithm for discrete element simulation of arbitrary geometries", *Engineering Computations*, Vol.12, No.2, pp.185-201.

Wong, J. C., Rahardjo, H., Toll, D. G. and Leong, E. C. (2001). "Modified triaxial apparatus for shearing-infiltration test", *Geotechnical Testing Journal*, Vol.24, No.4, pp.370-380.

Yang, R. Y., Zou, R. P. and Yu, A. B. (2003). "Numerical study of packing of wet coarse uniform spheres" *Particle Technology and Fluidization, AIChE Journal*, Vol.49, No.7, pp.1656-1666.

Zapata, E. C., Houston, N. W., Houston, L. S. and Walsh, D. K. (2000). "Soil-water characteristic curve variability", *Advances in Unsaturated Geotechnics*, ASCE, Vol.99, pp.86-87.

Zhang, D. Z. (2005). "Evolution of enduring contacts and stress relaxation in dense granular medium", *Physical Review E: Statistical, Nonlinear and Soft Matter Physics*, Vol.71, No.4, p.41303-41400.

Zheng, Q., Durben, D. J., Wolf, G. H. and Angell, C. A. (1991). "Liquids at large negative pressures: water at the homogeneous nucleation limit", *Science*, Vol.254, pp.829-832.

Zheng, J. and Streator, J. L. (2003). "A micro-scale liquid bridge between two elastic spheres: Deformation and stability", *Tribology Letters*, Vol.15, No.4, pp.453-464.

Znidarcic, D., Illangasekare, T. and Manna, M. (1991). "Laboratory testing and parameter estimation for two-phase flow problems", *Geotechnical Special Publication 27, ASCE*, pp.1089-1099.